Population Balance Model-Based Optimal Control of Batch Crystallisation Processes for Systematic Crystal Size Distribution Design

by

Erum Aamir

A doctoral thesis submitted in partial fulfilment of the requirements for the award of Doctor of Philosophy of Loughborough University

Department of Chemical Engineering

June 2010

Certificate of Originality

Dedicated to my husband and our parents

Abstract

During recent years crystallisation has found applications in many chemical industries, such as pharmaceutical, petrochemical, micro-electronics and food industries. Crystallisation is a basic step for purification or separation for a large variety of organic, inorganic and pharmaceutical compounds. Most of the product qualities are directly related to the shape of the crystal size distribution (CSD). The main difficulty in batch crystallisation processes is to accomplish a uniform and reproducible CSD. On-line control during the process allows for improved crystalline product quality, shorter process times and reduction or elimination of compromised batches. The actual prediction and estimation of the shape of the distribution at the end of the batch can provide useful information for monitoring or designing the operating curve for the supersaturation controller. Model-based approaches provide consistency of the CSD, can be used for better control and also for product design by reverse engineering the process to achieve the desired CSD and shape.

This research presents a novel methodology for solving the population balance equation (PBE) for the estimation of the shape of the crystal size distribution for batch crystallisation processes. The approach combines the quadrature method of moments (QMOM) and the method of characteristics (MOCH), and provides a computationally efficient technique for the reconstruction of the whole crystal size distribution. The technique was used to estimate the kinetic parameters for the size-dependent growth and secondary nucleation, for potash alum-water system using industrial pilot plant data provided by BASF, Chemical Company. The combined technique was also used to estimate the size-dependent dissolution parameters for potash alum-water system, using laboratory scale data. The QMOM-MOCH solution approach is evaluated in a model-based dynamic optimization study, with the aim to obtain the optimal temperature profiles, which drive the system in both the supersaturated and under-saturated region, to achieve desired target CSD. Using growth, dissolution and nucleation parameters the technique was used to optimise the temperature trajectories to obtain bimodal and mono-modal distributions. The technique can serve as a soft sensor for predicting the CSD, or as a computationally efficient algorithm for off-line design or on-line adaptation of operating policies based on knowledge of the full CSD data.

Additionally, the PBE model was solved using the method of characteristics under the assumption of constant supersaturation. At constant supersaturation growth is the dominating phenomenon, yielding a simplified analytical expression for the prediction of the CSD. The research presents the new methodology for the systematic design of the setpoint operating curves for supersaturation controlled crystallisation processes, which produces a desired target crystal size distribution (CSD) at the end of the batch. A design parameter, was introduced as a function of the supersaturation and time, and is evaluated for supersaturation controlled processes. Based on the design parameter and the simplified analytical model, the supersaturation setpoint and batch time are determined using an optimisation approach to obtain a target distribution with a desired shape. Two additional methods are also proposed that use the seed in conjunction with the supersaturation setpoint design, and analytical CSD estimator for shaping the product CSD. The first approach designs a seed recipe as a mixture of crystals resulting for example from standard sieve analysis. In this approach the seed was introduced at the beginning of the batch. The second approach introduces the dynamic seeding concept, which allows an easily implementable methodology to achieve complex target CSDs using seed with mono-modal distribution as a process actuator.

These methodologies were validated for potassium dichromate-water system. Size-dependent growth kinetic parameters for the potassium dichromate-water system were identified using as experimental setup developed at Loughborough University. The experiments presented in the thesis also illustrates the simultaneous application of *in situ* Process Analytical Technology (PAT) tools, such as focused beam reflectance measurement (FBRM) for nucleation detection, attenuated total reflection (ATR) UV/Vis spectroscopy for concentration monitoring, as well as the in-line use of a Mastersizer for real-time CSD measurement in the case of the potassium dichromate in water system.

The approaches provide a comprehensive framework for model-based dynamic optimisation of crystallisation processes, which combines efficient numerical solution approaches of the PBE with the formulation of novel optimisation problems. The techniques presented include controlled dissolution, simultaneous optimisation of operating policies and seed recipes and dynamic seeding. Simulation and experimental evaluations of the proposed approaches demonstrate the potential of the techniques to provide significant improvement in the current state-of-the-art in crystallisation control.

Table of Contents

List of Figures

List of Tables

List of Symbols

a	parameter for gamma distribution give in terms of moment equation (3.6)
$a_{0,\ldots,3}$	coefficient of calibration parameters
$A_{0,\ldots,3}$	absorbance measured using ATR/UV-Vis spectrometer
$b_{0,1}$	coefficient of density calibration parameters
b	nucleation order and daughters nuclei in equation (2.5) and (2.7)
B	nucleation rate
c_i	initial concentration
$c_{p,s}$	heat capacity of slurry
$c_{p,w}$	heat capacity of water
Δh_c	heat of crystallisation
$c.v$	coefficient of variance
$C(0)$	initial concentration at time $t = 0$
$C(t)$	concentration at any time t
$C(t_f)$	final concentration at time $t = t_f$
$C(t_{batch})$	solute concentration at the end of the batch
C_{sat}	equilibrium concentration
$C_{f,\max}$	maximum acceptable concentration
$C_{sat}(t)$	equilibrium concentration at any time t
C	Celsius
C_s	solubility of a compound (Table 2.3)
C_k	simulated concentration values at the discrete time steps
$C_k^{\exp}$	experimental concentration values at the discrete time steps
d_{43}	weighted mean size diameter
d_{32}	Sauter men size diameter
d	dissolution order
d_p	diameter of the particle
D	dissolution rate
ΔE	activation energy (Table 2.2)
ΔE_g	growth rate activation energy (Table 2.3)
f	frequency
$f_n(L,t)$	crystal size distribution expressed as number density function
$f_{n,0}(L_0)$	initial seed distribution
$f_{seed}(L_0)$	initial seed distribution

$f_{n,i}$ target population density function

$f_{n,G}$ Gaussian population density function

$f_{n,LG}$ lognormal population density function

$f_{n,BM}$ bimodal population density function

$\tilde{f}_{n,i}$ simulated population density function

$f_{v,i}$ discretised simulated volume probability function

$\tilde{f}_{v,i}$ discretised target volume probability function

f_{v}^{fitted} discretised fitted volume probability function

f_{v}^{target} target volume probability function

$f(\varphi)$ correction factor for nucleation on foreign surfaces

F aggregation kernel

g growth order and breakage kernel in equation (2.5) and (2.7)

G rate of crystal growth

H Heaviside function

i empirical constant, $i = 0,1,2,...,\infty$.

k cake permeability in equation (2.1), discrete measurement steps in eq (8.2) and discrete time steps, from $k = 1,...,K$

k_b nucleation rate constant

k_{bcf} Burton, Cabrera, and Frank growth rate parameter

$k_{b,\text{hom}}$ heterogeneous nucleation constant

$k_{b,\text{het}}$ heterogeneous nucleation constant

$k_d^{'}$ mass transfer coefficient

k_d dissolution rate constant

k_g growth rate constant

k_v volumetric shape factor

l measured discretisation points from $1,...,N_d$

L characteristic length

$\overline{L}$ mean for distribution function (in chapter 3 only)

$\overline{L}_s$ mean for seed distribution

ΔL difference between two consecutive size ranges

L_l discretised sizes for measured data from $l = 1,...,N_d$

L_i particle size in interval i, and the abscissas for QMOM in equations (2.2), (2.3), (4.4), (4.5), (4.6) and (4.19)

L_m midpoints size for discretisation points in chapter 3 and mean for distribution function

$L_{\min}$ lower boundary for size range

$L_{\max}$ upper boundary for size range

L_0 initial crystal/particle size

L_f final crystal/particle size

min	minutes
$\dot{m}$	mass flow of CSD measurement
$\dot{m}_j$	mass flow of heat transfer medium in the jacket
m_{seed}	mass of seed
$m_{s,i}$	amounts of seed introduced in vessel at discrete time
m_{sol}	mass of water used as solvent
m_{slurry}	mass of slurry
M	molecular weight of the solid (Table 2.3)
$M_{w,anh}$	molecular weight for the anhydrous form of potash alum
$M_{w,hyd}$	molecular weight for the hydrated form of potash alum
n	number of terms in a series
n_e	number of evaluation points
N	empirical constant and points for smooth profile
N_b	equally spaced time intervals of Δt stages
N_d	number of discretisations
N_q	number of quadrature points
N_y	number of measured model out puts (y)
N_{df}	degrees of freedom
N_G	number of Gaussians
p	growth constant
P	oscillating period in equation (5.1) and precision matrix in equations (5.10) and (5.11)
q	dissolution constant
rpm	revolutions per minute
R	gas law constant (Table 2.3)
r_0	size of newly nucleated crystals
r_H	geometric progression ratio
s	second
s_R	residual variance
S	absolute supersaturation
$-S$	absolute dissolution
S_{sp}	supersaturation set point
$S(t)$	supersaturation at any time t
$S_{\max}$	operation boundary for supersaturation without producing nuclei
S_{MSZW}	metastable zone width
ΔS_{MSZW}	safety back-off from the MSZ limit to provide robust performance
t	time
t_{batch}	total duration of the batch
$t_{batch,\min}$	minimum batch time

t_f	final batch time, (min)
t_k	discrete time steps
$t_{f,\max}$	total batch time, (min)
$t_{growth,i}$	growth time for dynamic seed methodology
t_{next}	initial time for the next integration when nucleation event occurs
T	temperature
T_0	initial temperature at the point of seeding
T_i	initial temperature at the end of the batch
T_f	final temperature
T_{sp}	temperature setpoint
V	volume and covariance matrix in equation (5.10) and (5.11)

List of Greek letters

$\alpha_T(j)$	elements of the vector containing slopes for the temperature trajectories
α	parameter for calculating size range in equation (3.20) and is the scale parameter for gamma distribution in equation (3.2)
α_1, α_2	parameters for bimodal distribution (Chapter 3)
β	seed design vector and shape parameter for gamma distribution in equation (3.2)
$\beta_{\min}$	vectors of lower bounds on seed recipe
$\beta_{\max}$	vectors of upper bounds on seed recipe
δ	Kronecker delta
∂	partial
Δ	change
ε	cake porosity
$\overline{\varepsilon_0}$	average cake porosity of uniform sized spheres
ϕ	control design parameter
ϕ_s	surface shape factor (Table 2.3)
ϕ_v	volume shape factor (Table 2.3)
γ	growth constant
λ	parameter for gamma distribution give in terms of moment, equation (3.6)
μ_0	zeroth moment
μ_1	first moment
μ_2	second moment
μ_3	third moment
μ_4	fourth moment
μ_5	fifth moment
$\mu_{seed,3}$	third moment of seed crystals
$\mu_{N,3}$	third moment of nucleated crystals
$\mu_i(t)$	moment at any time t. where $i = 0,1,...,\infty$
θ_b	vector containing nucleation parameters
θ_d	vector containing dissolution parameters
θ_g	vector containing growth parameters
$\theta_{\min}$	vectors with specified minimum bounds for each parameter
$\theta_{\max}$	vectors with specified maximum bounds for each parameter
$\hat{\theta}$	nominal parameter vector

ρ_c density of crystal

σ_s relative supersaturation and standard deviation for seed distribution in equations (3.32), (3.36) and (3.37).

σ standard deviation

σ_{var} variance of distribution

w_i weight fractions of seed from particular sieve fractions in the final mixture and weights from quadrature approximation in equation (4.4),(4.5),(4.6) and (4.19).

w_c scaling parameter in equation (5.5)

w_j scaling parameter in equation (5.5)

$w(x)$ weighting function for orthogonal polynomials

ζ dissolution constant

$\mathcal{L}$ consecutive sieve sizes

$^\circ$ degree

τ_i discrete time steps

$\mathcal{Z}$ measure of distance along the characteristic curve.

List of Acronyms

API	Active Pharmaceutical Ingredient
ATR	Attenuated Total Reflection
CLD	Chord Length Distribution
CSD	Crystal Size Distribution
DAE	Differential Algebraic Equation
DD	Direct design
DPB	Discretised Population Balance
DMC	Dynamic Monte Carlo
DNC	Direct Nucleation Control
DQMOM	Direct Quadrature Method of Moments
FBRM	Focused Beam Reflectance Measurement
FEM	Finite Element Method
FTIR	Fourier Transform Infrared
FVM	Finite Volume Method
FQMOM	Fixed Quadrature Method of Moments
GUI	Graphical User Interface
IPA	Iso-proponal
JMT	Jacobian Matrix Transformation
MC	Monte Carlo
MoC	Method of Classes
MOCH	Method of Characteristics
MPC	Model Predicted Control
MSZ	Metastable zone
MSZW	Metastable zone width
NNLS	Non-negative least square
NMPC	Non-linear model predictive control
ODE	Ordinary Differential Equation
pdf	Population density function
PBE	Population Balance Equation
PBM	Population Balance Model

PD	Product Difference
PDEs	Partial Differential Equations
PPDC	Parallel Parent and Daughter Classes
PVM	Particle Vision Measurement
QbD	Quality by design
QMOM	Quadrature Method of Moments
ROZ	Robust operating zone
SEM	Scanning Electron Microscope
SMOM	Standard Method of Moments
SQP	Sequential Quadratic Programming
SSC	Supersaturation controlled
SSE	Sum Squared Error
SWMCL	Square weighted mean chord length
UV/Vis	Ultra-violet/Visible

Acknowledgements

I am deeply in debt to my supervisors, Dr Zoltan K Nagy and Prof Christopher D Rielly for their guidance, suggestions, constructive criticism and encouragement. Their patience and understanding helped me sail through the hard times. This research work was not possible without their endless support, guidance and devotion. I am grateful to Dr Zoltan K Nagy and Department of Chemical Engineering for awarding me the scholarship and giving me an opportunity to carry out my research.

Special thanks to Dave Smith for his help and support in the configuration of experimental setup for use of on-line Malvern Mastersizer. I would like to extend my deep gratitude to Mr Jonathan Veal from Sympatec, for taking personal interest and effort to make Sympatec Qicpic available for my use.

Special appreciation is also due to the staff of the Chemical Engineering specially Paul Izzard, Chris Manning, Jim, Terry, Kim, Monica, Steve, Mark and Tony to solve the problems related to my experimental rig and helping me meeting the deadlines for my experiments. I would also like to thank Sean and Graham for their support in the labs.

Special gratitude to my friends Heema, Savita, Mu and Bahareh for their support, trust and friendship throughout my PhD. Their support meant a lot during tough times and bad days. I would also like to thank Kevin for his friendship and support. I would also like to thank Pharmaceutical Systems Engineering (PSE) group; Rushdi, Saleemi and Krystel for their support and help.

I would like to thank my husband who encouraged me to do PhD. He managed with my hectic schedules and his support always gave me a new energy to finish my work. Last but not least my parents whose prayers and love were always a source of encouragement for me.

Chapter 1
Introduction

1.1 Background

Crystallisation is a widely used separation technique for solid-liquid separation due to its ability to provide high purity separation. Crystallisation has a wide range of applications in different industries, such as food, fine chemical and pharmaceutical industries. According to estimates, 60% of the end products in the chemical industries are manufactured as solid particles with an additional 20% using powder ingredients (Christofides *et al.*, 2008). Crystallisation is particularly used in the processing of high value-added products. Crystallisation is also used for purification and separation in the petrochemical industry. In the pharmaceutical industries, drug design methods often make use of protein crystallisation (Olesberg *et al.*, 2000; Shi *et al.*, 2005; Wiencek, 2002). Some pharmaceuticals are crystallised for special bioavailability and stability reasons during the preparation of various drug delivery devices (Garcia *et al.*, 1999; Mangin *et al.*, 2006). Crystallisation applications are also found in the microelectronics industry for silicon production for the manufacture of semiconductors (Middlebrooks, 2001). The possibility of growing pure crystals of controlled size distribution has made crystallisation one of the most important purification and separation technique in the food industries, particularly in the sugar and dairy industries (Vu *et al.*, 2006) because of stability and texture issues (Hartel, 2002; Patience *et al.*, 1999).

Most of the crystallisation applications discussed above are batch processes. Batch crystallisation is an attractive mode of operation owing to a number of reasons. Batch production is more economical when small product volumes are required. Batch crystallisation might be the only available option for manufacturing products to meet certain specific regulatory requirements and specifications, such as viscosity, toxicity, hygiene standards in food industry, or specific bio-performance and dissolution properties of active pharmaceutical ingredients. Batch crystallisation is the best available option for multi-product manufacturing (Barker and Rawtani, 2005) because it is simpler than continuous

processes and provides the flexibility of reusing the same equipment for processing different chemical substances. Batch crystallisers are also cheaper and easier to develop than continuous crystallisers (Tavare and Chivate, 1995).

The key concern in industrial batch processes is to maximise the production efficiency while improving the quality and consistency of the final products. The development of crystallisation process from laboratory to industrial scale is a tedious process, requiring high financial investment, time and effort, due to the complex hydrodynamics and kinetics (characteristics of these systems). Scientists and researchers have spent considerable time and effort in the development of batch crystallisation processes for the production of crystalline compounds (Braatz, 2002; Braatz and Hasebe, 2002; Hounslow and Reynolds, 2006) with consistent crystal properties i.e. purity, morphology, size distribution and polymorphic form. Despite batch crystallisation being one of the oldest unit operations there is a disproportionate number of problems associated with its control, resulting from the complex dynamics of the process and the generally significant uncertainties related to the exact mechanisms of the governing phenomena.

The shape of the crystal size distribution (CSD), obtained from the crystallisation process, strongly affects the efficiency of downstream operations such as filtration, drying and washing (Chung *et al.*, 2000; Mullin, 2001; Wibowo *et al.*, 2001). This may also have considerable impact on the bioavailability of the active pharmaceutical ingredient (API). Most of the product properties e.g. dissolution rate, bulk density, flow-ability, packing properties, etc. are also directly related to the CSD (Chung *et al.*, 2000). Some of these properties can be controlled by expressing them in terms of the moments of the CSD, however most properties require the detailed knowledge of the entire shape of the CSD. Knowledge and prediction of the entire shape of the distribution allows the design and adaptation of operating policies to achieve improved product quality, and to accomplish novel quality-by-design (QbD) procedures (Braatz, 2002).

The major challenge in batch crystallisation is to produce a uniform and reproducible CSD (Braatz, 2002; Wibowo and Ng, 2001), which has been addressed by several approaches in the literature (Aamir *et al.*, 2009b; Braatz and Hasebe, 2002; Chung *et al.*, 2000; Nagy *et al.*, 2008b; Worlitschek and Mazzotti, 2004). Although these approaches can provide improved consistency of the CSD, they do not address the actual design of the CSD. On-line

estimation and control during batch crystallisation offers the possibilities for improved crystal product quality, shorter process times and reduction or elimination of compromised batches (Braatz, 2002; Chiu and Christofides, 2000; El-Farra *et al.*, 2006; Nagy and Braatz, 2003a; Zhang and Rohani, 2003). The prediction and estimation of the shape of the distribution at the end of the batch can provide useful information for monitoring or designing the operating curves. Model-based approaches can be used for better predictive control (Chung *et al.*, 1999; Fujiwara *et al.*, 2005; Grosso *et al.*, 2009; Larsen *et al.*, 2006; Rawlings *et al.*, 1993; Sheikhzadeh *et al.*, 2008a, b) and also for product design by reverse engineering the process to achieve the desired CSD (Hounslow and Reynolds, 2006; Lee *et al.*, 2002; Rusli *et al.*, 2006). Most work in literature has been carried out to obtain large crystals with narrow distribution. The major focus of this research is to develop model-based control strategies which are able to predict and control the shape of the crystal size distribution (CSD) at the end of the batch, opening the ways towards novel product engineering and integrated process design approaches.

1.2 Research methodology

A schematic of the overall research methodology is shown in Figure 1.1. The research is comprised of population balance modelling of seeded batch crystallisation processes with the development of efficient solution approaches, simulation studies and experimental programme for the implementation of the developed open-loop optimal control strategies. Experimentation was carried out to gather the measured data for state variables such as temperature, concentration and CSD using on-line, *in situ* and off-line measurement techniques, as shown in Figure 1.1. The population balance model was initialised using the information gathered from these experiments such as moments calculated from the seed distribution, initial concentration, batch times and temperature trajectories. The population balance model was solved using an efficient and novel approach based on the combination of the quadrature method of moments (QMOM) and method of characteristics (MOCH). The QMOM technique was used to calculate the dynamic evolution of the moment of the distribution, the change in supersaturation with time, $S(t)$, and to conserve the overall mass balance, as shown in Figure 1.1. The MOCH was used to obtain the dynamic evolution of the entire CSD throughout the batch, while using the dynamic supersaturation profile obtained from QMOM.

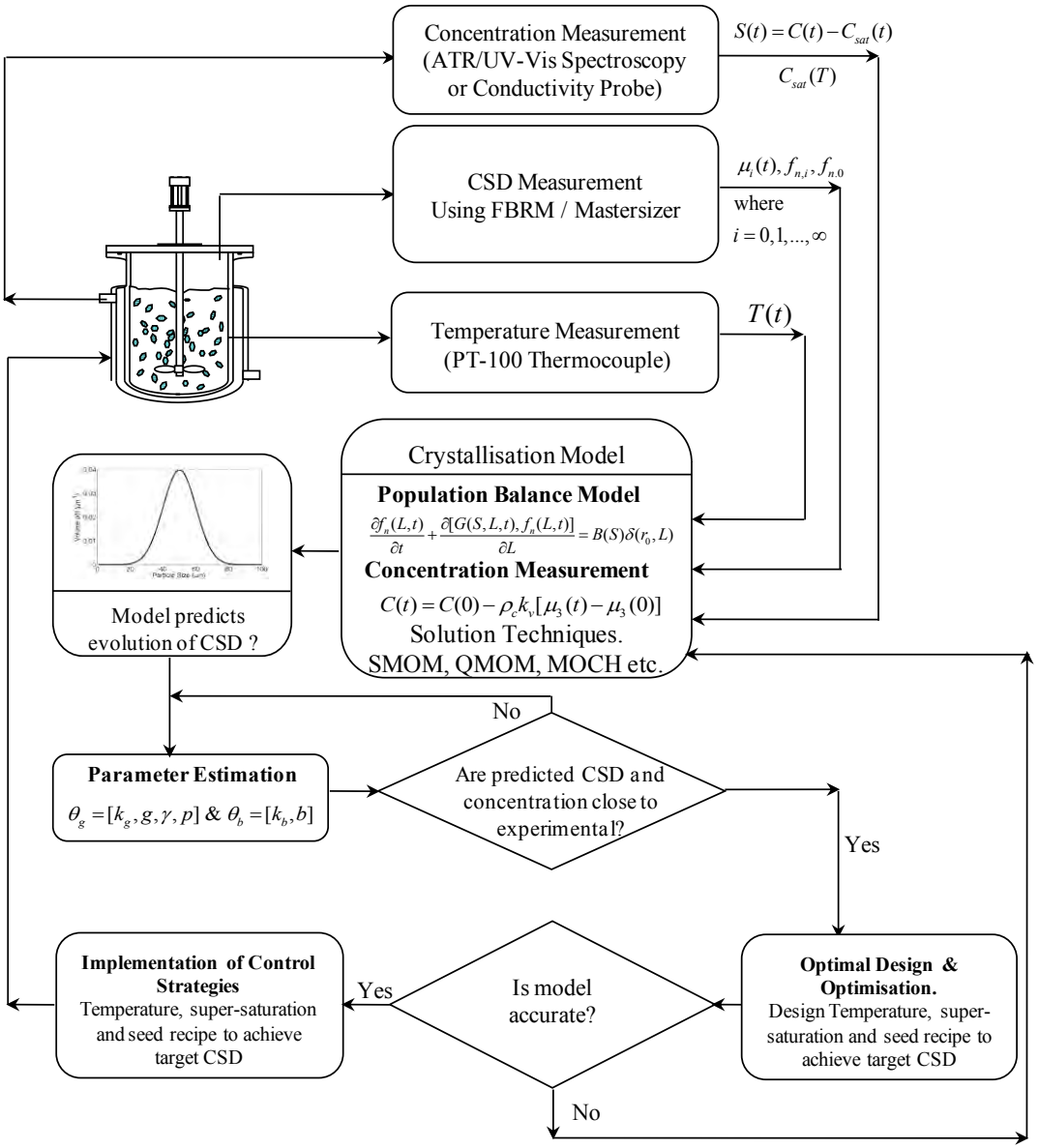

Figure 1.1: The mains steps for the development of model predictive control algorithms for CSD shape control.

Empirical relationships were used to model the growth, dissolution and nucleation kinetics for the crystallisation processes. The model parameters were estimated using concentration and volume population density function measurements from the experiments. The parameters were determined to fit the experimental concentration and CSD at the same time. After parameter estimation the model validation was carried out for new sets of experiments. Once the models were validated, off-line optimisation was carried out, using the model. To

achieve the required shape of the crystal size distribution, temperature and supersaturation trajectories as well as seed mass and seed distributions were optimised, as shown in Figure 1.1. The optimal results were validated using laboratory scale experiments. The model systems used in the research were:

- Potash alum in water
- Potassium dichromate in water

For the qualitative and quantitative monitoring of the crystallisation experiments and products a series of *in situ* process analytical technology (PAT) tools, such as focused beam reflectance measurement (FBRM), conductivity, attenuated total reflectance (ATR) UV/Vis spectroscopy, and on-line laser diffraction based CSD measurement were used along with off-line optical and scanning electron microscopy (SEM).

1.3 Aims and objectives

The overall aim of this research was to develop population balance model-based optimal control approaches for batch crystallisation processes for CSD design. The following objectives were identified to achieve the overall aim of the research:

- To identify approaches to reconstruct the CSD in real-time, based on computationally efficient algorithms.
- To determine the kinetics involved in the studied crystallisation processes, which can represent the processes.
- To develop an algorithm which can be applied for the solution of population balance equations with generic size-dependent growth, dissolution and nucleation kinetics and can provide a generic framework for the efficient solution of PBEs.
- Experimental determination of the key process parameters such as temperature, concentration and CSD, and their use for parameter estimation of the kinetics of the systems.
- Validation of the kinetic parameters using experimental data.
- Evaluation and optimisation of temperature and supersaturation trajectories, and seed recipes to obtain the required shape of the product CSD.

- To develop a systematic methodology for the analysis and design of supersaturation controlled crystallisation processes.
- To evaluate the effect of the seed preparation method on the product CSD and on the prediction ability of the models.
- To carry out the experimental evaluation of the developed control methods using two different inorganic compounds:
    - Potash alum-water system
    - Potassium dichromate-water system

1.4 Main contribution of this work

The main contributions of the work presented in the thesis can be summarised as follows:

- Development of a new solution approach for population balance equations (PBEs), which combines the advantages of QMOM and the MOCH to provide a computationally efficient technique for the prediction of the entire CSD. The algorithm (combined QMOM-MOCH) can be applied for the solution of population balance equations with generic size-dependent growth, dissolution and nucleation kinetics providing a general framework for the efficient solution of PBEs.

- Determination of optimal temperature trajectories, which take into account growth, nucleation and dissolution mechanisms to produce the required shape of the product CSD. The approach is evaluated for the potash alum-water system for which the size-dependent growth and secondary nucleation parameters were identified based on industrial pilot scale experimental data, and size-dependent dissolution kinetics was obtained from laboratory experiments.

- Development of an analytical CSD estimator, which can be used in the case of supersaturation controlled, growth-dominated processes. It is shown that the proposed approach provides a computational efficient CSD estimation technique, which can be used for off-line parameter estimation, crystallisation design or for on-line estimation and control.

- Development of a direct design approach for supersaturation controlled (SSC) crystallisation systems, in which the supersaturation trajectories can be defined in terms of the temperature trajectories. Temperature trajectories in the time domain can be designed for a desired supersaturation set-point, S_{sp}, from the solubility curve, concentration and moments of the crystal size distribution. The experimental validation of the direct design approach is also carried out for the potassium dichromate-water system. For the experimental investigation an experimental setup was specially designed, which includes *in situ* process analytical technology (PAT) tools, such as focused beam reflectance measurement (FBRM), attenuated total reflectance (ATR) UV/Vis spectroscopy, as well as on-line CSD measurement using Malvern Mastersizer.

- Systematic design of optimal seed recipes for crystallisation processes, to achieve a desired target CSD with a desired shape. The seed recipe is obtained by blending different mixtures of seeds resulting from sieve analysis. The optimal seed recipe is obtained by solving a constrained non-linear optimisation problem with the objective to achieve a desired shape of the CSD at the end of the batch, while operating within equipment and operational constraints (e.g. fixed temperature profile). One of the novelty of the proposed method is that the optimisation automatically selects between existing seed fractions, which practically would result from standard sieve analysis, and simultaneously determines the amounts and sieve fractions (with fixed CSDs), which need to be mixed to produce the seed. Hence the proposed approach provides a practical framework for seed recipe design. A systematic methodology for dynamic seeding by introducing a mono-modal seed in the crystalliser during the crystallisation processes to obtain the desired shape of the CSD is also presented in this thesis. The novel dynamic seeding methodology is the first approach that proposes to use seeding as an actuator rather than initial condition for the crystallisation process.

- Experimental evaluation of the seed recipe design approach for the potassium dichromate-water system, for which size-dependent growth kinetic parameters have been identified from data obtained using the specially designed experimental setup

with ATR/UV-Vis based *in situ* concentration and on-line CSD measurements. The seed recipe optimisation methods are designed for processes with generic apparent size-dependent growth kinetics.

1.5 Thesis structure

A brief description of each chapter of the thesis is as follows:

Chapter 2: Literature review: This chapter presents a review of the literature to provide a relevant context of the research. The chapter is divided in three main parts. In the first part the main mechanisms and kinetics of crystallisation processes are summarised and a selection of relationships for modelling of growth, dissolution and nucleation are presented. The second part provides an overview of different numerical techniques available for the solution of PBE for the modelling of crystallisation processes. The last part provides a brief review of the optimisation and control strategies used for crystallisation processes.

Chapter 3: Techniques to reconstruct the CSD from moments: In Chapter 3 techniques to reconstruct the crystal size distribution using moments have been evaluated. The advantages and the limitations of the techniques are highlighted.

Chapter 4: Combined QMOM-MOCH approach for the efficient solution of population balance equations for batch crystallisation processes: A novel methodology for the solution of PBEs is presented in this chapter. The methodology is developed to take into account size independent or size-dependent dissolution and growth, as well as secondary nucleation kinetics for the modelling of batch crystallisation processes. The approach provides a numerically very efficient framework for the prediction of the shape of the entire CSD for the whole duration of the batch.

Chapter 5: Model identification and validation for the potash alum-water system: The results of the industrial pilot plant experiments for the potash alum-water system are presented in this chapter. Details of materials, experimental conditions and experimental results are provided. Using the experimental data, the parameter estimation and validation has been carried out for the size-dependent growth and secondary nucleation mechanisms. For the estimation of the kinetic parameters for the size-dependent dissolution, experiments

were carried out using a laboratory scale setup. The kinetic parameters for growth, nucleation and dissolution have been identified and validated.

Chapter 6: Dynamic optimisation of temperature trajectories for shaping the product CSD: Temperature trajectories were optimised to obtain the desired shape of the product CSD. These trajectories take into account growth, nucleation and dissolution mechanisms. For the efficient solution of population balance equation, the combined QMOM-MOCH approach (described in Chapter 4) has been used.

Chapter 7: A systematic framework for CSD control of supersaturation controlled (SSC) crystallisation processes, using direct design (DD), seed recipe optimisation and dynamic seeding: The chapter presents the development of an analytical CSD estimator, which can be used in the case of supersaturation controlled, growth-dominated processes, for off-line parameter estimation, crystallisation design or for on-line estimation and control. Based on the analytical estimator a direct design (DD) approach has been developed for supersaturation controlled (SSC) crystallisation systems, in which the constant supersaturation trajectories in the phase diagram can be defined in terms of temperature trajectories, in the time domain, to produce a desired CSD. A novel SSC design parameter is introduced, which can be used for the systematic analysis of the correlation between batch time and supersaturation and their effect on the product CSD. The chapter also presents a novel framework for the simultaneous SSC design and seed recipe optimisation, and introduces the concept of dynamic seeding for CSD control.

Chapter 8: Experimental evaluation of the direct design (DD) approach for SSC crystallisation processes for shaping the CSD: The chapter presents experimental results for the model identification and validation for the potassium dichromate-water system. Cubic and linear temperature profiles were implemented, and the dynamic concentration and CSD measurements were used for parameter identification and model validation. In the second part of the chapter the experimental results are presented, which were carried out to test the direct design approach.

Chapter 9: Experimental and simulation-based evaluation of seed quality and seed recipe design for shaping the product CSD in batch crystallisation: The first part of the chapter provides a detailed evaluation of the effect of various seed preparation methods on

the final product CSD for the batch cooling crystallisation of potassium dichromate in water. Various seeds (crystalline-sieved, milled-washed-sieved and milled-sieved) were used in the experiments, and the effect of the seed quality was investigated using various PAT tools. In the second part of the chapter the experimental evaluation of seed recipe design was carried out for the potassium dichromate-water system. Results and detailed discussion for these experiments are provided.

Chapter 10: Conclusions and recommendation for future work: This chapter provides a summary of the main simulation and experimental results presented in the thesis. The conclusions of the research along with proposals for future work are also presented.

Chapter 2
Literature review

2.1 Introduction

Crystallisation processes can be challenging to control because of the complex non-linear dynamics associated with variations in solution kinetics and non-ideal mixing. The first section of the chapter provides an overview of crystallisation processes followed by a review of the methods for modelling of batch crystallisation processes and on overview of the solution approaches for the population balance equation. A brief presentation of the main measurement techniques used for different state variables is also presented. A concise summary of the literature related to the optimisation and control of crystallisation processes is provided.

2.2 The crystallisation process

2.2.1 Fundamentals of crystallisation processes

A significant proportion of materials are produced and marketed in crystalline form (Braatz *et al.*, 2002). According to statistics 90% of the Active Pharmaceutical Ingredients (API's) are found in crystalline form (Choong and Smith, 2004a). Crystallisation may occur as the formation of solid particles from a vapour, as solidification of a liquid melt, or as the formation of dispersed solids from a solution. Hence the formation of solid particles requires a phase change.

The concepts of solubility, supersaturation and metastable zone width (MSZW) are vital in developing and characterising the behaviour of crystallisation system. The solubility is defined as the amount of a substance (solute) that can be dissolved in a given amount of solvent at given set of temperature and pressure conditions. A saturated solution is defined as the solution that is in equilibrium with excess of the solute present in the solution. Under certain conditions, a solution can dissolve more solute than defined by the condition of

saturation at a particular temperature and is referred to as supersaturated solution. Supersaturation is the main driving force for crystallisation processes and is often expressed as the difference in concentration of the solute (C) and the saturation concentration at a particular temperature (C_{sat}), called as absolute supersaturation: $S = C - C_{sat}$, with units consistent with the units of the concentrations (e.g. kg solute/kg solvent or kg solute/kg solution). Alternatively the relative supersaturation can also be used, which is defined as: $\sigma_s = (C - C_{sat}) / C_{sat}$, which is a dimensionless quantity.

Crystallisation from solution involves at least a two component system: a solute and a solvent. The phase relationship of the system can be illustrated by a composition versus temperature $(C-T)$ diagram known as the equilibrium phase diagram. In the equilibrium phase diagram, shown in Figure 2.1, there are two curves: solubility curve and nucleation curve. The solubility curve AB is determined by thermodynamics and is a function of temperature, solvent and impurities present in the system (which may influence e.g. the solvent activity). At the solubility curve the solution is said to be in saturation equilibrium. The curve CD is the nucleation curve where the spontaneous nucleation starts. The nucleation curve is thought of as a region where the nucleation rate increases rapidly rather than a sharp boundary. These two curves divide the phase diagram in three important zones, as shown in Figure 2.1:

- Undersaturated zone - a region in which crystals present will dissolve (region below equilibrium solubility curve AB). The dissolution rate of disappearing crystals depends on the degree of undersaturation, which is expressed similarly to the supersaturation.
- Metastable zone - a supersaturated region in which crystals will grow (region that lies in between the equilibrium solubility curve AB and nucleation curve CD) with a rate defined by the level of supersaturation. The metastable limit is not a thermodynamic property and kinetically not very well defined (Barrett and Glennon, 2002) . It depends on a number of parameters such as temperature, rate of generating the supersaturation, solution history, impurities and fluid dynamics. The metastable zone width (MSZW) may vary to different extents for different systems and is said to be the point after which continuous nucleation occurs. Seed crystals would grow within the MSZW but no significant amount of new nuclei should form. MSZW is

therefore an important property in assessing the tendency of a system to crystallise and in deciding the crystallisation technique. Many techniques have been suggested and used to determine the MSZW and solubility curve, including the use of Focused Beam Reflectance Measurement (FBRM), turbidity probe, attenuated total reflectance (ATR) spectroscopy, calorimetry and image analysis (Barrett and Glennon, 2002; Kougoulos *et al.*, 2005; Simon *et al.*, 2009a, b). Information about the MSZW has been used for the estimation of the nucleation kinetics (Nagy *et al.*, 2008c). In other words, optimum crystallisation processes can only be accomplished if the MSZW is known and controlled during the entire process. This necessitates control strategies capable of using the online information measured through sensors.

- Labile or unstable zone - a supersaturated region in which solution will nucleate spontaneously (region above the nucleation curve CD).

Supersaturation can be created in crystallisers by different modes. The most widely used method is by cooling a solution through indirect heat exchange. This is the preferred approach when the solubility of the solute decreases significantly with temperature and hence the solution becomes supersaturated. In Figure 2.1, cooling trajectory is shown by $(abcd)$. Starting from point a in the undersaturated region, the equilibrium solubility curve is crossed at point b and enters into the metastable region.

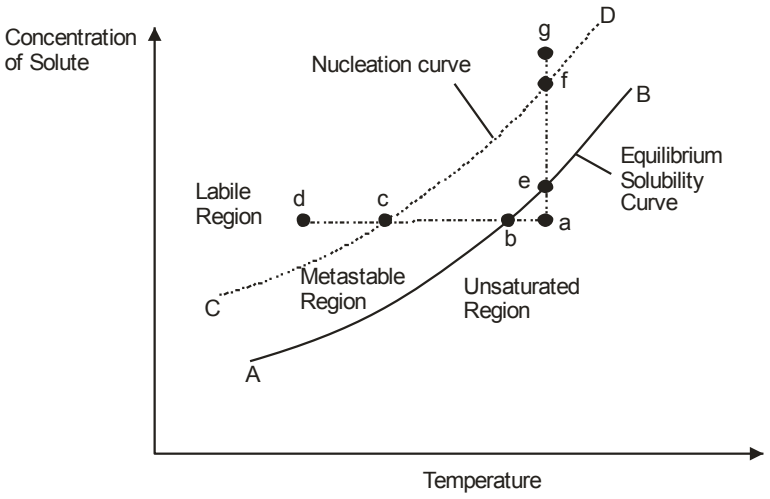

Figure 2.1: Supersaturation in crystallisation processes (Smith, 2005).

As soon as the system crosses the solubility curve and enters the metastable region, the solution becomes supersaturated. In Figure 2.1, crystallisation will not start until it has been sub-cooled to point c on the nucleation curve. Evaporation of solvent is another mode to generate supersaturation in the system and is often used when the solute has weak dependency of solubility on temperature. Solvent is removed gradually from solution by evaporation and this increases the concentration of the solute in the solution. In Figure 2.1, evaporation trajectory is shown by $(aefg)$. Starting from point a in the undersaturated region, the equilibrium solubility curve is crossed at point e and enters into the metastable region by slowly removing the solvent by evaporation. Crystallisation will not start until the concentration reaches point f on the nucleation curve by evaporating the solvent.

Another way to create supersaturation in crystallisation process is to add an extraneous substance, generally known as anti-solvent. The selection of anti-solvent depends on several factors:

- should be miscible with the solvents;
- must change the solubility of solute in the primary solvent;
- its polarity should be different from the primary solvent polarity.

The disadvantage of this technique is an added unit for the separation of this extraneous material, which can add complexity to the solution and increase cost. A pH switch can also be used to adjust the solubility of sparingly soluble salts in aqueous solution. Alternatively, a chemical reaction can produce solute (precipitation) when the concentration of the reaction product is higher than its solubility in a solution. Therefore, the solution becomes supersaturated with respect to the new compound. This is an attractive option when reaction and separation can be done simultaneously. Some of the above mentioned techniques can also be combined together to induce supersaturation in the system such as the combined cooling-evaporation method known as vacuum crystallisation or the combined cooling-antisolvent addition method (Nagy *et al.*, 2006a, b, 2008b; Woo *et al.*, 2009a; Zhou *et al.*, 2006a).

The main steps for the development of a typical crystallisation process can be summarised as:

- To determine the solubility of a substance in solvent. For crystallisation to occur the solution should be in a supersaturated state at the process temperature. Otherwise, the system is under-saturated and solids will dissolve. Thus determination of the solubility curve for a specific system is a crucial step in crystallisation design.

- Selection of the mode to induce supersaturation in the system. The most common approach is either to follow a cooling profile in time, to use evaporation of the solvent (Tavare and Chivate, 1977) or the addition of a poor solvent (anti-solvent). Some of these techniques can also be combined together to induce supersaturation in a system. Another attractive option includes chemical reaction (precipitation).

- To determine the metastable zone width in which crystals will grow and nucleation can be avoided.

The major interest in the design and control of crystallisation processes has been directed towards avoiding excessive nucleation and very broad distributions. This is because many problems in downstream processes can be attributed to poor crystal characteristics established in the crystallisation step. Table 2.1 summarizes the potential problems that can be created at the crystallisation step for the downstream processes. The CSD may contain too many fines, can be too broad or too narrow and the average crystal size may be too large or too small. For example an unacceptably long filtration time can be caused due to small average crystal size or wide crystal size distribution. Similarly, fines from the crystalliser can also clog the filter medium. Cake permeability (k) and porosity (ε) are the most important variables, which can be influenced by the CSD. These properties can be related to CSD by equations (2.1)-(2.3). Permeability can be estimated using the generalized Blake-Kozeny equation (MacDonald *et al.*, 1991):

$$k = \frac{1}{180}\frac{\varepsilon^3}{(1-\varepsilon)^2}\left(\frac{\mu_2}{\mu_1}\right)^2, \tag{2.1}$$

where μ_1 and μ_2 are the first and second moments. The cake porosity can be determined using the CSD (Ouchiyama and Tanaka, 1984) by

$$\varepsilon = 1 - \frac{\sum_{i=1}^{m} L_i^3 f_{n,i}}{\sum_{i=1}^{m} (L_i - L_m)^3 H(L_i - L_m) f_{n,i} + \frac{1}{\bar{n}} \sum_{i=1}^{m} [(L_i - L_m)^3 - (L_i - L_m) H(L_i - L_m)] f_{n,i}}, \tag{2.2}$$

$$\bar{n} = 1 + \frac{4(7 - 8\bar{\varepsilon}_0) L_m}{13} \frac{\sum_{i=1}^{m} (L_i + L_m)^2 [1 - \frac{3}{8} \frac{L_m}{(L_i + L_m)}] f_{n,i}}{\sum_{i=1}^{m} [L_i^3 - (L_i - L_m)^3 H(L_i - L_m)] f_{n,i}}, \tag{2.3}$$

where H is the Heaviside function, L_m is the mean particle size, L_i is the particle size in interval i, $f_{n,i}$ is the number fraction of particles in the size interval i, $\bar{\varepsilon}_0$ is the average porosity of uniformly sized spheres.

Table 2.1: Potential problems related to CSD in crystallisation and downstream processes.

Equipment	Potential Problems	Possible Crystal Size Distribution Sources				
		Too much fines	CSD too wide	CSD too narrow	Avg. size too small	Avg. size too large
Filtration	Filtration time is too long		√		√	
	Filter medium is easily clogged	√				
Washing	Washing time is too long		√		√	
	Solvent requirement is too high leading to expensive recovery cost		√		√	
Re-crystallisation	If impurity inclusion level is too high, re-crystallisaiton is necessary					√
Drying	Drying time is too high		√		√	
	Too much dust in drying system	√				
Deliquoring	Deliquoring time to achieve a specified saturation level is too long.		√		√	
	Residual liquid content of the cake is too high	√		√		

Long washing and drying time can be because of small average crystal size and wide CSD (Wakeman and Tarleton, 1999). Another commonly encountered problem is the reduction in crystal purity in the form of inclusions. These inclusions are caused during crystal growth when small pockets of mother liquor are often trapped in the crystal interior. Since the

mother liquor contains the solvent and other solutes, inclusions have a significant effect on the crystal quality and re-crystallisation is the only way to purify the crystals.

To develop an integrated system for the production of solid products, which would take into account the separation/isolation as well as the downstream processing steps, it is important to control the CSD produced during the crystallisation step. Crystallisation is a complex phenomenon with highly interrelated kinetic mechanisms. To develop a model-based control strategy for CSD it is important to understand these complex mechanisms and their influence on each other. Knowledge of these kinetic mechanisms, such as nucleation, growth, aggregation and dissolution along with macroscopic phenomena is required for modelling of the crystallisation process. The overall physico-chemical process of crystallisation can be viewed in terms of the following main mechanism:0

1. Nucleation mechanism;
2. Growth/dissolution mechanisms;
3. Aggregation and breakage mechanisms.

2.2.2 Mechanisms of crystallisation processes

The primary particle formation processes, which occur during crystallisation, are nucleation, which determines the initial formation of crystals, and crystal growth, which determines the subsequent size. A further growth process is known as aggregation. Breakage may also occur due to collision of crystals with each other and walls of the container and stirrer.

Nucleation

Nucleation is the formation of a solid crystalline phase. Both the nucleation and the growth depend on the degree of supersaturation, but usually to different orders (Dixit and Zukoski, 2002; Dunham *et al.*, 1997; Garside and Davey, 1980). Nucleation mechanisms are commonly lumped into one of two categories – primary and secondary nucleation (Hounslow *et al.*, 1988; Jones, 2002; Mullin, 2001).

Primary nucleation is the formation of a solid phase from a clear liquid and it is more prevalent in un-seeded crystallisation (Hardenberg *et al.*, 2004; Jones *et al.*, 1993; Scott *et al.*, 1997). Primary nucleation is usually categorised as homogeneous nucleation and heterogeneous nucleation. Homogeneous nucleation occurs in the pure bulk solution. It is

determined by the formation of stable nuclei in a supersaturated solution, which means molecules of solute come close together to form clusters in an arranged order (Pollanen *et al.*, 2006). Heterogeneous nucleation is induced by foreign surfaces such as impurities present in the solution and can become significant at much lower supersaturation levels than homogeneous primary nucleation. However, it is difficult to distinguish between the homogeneous and heterogeneous nucleation for most practical cases.

Secondary nucleation is caused by the presence of crystals and can be induced by:

- contact of crystals with an external surface
- continuous removal of dendrites due to free energy driving force
- fluid shear
- initial breeding
- fracture/attrition

Secondary nucleation is generally more easily controlled than primary nucleation and is the most dominant mechanism in most industrial crystallisation processes (Rawlings *et al.*, 1993). Attrition can be induced by agitation or pumping and can generate significant secondary nucleation in industrial crystallisation systems. The greater the intensity of agitation the greater the rate of secondary nucleation. Table 2.2 summarises some commonly used empirical relationships to capture nucleation kinetics for particular process conditions. The modelling of nucleation is highly complex due to the variety of mechanisms, collectively termed as nucleation (Kalani and Christofides, 2002; Kumar and Ramkrishna, 1997). The types of nucleation are shown in Figure 2.2.

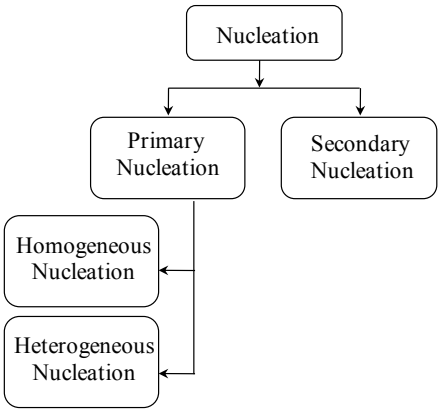

Figure 2.2: Types of nucleation.

Table 2.2: Summary of some commonly used empirical relationships for nucleation.

Mechanisms	Expression	References	Remarks
Primary Nucleation*	$B = k_b S^b$	(Mullin and Nyvlt, 1971)	
Homogeneous Nucleation	$B = k_{b,\text{hom}} \exp\left[\frac{-16\pi\sigma^3\nu^2}{3k^3T^3(\ln(\sigma_s+1))^2}\right]$	(Mullin, 2001)	
Heterogeneous Nucleation	$B = k_{b,het} \exp\left[\frac{-16\pi\sigma^3\nu^2 f(\varphi)}{3k^3T^3(\ln(\sigma_s+1))^2}\right]$	(Sohnel and Garside, 1992)	Extra factor $f(\varphi)$ corrects nucleation on foreign surfaces
Secondary Nucleation*	$B = k_b S^b \mu_2$	(Garside and Davey, 1980)	
	$B = k_b S^b \mu_3$	(Scott *et al.*, 1997)	
	$B = k_b \exp\left[-\frac{\Delta E}{T}\right] \sigma_s{}^b \mu_3^k$	(Larson and Helt, 1977)	Temperature dependent k_b
	$B = k_b \sigma_s^b \mu_3 (L_{\min})^j$	(Jones *et al.*, 1993; Matthews and Rawlings, 1996)	$L_{\min}$ is the minimum size required for a crystal to participate in collisions that produce secondary nucleation
	$B = k_b S^b N^l \mu_2^j$ $B = k_b S^b N^l \mu_3^j$	(Patience, 2002)	Includes crystal agitation and crystal-crystal effects

Note 2.1: "*" indicates that both absolute and relative supersaturation can be used. Variables are defined in nomenclature list.

Growth and dissolution

The newly born nuclei grow with time. Two successive steps are required for crystal growth:

- mass transport of solute molecules from the solution to the crystal surface by diffusion, convection or the combination of both mechanisms (see Figure 2.3); and
- incorporation of the material into the crystal lattice through surface adsorption, also described as surface reaction step, as shown in Figure 2.3.

The second step is further subdivided into a number of stages which are as follows:

- adsorption of the growth unit on the crystal surface first;
- release of part of its solvation shell, followed by the diffusion of growth unit into the adsorption layer until it is either incorporated into the lattice or leaves the adsorption layer and returns back into the solution;

- if the growth unit reaches into the layer where it can be added to the lattice, it loses the remainder of its solvation shell before its incorporation in the lattice.

The solute molecules reach the growing faces of the crystal by diffusion through the liquid phase. At the surface they become organized into the lattice space through an adsorbed layer (Volmer, 1939), as shown in Figure 2.3. Neither the diffusion step nor the surface reaction step proceeds as long as the solution is supersaturated (Granberg and Rasmuson, 2005). Since the kinetic processes occur consecutively, the solution concentration adjusts itself in such a way that the rates of the two steps are equal in a quasi steady state. In most cases, several mechanisms influence the rate of crystal growth. The processes take place in series and hence the slower mechanism will control the overall rate (Mullin, 2001). If the growth rate is limited by mass transfer through a laminar film then the growth is said to be diffusion controlled. Table 2.3 summarises some commonly used empirical relationships for the growth mechanisms used for modelling of particular conditions and hydrodynamics.

Crystal growth rate is also expressed as a rate of increase in length (Bravi and Mazzarotta, 1998; Garside and Jancic, 1978). The overall crystal growth in one characteristic dimension (L) can be expressed as:

$$G = \frac{dL}{dt} \tag{2.4}$$

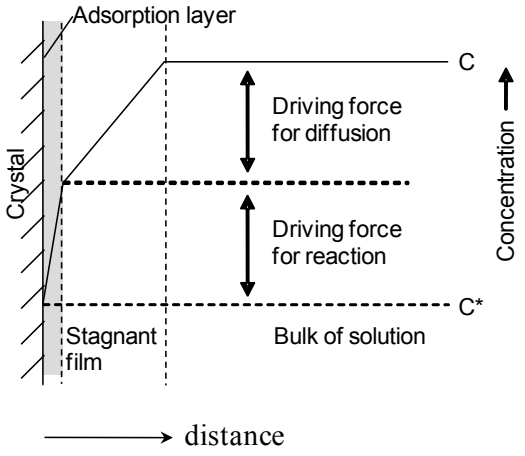

Figure 2.3: Growing crystal - solution interface.

Table 2.3: Summary of some commonly used empirical relationships for growth and dissolution.

Mechanisms	Expression	References	Remarks
Size-independent growth *	$G = k_g S^g$	(Beckmann and Randolph, 1977; Choong and Smith, 2004b)	Commonly used growth expression
Size-dependent growth*	$G = k_g S^g (1+\gamma L)^p$ $G = k_g S^g (1+\gamma L)$	(Garside and Jancic, 1978; Granberg and Rasmuson, 2005)	
Power law growth*	$G = k_g S^g L^p$	(Garside, 1984, 1985; Garside and Jancic, 1978)	
Burton , Cabrera and Frank (BCF) model of Growth	$G = \frac{k_g}{k_{bcf}} S^2 \tanh\left(\frac{k_{bcf}}{\sigma_s}\right)$,	(Larsen *et al.*, 2006; Rawlings *et al.*, 1993)	Include effects of surface defects
Arrhenius type growth expression*	$G = k_g \exp\left[-\frac{\Delta E_G}{RT}\right]\sigma_s^g$	(Rawlings *et al.*, 1993)	Semi-empirical relationship, temperature dependent k_g
Size-independent dissolution *	$D = k_d(-S)^d$	(Sahin *et al.*, 2000)	
Linear size-dependent dissolutio *	$D = k_d^{'} \frac{\phi_s M}{3\rho\phi_v} C_s(-\sigma_s)$	(Mangin *et al.*, 2006)	Dissolution mechanism controlled by mass transfer
Size-dependent dissolution*	$D = k_d(-S)^d(1+\zeta L)^q$	(Aamir *et al.*, 2009a)	

Note 2.2: "*" indicates that both absolute and relative supersaturation can be used. In the expressions $(-S)$ is the absolute under-saturation and $(-\sigma_s)$ is the relative under-saturation. Variables are defined in the nomenclature list.

The reverse process of the crystallisation is known as dissolution, which occurs in the under-saturated region (shown in Figure 2.1). As dissolution proceeds, the concentration of the solute increases. If given enough time at fixed conditions, the solute will eventually dissolve up to a maximum solubility where the rate of dissolution equals to the rate of crystallisation (Smith, 2005). It is well understood that neither nucleation nor growth can occur unless the solute concentration exceeds the saturation value (Rawlings *et al.*, 1993). Some commonly used relationships for the dissolution are summarised in Table 2.3. Additionally to growth and nucleation, the enlargement of the particles and the birth of new smaller particles can be the result of other mechanisms.

Aggregation and breakage

Another important phenomenon in the crystallisation process is aggregation. Aggregation is a particle size enlargement process, which joins fines in an assembly. The particle characteristics obtained in the product depend strongly on the mechanism of aggregation. Aggregation results in relatively rapid size enlargement. There are two main types of aggregations: primary and secondary. First, a crystalline particle may undergo a form of mal-growth, related to its crystallography, which comprises of individual crystals within the structure of parallel units, dendrites or twins. Secondly, crystals suspended in liquids may undergo collisions induced by the flow and join together i.e. aggregate to form a larger particulate entity, which may subsequently be disrupted and re-dispersed or fused to form an aggregate. Both types of aggregation occur simultaneously. Researchers and scientists have extensively studied and modelled the aggregation processes (David *et al.*, 2003; Lee *et al.*, 2001; Lewiner *et al.*, 1999; Wachi and Jones, 1992; Yu *et al.*, 2005; Zumstein and Rousseau, 1989).

Particle formation can also occur via particle breakage processes that start with existing particles and form new smaller ones of varying sizes. The breakage of the particles can occur due to several reasons, which include particle-particle collisions, collisions of particles with the walls of the container and impeller, etc. Breakage processes have also been under intense investigation by researchers (Diemer and Olson, 2002a, b, c; McCoy and Madras, 2004; Soos *et al.*, 2006).

For modelling of crystallisation processes, most often empirical relationships for the kinetic mechanisms are used. The parameters of the kinetic mechanisms are identified for a set of operating conditions. Empirical relationship for secondary nucleation is used for seeded batch cooling crystallisation, due to the presence of crystals and crystal-crystal collisions. Primary nucleation is used if the system nucleates in an un-seeded crystallisation process. The selection of empirical relationship for growth depends on the compound and the way in which the crystals for that compound have grown. The systems considered in this work are considered to be governed mainly by the growth and nucleation mechanisms only. Hence, the aggregation and breakage mechanisms have not been discussed in detail. After identifying the kinetic mechanism, the next step is the selection of a model and an efficient technique to solve the system of equations.

2.3 Population balance modelling of batch crystallisation processes

For complex processes such as crystallisation and polymerisation, modelling can be a valuable tool for process analysis, design, scale-up, monitoring and control (Borcho, 2002; Ramkrishna, 2000).

It is worth noting that a single model of crystallisation system is not able to predict a wide range of process development and operating activities. The choice of model and its structure depends on the control objectives (Kalbasenka, 2009; Roffel and Betlem, 2006). The following aspects may be considered before the selection of a model:

- Generally models derived from first principles are preferred compared to empirical models due to their better prediction ability and validity for broader operating ranges. Models derived from first principles are based on laws of conservation, such as material and energy conservation. The technique has advantage of preserving the physical insight into the process as the model variables coincide with the process variables. However, development of first principle models is generally time-demanding. Additionally, due to the complex kinetics of the crystallisation processes, empirical or semi-empirical models are often used. Generally the approach adopted is to apply population balance equations with empirical kinetic models. Empirical relationships (described in section 2.2.2) are most often used to model, growth, nucleation and dissolution kinetics. However it has to be emphasized that in these cases the kinetic models are generally system specific and may not be robust and portable enough between different experimental setups, or for example for scale-up studies.

- For control and optimisation purposes the process model should be simple. Therefore, lumped parameter models are preferred over distributed parameter systems, as they are simple and computationally more efficient to solve. Hence crystallisation processes are in the optimisation and control literature are generally considered well-mixed and are modelled as lumped parameter systems, hence results need to be evaluated carefully especially in the case of larger scale processes.

- Batch crystallisation is a highly non-linear process and contains a large number of time-varying kinetic and transport parameters. Therefore crystallisation processes cannot be modelled over a broad range of operating conditions using linear models, and classical linear control theory cannot be used for controller synthesis. More

complex nonlinear control techniques and dynamic optimisation approaches are required batch crystallisation control and optimisation, which generally involve the repeated solution of the population balance equation.

The population balance framework has been accepted for some time as the most fundamental approach for modelling particulate, droplet or bubble dynamics in multiphase polymerisation, crystallisation and precipitation systems. The classical framework of modelling crystallisation processes consists of coupled population, mass and energy balances. The main mechanisms of crystallisation processes such as nucleation, growth, aggregation and breakage are well established. Many researchers have applied and analysed the population balance equation (PBE) in the case of these crystal formation mechanisms (Bove *et al.*, 2005; Costa *et al.*, 2007; Hulburt and Katz, 1964; Mahoney and Ramkrishna, 2002b; Randolph and Larson, 1988). The population balance equation is a material balance that accounts for the distribution in particle size, location and other state variables. The population balance modelling framework provides a deterministic description of the dynamic evolution of the crystal size distribution by forming a balance to calculate the number of crystals in the crystalliser (Hounslow, 1998; Hulburt and Katz, 1964; Ramkrishna, 2000). The solution of such balance is the distribution of the number of crystals across the temporal and spatial domains, where the spatial domain may include both internal and external coordinates. The external coordinates typically consist of the ordinary (x, y, z) Cartesian coordinate system specifying the location of the crystals, whereas the internal coordinates represent the characteristic sizes of the crystals (Mahoney and Ramkrishna, 2002a; Ramkrishna and Borwanker, 1973, 1974).

A dynamic population balance equation for a closed homogeneous system can be written using one characteristic size (L) as the single internal coordinate and neglecting all external coordinates (Hulburt and Katz, 1964; Randolph and Larson, 1988; Marchisio *et al.*, 2003a; Rod and Misek, 1982) as follows:

$$\underbrace{\frac{\partial(f_n(L))}{\partial t}}_{\text{population density function}} = \underbrace{\delta(L-r_0)B}_{\text{nucleation}} + \underbrace{\frac{\partial\left[G(L)f_n(L)\right]}{\partial L}}_{\text{growth}} + \underbrace{\int_L^{\infty} b(L,\lambda)g(\lambda)\,f_n(\lambda)\,\mathrm{d}\lambda}_{\text{birth due to breakage}} + \underbrace{\frac{L^2}{2}\int_0^L \frac{F\left[(L^3-\lambda^3)^{1/3},\lambda\right]f_n\left[(L^3+\lambda^3)^{1/3}\right]f_n(\lambda)}{(L^3-\lambda^3)^{2/3}}\mathrm{d}\lambda}_{\text{birth due to aggregation}} - \underbrace{g(L)f_n(L)}_{\text{death due to breakage}} - \underbrace{f_n(L)\int_0^{\infty} F(L,\lambda)f_n(\lambda)\,\mathrm{d}\lambda}_{\text{death due to aggregation}} \quad , \tag{2.5}$$

where $f_n(L)$ is the crystal size distribution expressed as a number density function, i.e. number of crystals within a size range per unit volume, F is the aggregation kernel, g is the breakage kernel, G is the growth rate, B is the nucleation rate and b is the daughter particle size distribution, and $\delta(L-r_0)$ is the continuous Dirac delta function $(\delta = 1 \; if \; L = r_0 \text{ and } \delta = 0 \; if \; L \neq r_0)$ respectively. The solution of equation (4.1) is the initial value problem with initial condition given by the size of the seed distribution $f_n(L,0) = f_{n,0}(L_0)$. The boundary condition is $f_n(0,t) = \dfrac{B(S;\theta_b)}{G(S,L;\theta_g)}$. There are various approaches to solve the equation (2.5) which are discussed in the next section.

2.4 Numerical techniques for the solution of population balance equations

The solution of the generic population balance equation (PBE) usually requires computationally expensive, complex numerical solution techniques (Gerstlauer *et al.*, 2006; Ramkrishna, 2000). These approaches can be categorised in four main groups:

a. Standard method of moments (SMOM).
b. Numerical non-linear model reduction approaches (e.g. method of characteristics (MOCH) and quadrature method of moments (QMOM)).
c. Direct numerical solution approaches involving finite-element or finite-volume discretisation of the partial differential equation (discretised population balances, DPB).
d. Dynamic Monte Carlo simulation (DMC).

All four approaches ultimately transform the equation (2.5), which is a partial differential equation (PDE) into a set of ordinary differential equations (ODEs). The first method characterises the distribution only through its moments whereas the other approaches give the time dependence of the entire distribution or transform them into algebraic equations. There are large differences between the various numerical approaches for the aforementioned solution categories, especially within category (b) and (c). This section describes briefly the main advantages and short-comings of the most common approaches in each category.

2.4.1 Standard method of moments (SMOM)

The standard method of moment (SMOM) is one of the simplest and most widely used methods of solving population balance equations. The PBE in equation (2.5) can be further simplified by using a moment transformation, by multiplying the population balance equation by L^k (in a length based PBE) and integrating it from zero to infinity (John *et al.*, 2005; Kiparissides *et al.*, 2006; Salvatori *et al.*, 2005).

The k^{th} moment is defined as,

$$\mu_j(t) = \int_0^\infty f_n(L,t)L^j dL \qquad \text{where} \quad j = 0,1,2,\ldots,\infty. \tag{2.6}$$

After the moment transformation, the PBE can be represented by a set of moment equations and the k^{th} moment is given by (Hulburt and Katz, 1964; Randolph and Larson, 1988),

$$\begin{aligned}\frac{d\mu_k}{dt} = &\underbrace{\int_0^\infty L^k B\delta(L-r_0)dL}_{\text{nucleation}} + \underbrace{\int_0^\infty kL^{k-1}G(L)f_n(L)dL}_{\text{growth}} + \underbrace{\int_0^\infty L^k \int_o^\infty g(\lambda)b(L,\lambda)\,f_n(\lambda)\,\mathrm{d}\lambda dL}_{\text{birth due to breakage}} \\ &\underbrace{-\int_0^\infty L^k g(L)f_n(L)dL}_{\text{death due to breakage}} + \underbrace{\frac{1}{2}\int_0^\infty f_n(L)\int_0^\infty F(L,\lambda)(L^3+\lambda^3)^{\frac{k}{3}} f_n(L)d\lambda dL}_{\text{birth due to aggregation}} \\ &\underbrace{-\int_0^\infty L^k f_n(L)\int_0^\infty F(L,\lambda)f_n(L)d\lambda dL}_{\text{death due to aggregation}}\end{aligned} \quad . \tag{2.7}$$

The equation (2.7) is solvable for growth (except for size-dependent growth) and nucleation problems. One of the disadvantages of the method is the mathematical complication in the equations when the growth rate is described by a size-dependent mechanism. This method

also suffers from closure problem for cases involving aggregation and breakage mechanisms in equation (2.7), since the integrations cannot be written in terms of the moments only. The closure problem can be eliminated using quadrature method of moments, which will be described in next section. Equation (2.7) can be simplified for growth and nucleation mechanisms only:

$$\frac{d\mu_k}{dt} = \int_0^\infty L^k B\delta(L - r_0)dL + \int_0^\infty kL^{k-1}G(L)f_n(L)dL\,. \tag{2.8}$$

Expanding the equation (2.8) for the first four moments (starting from the zeroth moment), for size-independent growth and nucleation mechanisms only, gives the following results:

$$\frac{d\mu_0}{dt} = B\,, \tag{2.9}$$

$$\frac{d\mu_1}{dt} = G\mu_0 + Br_0\,, \tag{2.10}$$

$$\frac{d\mu_2}{dt} = 2G\mu_1 + Br_0^2\,, \tag{2.11}$$

$$\frac{d\mu_3}{dt} = 3G\mu_2 + Br_0^3\,, \tag{2.12}$$

where r_0 is the size of the newly nucleated crystals and μ_0, μ_1, μ_2 and μ_3 are the zeroth , first, second and third moment respectively. The lower order moment (i.e. zeroth to third) are important because they are related to the physical properties of the CSD. The zeroth moment gives the total number of crystals per unit volume, μ_1 is related to the total length (characteristic size) of crystal, μ_2 is related to the total crystal surface area, and μ_3 gives the volume of all crystals.

The method gives the exact solution for the moments of the distribution. However, in addition to the limitations mentioned above, reconstructing the real distribution from its moments is numerically unstable (Giaya and Thompson, 2004; Nallet *et al.*, 1998; White, 1990). Therefore the retrieval of the exact and full distribution shape using the standard method of moments is not possible, although several inversion approaches have been proposed for coarse approximation of the distribution (Flood, 2002; Randolph and Larson, 1971). Alternatively, orthogonal polynomials can be used to correct the population density

functions (pdf's) by preserving the original moments. These methods have various limitations and are discussed in detail in Chapter 3. Although the SMOM generally cannot provide enough information about the shape of the distribution, the following terms can be defined in terms of lower order moments:

- The variance of the distribution function, which quantifies the width of the distribution:

$$\sigma^2_{\text{var}} = \frac{\int_0^\infty (L - L_m)^2 f_n(L,t) dL}{\int_0^\infty f_n(L,t) dL} = \frac{\mu_2}{\mu_0} - \frac{\mu_1^2}{\mu_0^2}. \tag{2.13}$$

- The coefficient of variation, which quantifies the width of the distribution function relative to its mean:

$$c.v. = \frac{\sigma_{\text{var}}}{L_m} = \sqrt{\frac{\mu_0 \mu_2}{\mu_1^2} - 1}. \tag{2.14}$$

- Number mean size providing information about the mean particle size (more sensitive for small particles sizes):

$$d_{10} = \frac{\mu_1}{\mu_0}. \tag{2.15}$$

- Weight mean crystal size, which provides information about the mean particle size (with more sensitivity towards larger particles):

$$d_{43} = \frac{\mu_4}{\mu_3}. \tag{2.16}$$

- Sauter mean diameter, which gives information related to the ratio between the volume of the dispersed phase to its surface area:

$$d_{32} = \frac{\mu_3}{\mu_2}. \tag{2.17}$$

2.4.2 Numerical nonlinear model reduction approaches

The approaches considered in this category are commonly called "global methods" and are also considered as nonlinear model reduction techniques for the PBE. This category includes different variants of the "method of weighted residuals", which have been frequently used in

the crystallisation-control community for general solution of the PBE. The algorithms are based on the idea of approximating the population density function (pdf) as a linear combination of chosen basis functions. The coefficients of the linear combination are obtained by minimizing the residuals between the approximation and the distribution such that for a chosen set of weighting functions, the residual will be orthogonal and hence will represent the pdf with a small number of terms. There are various possibilities to select the basic functions; e.g. Laguerre polynomials have been used with very good computational performance in Non-Linear Model Predictive Control (NMPC) schemes for crystallisation processes (Rawlings *et al.*, 1993). The difficulty associated with these techniques is related to the choice of the proper basis functions. Note that the SMOM can be also considered as a model reduction technique, being the particular case when the weighting functions are considered as polynomials. Generally, the accuracy of the weighted residual approaches depends on the set of basis functions used for approximation. However it has been shown that if the only mechanism that governs the crystallisation is growth, good accuracy can be expected. This has been demonstrated for example for cases with growth rate proportional to the inverse of the characteristic crystal size by Kalani and Christofides, (2002).

Quadrature method of moments (QMOM)

The first approach discussed in this category is the quadrature method of moment (QMOM). The method was proposed by McGraw (1997) and has been used for a wide variety of applications of population balance models. The method is a particular case of the generic weighted residual approach, which uses a particular form for the basis function (quadrature approximation given by the quadrature theory) that allows an explicit calculation of the weights from the moments, hence providing a solution to the moment closure problem from the SMOM. The QMOM proposed by McGraw (1997) is based on the product difference (PD) algorithm (Gordon, 1968). The PD algorithm is employed to calculate the weights (w_i) and the abscissas (L_i) from the moments following the quadrature approximation (McGraw, 1997),

$$\mu_k = \int_0^\infty f_n(L) L^k dL \approx \sum_{i=1}^{N_q} w_i L_i^k, \qquad \text{where} \qquad k = 0,1,2,\ldots,\infty. \tag{2.18}$$

where N_q is the number of quadrature points, w_i are the corresponding quadrature weights and L_i are the abscissas, which can be determined through the product-difference (PD) algorithms or via direct solution of a differential-algebraic equation (DAE) system (Gimbun *et al.*, 2009), based on the idea of minimizing the error committed by replacing the integral from the moment definition with its quadrature approximation.

After applying the quadrature rule, equation (2.7) can be written as (Alopaeus *et al.*, 2006):

$$\begin{aligned}\frac{d\mu_k}{dt} = & \underbrace{\delta(0,k)B}_{\text{nucleation}} + \underbrace{k\sum_{i=1}^{N} w_i L_i^{k-1} G(L_i)}_{\text{growth}} + \underbrace{\sum_{i=1}^{N} w_i g(L_i) b(k, L_i)}_{\text{birth due to breakage}} \\ & + \underbrace{\frac{1}{2}\sum_{i=1}^{N} w_i \sum_{j=1}^{N} w_j (L_i^3 + L_j^3)^{\frac{k}{3}} F(L_i, L_j)}_{\text{birth due to Aggregation}} - \underbrace{\sum_{i=1}^{N} w_i g(L_i) L_i^k}_{\text{death due to breakage}} , \\ & - \underbrace{\sum_{i=1}^{N} w_i L_i^k \sum_{j=1}^{N} w_j F(L_i, L_j)}_{\text{death due to aggregation}}\end{aligned} \tag{2.19}$$

Now the closure problem has been eliminated and hence the PBE given by (2.7) is solvable by means of the quadrature method of moments by following the evolution of w_i and L_i. The QMOM gives a coarse approximation of the change in the shape of the CSD, however the weights and abscissas do not directly provide the shape of the distribution. The application of the QMOM has been extended to aggregation, coagulation and breakage mechanisms (Fan *et al.*, 2004; Marchisio *et al.*, 2003b; Rosner *et al.*, 2003; Rosner and Pyykonen, 2002; Wright *et al.*, 2001).

The PD algorithm however is not always the best approach for computing the Gauss quadrature approximation, since the computation of the weights and abscissas is sensitive to small errors in the moments. Thus, the applicability of QMOM is limited to no more than six quadrature points (Gordon, 1968) and often even fewer for some cases, such as diffusion-controlled growth with secondary nucleation. Apart from the product difference algorithm based QMOM, there are several other variations of the approach, such as fixed quadrature method of moments (FQMOM) (Alopaeus *et al.*, 2006), Jacobian matrix transformation (JMT) (McGraw and Wright, 2003) and direct quadrature method of moments (DQMOM) (Fan *et al.*, 2004); however these techniques are not widely used.

Method of characteristics (MOCH)

Another efficient technique to solve population balance equations is the method of characteristics (MOCH) (LeVeque, 1992). The technique provides an elegant way to determine the evolution of the crystal size distribution for crystallisation processes. It has been used for the crystal size determination in case of size-independent growth and nucleation by many researchers (see e.g. Hounslow and Reynolds (2006)). The method of characteristics for first order PDEs determines lines, called characteristic lines (or characteristics), along which the PDE degenerates into a set of ODEs. The ODE can be solved and transformed into a solution for the original PDE. The equation for each characteristic line $L(t)$ is:

$$L(t) \equiv \int_0^t G(S(t))dt\,, \qquad \text{i.e.} \quad \frac{dL}{dt} = G(t)\,. \tag{2.20}$$

To illustrate the technique it's application to the solution of the PBE is illustrated next for a crystallisation process with size-independent growth the only governing phenomenon.

The population balance equation for a crystallisation process with one dimensional growth and no nucleation can be obtained by rearranging equation (2.5),

$$\frac{\partial f_n(L,t)}{\partial t} + \frac{\partial \left[G(S,L) f_n(L,t)\right]}{\partial L} = 0\,, \tag{2.21}$$

where f_n is the pdf, which can be a function of the characteristic size (L) and time (t). If the growth rate G only depends on the supersaturation $S(t)$, equation (2.21) can be transformed into a homogeneous hyperbolic equation,

$$\frac{\partial f_n(L,t)}{\partial t} + G(S)\frac{\partial f_n(L,t)}{\partial L} = 0\,. \tag{2.22}$$

The aim of the method of characteristics is to solve the PDE by finding curves in the $(L-t)$ plane, which reduces the partial differential equation to a system of ODEs. The $(L-t)$ plane can be expressed in a parametric form by $L = L(\mathcal{Z})$ and $t = t(\mathcal{Z})$, where the parameter $\mathcal{Z}$ gives the measure of distance along the characteristic curve. Therefore,

$$f_n(L,t) = f_n(L(\mathcal{Z}), t(\mathcal{Z}))\,, \tag{2.23}$$

and applying the chain rule gives,

$$\frac{dL}{d\mathcal{Z}}\frac{\partial f_n}{\partial L}+\frac{dt}{d\mathcal{Z}}\frac{\partial f_n}{\partial t}=\frac{df_n}{d\mathcal{Z}}. \tag{2.24}$$

Comparing equations (2.22) and (2.24) a set of ODEs can be derived:

$$\frac{dt}{d\mathcal{Z}}=1, \tag{2.25}$$

$$\frac{dL}{d\mathcal{Z}}=G(S), \tag{2.26}$$

$$\frac{df_n}{d\mathcal{Z}}=0, \tag{2.27}$$

with initial conditions (corresponding to $\mathcal{Z}=0$) $t=0$, $L=L_0$ and $f_n(L,0)=f_{n,0}(L_0)$. From equation (2.25)-(2.27) $\mathcal{Z}=t$ and the actual characteristic equations can be written as:

$$\frac{dL}{dt}=G(S), \tag{2.28}$$

$$\frac{df_n}{dt}=0. \tag{2.29}$$

To obtain the dynamic evolution of the crystal size distribution, $f_n(L,t)$, equation (2.26) and (2.27), with prescribed growth expressions can be integrated repeatedly for different initial values $[L_0, f_{n,0}(L_0)]$ where $f_{n,0}(L_0)$ is the seed distribution. The initial conditions start from along the L axis of the $L-t$ plane, with values calculated by choosing a discretisation interval ΔL_0 and using $t_0=0$ and $L_0=\max(0, L_{0,\max}-k\Delta L_0)$, $k=0,1,\ldots,N$, where N is the number of discretisation points. The discretisation interval ΔL_0 will determine the number of integrations (the number of characteristic lines) and hence the resolution of the dynamic evolution of the seed CSD. The growth rate is a function of supersaturation, which is changing with time, $S(t)$ which can be determined from the mass balance and the third moment of the distribution obtained from the SMOM, using equation (2.8). Growth rate is a function of the supersaturation, $G=k_gS^g$, with g and k_g being the growth kinetic parameters. The supersaturation (S) is expressed as the difference between the solute concentration $C(t)$ and equilibrium concentration $C_{sat}(T)$ at time t, $S(t)=C(t)-C_{sat}(T)$. The equilibrium concentration (solubility) is a function of the temperature (T), which is

generally a function of time during the batch, $T(t)$, hence $C_{sat} = C_{sat}(t)$. The solute concentration can be calculated from the material balance:

$$C(t) = C(0) - k_v \rho_c (\mu_3(t) - \mu_3(0)), \tag{2.30}$$

where ρ_c is the density of crystals and k_v is the volumetric shape factor. The third moments are computed from the SMOM.

To illustrate the methodology a simulation was performed for a real crystallisation process (crystallisation of potash alum in water) using the experimental conditions described in Chapter 5, however considering the following fictitious size-independent growth parameters: growth rate constant $k_g = 12.5 \ \ \mu m / s$ and growth order $g = 1.2$. A batch time of 5400 s was used in the simulations. The actual temperature trajectory from the experiment (shown in Figure 5.4(a)) was used for the simulation. Because of the particular experimental conditions the supersaturation was changing during the batch. The initial conditions for the simulations were given based on the initial experimental concentration and on the measured seed distribution used in the experiments (described in Chapter 5).

Figure 2.4 (a) illustrates the evolution in time of the characteristic lines for the crystallization process using the size independent growth mechanism. All characteristic lines have the same slope at a given time and the pdf values are constant during the whole batch according to the size-independent growth mechanism and no nucleation. The CSD can be represented at any time by plotting the pdf values versus the corresponding L values obtained from the characteristic lines. The dynamic evolution of the CSD during the batch is illustrated in Figure 2.4 (c).

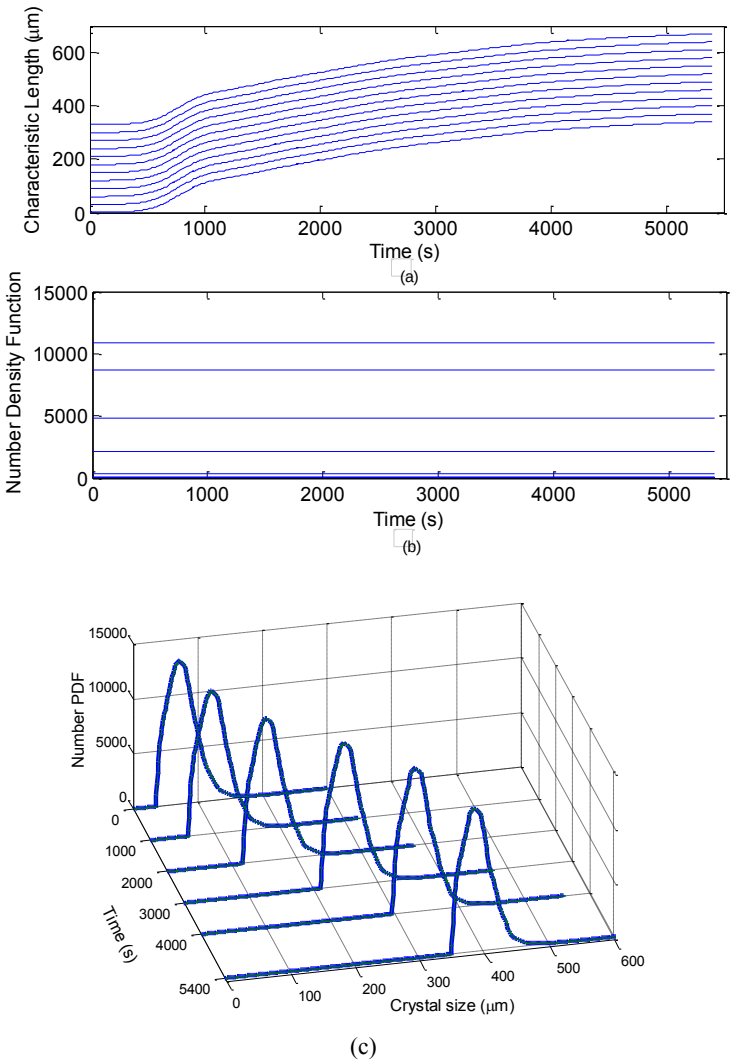

(c)

Figure 2.4: Simulation results of a crystallisation process with size-independent growth, using the method of characteristics. a) Characteristic lines for size (the slopes of all characteristic lines are the same due to the size independent growth mechanism). b) Characteristic lines for the $f_n(L,t)$ (showing constant values due to size independent growth and no nucleation). c) Evolution of the CSD obtained from the characteristic lines at different time steps.

2.4.3 Direct numerical solution

The direct numerical solution approaches based on various finite-element, finite-difference or finite-volume schemes, such as the Upwind, Lax-Wendroff or Beam-Warming method (Costa *et al.*, 2007; LeVeque, 1992), or different high resolution approaches, like Hi-Res Van Leer are usually computationally too expensive for control purposes (Christofides, 2002). However, these are often applied in open-loop control simulation studies.

Finite difference methods and discretised population balance equations (DPE)

These are frequently used approaches for solving generic population balance equations. These methods turn the population balance equation into a discretised population balance equation consisting of a set of ODEs equal to the number of classes. The computational effort for the numerical solution can be significantly reduced using a grid according to a geometric progression (Rigopoulos and Jones, 2003). Coarse discretisation produces a fast solution if there are no discontinuities. These techniques can be applied in principle to any mechanism, however have the following limitations:

- Because of the numerical diffusion, the method often leads to the broadening of sharp discontinuities (Mahoney and Ramkrishna, 2002a) which may arise along the curve that divides the states resulting from the initial conditions from those arising from the boundary conditions.

- High resolution is required to ensure the number and mass conservation of the population (Patankar, 1980).

Recently, combined Lax-Wendroff/Crank-Nicholson method has been applied for solving the population balance equations (Bennett and Rohani, 2001), which shows promising results and is free from numerical instabilities.

Marchal *et al.* (1988) introduced the method of classes to solve a PBE considering agglomeration, breakage and size dependent growth mechanisms. The method discretises the size domains in the grids generating bins. The mean size in each class is assumed to be the characteristic size for all the particles which belong to that class. The density function in each bin is considered constant in this method. The method of classes has been frequently used to solve the population balance equation in crystallisation, precipitation and polymerisation processes (Blandin *et al.*, 2001; David *et al.*, 1991; Litster *et al.*, 1995; Monnier *et al.*, 1997; Puel *et al.*, 2003a, b). The main drawbacks of the technique are:

- The computational time increases with increasing number of discretisations. To avoid this, adaptive discretisation has been suggested (Kumar and Ramkrishna, 1996b; Peglow *et al.*, 2006). Adaptive discretisation reduces the number of ODE's without affecting the precision of the results.

- The method can exhibit oscillatory behaviour and hence may produce negative pdf's (Kumar and Ramkrishna, 1996a, 1997).

Finite volume method (FVM)

The finite volume method (FVM) is a standard approach used in computational fluid dynamics, however it has been often used also for the solution of population balance equations (Gerstlauer *et al.*, 2001; Gunawan *et al.*, 2004, 2008; Ma *et al.*, 2002a). The finite volume method (FVM) involves the discretisation of the spatial domains and uses piece-wise functions to approximate the derivatives of the distribution function with respect to the spatial variables. The values of growth rate, nucleation rate and number density at the cell boundaries are required to calculate the values at each grid point. The simplest interpolation formula that can be used to approximate the number density at each cell boundary is the upwind interpolation scheme. This approach however also suffers from numerical diffusion unless a very fine grid mesh is used. Mesbah *et al.* (2009) have recently shown that high order finite volume methods in combination with flux limiting functions can lead to high order accuracy on a coarse grid mesh.

Finite element method (FEM)

The hyperbolic population balance equation can be solved in its continuous form using the Finite Element Method (FEM). This technique approximates the solution using piecewise low-order polynomials that are local and capable of capturing highly irregular solutions (Rigopoulos and Jones, 2003). Orthogonal collocation based finite element method has been used with modest computation burden for the modelling of both continuous and batch crystallisation systems (Rawlings *et al.*, 1992). Steady-state population balance equations were solved using collocation and Galerkin FE algorithms by Hounslow (1998). Lagrange cubic interpolation polynomials were used along with equally spaced nodes within each element for the solution of PBE's. The results showed that the number density function is predicted reasonably well using very few numbers of (Hounslow, 1998; Nicmanis and Hounslow, 1998). Rigopoulos and Jones (2003) used a FE scheme with linear collocation elements and an upwind propagation of the growth term. The authors claimed that the method is computationally faster than higher order FE collocation methods. Generally FEM is not an attractive option for model-based control approaches due to its significant computational requirement and relatively large implementation complexity.

2.4.4 Dynamic Monte Carlo (DMC) simulations

The DMC approach is the most generic solution approach since it can be applied for all cases of PBEs. However, it is computationally too expensive for on-line implementations. The computation of the dynamic evolution of the CSD using stochastic dynamic Monte Carlo (DMC) simulations has been reported for several particulate processes (Haseltine *et al.*, 2005; Ramkrishna, 1981; Shah *et al.*, 1977; Spielman and Levenspiel, 1965; Zhao *et al.*, 2005a, b). Monte Carlo simulations are time consuming but present some important advantages when applied to the solution of the general PBE. Firstly they provide information about the history of each particle in the population and secondly they can be easily implemented to higher dimensional problems.

2.4.5 Summary

A brief overview of various techniques used for the solution of generic population balance equations has been presented. The key advantages and disadvantages of the techniques are summarised in Table 2.4. A number of techniques are available for solution of population balance equations. Techniques such as the standard method of moments (SMOM) and quadrature method of moments (QMOM) are useful to compute average properties of the CSD expressed by the lower order moments of the distribution. The QMOM provides the additional benefit compared to the SMOM that it can be applied to size-dependent growth, aggregation and breakage mechanisms. Both methods are computationally very efficient, however they cannot retrieve the complete shape of the distribution.

Table 2.4: Comparison for different numerical methods for the solution of population balance equations.

Numerical Method	Advantages	Disadvantages	Remarks
Method of Moments	Simple and computationally efficient Moment transformation is possible for size independent growth and nucleation	Closure problem in case of size-dependent growth, aggregation and breakage. Cannot retrieve the complete CSD	It can be used in case of simple crystallisation model when growth and nucleation are considered but cannot be used for CSD retrieval
Quadrature method of moments	Computationally efficient Moment transformation is possible for size-dependent growth, aggregation and breakage	Gives the coarse approximation of CSD but cannot retrieve the full CSD	Cannot be used to develop a model-based control strategy for shaping the CSD as it cannot retrieve the complete distribution
Method of characteristics	Simple and computationally efficient Can retrieve complete CSD	Considers growth and nucleation only	It is an attractive option for controlling the CSD as it retrieves complete CSD in real time; while the crystallisation process is governed by growth and nucleation phenomena only.
Finite Difference Methods and DPE	Provides universal framework for the solution of generic PBMs	Sharp discontinuity may be obtained which can broaden because of numerical diffusion. Very large resolution is required for number and mass conservation May show spurious oscillations and negative pdf values. May show errors in the retrieved distribution.	It is computationally inefficient due to the generally large discretization. Difficulty in predicting/avoiding the occurrence of errors in the obtained CSD. Not a preferred option for model based control and optimisation.
Method of classes (MOC)	Discretises the size domain in grids generating bins	It becomes computationally inefficient as the number of discretisation increase with the number of classes. May show spurious oscillations and hence can generate negative pdf values.	Not an attractive option for model based optimisation and control.
Finite element / Finite volume	Provides a universal framework for the solution of generic PBMs	Computationally inefficient since the solution of integrals is required	Not an attractive option for model based optimisation and control.
Dynamic Monte Carlo	Provides information about the history of each particle in the population. Can be easily implemented to higher dimensional problems.	Computationally inefficient	The technique is time consuming and is not an attractive option for on-line control

The method of characteristic is a computationally efficient approach, capable of retrieving the CSD. However large number of characteristic lines (fine discretisation) is needed to accurately compute the moments from the distribution, needed to conserve the mass and acquire the change in supersaturation with time, $S(t)$. Additionally, the method cannot be readily applied to aggregation, breakage and certain nucleation mechanisms.

Other techniques are also used for the solution of generic population balance equations such as the method of classes, finite element, finite volume and kinetic Monte Carlo methods. However these techniques may suffer from spurious oscillations, numerical diffusion and are computationally inefficient hence are not an attractive option for model-based optimisation and control. When fast computation is a requirement and the information about the moments of the distribution only is sufficient the moment methods and the method of characteristics seems to be the most feasible numerical techniques.

2.5 Measurement techniques for state variables

During experiments the data is gathered for state variables such as temperature, concentration and CSD using on-line, *in situ* and off-line measurement techniques. The population balance model is initialised using the information gathered from these experimental measurements, e.g. moments calculated from the seed distribution, initial concentration, and temperature trajectories. The measurement of these key variables is required for several reasons:

- To obtain insight into limiting processing and main governing phenomena.
- To design the experiments and obtain data for model parameter identification.
- To design controllers to maximize product quality and minimize operating costs.
- To drive the process to its desired state.

In all cases, the experimental data should provide sufficient information about the system under investigation. Two types of experimental data are generally required: one, which gives the information about the solution phase, and another, which gives the information related to the solid phase. The information about the solution phase in provided by the solution temperature, supersaturation and concentration, while crystal size distribution provides

information about the dispersed solid phase. The corresponding measurement techniques can be classified into three main categories:

- On-line measurements: these techniques provide information during the course of the batch.
- *In situ* measurements: these techniques consist of measurements made directly in the process medium.
- Off-line measurements: these techniques are used to characterise the properties based on samples taken from the process and often analysed after the process completed.

The model-based predictive control (MPC) approaches use the model of the crystalliser and measurements of important variables to compute optimal control actions corresponding to a certain objective function (Rawlings, 2000). Model identification is considered reasonably complete when the parameter uncertainty and the model reliability have been assessed. A wide variety of experimental techniques have been used for parameter estimation for crystallisation processes. In most of the practical situations, not all variables can be reliably measured. Therefore, those unmeasured variables should be estimated using available measurements and the model, using state estimators or observers (Eek and Dijkstra, 1995; Motz and Gilles, 2008; Nagy and Braatz, 2003a). For batch cooling crystallisation, the states of interest are the solution temperature, concentration and the crystal size distribution (CSD). Different techniques can be used to measure the concentration and CSD which are summarized below.

2.5.1 Temperature measurement

Thermocouples are used to measure the temperature. Some important factors which need to be considered while selecting a thermocouple are; temperature range, medium, required response time and accuracy. Generally the temperatures for the slurry, inlet and outlet jacket temperatures are obtained from PT-100 thermocouples. These thermocouples have quick response time and are accurate within 0.15 °C.

2.5.2 Concentration/supersaturation measurement

Supersaturation is the main driving force for all kinetic mechanisms such as dissolution, growth, nucleation and aggregation, which occur during crystallisation processes. It is important to control the extent of the supersaturation during crystallisation since the size, shape and solid-state phase of the product crystals are dependent on the supersaturation profile achieved during the crystallisation process. One way to enhance the control of CSD is to use supersaturation control (SSC) (Doki *et al.*, 2004; Gron *et al.*, 2003; Liotta and Sabesan, 2004), which drives the process within the metastable zone to avoid or to produce controlled nucleation (Woo *et al.*, 2009a). Usually the supersaturation setpoint (S_{sp}) curve is chosen experimentally and is followed in the phase diagram using a supersaturation controller, based on concentration measurement. In seeded crystallisation, the supersaturation is usually maintained at a desired constant value throughout the entire batch by the application of properly designed control algorithms (Chung *et al.*, 1999; Fujiwara *et al.*, 2005; Zhang and Rohani, 2003). Concentration and supersaturation measurement sensors can be selected based on the properties of the solution and the methods used to correlate the measured property to the concentration can largely vary from application to application (Loffelmann and Mersmann, 1999, 2002). Some of the most traditional ways to measure the concentration of the solute in the continuous phase are briefly described next.

Conductivity

The solute concentration can be measured using conductivity probes for conducting solutions, such as salts. The technique has been demonstrated in the case of crystallisation processes by Hlonzy *et al.* (1992) and Nyvlt *et al.* (1994), for the crystallisation of inorganic salts. Conductivity measurement has several potential problems. First of all, it can only be applied for a limited number of conducting crystallisation systems, which excludes most organic compounds and solvents. The probe can be clogged with crystals during measurements. When crystals touch the probe, it can produce noise in the measured data (Hlozny *et al.*, 1992; Nyvlt *et al.*, 1994). Measurement can be influenced by the solid content making the correlation of the conductivity signal with the concentration difficult. Frequent re-calibration of the probe limits its usefulness in long-term industrial crystallisation applications. It is difficult to apply this technique to batch cooling

crystallisation processes because conductivity is also strongly (and generally nonlinearly) affected by temperature.

Refractive index

Another technique to measure concentration is the refractive index, which is well correlated to the concentration for many solutions (Zhou *et al.*, 2006b). The technique can work if there is a significant change in refractive index with change in concentration (Braatz *et al.*, 2001). However the technique is sensitive to ambient light and air bubbles.

Density

Another way to measure the change in concentration is to measure the change in density. To measure the density, a sample of slurry (crystals along with solution) is taken out of the crystalliser, crystals are filtered and then the density of the liquid phase is measured. The technique has also been used on-line for potassium nitrate-water system (Miller and Rawlings, 1994). This approach requires an external sampling loop, which can lead to following problems:

- clogging of the filters, which are used to separate the solution and crystals,
- temperature fluctuation in the sampling loop, which can cause the solution to nucleate and hence creating errors in the measurements.

Spectroscopy

A major limitation of all aforementioned techniques is the lack of ability to measure the concentration of multiple dissolved species or to consider multiple solvents (Braatz *et al.*, 2001). Most pharmaceutical crystallisation processes have multiple solutes and/or solvents. Modern equipment such as Attenuated Total Reflectance (ATR) Fourier Transform Infrared (FTIR), and ultra-violet–visible (UV-Vis) spectrometers coupled with chemometrics can be used to track the changes in the concentration with time (Berglund and Feng, 2002; Dunuwila and Berglund, 1997; Fujiwara *et al.*, 2002).

The applications of spectroscopic techniques have increased in recent years (Liotta and Sabesan, 2004; Pollanen *et al.*, 2005; Yu *et al.*, 2006) because they provide the following main advantages: they do not clog with crystals (although nucleation and crusting on the probe window may be a problem), give *in situ* measurements and can effectively monitor the

change in concentration/supersaturation (Gron *et al.*, 2003; Gron and Roberts, 1999; Lewiner *et al.*, 1999). The signal also depends on the temperature, which however can be taken into account using suitable calibration models.

2.5.3 Crystal Size Distribution (CSD) measurement

CSD can be measured by a series of methods described next.

Sieve analysis

Sieve analysis is a simple, portable, inexpensive and widely used method for the measurement of particle size. Generally the equipment allows the use of a wide range of sieve sizes to measure the particle sizes, ranging from 10 μm to 5500 μm (depending on the availability of sieves). The key variables that influence sieving include: particle shape, presence of very fine particles, initial sieve loading, and hardness of particles, time and method of agitation. Reproducibility is often poor due to these variables. Although sieving provides a good method for the evaluation of the quality of the crystalliser product, it is time consuming and cannot be used for online measurement of particle size distribution (Adi *et al.*, 2007; Ludwick and Henderson, 1968).

Laser diffraction

- Laser diffraction is based on the principle that particles passing through a laser beam will scatter light at an angle that is directly related to their size. Large particles therefore scatter light at narrow angles with high intensity, whereas small particles scatter at wider angles but with low intensity. To determine the particle size from the diffraction pattern two theories are used: the Fraunhofer and the Mie theory (Monnier *et al.*, 1996). The theories are based on the assumptions that

- the particles are spherical and

- the suspension is dilute.

Equipment, such as the Malvern Mastersizer and Malvern Insitic are based on the principle of laser diffraction. Malvern Mastersizer can be used to obtain both on-line as well as off-line measurement of the CSD. They are able to measure a size range of 0.01 to 1000 μm. For on-line CSD measurement a sampling loop is required, which may introduce problems

related to nucleation or breakage. Additionally for systems, with larger solid content the measurement loop must include an additional dilution loop, with flow that may be tailored during the crystallisation (if the solid content increases) to maintain the required obscuration number for the measurements.

Laser backscattering

Another solid phase measurement technique is based on the laser backscattering method. The Lasentec Focused Beam Reflectance Measurement (FBRM) instrument works on this principle. The equipment provides the chord length distributions of the crystal size. The laser beam is focused by a rotating lens, which causes the beam to scan in a circular motion through a sapphire window at a fixed high speed (generally 2 m/s). The light is scattered in all directions when the laser intersects the crystal, and the probe collects the light which is scattered back by the crystal. The time period of the back scattering is recorded and is multiplied with the scanning speed of the beam to give the distance between the two edges of the crystal. Therefore the distance measured by the FBRM is called chord length. Using FBRM coupled with inverse geometric modelling the chord length distribution (CLD) can be transformed into size distribution (Hukkanen and Braatz, 2003; Ruf *et al.*, 2000) when the shape of the crystals is known and is well-defined. The equipment can measure from a size range of approximately 0.5 to 1000 μm. A method is also required to convert the chord length distribution to CSD and vice-versa for on-line estimation and control.

The above mentioned techniques (such as the Mastersizer, and FBRM) have many advantages (Fujiwara *et al.*, 2002; Hukkanen and Braatz, 2003) such as minimal calibration and easy automation for possible use as a feedback signal for control purposes. A weakness of the aforementioned CSD sensors is that the distribution of crystal shapes cannot be directly determined. For example, a collection of rod-like crystals are characterised mathematically by a two dimensional distribution, but the light scattering instruments only provide one-dimensional distributions. It is impossible to uniquely determine a two-dimensional distribution from a one-dimensional distribution. FBRM along with ATR-FTIR was used to monitor the polymorphic transformation in the case of D-mannitol (O'Sullivan and Glennon, 2005). The authors used FBRM successfully to investigate the crystallisation system and to identify different polymorphic forms of the compound. The FBRM was also used for monitoring the efficiency of the fine removal process in a modified mixed

suspension mixed product removal crystalliser (MSMPR), along with particle vision imaging using the Lastentec particle vision measurement (PVM) probe (Kougoulos *et al.*, 2005). Due to the nature of the organic crystals and their opacity, FBRM results were not satisfactory for small size particles.

The *in situ* process analytical tools have been extensively used for monitoring and control of particulate system. More detailed information about these tools can be found in several review papers (see e.g. Braatz *et al.*, 2002; Lawrence *et al.*, 2004; Yu *et al.*, 2004) and books (e.g. Bakeev, 2005).

Image analysis

Image analysis is the simplest technique to monitor the crystal size and shape in crystallisation processes. It is a direct observation technique and it does not require any assumptions for the size or shape of the crystals. In recent years, many applications of on-line and off-line image analysis techniques have been reported for monitoring the shape and size of the particles. Image analysis can be used for the classification of crystals based on their polymorphic and morphological forms. A method has been developed based on on-line imaging and image analysis, which can be used for classification of polymorphic forms in real-time by De Anda *et al.*, (2005).

Two dimensional information can be obtained *in situ* from the Lasentec Particle Vision Measurement (PVM) system, which provides pictures of the crystals in the solution using a probe inserted directly into the dense crystal slurry (Barrett and Glennon, 2002; Fevotte, 2002; Kempkes *et al.*, 2008). This video microscope can collect 10-30 pictures a second, providing two dimensional snapshots of the crystals in real time. On-line video microscopy can measures crystals as small as 1-15 μm, which is not as small as by laser scattering instruments. The quality of images limits the ability of the imaging software to automatically identify individual particles and quantify the characteristics of these particles. On-line video microscopy has the advantage that the crystals are directly observed, allowing shape information to be obtained. PVM is suitable for using in industrial crystallisers (Braatz, 2002), therefore, process video microscopy is becoming increasingly used to image the crystals as they grow in solution, to visualize the extent of agglomeration and changes in crystal size and shape. An on-line high speed imaging system was developed by

GlaxoSmithKline and has been used for the monitoring of size and shape of crystals during batch cooling crystallisation (Dharmayat *et al.*, 2006). Image analysis based methods have also been used for monitoring nucleation and polymorphic transformation. Simon *et al.*, (2009a, b) developed the external and internal Bulk Video Imaging (eBVI and iBVI), based on low cost video hardware (simple camera for the eBVI and endoscope for iBVI), and showed that the method can provide earlier detection of nucleation than spectroscopy or FBRM based approaches. The authors also used the BVI approach to monitor the polymorphic transformation during the crystallisation of caffeine.

2.6 Crystallisation control and optimisation

Particulate processes are widely used and applied in industry for the manufacturing of a large variety of products, such as in the crystallisation of proteins (Wiencek, 2002), production of latexes by emulsion polymerisation (Immanuel and Doyle, 2002) and aerosol synthesis of titania powders (Kalani and Christofides, 2000). The PSD of the particulate (dispersed) phase strongly influences both the mechanical and physicochemical properties of the product materials. This has motivated a growing attention on the control of particulate processes and has often resulted in model-based control approaches due to the underlying complexities of the phenomena involved (Braatz, 2002; Christofides *et al.*, 2008; Nagy, 2009).

Model-based control strategies have been widely used for various particulate processes including emulsion polymerisation (Doyle *et al.*, 2002; Immanuel and Doyle, 2003), granulation (Wang *et al.*, 2006), fermentation (Henson *et al.*, 2002; Zhu *et al.*, 2000), cellular biological systems (Stelling *et al.*, 2004), aerosol (Kalani and Christofides, 2002) and thermal spray coating processes (Li *et al.*, 2004). In the last decade much effort has been devoted to the development of model-based control strategies of the CSD for crystallisation processes (Aamir *et al.*, 2010; Aamir *et al.*, 2009b; Braatz and Hasebe, 2002; Ma *et al.*, 2002a; Nagy and Braatz, 2003a; Shi *et al.*, 2006; Shi *et al.*, 2005). Most of the strategies used for control and optimisation rely on lumped parameter system, assuming homogeneous systems. The discrepancies with the experimental data are usually reduced through the adjustment of only few sensitive parameters, generally related to the kinetics of the crystallisation. This makes the updated model/parameters valid only in the vicinity of the

current operating conditions. In light of this, a knowledge-based approach to the problem, based on the actual understanding of the process, the implementation of a detailed mechanistic model and a robust run-to-run or within run adaptive model update are crucial aids to the parameter identification. In recent years, the availability of more accurate mathematical models, solution techniques for complex mathematical systems, advances in on-line measurements and control theory created the ground for advancements in the field of nonlinear optimisation and control of the CSD in crystallisation processes (Braatz, 2002; Larsen *et al.*, 2006; Yu *et al.*, 2007). Different strategies have been proposed to control the crystal size distribution. They include feed forward (open-loop) control, batch-to-batch strategies and on-line model-based control.

The model-based control approaches for crystallisation processes can be divided in two main categories: (i) open-loop (feed-forward) control and (ii) on-line model-based feedback control approaches. Open-loop (or feed-forward) control approaches are techniques for which the process outputs have no effect on the inputs, whereas feed-back control systems are implemented in a closed-loop setting with the outputs that affect the inputs in such a way to keep the outputs at the desired value (Braatz, 2002; Chew *et al.*, 2007; Immanuel and Doyle, 2002; Nagy and Braatz, 2004). Note that open-loop or closed-loop control approaches are defined with respect to some final product property at the end of the batch. In the case of open-loop control approaches the operating conditions are optimised off-line based on model predictions to achieve a desired product property at the end of the batch (e.g. maximize mean size). The resulting optimal operating policies (e.g. temperature versus time or anti-solvent addition rate versus time profiles) then are implemented using simple feedback tracking control systems.

The operation of crystallisation processes using programmed temperature profiles, derived based on the assumption of constant supersaturation, was introduced in the 1970s (Jones and Mullin, 1974; Mullin and Nyvlt, 1971). The application of programmed temperature profiles yields better CSD properties compared to the natural or linear cooling, traditionally used for crystallisation operation. Performing the open-loop optimisation off-line with nominal values of the model parameters and then implementing the optimal trajectory is the most frequently used model-based control approach. One of the first applications of optimal control theory to crystallisation processes was reported by Jones and Mullin in (1974). The author computed optimal cooling trajectories that maximized the final size of the seed crystals for a batch crystallisation process. In the past few decades optimal control has been widely recommended to improve batch crystallisation operations (Rawlings *et al.*, 1993).

The final CSD is dependent on the supersaturation profile created over the batch time, hence the supersaturation profile (generated e.g. by cooling, anti-solvent addition or evaporation) is the most important decision variable in the optimisations. Various objective functions have been used in the optimisations. A detailed review of the optimisation approaches for the properties of the CSD expressed by its moments were given by (Ward *et al.*, 2006) and are summarised in the Chapter 3. The optimal operating profile is strongly influenced by the objective optimised. For example the solution of the optimal control problems with the aim to maximize the weight-average mean crystal size generally leads to convex cooling profiles, whereas the minimization of the coefficient of variation of the CSD in un-seeded crystallisation processes results in fast cooling during the initial part of the operation to generate nuclei in short time period (Nagy and Braatz, 2003b). Detailed overviews of model development and advances in crystallisation control approaches are given in several comprehensive review articles (Braatz, 2002; Braatz *et al.*, 2002; Larsen *et al.*, 2006; Rawlings *et al.*, 1993; Yu *et al.*, 2007). Using optimal temperature trajectories the improvement in the mean crystal size of a potassium nitrate system was reported (Miller and Rawlings, 1994). The mean crystal size and crystal quality of adipic acid was improved using optimal temperature trajectories (Costa *et al.*, 2005).

Anti-solvent addition profile was optimised to improve the product CSD by (Nowee *et al.*, 2008a). More recently model-based optimisation was applied to the combined cooling and anti-solvent crystallisation of lovastatin (Nagy *et al.*, 2008b). The authors showed that the optimal operating trajectories and whether the crystallisation process is controlled by cooling, anti-solvent addition or a combination of the two approaches strongly depend on the objective function used in the optimisation. Hence the model-based optimisation approach in this case has become not only a methodology to determine the best operating curve but also a process design tool, capable of automatically selecting the best supersaturation generation methodology for the process (cooling or anti-solvent addition).

The significant improvement in the computational performance allowed the solution of more complex optimal control problems or the use of more comprehensive models in the optimisation. For example (Ma *et al.*, 2002b) considered two-dimensional growth, solving a corresponding two-dimensional PBE for temperature optimisation in the cooling crystallisation of potassium dihydrogen phosphate (KDP) in water. Costa *et al.* (2005) incorporated aggregation and (Hu *et al.*, 2005) considered growth rate dispersion in their model-based optimisation studies. The paper by (Woo *et al.*, 2006) provides and exemplary case study of using combined computational fluid dynamics (CFD) and PBM for model-based optimisation. The authors used an efficient high resolution finite volume scheme to

solve the coupled PBM-CFD model, which also incorporated the effect of micromixing, for an anti-solvent crystallisation system. The complex model was used for open-loop optimisation however the approach is computationally too expensive for real-time model predictive control.

Parameter uncertainties can also be considered during the optimisation to achieve robust open-loop optimal operating trajectories (Nagy and Braatz, 2004), which minimizes the variability in the product property due to errors in the model. Open-loop optimisation of the temperature trajectories for polymorphic crystallisation was illustrated by (Hermanto *et al.*, 2007).

In addition to the supersaturation profile the seed mass and seed distribution can also be optimised to achieve a desired product property (Bohlin and Rasmuson, 1996; Chung *et al.*, 1999; Kalbasenka *et al.*, 2007). A more detailed overview of these approaches, as well as a novel methodology that simultaneously designs supersaturation profile and seed recipe, or applies dynamic seeding, for the control of the shape of the CSD are provided in Chapters 7 and 9.

A product engineering approach has been proposed by several authors who considered the integrated design of crystallisation and downstream process units to achieve desired performance of the integrated process chain or to produce target end-product quality (Hounslow and Reynolds, 2006; Wibowo *et al.*, 2001).

In addition to the overview of the open-loop model-based control approaches provided in this section there is a vast literature related to the model-free control (direct design) approaches for crystallisation processes, which are based on the application of supersaturation control approaches to control the crystallisation process in the phase diagram. This literature is briefly reviewed in Chapter 7, for more details see e.g. the review papers by Fujiwara *et al.* (2005) and Nagy *et al.*, (2008a, b). These approaches provide fast, robust and reliable control, of crystallisation processes, which can be supported in an industrial environment; however they are designed based on heuristics and trial-and-error experimentations. Hence, the application of these approaches to the control of crystallisation systems is not directly within the scope of the thesis; however a novel methodology to analyse and provide a systematic framework for direct design (based on a simplified model-based optimisation approach) is presented in Chapters 7 and 8.

In addition to the open-loop model-based control approaches significant effort has been devoted to the development and implementation of closed-loop model based control approaches (Larsen *et al.*, 2006; Nagy and Braatz, 2003a; Rawlings *et al.*, 1993;

Sheikhzadeh *et al.*, 2008b). Although these control approaches in principle solve similar dynamic optimisation problems as the open-loop model-based control techniques their implementation complexity is significantly larger than in the latter case. The main difficulties arise from the requirement of on-line state and parameter estimation approaches as well as due to the necessity of computing the solution of the optimisation problem within the sampling period in the process (real-time implementation). These approaches provide the benefits of inherent robustness due to their closed-loop architecture and the ability to adapt the operating conditions to unforeseen disturbances. Nevertheless, the practical application of these approaches is still very scarce both in laboratory as well as industrial environments, due the increased complexity of the control algorithm but also because of regulatory constraints related to the changing/adaptation of operating conditions. Due to their currently very limited applicability these approaches are not considered in this thesis and the focus of the research is directed towards the development and evaluation of efficient open-loop model-based optimal control approaches for CSD control in crystallisation processes.

2.7 Conclusions

Crystallisation is a widely used technique in different chemical industries, very often used in the production of pharmaceuticals and fine chemicals. The driving force for crystallisation process is the supersaturation. Supersaturation can be created in a crystalliser by different operating modes i.e. cooling, evaporation, reaction and anti-solvent addition. Some of these techniques can also be combined together to induce supersaturation in the system.

Determination of the solubility curve, nucleation curve and metastable zone width is of key importance for the development of a crystallisation processes. The metastable zone is the region bounded by the equilibrium (solubility) and the metastable (nucleation) curves, where the solution is supersaturated while spontaneous crystallisation does not occur. Seed crystals may also grow within the metastable zone. The metastable zone width is therefore an important factor in assessing the tendency of a system to crystallise and in deciding the crystallisation technique.

After achieving supersaturation, crystallisation from solution can be considered as a two step process. The first step is a phase separation and called as nucleation, and the second step is the subsequent growth of nuclei to crystals. The small crystals grow larger in size as more

and more solute molecules deposit on the surface of the crystals. Generally growth and nucleation are the two basic phenomena, which govern crystallisation processes.

To model a particulate system such as crystallisation, population balance equations have been accepted for some time as the most fundamental framework. The population balance equation is a material balance that accounts for the distribution in particle size, location and other state variables. There are various approaches to solve the population balance equations.

The most commonly used method is the standard method of moments (SMOM). This solution technique has closure problem in case when the growth is size dependent or when agglomeration and breakage mechanisms also need to be included in the model. Robust retrieval of the full CSD using the standard method of moments is not possible, although it gives the exact solution for the moments of the distribution. To control the CSD it is important that the solution technique should be able to retrieve the entire CSD. Therefore SMOM alone is not a suitable technique for distribution shaping control algorithms.

Another important technique is the quadrature method of moments (QMOM), which solves the closure problem in the case of size dependent growth, agglomeration and breakage. QMOM can be used to solve the PBE for most crystallisation mechanisms. However, the retrieval of the full CSD is still not possible as the method only gives a coarse approximation of the distribution. Therefore this technique alone is not suitable again for distribution shaping control. The method of characteristics is another promising technique for the solution of PBEs, which gives the complete dynamic evolution of the CSD. Most of the crystallisation systems in the literature, for which the MOCH is applied, are processes with size independent growth and nucleation, with virtually no applications reported for processes with size-dependent growth and nucleation. The aforementioned techniques (SMOM, QMOM and MOCH) are simple and computationally efficient, which make these techniques an attractive option for model-based control and optimisation, however only the MOCH can provide the full shape of the distribution (in particular cases), suitable for distribution shaping control.

The method of classes turns the population balance equation into a discretised population balance equation with a resulting set of ODEs with a number equal to the number of classes.

The computational effort for the numerical solution can be high due to the large number of classes. The method is able to retrieve the full CSD information, however it can exhibit spurious oscillations and hence give negative pdf values in the CSD estimate. The approach is also computational inefficient due to the generally large number of classes required and hence it is not the best option for model-based control.

The finite volume methods (FVM) involve the discretisation of the spatial domain and the use of piece-wise functions to approximate the derivatives of the distribution function with respect to the spatial variables. Calculation at each grid point requires the values of growth and nucleation rate as well as the number density at the cell boundaries. The simplest interpolation formula that can be used to approximate the number density at each cell boundary is the upwind interpolation scheme. The approach is applicable to a generic PBE with all mechanisms, however may suffer from numerical diffusion unless a very fine grid mesh is used, increasing the computational burden potentially too much for model-based control and optimisation.

The hyperbolic population balance equation can be solved in its continuous form using the Finite Element Methods (FEM). These techniques approximate the solution using piecewise low-order polynomials but require more computational time due to additional integrations. The dynamic evolution of the size distribution in a particulate process with any mechanisms can also be obtained via stochastic Monte Carlo (MC) simulations. However, due to its computational inefficiency, the method is not an attractive option for model-based control.

Online measurements of state variables such as temperature, concentration and CSD are also required for model-based estimation and control. In most of the practical situations not all variables can be (reliably) measured. Therefore, those unmeasured variables should be estimated using available measurements and the crystallizer model using state estimators or observers. Estimation of unmeasured properties to predict the future behaviour can be used to adjust the operating conditions. In recent years, the availability of more accurate mathematical models, solution techniques for complex mathematical systems, advances in on-line measurements and control theory created the ground for advancements in the field of nonlinear optimisation and control of the particle size distribution in crystallisation processes. Different strategies have been proposed to control the crystal size distribution including feed forward control, batch-to-batch strategies and on-line model-based control.

For the implementation of these control strategies a robust model is required, which is able to capture the dynamic evolution of the distribution, and can be solved in a computational efficient way. Therefore, it is important to have numerical solution techniques, which are able to provide information about the distribution using the data from the available measurements of the state variables. Several techniques to obtain the dynamic evolution of the CSD have been reviewed in this chapter. However, all techniques have some limitations; hence there is a clearly identified requirement for the development of computationally efficient methodologies that can be used to predict the entire shape of the crystal size distribution throughout the batch. The methodology should be robust enough to be used for on-line estimation and control and should be applicable for a wide range of operating conditions.

Chapter 3
Techniques to reconstruct crystal size distribution from moments

3.1 Introduction

In Chapter 2 models were reviewed for their ability to predict the shape of the CSD. The SMOM and QMOM give coarse approximations and the statistics of the CSD. Researchers have tried to develop methods for the reconstruction of the crystal size distribution (CSD) from moments. Moments may also be estimated from the experimentally measured CSD or numerically determined from different distribution functions. A number of instrument types can be used to measure the CSD, as described in section 2.5. Converting experimental measurements to moments is a crucial step in the process of obtaining moments, since as small as 5% error in the moments can lead to large errors in the approximated shape of the distribution. Predicting the CSD using moments provides an insight to the limiting factors of the controller design, which can help to improve product quality and reduce operating cost.

Table 3.1 summarizes different forms of objective functions used in the literature (Ward *et al.*, 2006) to achieve different physical properties of the crystals, based on lower-order moments. The final product CSD depends strongly on the selected optimisation objective function (Chung *et al.*, 2000; Ge *et al.*, 2000). The properties used in the objective functions include for example average crystal size, maximum growth and variation in size of crystals. Multi-objective optimisation techniques can also be used to optimise several statistics of the CSD at the same time. Several multi-objective optimisation functions used by different researchers are summarised in Table 3.1. Table 3.1 shows that most of these properties are expressed by lower-order moments i.e. zeroth to fourth order moments. Lower-order moments are generally used as they are subject to less error than higher order moments (Flood, 2002; Marchisio *et al.*, 2003a). Although various properties of the CSD can be optimised based on several lower order moments, it is generally not clear that how many moments are required for the reconstruction of a complete crystal size distribution.

Table 3.1: Summary of objective functions used for the optimal control of batch crystallisation processes.

Single attribute objective functions	Multiple attribute objective functions	Moments considered	Author
Maximise the size of crystals, $-\mu_{seed,1}$	--	First moment of seed.	(Jones, 1974)
Maximise number average size of crystals, $-\mu_1 / \mu_0$	Maximise average number size and minimise variation in size of crystals, $\left[\frac{\mu_2}{\mu_0}\right] - \left[\frac{\mu_1}{\mu_0}\right]^2 - \alpha\left[\frac{\mu_1}{\mu_0}\right]$	Zeroth, first, second moments.	(Chang and Epstein, 1982)
Minimise variation in size of crystals, $\sqrt{\mu_2\mu_0 / \mu_1^2 - 1}$	--	Zeroth, first and second moments.	(Chung *et al.*, 2000)
Minimise the growth of nucleated crystals and variation in size of crystals, $\mu_{N,3} / \mu_{seed,3}$	--	Third moment of nucleated crystals and seed.	(Chung *et al.*, 2000; Miller and Rawlings, 1994; Rawlings *et al.*, 1992)
Maximise the weight average size of the crystals, $-\mu_4 / \mu_3$	--	Fourth & third moments.	(Berglund and Feng, 2002; Choong and Smith, 2004a, b; Chung *et al.*, 2000)
--	Maximise the average size of crystals and minimise the variation in size of crystals, $-\mu_4 / \mu_3 + 0.0005\sqrt{(\mu_5\mu_3 / \mu_1^2) - 1}$	First, third, fourth and fifth moments.	(Zhang and Rohani, 2003)
--	Minimise the growth of nucleated crystals, maximise the average size of crystals and minimise the variation in size of crystals, $-0.00081\mu_4 / \mu_3 + 0.025\mu_3 / \mu_{N3} + 0.1\sqrt{(\mu_2\mu_0 / \mu_1^2) - 1}$	Zeroth, first, second, third, fourth moments and fourth moment of nucleated crystals.	(Ge *et al.*, 2000)
Minimise variation in size of crystals, $\sqrt{\mu_5\mu_3 / \mu_4^2 - 1}$	--	Third, fourth and fifth moments.	(Choong and Smith, 2004b)

3.2 Approaches to reconstruct the CSD

Several techniques will be used to reconstruct the distribution from the moments. Figure 3.1 gives the overall structure of Chapter 3, describing different techniques used to reconstruct the distribution from moments.

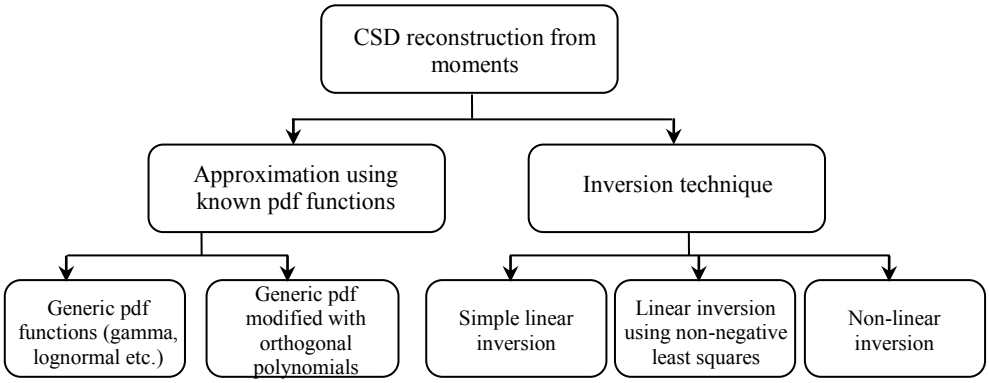

Figure 3.1: Classification of the distribution reconstruction methods from moments evaluated in Chapter 3.

The most commonly used method to reconstruct distribution, is to assume a generic form of the distribution, such as Gaussian, lognormal, bimodal distribution etc (John *et al.*, 2005), and to determine the shape by obtaining the parameters of these distributions from the moments. Reconstruction based on known distribution functions is a powerful and fast method and gives result instantaneously, but the method requires *a priori* knowledge of the shape and distribution (Diemer and Olson, 2002a, b; Giaya and Thompson, 2004; John *et al.*, 2005). In the case of a new application, with an unknown CSD, this method may not work well. Additionally most chemical processes do not possess a simple Gaussian or lognormal distributions. Thus, improved methods of CSD prediction are based on the lower order moments coupled with mathematical functions. Some of these techniques use orthogonal polynomials to correct the population density functions (pdf) by preserving the original moments.

3.2.1 Orthogonal polynomials

In this method, the most often used distributions are: lognormal distribution, gamma distribution and Gaussian (or normal distribution). These can be used to approximate the

shape of the actual distribution. This method uses a basic pdf in combination with orthogonal polynomials, which modify the shape of the core pdf (Hulburt and Katz, 1964). The coefficients of the polynomial are calculated so that the moments of the modified pdf are preserved. Orthogonal polynomials are classes of polynomials $\{p_n(x)\}$ defined over a range of $[a, b]$ that obey an orthogonality relation,

$$\int_a^b w(x)p_m(x)p_n(x)dx = \delta_{mn}c_n \,, \tag{3.1}$$

where $w(x)$ is a weighting function and δ_{mn} is the Kronecker delta ($\delta_{mn} = 0$ for $m \neq n$ and $\delta_{mn} = 1$ for $m = n$). If $c_n = 1$, then the polynomials are not only orthogonal, but orthonormal (MathWorld, 2009). Orthogonal polynomials have very useful properties in the solution of mathematical and physical problems. Orthogonal polynomials provide a natural way to solve, expand and interpret the solutions to many types of differential equations (Randolph and Larson, 1988).

Table 3.2: List of orthogonal polynomials used to modify some basic distribution functions.

Distributions	Orthogonal Polynomials
Gamma	Laguerre
Gaussian	Hermite
Beta	Jacobi
Uniform	Legendre

Table 3.2 summarises the most commonly used basic distribution functions with the corresponding orthogonal polynomials used as weighting functions. In this chapter the major emphasis is on the gamma distribution modified using Laguerre polynomials. The gamma distribution is given by:

$$f_n(L) = \frac{L^{\alpha-1}}{\Gamma(\alpha)\ \beta^{\alpha}} e^{\frac{-L}{\beta}}, \tag{3.2}$$

where Γ is the gamma function, α is the scale parameter, β is the shape parameter, L is the characteristic length in μm and $f_n(L)$ is the number pdf. The gamma function extends the factorial function to real numbers and is defined as:

$$\Gamma(z) = \int_0^\infty e^{-t} t^{z-1} dt. \tag{3.3}$$

If z is a positive integer, then $\Gamma(z) = (z-1)!$. The gamma distribution can be coupled with Laguerre polynomials to modify the gamma distribution while preserving the original moments. The n^{th} order Laguerre polynomials $P_n(z)$ are defined by a contour integral, which encloses the origin but not the point $z = 1$, (MathWorld and Arfken, 1985; Randolph and Larson, 1971):

$$P_n(z) = \frac{1}{2\pi i} \oint \frac{e^{\frac{-zt}{(1-t)}}}{(1-t)t^{n+1}} dt. \tag{3.4}$$

The first three Laguerre polynomials are

$$\begin{aligned} P_0(z) &= 1, \\ P_1(z) &= -z + 1, \\ P_2(z) &= \frac{1}{2}(z^2 - 4z + 2), \end{aligned}$$

and can be generalized for any $n \geq 1$ using a recurrence relationship:

$$P_{n+1}(z) = \frac{1}{n+1}\left[(2n+1-z)P_n(z) - nP_{n-1}(z)\right]. \tag{3.5}$$

The crystal size distribution (CSD) may be approximated in terms of a gamma pdf with polynomial correction terms involving Laguerre polynomials having moment dependent coefficients. The parameters required for gamma distribution are the zeroth, first and second moments. Thus the polynomial corrections having coefficients involving the third and higher moments are used only. This representation is given by Randolph and Larson (1971) as:

$$f_n(L) = \frac{\left(\frac{\lambda}{a}\right)\left(\frac{\lambda L}{a}\right)^{\lambda-1} e^{\frac{-\lambda L}{a}}}{(\lambda-1)!}\left[\mu_0 + \sum_{n=3}^{j} k_n l_n^{(\lambda)}(z)\right], \tag{3.6}$$

where μ_0 is the zeroth moment and the parameters a and λ are related to the parameters of the gamma distribution, and are given in terms of moments, $a = \mu_1 / \mu_0$, $\lambda = a^2 / ((\mu_2 / \mu_0) - a^2)$ and $z = (\lambda L / a)$. The complete derivation is described by Randolph and Larsen (1971). The n^{th} order Laguerre polynomials are given as:

$$l_n^{\lambda}(z) = \sum_{j=0}^{n} (-1)^j \frac{n!(n+\lambda-1)!}{j!(n-j)!(n+\lambda-1-j)!} z^{n-j}, \tag{3.7}$$

$$k_n = \sum_{j=0}^{n} (-1)^j \frac{(\lambda-1)!\left(\frac{\lambda}{a}\right)^{n-j}}{j!(n+\lambda-1-j)!(n-j)!} \mu_{n-j}. \tag{3.8}$$

An interface has been developed in MATLAB, which calculates the form of gamma distribution with Laguerre polynomials as an approximation for different types of distributions. The sum squared errors (SSE) are calculated for the difference between the target distribution and the approximated distribution. These SSE are calculated as:

$$SSE = \frac{1}{n_e} \sum_{i=1}^{n_e} (f_{n,i} - \tilde{f}_{n,i})^2, \tag{3.9}$$

where $f_{n,i}$ is the target distribution, $\tilde{f}_{n,i}$ is the approximated value of the population density function and n_e is the number of the evaluation points.

Figure 3.2 shows the results for the approximation properties using gamma with Laguerre polynomials for some commonly used distributions including Gaussian, lognormal and bimodal distribution. The forms of the three target distributions are:

$$f_{n,G} = \frac{1}{\sqrt{2\pi}\sigma} e^{-[(L-\bar{L})^2]/(2\sigma^2)}, \tag{3.10}$$

$$f_{n,LN} = \frac{1}{L\sigma\sqrt{2\pi}} e^{[-(\log(L)-\log(\bar{L}))^2]/(2\sigma^2)}, \tag{3.11}$$

$$f_{n,BM} = e^{[-(L-\alpha_1)^4+\alpha_2(L-\alpha_1)^2]}. \tag{3.12}$$

Lower-order moments were used to approximate these basic distributions and the moments were calculated numerically for the respective distribution functions. Figure 3.2 (a) shows the comparison of the reconstructed distribution for Gaussian distribution and gamma distribution with Laguerre polynomials. The method was able to capture the shape of the Gaussian distribution well by using the first four moments only. It can also be observed from Figure 3.2 (b) that the shape of the lognormal distribution was also captured well using gamma distribution with Laguerre polynomials, using only the first four moments. However the shape of the bimodal distribution was not captured well by the gamma distribution with

Laguerre polynomials, as shown in Figure 3.2 (c). The results indicate that gamma with Laguerre polynomials can produce good approximations for Gaussian and lognormal distribution using lower-order moments. However the approach was not able to approximate the bimodal distribution using lower-order moments only.

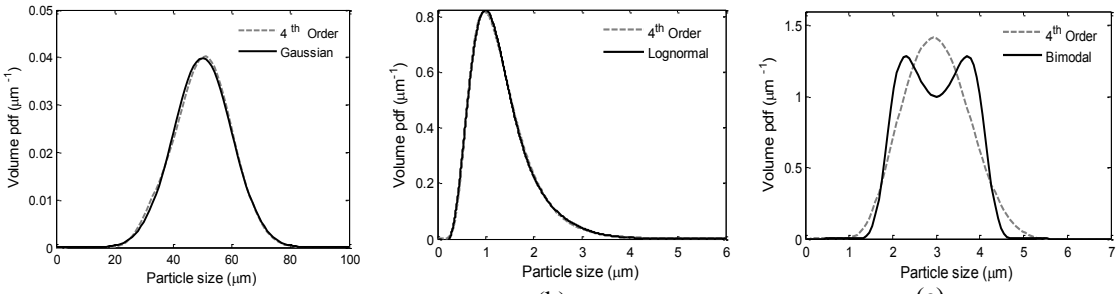

Figure 3.2: Comparison of approximation of different distribution using 4th order gamma with Laguerre polynomials for a) Gaussian distribution ($\bar{L} = 50$ and $\sigma = 10$) b) lognormal distribution ($\bar{L} = \log(1.2)$ and $\sigma = 0.3$) and c) bimodal distribution ($\alpha_1 = 3$ and $\alpha_2 = 1$).

Therefore higher-order moments (from 10-16) were used to reconstruct the bimodal distribution. As the number of moments has increased a better reconstruction of the bimodal distribution has been obtained, as shown in Figure 3.3. The sum squared errors for 10th and 16th order approximation were 0.33 and 0.18 respectively, which confirms that by increasing the number of moments, a better CSD approximation can be obtained even for bimodal distribution, however negative values in the pdf's can also be observed when higher moments were used.

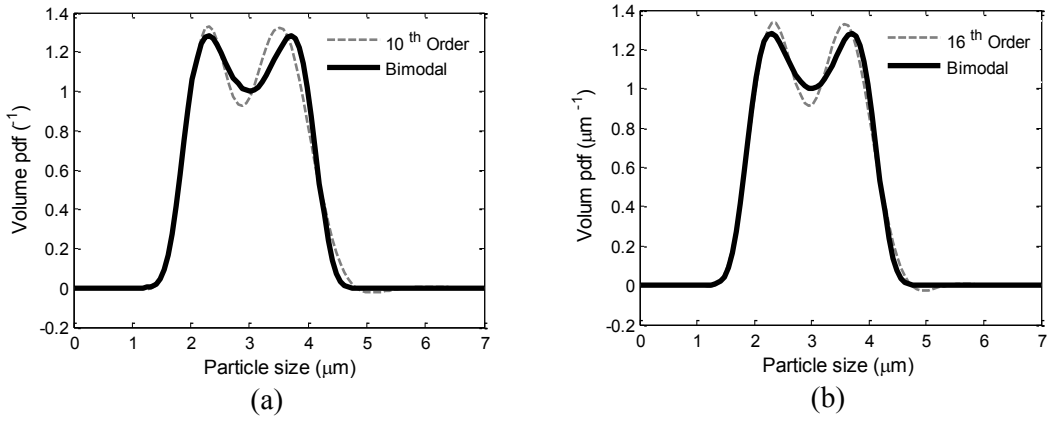

Figure 3.3: Comparison of a bimodal distribution ($\alpha_1 = 3$ and $\alpha_2 = 1$) with the approximation from gamma with Laguerre polynomials a) using up to 10th order moments and b) using up to 16th order moments.

The reconstructed distribution results for Gaussian and lognormal distribution has been obtained using lower-order moments but higher order moments were required for bimodal distribution. Therefore the higher-order moments were used for simple Gaussian and lognormal distribution to check the capability of the technique. Results shown in Figure 3.4 (a and b), indicate that higher order corrections involving Laguerre polynomial terms produce oscillations about the gamma distribution. These oscillations grow larger with increasing number of terms. However the reconstruction of the bimodal distribution has improved with higher-order of moments, as already shown in Figure 3.3 (c).

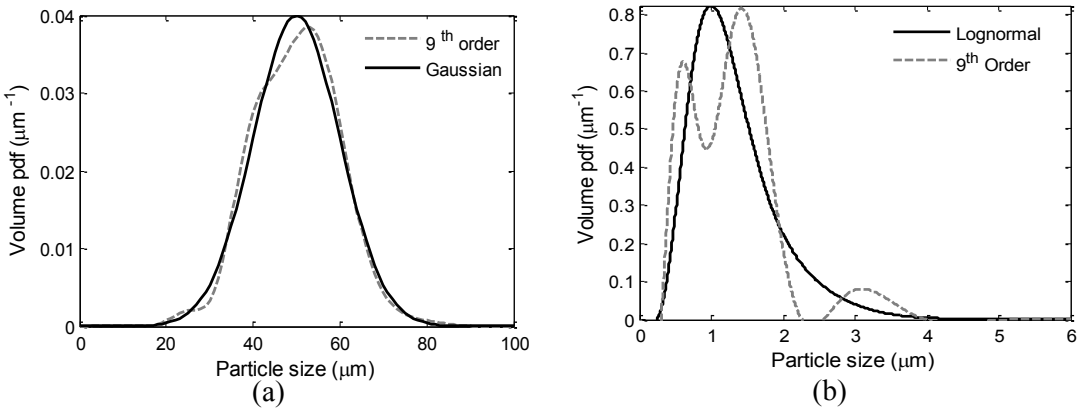

Figure 3.4: Approximation of distributions using gamma with Laguerre polynomials using 9th order moments a) Gaussian distribution ($\bar{L} = 50$ and $\sigma = 10$) and b) lognormal distribution ($\bar{L} = \log(1.2)$ and $\sigma = 0.3$).

The results indicate that the technique has some limitations. These are mainly related to how different the shape of the target distribution is from the gamma distribution. Since the Laguerre polynomial modifies the basic shape of the gamma distribution in the case when the approximated distribution has a very different shape, the quality of the approximation with smaller number of polynomial terms, is poor, as shown in Figure 3.2 (c). In this case generally a higher order approximation is required, as shown in Figure 3.3 (a and b). However, when higher order coefficients are used for the approximation of simpler distributions (e.g. Gaussian and lognormal) the approximated distribution often exhibits oscillations. Hence the main disadvantage of the approach is the difficulty in the determination of the suitable number of polynomial terms, which requires *a priori* knowledge about the shape of the distributions. Additionally if during the crystallisation process the shape of the distribution changes (e.g. from mono-modal to bimodal due to nucleation) the number of Laguerre polynomial terms should be adapted. In the previous

technique the CSD was reconstructed by assuming *a priori* shape. Another way to approximate the CSD is to use moments of the distributions in inversion approaches.

3.2.2 Linear inversion technique

Another category of distribution reconstruction techniques is based on moment inversion. The j^{th} moment of a distribution is written as:

$$\mu_j = \int_0^\infty f_n L^j dL, \tag{3.13}$$

for which, the first-order approximation is given as:

$$\mu_j = \sum_{k=1}^{N_d} f_{n,k} L_{m,k}^j \Delta L_k, \tag{3.14}$$

where $f_{n,k}$ is the value of the population density function f_n at the midpoint $L_{m,k}$ of a size range ΔL_k and N_d is the number of discretisation points. Figure 3.5 gives a graphical representation of the discretisation points for the linear inversion technique.

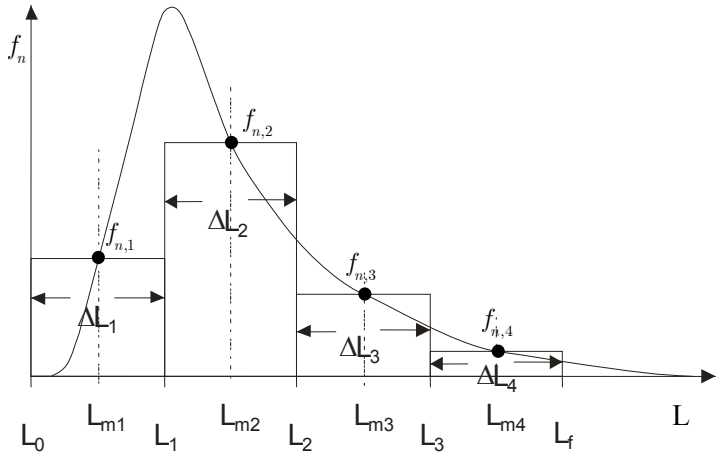

Figure 3.5: Graphical representation of the discretisation points and mid points, for the linear inversion technique.

Rewriting equation (3.14) as a linear combination of N_d ordinate values of the distribution $f_{n,k}$ gives

$$\mu_j = \sum_{k=1}^{N_d} a_k^{(j)} f_{n,k}, \tag{3.15}$$

where $a_k^{(j)} = L_{m,k}^{j} \Delta L_k$. The number of discretisation is given by N_d. Expanding the above relationship for $k = 1$ to N_d gives:

$$\begin{aligned}
&\mu_0 = f_{n,1}\Delta L_1 + f_{n,2}\Delta L_2 + ... + f_{n,N_d}\Delta L_{N_d} \\
&\mu_1 = f_{n,1}L_{m,1}\Delta L_1 + f_{n,2}L_{m,2}\Delta L_2 + ... + f_{n,N_d}L_{m,N_d}\Delta L_{N_d} \\
&\vdots \\
&\mu_{N_d-1} = f_{n,1}L_{m,1}^{N_d-1}\Delta L_1 + f_{n,2}L_{m,2}^{N_d-1}\Delta L_2 + ... + f_{n,N_d}L_{m,N_d}^{N_d-1}\Delta L_{N_d}.
\end{aligned} \tag{3.16}$$

Rewriting equation (3.16) in matrix form $\mu = Af_n$, (3.17), where $\mu_{(N_d,1)}$ is a column vector with N_d elements, $A_{(N_d,N_d)}$ is a $N_d \times N_d$ matrix and $f_{n,(N_d,1)}$ is a column vector with N_d elements containing the values of the number density function results in a system of linear equations, as the only unknown are the values of f_n. Equation (3.17) is a simple linear system of equation $\mu = Af_n$ with the solution $f_n = A^{-1}\mu$. The moments required can either be calculated numerically from a model or can be determined from experimental data. For following examples the used moments were calculated numerically from known distribution functions, and the whole distribution is divided into equal parts $\Delta L = \Delta L_1 = ... = \Delta L_{N_d}$. The methods to calculate the mid points, discretisation points, size ranges and their effects are described in detail in Section 3.3.

$$\mu = \begin{bmatrix} \mu_0 \\ \mu_1 \\ \vdots \\ \mu_{N_d-1} \end{bmatrix}, \; f_n = \begin{bmatrix} f_{n,1} \\ f_{n,2} \\ \vdots \\ f_{n,N_d} \end{bmatrix}, \quad A_{(N_d,N_d)} = \begin{pmatrix} \Delta L_1 & \Delta L_2 & \cdots & \Delta L_{N_d} \\ L_{m,1}\Delta L_1 & L_{m,2}\Delta L_2 & \cdots & L_{m,N_d}\Delta L_{N_d} \\ \vdots & \vdots & \cdots & \vdots \\ L_{m,1}^{N_d-1}\Delta L_1 & L_{m,2}^{N_d-1}\Delta L_2 & \cdots & L_{m,N_d}^{N_d-1}\Delta L_{N_d} \end{pmatrix} \tag{3.17}$$

Figure 3.6 shows the results of reconstruction of CSD for commonly used distribution functions by using linear inversion technique. Different number of discretisations was used to approximate the shape of the distributions. It can be observed that linear inversion method

gives reasonable approximation for Gaussian distribution, as shown in Figure 3.6 (a-c). The sum squared errors for these distributions are given in Table 3.3.

Table 3.3: The sum square errors (SSE) calculated for different distribution functions and discretisation numbers for linear inversion.

Distributions	Sum Squared Error (SSE)		
	3 discretisation points	5 discretisation points	8 discretisation points
Gaussian	0.22	0.01	0.03
Lognormal	0.21	0.02	0.46
Bimodal	0.45	0.38	0.11

Figure 3.6 (a-c) shows that increasing the number of discretisation give better approximation for the Gaussian distribution. However the technique gives negative pdfs for Gaussian distribution at more than ten discretisation points. The sum square error value was the smallest in the case of five discretisation points, as given in Table 3.3. The SSE is similar using eight discretisation points. However in this case eight moments are required, which are practically difficult to obtain. Similarly, in the case of lognormal distribution, the shape of the lognormal distribution was captured well using five discretisation points and no negative pdf values were observed. The value of SSE is also the smallest for five discretisation points, which corresponds to the reconstructed distribution shown in Figure 3.6 (e). Negative pdf values were observed at eight discretisation points for the lognormal distribution, as shown in Figure 3.6 (f), hence indicating that higher discretisation points cannot be used in this particular case. In the case of lognormal distribution the best reconstruction of the shape was achieved using $N_d = 5$, as shown in Figure 3.6 (e). The shape of the bimodal distribution cannot be captured using only three or five discretisation points, as shown in Figure 3.6 (g) and (h). Using higher number of discretisation points ($N_d = 8$) the shape of the bimodal distribution is captured better, as shown in Figure 3.6 (i), however some negative pdf values started to appear. These results indicate that the major problem with the linear inversion approach is the generation of negative values in the reconstruction of the distribution. Increasing the number of moments produced negative pdf values in case of lognormal and bimodal distribution. The other common problem related to linear inversion technique is ill-conditioning, which has been described in detail in the literature (Flood,

2002; John *et al.*, 2005; Mesbah *et al.*, 2009), therefore examples for ill-conditioning are not included in the thesis.

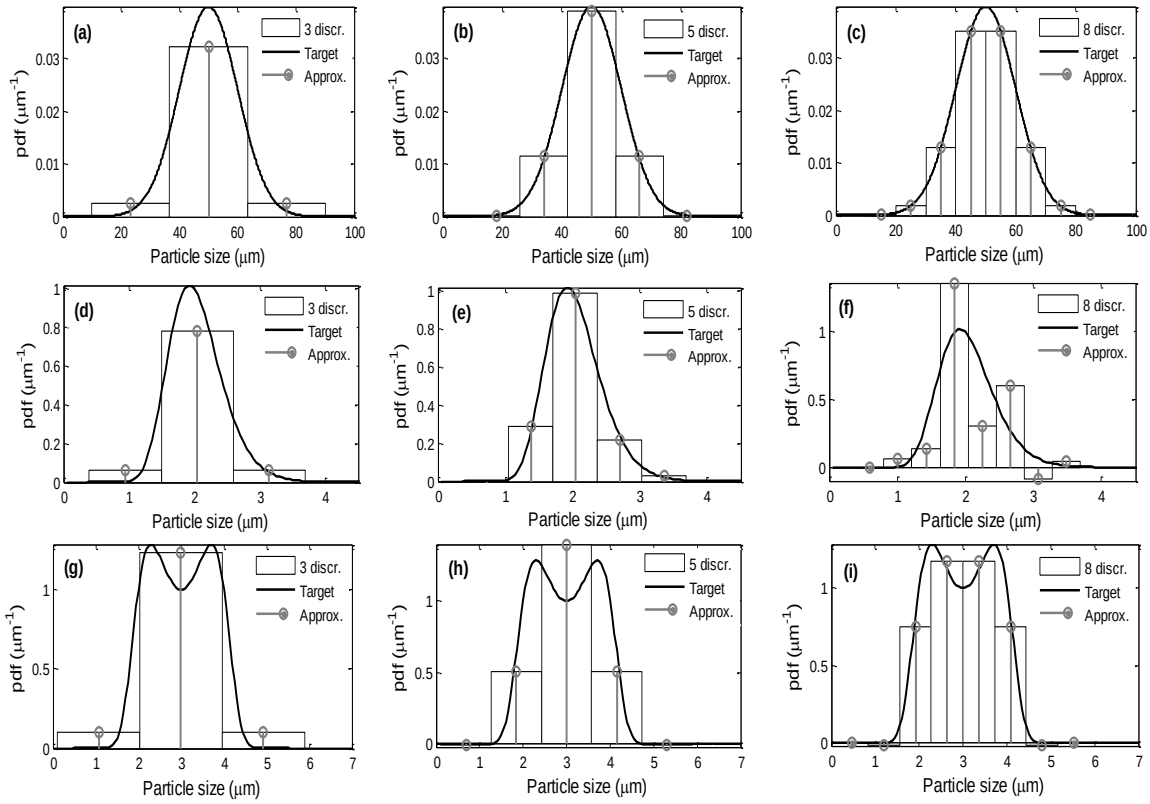

Figure 3.6: The approximation of CSD using linear inversion technique using 3, 5 and 8 discretisation points. Gaussian distribution (a-c) ($\bar{L} = 50$ and $\sigma = 10$), lognormal distribution (d-f) ($\bar{L} = \log(2.0)$ and $\sigma = 0.2$) and bimodal distribution (g-i) ($\alpha_1 = 3$ and $\alpha_2 = 1$).

The linear inversion technique can be improved by solving it as an optimisation problem using hard constraints for positive pdf values. The mathematical form for constrained linear inversion technique is given by:

$$\min_{f_{n,i}} \sum_{j=1}^{2N_d-1} (\mu_j - \sum_{i=1}^{N_d} L_{m,i}^j \Delta L_i f_{n,i})^2, \tag{3.18}$$

subject to: $f_{n,i} \geq 0.$

This problem is solved to achieve the best fit for the distribution using the *lsqnonneg* function in MATLAB (Mathworks, Inc), which implements the non-negative least square (NNLS) optimisation approach. The constraint $f_{n,i} \geq 0$ is added so that negative values can be avoided. The number of moments used is $2N_d$. The system is over-determined, since $2N_d$

equations are used for a number of unknowns equal to N_d. Figure 3.7 shows the results of the CSD reconstruction using the constrained linear inversion technique. The results indicate that poor approximation of the Gaussian distribution was achieved although there are no negative values in the distribution. The comparison of the SSE values is given in Table 3.4. It can be observed that the SSE values were 0.01 and 0.89 for the linear and optimisation-based linear inversion techniques, respectively. The distribution reconstructed by the linear inversion technique is better than the optimised linear inversion technique, due to the difficulty in finding the global optimum in the latter case. In the case of the lognormal and bimodal distributions, the optimisation-based linear inversion eliminates the negative pdf values, however overall the approximation is worse than in the case of simple linear inversion.

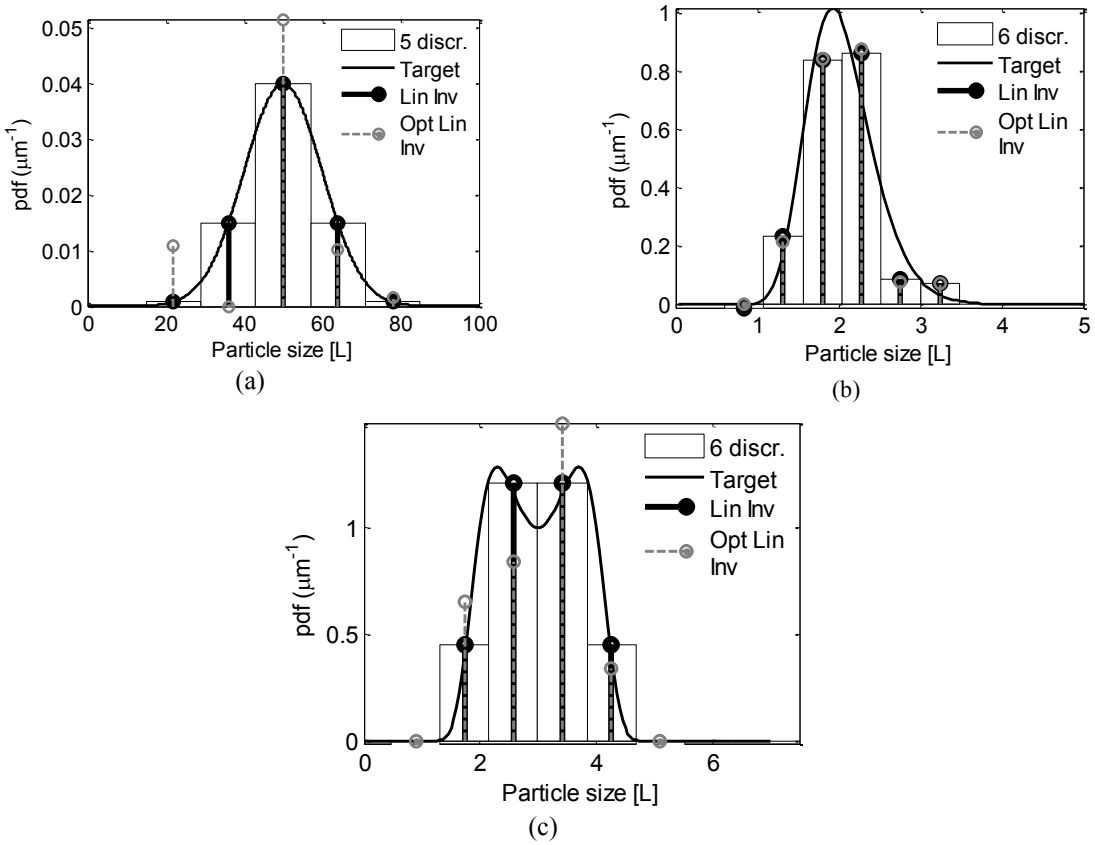

Figure 3.7: Comparison of linear and optimisation-based linear inversion techniques: a) Gaussian ($\bar{L} = 50$ and $\sigma = 10$); b) lognormal ($\bar{L} = \log(2.0)$ and $\sigma = 0.2$) and c) bimodal distribution ($\alpha_1 = 3$ and $\alpha_2 = 1$).

Table 3.4: The sum square errors (SSE) calculated for different distribution functions shown in Figure 3.7 using the linear and optimisation-based linear inversions.

Distribution	Sum Squared Error (SSE)	
	Linear inversion	Optimisation-based linear inversion
Gaussian (5 discretisations)	0.01	0.89
Lognormal (6 discretisations)	0.12	0.25
Bimodal (6 discretisations)	0.24	0.49

3.2.3 Non-linear inversion technique

In the non-linear inversion technique, f_n and L are treated as unknowns and the distribution is discretised into N_d intervals. In this case ΔL is not equally spaced and the L_m and ΔL are calculated from the respective length intervals, where L_0 and L_f are the initial and final particle sizes determined by the algorithm described in Figure 3.9. The methods to calculate the mid points, discretisation points, size ranges and their effects are described in detail in Section 3.3. Initially the discretisation steps are initiated as:

$$L = L_0 : (L_f - L_0) / N_d : L_f , \tag{3.19}$$

both L_0 and L_f are fixed and then L_m and ΔL are calculated using the following relationships:

$$\begin{aligned} &\Delta L_1 = L_1 - L_0 \quad \text{and} \quad L_{m,1} = (L_0 + L_1)/2, \\ &\Delta L_2 = L_2 - L_1 \quad \text{and} \quad L_{m,2} = (L_1 + L_2)/2, \\ &\vdots \\ &\Delta L_{N_d} = L_f - L_{f-1} \quad \text{and} \quad \Delta L_{m,N_d} = (L_f + L_{f-1})/2. \end{aligned} \tag{3.20}$$

The set of non-linear equations for the non-linear inversion is as follows:

$$\begin{aligned} &f_{n,1}\Delta L_1 + f_{n,2}\Delta L_2 + \ldots + f_{n,N_d}\Delta L_{N_d} - \mu_0 = 0 \\ &f_{n,1}L_{m,1}\Delta L_1 + f_{n,2}L_{m,2}\Delta L_2 + \ldots + f_{n,N_d}L_{m,N_d}\Delta L_{N_d} - \mu_1 = 0 \\ &\vdots \\ &f_{n,N_d}L_{m,1}^{2N_d-1}\Delta L_{N_d} + f_{n,N_d}L_{m,2}^{2N_d-1}\Delta L_{N_d} + \ldots + f_{n,N_d}L_{m,N_d}^{2N_d-1}\Delta L_{N_d} - \mu_{2N_d-1} = 0. \end{aligned} \tag{3.21}$$

Since there are two sets of unknowns (f_n and L) in the non-linear inversion, $2N_d$ moments are required for the calculation of the distribution. To solve this system, the *fsolve* MATLAB function was used. Figure 3.8 shows the results obtained using the non-linear inversion technique.

Table 3.5: The sum square error (SSE) calculated for the reconstruction of different distribution functions for different discretisation numbers using the non-linear inversion approach.

Distribution	Sum Squared Error (SSE)		
	3 discretisation points	5 discretisation points	8 discretisation points
Gaussian	0.31	0.05	0.08
Lognormal	0.28	0.10	0.32
Bimodal	0.68	0.44	0.11

For comparison purpose the same number of discretisation points was used as for the linear inversion technique. Comparing the results shown in Figure 3.6 and Figure 3.8 for the same number of discretisation points indicates that the linear inversion generally gives better results for Gaussian, lognormal and bimodal distributions than the non-linear inversion technique. This is also evident by the sum square errors calculated for the two techniques and shown in Table 3.3 and Table 3.5.

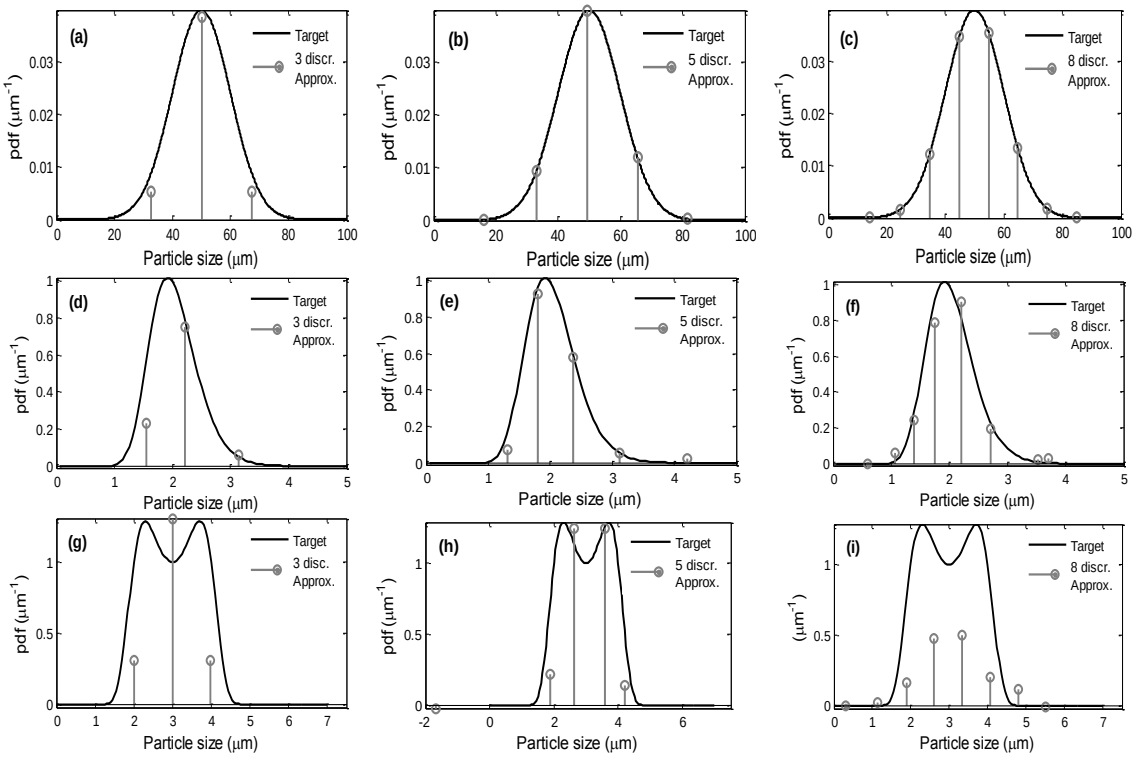

Figure 3.8: The approximation of CSD using non-linear inversion technique using 3, 5 and 8 discretisation points. Gaussian distribution ($\bar{L} = 50$ and $\sigma = 10$) (a-c), lognormal distribution ($\bar{L} = \log(2.0)$ and $\sigma = 0.2$) (d-f) and bimodal distribution ($\alpha_1 = 3$ and $\alpha_2 = 1$) (g-i).

Other major problems have also been observed in the non-linear inversion technique. Increasing the number of discretisations increases the number of evaluations and number of

iterations to acquire the best solution, increasing significantly the computational effort required to obtain the solution. The problem also becomes numerically more ill-conditioned, and hence more difficult to solve. Therefore the non-linear inversion technique cannot be used successfully for CSD approximation. The negative pdf values can be eliminated in non-linear inversion technique by using constraints and solving the inversion as an optimisation problem. The mathematical representation is given by:

$$\min_{f_{n,i},L_{m,i}} \sum_{j=1}^{2N_d-1} (\mu_j - \sum_{i=1}^{n} L_{m,i}^{j} \Delta L_i f_{n,i})^2 , \tag{3.22}$$

subject to: $f_{n,i} \geq 0$.

This problem was solved using the *fmincon* function in MATLAB (Mathworks, Inc). The constraint $f_{n,i} \geq 0$ was added to remove the negative values of the pdf. The number of moments used was $2N_d$. The system was not over-determined as in this case we have two unknowns. No significant improvement in the results was obtained by solving the problem as a constrained optimisation, the negative pdf's were removed, however the overall CSD approximation has become worse compared to the approximation using the solution as a system of nonlinear equations.

All aforementioned inversion techniques require input of the moments, the initial and the final value for the particle size, number and length of discretisation points and intervals and the calculation of mid points for the discretisation intervals. Therefore, all these factors are of key importance. If the given range of particle size is very large and the distribution lies in a very small range, it is possible that that the whole distribution is embedded in a few discretisation intervals only. It is also possible that if the given range is very small and the actual distribution is broad enough, the whole distribution cannot be captured. Even a slight change in the range can give variations in the approximations. Similarly errors in the moments can also lead to significant errors in the results of the inversion techniques. The most important factors, which can affect the results of the inversion techniques, are discussed in the next section.

3.3 Factors affecting the moment inversion technique

3.3.1 Selection of size range

For the reconstruction of the distributions the selection of the size range is important to avoid negative values in the reconstructed pdf's. The methodology for selecting the size range is given in Figure 3.9. Instead of using a trial-and-error approach the size range is selected using the moments of the distribution obtained e.g. from a moment based model. Then the mean and standard deviation are calculated using the moments with the following relationships:

$$\bar{L} = \frac{\mu_1}{\mu_0} \quad \text{and} \quad \sigma = \sqrt{\left(\frac{\mu_2}{\mu_0}\right) - \left(\frac{\mu_1}{\mu_0}\right)^2}, \tag{3.23}$$

where $\bar{L}$ is the mean, σ is the standard deviation, μ_0, μ_1 and μ_2 are the zeroth, first and second order moments, respectively. The mean and standard deviation are used to derive the lower and the upper bounds for the size range, using a size range parameter α. The value of α selected was 3, 3.5 or 4. The selection of value of α is based on the fact that three sigma covers 99.97% of the whole distribution (note that this is true for Gaussian distribution only; for significantly skewed distributions a different approach for the determination of α may be required), hence a value between 3 to 4 should provide a size range large enough to cover the range of the distribution, without being too broad to generate inversion problems, due to the size bins where the distribution has zero values. For all results shown previously in Section 3.2 the value of $\alpha = 4.0$ was used.

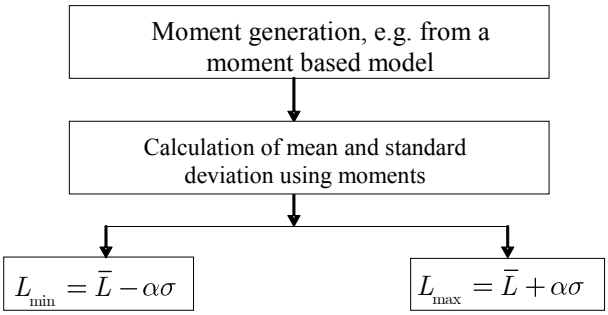

Figure 3.9: Algorithm for calculating the size range for the distribution reconstruction by inversion of moments.

3.3.2 Number and type of the discretisation intervals

The calculation of the discretisation points is also very important for the inversion approach. For the linear inversion technique the discretisation points may be equally spaced in accordance to an arithmetic progression or calculated based on a geometric progression. For the equally spaced discretisation the size bins are calculated as follows;

$$\Delta L = \Delta L_1 = \Delta L_2 = ... = \Delta L_{N_d} = (L_f - L_0) / N_d \,, \tag{3.24}$$

and the discretisation points (edges of the size bins) are calculated as $L_i = L_{i-1} + \Delta L,\ i = 1,...,N_d$. When a geometric progression is used the edges of the size bins are not equally spaced; they follow a geometric progression characterized by a constant ratio (r_G) between two neighboring sizes: $r_G = L_i / L_{i-1},\ i = 1,...,N_d$. For a generic geometric progression the ration r_G can be calculated by $r_G = (L_f / L_0)^{1/N_d}$.

3.3.3 Calculation of mid points

Three different techniques can be used for the calculation of the mid points for the inversion techniques as required for equations (3.16) and (3.21): arithmetic mean, geometric mean and Hounslow mean.

a. Arithmetic mean

Considering L_0 as the initial (minimum) and L_f the final (maximum) particle size (in μm), the arithmetic mean values for the size bins are:

$$L_{m,1} = (L_0 + L_1) / 2,\quad L_{m,2} = (L_1 + L_2) / 2\ \ ,...,\ L_{m,N_d} = (L_{N_d-1} + L_f) / 2. \tag{3.25}$$

As ΔL represents the discretised length which are equally spaced therefore calculating L_m in form of ΔL will give:

$$L_{m,1} = L_0 + (\Delta L_1 / 2), L_{m,2} = L_1 + (\Delta L_2 / 2),..., L_{m,N_d} = L_{N_d-1} + (\Delta L_{N_d} / 2)\,. \tag{3.26}$$

b. Geometric mean

In many CSD measuring instruments such as Malvern Mastersizer, Coulter and Malvern Insitec the geometric mean is used to calculate the mean of the size intervals. The geometric mean corresponding to the size bins can be defined as:

$$L_{m,1} = \sqrt{L_0 L_1},\quad L_{m,2} = \sqrt{L_1 L_2},\ \ldots\ , L_{m,N_d} = \sqrt{L_{N_d-1} L_f}. \tag{3.27}$$

Calculating L_m in terms of ΔL will give:

$$L_{m,1} = \sqrt{L_0(\Delta L_1 + L_0)}, L_{m,2} = \sqrt{L_1(\Delta L_2 + L_1)}, \ldots, L_{m,N_d} = \sqrt{L_f(L_f - \Delta L_{N_d})}\,. \tag{3.28}$$

c. Hounslow mean

The Hounslow mean was developed specifically for discretised population balance equations (Hounslow *et al.*, 1988) and is given by the following expression:

$$L_{m,k}^j = L_{k-1}^j \left[\frac{r_H^{\,j+1} - 1}{(r_H - 1)(j+1)} \right], \tag{3.29}$$

The Hounslow mean is used in conjunction with constant ratio discretisation (in general $r_H = L_j / L_{j-1} = \sqrt[3]{2}$). Generally the Hounslow mean is more difficult to use than the arithmetic or geometric means, since the mean varies with the moment it is used for (Flood, 2002). The mean for the zeroth moment is the lower limit of the size interval, the mean for the first moment is slightly larger than the geometric mean, whereas the mean for the large moments approaches the upper limit of the size class. Figure 3.10 shows a comparison of the inversion approach using arithmetic and geometric means with linearly spaced discretisation intervals, as well as for constant ratio discretisation (Figure 3.10 (d)). The limits of the discretisation intervals were calculated according to Figure 3.9, using $\alpha = 4.0$ ($L_0 = \bar{L} - \alpha\sigma$ and $L_f = \bar{L} + \alpha\sigma$). A linearly distributed discretisation of $N_d = 6$ was used in Figure 3.10 (a-c), with a discretisation interval $\Delta L = (L_f - L_0)/N_d = (2\alpha\sigma)/N_d$. For the constant ratio discretisation (Figure 3.10(d)) $N_d = 3$ was used, yielding a ratio of $r_G = (L_f / L_0)^{1/3}$. The arithmetic mean gives a slightly better approximation than the geometric mean in case of the Gaussian and lognormal distributions, as shown by the SSE values in Table 3.6. However in the case of the bimodal distribution negative values in the pdf were observed at lower discretisation points using the arithmetic mean, and the geometric mean provided a slightly

better approximation (lower SSE value). Using the constant ratio discretisation (Figure 3.10 (d)) gives negative pdf values even for three discretisation points for the simple Gaussian distribution, independently whether arithmetic or geometric mean were used.

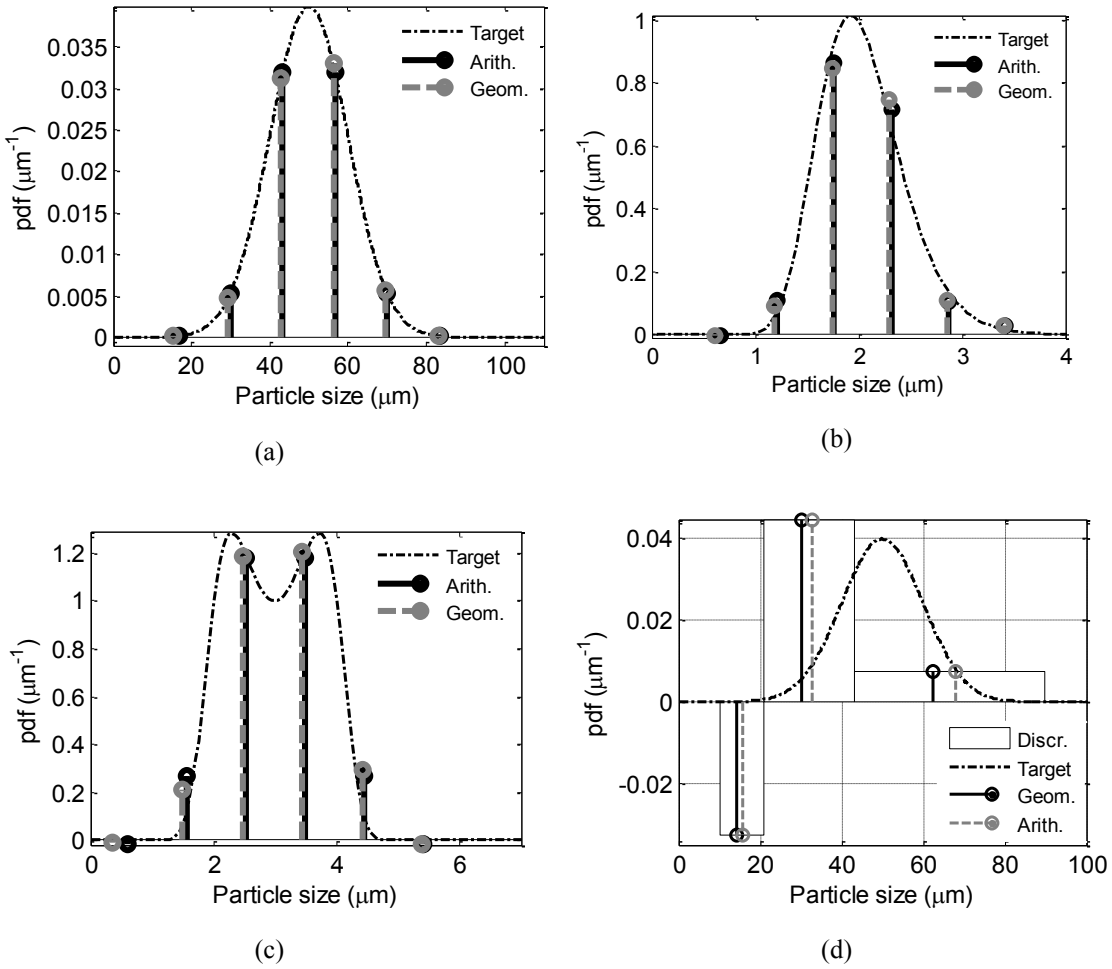

Figure 3.10: Comparison of approximated distribution using arithmetic and geometric mean for 6 discretisation points: a) Gaussian distribution ($\bar{L} = 50$ and $\sigma = 10$) b) lognormal distribution ($\bar{L} = \log(2.0)$ and $\sigma = 0.2$) c) bimodal distribution ($\alpha_1 = 3$ and $\alpha_2 = 1$) and d) arithmetic and geometric means using constant ratio discretisation, on three intervals for Gaussian distribution ($\bar{L} = 50$ and $\sigma = 10$).

Table 3.6: The sum square error (SSE) calculated for different distribution functions to compare the difference between using arithmetic and geometric mean for the inversion.

Distributions	No of discretisation	Sum Squared Error (SSE)	
		Arithmetic Mean	Geometric Mean
Gaussian	6	0.005	0.007
Lognormal	6	0.12	0.14
Bimodal	6	0.24	0.20

3.3.4 Error in moments

In all previous examples the moments used were obtained numerically from different distribution functions. This method gives exactly the required initial moments for the inversion. However even with the exact moments the reconstruction of the distribution was just satisfactory in some cases, and more often was not good enough to be used for model based control and optimisation approaches. Alternatively moments can be determined from the experimental measurement of CSD, as shown in Figure 1.1. However the errors in the experimental moments can be very high due to uncertainties and disturbances related to the measurement approaches. As both the inversion techniques and the approaches based on modified distribution functions using polynomial based corrections are based on the moments, therefore errors in the moments can lead to large errors in the CSD approximation.

3.4 Case study for seeded batch crystallisation processes

The distribution reconstruction techniques described in the previous sections were used to simulate the dynamic evaluation of the CSD for a seeded batch crystallisation process. The generic form of the population balance equation, for a well-mixed crystalliser, considering a single growth direction with one characteristic length L, is given as

$$\frac{\partial f_n(L,t)}{\partial t} + \frac{\partial (G(S,L;\theta_g) f_n(L,t))}{\partial L} = 0, \tag{3.30}$$

where $f_n(L,t)$ is the crystal size distribution expressed as the number density function (number of crystals per unit volume), t is the time, $G(S,L;\theta_g)$ is the rate of crystal growth, $S = (C - C_{sat})$ is the absolute supersaturation, C is the solute concentration, $C_{sat} = C_{sat}(T)$ is the saturation concentration with T being the temperature, and θ_g is a vector containing the growth kinetic parameters. For the simulations a system with linear size-dependent growth is considered with a particular growth rate given by

$$G = 1 + 0.02L. \tag{3.31}$$

It is considered that the seed charged to the crystallizer is normally distributed with a mean $\bar{L}_s = 50\ \mu m$ and standard deviation $\sigma_s = 10\ \mu m$:

$$f_n(L) = \frac{1}{\sigma_s \sqrt{2\pi}} e^{\frac{-(L-\bar{L}_s)^2}{2\sigma_s^2}}. \tag{3.32}$$

In the case of constant supersaturation the PBE (3.30) can be solved analytically using the method of characteristics (as explained in detail in Chapter 2). Rearranging equation (3.30) gives:

$$\frac{\partial f_n(L,t)}{\partial t} + G(S,L;\theta_g)\frac{\partial (f_n(L,t))}{\partial L} = -f_n(L,t)\frac{\partial (G(S,L;\theta_g))}{\partial L}. \tag{3.33}$$

Comparing equation (3.33) with equations (2.24) in Chapter 2 results in the following set of ordinary differential equations (ODEs) which give the characteristic equations of the PBE:

$$\frac{dL}{dt} = 1 + 0.02L, \tag{3.34}$$

$$\frac{df_n}{dt} = -0.02 f_n, \tag{3.35}$$

with initial conditions $[L_0, f_{n,0}(L_0)]$. Solving the system of ODE (3.34) and (3.35) the following time dependent expression for the evolving distribution can be obtained,

$$f_n(L,t) = \frac{1}{\sigma_s \sqrt{2\pi}} e^{\frac{\left[-(L+50)e^{-0.02t} - 50 - \bar{L}_s\right]^2}{2\sigma_s^2}} e^{-0.02t}. \tag{3.36}$$

The moments were calculated numerically using the equation (3.36) or alternatively they can be calculated using the QMOM explained in detail in Chapter 2.

The seed distribution was approximated using the linear inversion technique. For the linear inversion technique five discretisation points were used and the size range was selected using the algorithm shown in Figure 3.9 with $\alpha = 4.0$. It can be seen from Figure 3.11 (a) that although the linear inversion gives a good approximation of the seed CSD, a larger number of discretisation points would be required to attain the actual shape of the CSD. The sum squared errors between the seed distribution and the approximated distributions for different number of discretisations are shown in Figure 3.11 (b). It can be seen that at least four to five moments are required to attain a good approximation of the distribution. However, when more than five discretisation points are used the error increases again due to numerical errors caused by the ill-conditioning of the inversion problem. Thus the linear

inversion approach is unable to provide the shape of the distribution with a high enough resolution for CSD shape optimisation.

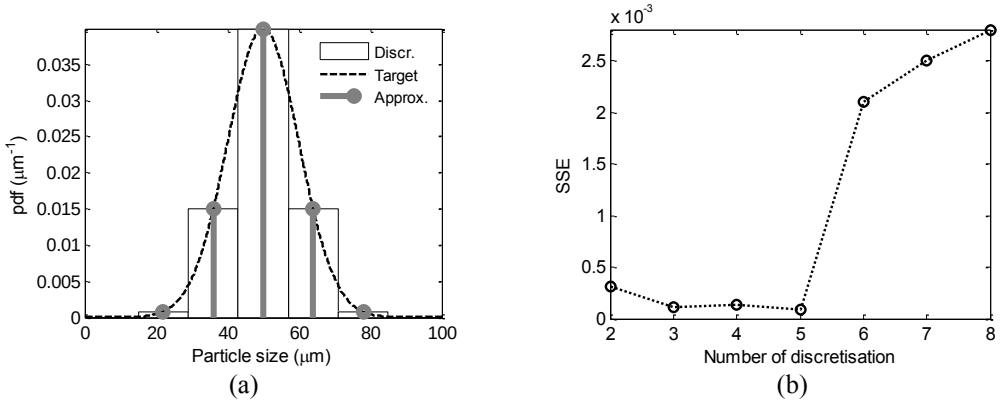

Figure 3.11: a) Approximation of the seed distribution using linear inversion technique with five discretisation points. b) Sum squared errors vs. number of discretisation corresponding to the linear inversion based approximation of the seed distribution.

Using five discretisation points and $\alpha = 4.0$ produced the best approximation for the seed distribution. Therefore five discretisation points with $\alpha = 4.0$ were used to approximate the distribution at several time steps during the batch. The total batch time for the simulated crystallisation process was 60 minutes. Figure 3.12 shows the comparison between the dynamic evolution of the exact CSD (obtained from equation (3.36)) throughout the batch and the reconstructed distribution using the linear inversion technique.

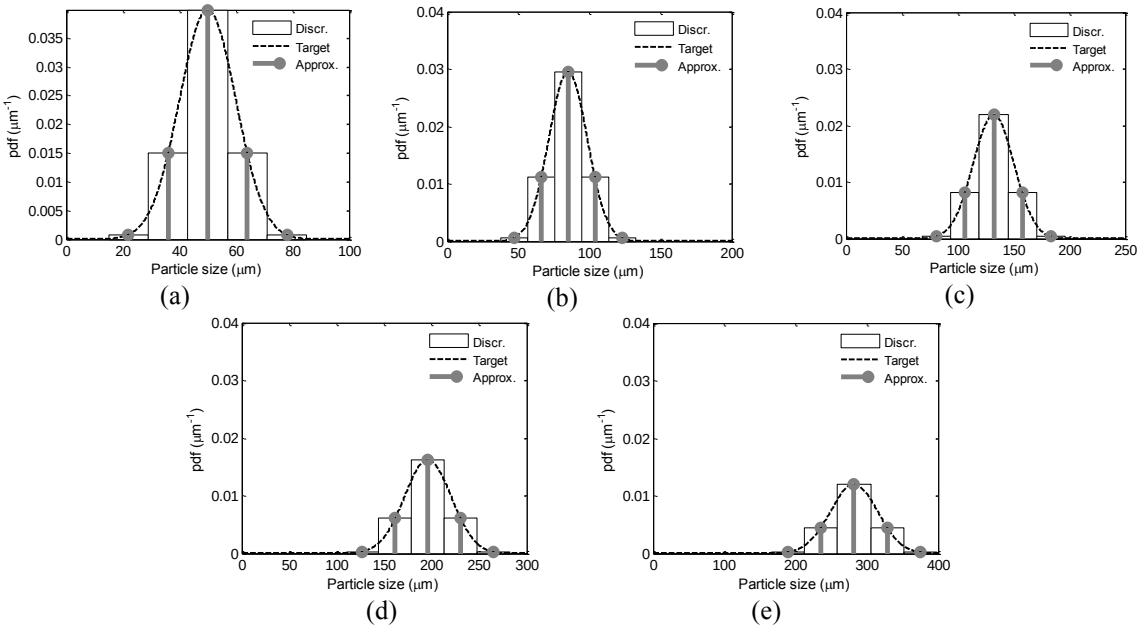

Figure 3.12: Comparison of the dynamic evolution of the exact and approximated (using the linear inversion technique) crystal size distributions for the simulated seeded batch crystallisation processes with linear size dependent growth kinetics, at a) t = 0 min, b) t = 15 min, c) t = 30 min, d) t = 45 min and e) t = 60 min.

Due to selected growth kinetics (i.e. linear size-dependent growth) the shape of the distribution broadened with time. The approximated distribution using linear inversion technique captured the dynamic evolution of crystal distribution very well. However the technique can only provide a coarse approximation. For on-line optimisation and control of the shape of the CSD higher resolution is required. Therefore in practical scenarios linear inversion technique might not be an attractive option for the approximation of the distribution for optimisation and control, however it may provide a quick and easy solution for qualitative and semi-quantitative CSD monitoring in certain applications.

The gamma distribution with Laguerre polynomials was also used to approximate the seed distribution. Figure 3.13 (a) shows a comparison of the seed distribution and the approximated distribution using the gamma with Laguerre polynomials. Figure 3.13 (b) indicates that the sum squared error was very low using up to 5th order polynomials. However, as the number of polynomials was increased, the error between the seed and the approximated distribution increased. When eighth order polynomial was used oscillations were observed in the approximated distribution.

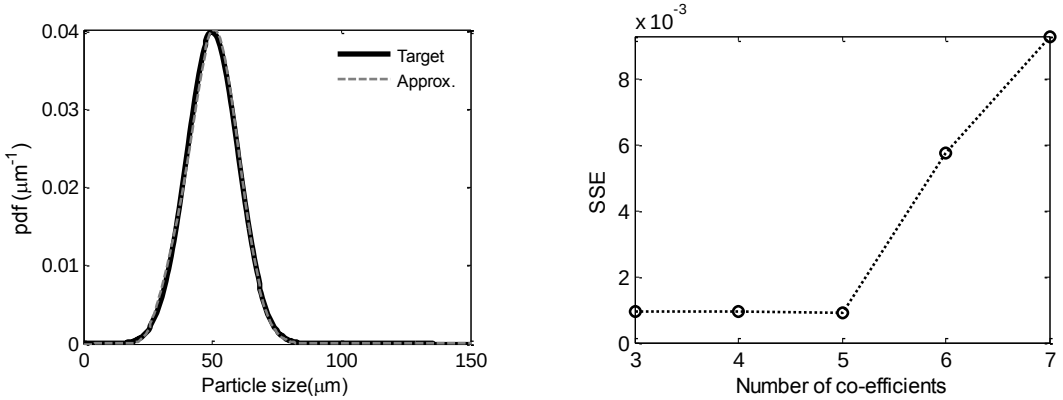

(a) (b)

Figure 3.13: a) Approximation of seed distribution using the gamma distribution with Laguerre polynomials using 5th order coefficients. b) Sum squared errors vs. order of Laguerre polynomials for the approximation of the target distribution.

The approach works very well with lower-order moments. Using first five moments only, the approximated distribution captured the shape of the seed distribution very well. Same number of coefficients of polynomial, (i.e. 5 coefficients of polynomials) was used to evaluate the approximation for several time steps, during the crystallisation process. The moments for several time steps were calculated from the analytical solution using equation

(3.36). Figure 3.14 show that the gamma distribution with Laguerre polynomials has approximated the distribution very well throughout the entire batch. Since the distribution has a simple shape, the gamma distribution with a low order Laguerre polynomial is able to provide a very good approximation.

Both approximation approaches worked well for the presented case study. This can be explained by the fact that although the shape of the distribution has changed during the batch (the distribution has broadened) the actual type of the distribution remains the same. The analytical solution given by equation (3.36) can be rearranged in the following form:

$$f_n(L,t) = \frac{1}{\sigma_s e^{0.02t}\sqrt{2\pi}} e^{\frac{-\{L-[(50+\bar{L}_s)e^{0.02t}-50]\}^2}{2(\sigma_s e^{0.02t})^2}}, \tag{3.37}$$

which indicates that the type of the distribution is Gaussian throughout the batch, with time dependent mean $\bar{L}(t) = (50+\bar{L}_s)e^{0.02t} - 50$ and time dependent standard deviation $\sigma(t) = \sigma_s e^{0.02t}$. In fact the distribution in this case could be easily approximated by a simple Gaussian distribution using the first three moments only to calculate the mean and standard deviation at any moment during the batch. However this approximation would rely on the knowledge that the distribution maintains its Gaussian type during the batch, information which would not be available in a generic case.

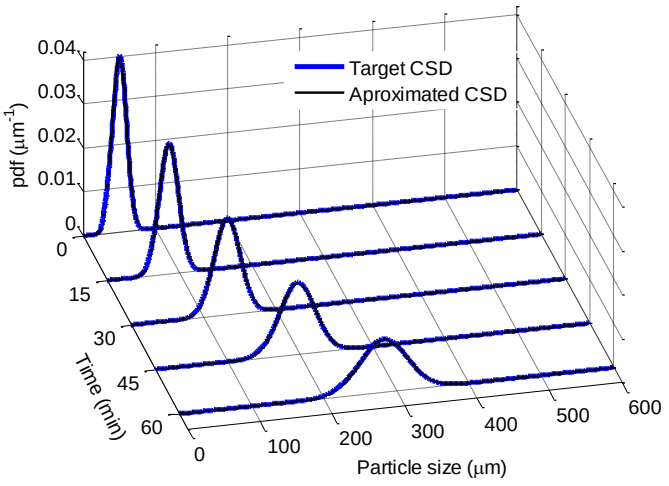

Figure 3.14: Comparison of dynamic evolution throughout the batch of the exact crystal size distribution and the approximated distribution using the gamma with Laguerre polynomials for the seeded batch crystallisation processes with linear size dependent growth kinetics.

To evaluate the capability of the approximation technique for a case when the type of the distribution changes during the batch, the dynamic evolution of the CSD obtained during an experiment was used next (the details of the experiment are given in Chapter 5). In the experiment a mono-modal seed was used, however due to secondary nucleation a bimodal distribution has developed during the crystallisation process. The moments were calculated from the measured CSDs. These moments were used off-line to reconstruct the distribution using the approximation based on gamma distribution with Laguerre polynomials.

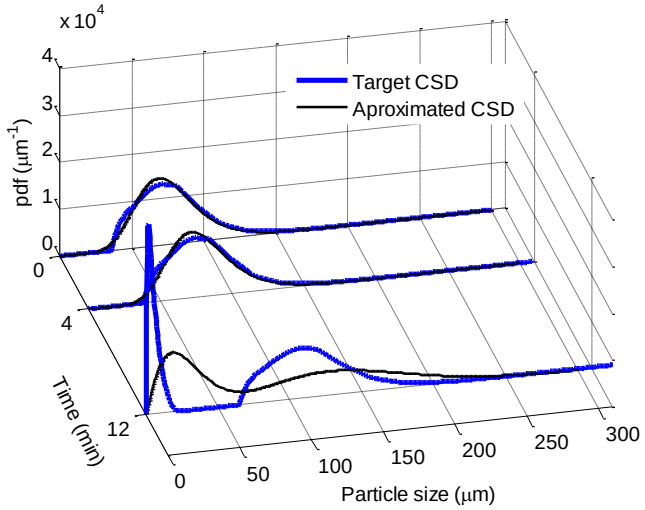

Figure 3.15: Comparison of the experimental CSD and the approximated distribution, using gamma distribution with 5th order Laguerre polynomials, for a seeded batch crystallisation processes throughout the batch.

Based on the mono-modal seed distribution 5th order Laguerre polynomials were selected as weighting functions for the gamma distribution. Figure 3.15, shows that the approximation is very good for the seed distribution and for the first part of the batch when the distribution remains mono-modal. However as soon as the distribution has changed from mono-modal to bimodal, the approximation was unable to capture the shape. As the bimodal features develops even further during the batch (after 15 minutes) the approximated distribution exhibits large oscillations even with the 5th order polynomial and thus are not shown in the figure for clarity of presentation.

These results indicate that the gamma+Laguarre approximation can be a very efficient CSD reconstruction method, which can be used in conjunction with the SMOM or QMOM, for cases when during the batch the CSD remains mono-modal. In these cases generally the

shape of the seed CSD would be available from off-line analysis, and could be used to tune the approximation method. Subsequently the SMOM or QMOM could be used for the prediction of the moments, which then can be used with the gamma+Laguerre approximation (with the number of polynomials determined based on the seed CSD) to reconstruct the CSD at any given time. This method could be used efficiently for supersaturation controlled and growth dominated processes. However when the crystallisation process involves multimodal distributions, e.g. due to secondary nucleation the approach may not be applicable. Therefore for more complex CSD design and control problems there is a strong incentive for methodologies that can predict the evolution of the shape of more complex distributions without requiring *a priori* information.

3.5 Conclusions

In this chapter different techniques were evaluated that can be used to predict the crystal size distribution by using lower order moments determined numerically for various distribution functions. The most common way of approximating the CSD is to assume a *priori* shape of the distribution, such as Gaussian, lognormal, bimodal, etc. Reconstruction based on known functions is a simple and fast method however requires information concerning the expected shape of the distribution. For new applications with an unknown CSD, or when the shape of the CSD can change during the process, this method is unlikely to be applicable.

Other techniques which can be used to approximate the CSD, such as gamma distribution with Laguerre polynomials, linear inversion, optimisation-based linear inversion, non-linear inversion and optimisation-based non-linear inversion techniques were also evaluated. Different types of distributions, such as Gaussain, lognormal and bimodal were approximated. It was observed that a gamma distribution modified with Laguerre polynomials approximated these distributions relatively well. The technique is able to capture some common distributions qualitatively, and most of the cases even quantitatively well, using lower order moments. When bimodal distribution is used higher order moments are required for the approximation; however negative pdf values and oscillatory behaviour was observed when higher order moments were used for the approximation of the simpler mono-modal distributions.

Linear inversion technique was also able to coarsely approximate various distributions; however negative pdf values were observed with higher discretisations. No significant improvement was observed using non-linear inversion technique, despite the significantly increased computational requirement compared to the linear inversion. The selection of mid points and discretisation points are very important factors and may affect the approximated CSD by these techniques.

The linear inversion and the gamma+laguarre approximation techniques were also tested for a seeded batch crystallisation process with growth the only dominating phenomenon, under the assumption of constant supersaturation and linear size-dependent growth mechanism. The linear inversion technique provided a good but coarse approximation of the CSD during the batch, however with increasing the number of discretisations the inversion problem has become ill-conditioned. This approach may provide a good qualitative and semi-quantitative approximation of the evolution of the CSD during a crystallisation process and could be used for monitoring purposes, however cannot provide the resolution and accuracy needed for CSD shape optimisation and control. Using gamma distribution with orthogonal polynomials approximated the seed distribution and the dynamic evolution of the shape of the CSD very well using lower order moments. This approach can provide an efficient CSD approximation method for growth dominated processes for which the distribution is mono-modal during the whole batch. However, in the cases when the shape of the distribution may change from mono-modal to bimodal or multimodal (e.g. due to secondary nucleation or breakage) the approach fails. The linear inversion and gamma+laguarre approximation techniques are unable to provide a generic approximation method for the CSD due to ill-conditioning, negative values in the pdf and oscillatory behaviour. Therefore efficient CSD reconstruction techniques are required, which are applicable for growth and nucleation mechanisms, and for complex CSD optimisation and control problems.

Chapter 4
Combined QMOM-MOCH approach for the efficient solution of PBE for batch crystallisation processes

4.1 Introduction

As discussed in Chapters 2 and 3, both the standard method of moments (SMOM) and the quadrature method of moments (QMOM) provide efficient solutions of the PBE and have been widely used in the literature for optimisation and control purposes (Fujiwara *et al.*, 2005; Nagy and Braatz, 2003a). However, these approaches only provide the moments of the CSD and not the entire distribution. Several techniques are available to reconstruct the distribution from its moments, e.g. using linear or non-linear inversion approaches (as discussed in Chapter 3). These techniques often have the disadvantage that they require a larger number of moments, produce negative pdf values and generally suffer from solution multiplicity and ill-conditioning problems. Approximate distribution functions (e.g. polynomial, normal, gamma or lognormal), or a weighted sum of distributions, using for example orthogonal polynomials as weighting functions, can also be used to reconstruct the shape of the distribution from the moments (Flood, 2002; Randolph and Larson, 1971) (also discussed in Chapter 3). However, the solution of such inverse problems is usually not unique. There is also a lack of systematic methodologies for the choice of the suitable type and number of base functions and distributions. Hence the approximate distribution functions resulting from both categories of reconstruction methods may be subject to spurious oscillations and the correctness of the resulting shape of distribution is difficult to evaluate in most practical cases. The method of characteristics (MOCH) in combination with the SMOM has been used successfully for processes with size-independent growth and nucleation (Hounslow and Reynolds, 2006), including the modelling and control of polymorphic transformations (Hermanto *et al.*, 2007; Ono *et al.*, 2004). However this approach does not apply in the more generic case of a PBE with size-dependent growth,

dissolution and secondary nucleation or when breakage and agglomeration mechanisms need to be considered.

The approach presented in this chapter combines the advantages of QMOM and the MOCH to provide a computationally efficient technique for the prediction of the entire CSD. The algorithm can be applied for the solution of population balance equations with generic size-dependent growth and nucleation kinetics and have a potential for more general framework for the efficient solution of PBEs even in the case of breakage and agglomeration. This is a novel approach, when these two approaches have been combined which provides an efficient solution for a model-based control of distribution shaping.

4.2 Novel methodology for the efficient solution of the PBE based on combined QMOM-MOCH

Crystallisation processes can often be modelled by considering the growth and nucleation mechanisms only. Considering a single growth direction with one characteristic length, L, and a well-mixed crystalliser with growth and nucleation as the only dominating phenomena the expression for the population balance equation (PBE) has a simplified form of

$$\frac{\partial f_n(L,t)}{\partial t} + \frac{\partial \left[G(S,L;\theta_g) f_n(L,t) \right]}{\partial L} = B(S;\theta_b)\delta(r_0,L), \tag{4.1}$$

where $f_n(L,t)$ is the crystal size distribution expressed in the number density function ($\#\ crystals/kg\ slurry$), t is time in (s), $G(S,L;\theta_g)$ is the rate of crystal growth ($\mu m\ s^{-1}$), $B(S,\theta_b)$ is the nucleation rate ($\#/s/\mathrm{kgslurry}$), $S = C - C_{sat}$ is the absolute supersaturation in ($kg/kg\ slurry$), C is the solute concentration expressed in $(kg\ solid/kg\ slurry)$, $C_{sat} = C_{sat}(T)$ is the saturation concentration with T being the temperature in $(°C)$, r_0 is the size of nuclei, $\delta(r_0,L)$ is the Dirac delta $(\delta = 1\ if\ L = r_0 \text{ and } \delta = 0\ if\ L \neq r_0)$, θ_g is the vector of growth kinetic parameters and θ_b is the vector of nucleation kinetic parameters. The solution of equation (4.1) is an initial value problem with initial condition given by the size distribution of the seed,

$$f_n(L,0) = f_{n,0}(L_0). \tag{4.2}$$

The boundary condition is $f_n(0,t) = \dfrac{B(S;\theta_b)}{G(S,L;\theta_g)}$.

4.2.1 Combined QMOM-MOCH approach for size-dependent growth and secondary nucleation

Equation (4.1) can be transformed into a system of ODEs by applying the standard method of moments (in the case of size-independent growth and nucleation) or the quadrature method of moments (in more generic cases including size-dependent growth, breakage and aggregation). Both methods allow the calculation of the evolution of the moments of the distribution, defined as

$$\mu_j = \int_0^\infty f_n(L) L^j dL, \qquad j = 0,1,2,\ldots,\infty. \tag{4.3}$$

The quadrature method of moments (QMOM) is a generic solution approach for the PBE (Marchisio *et al.*, 2003a; Marchisio *et al.*, 2003b; McGraw, 1997). It employs a quadrature approximation of the distribution function

$$f_n(L,t) \approx \sum_{i=1}^{N_q} w_i(t)\delta(L_i(t),L), \tag{4.4}$$

where N_q is the number of quadrature points. The corresponding weights, w_i, and abscissas, L_i, can be determined through the product-difference (PD) algorithm (Gordon, 1968) or via direct solution of a differential-algebraic (DAE) system (Gimbun *et al.*, 2009), based on the idea of minimizing the error committed by replacing the integral from the moment definition with its quadrature approximation,

$$\mu_j = \int_0^\infty f_n(L) L^j dL \approx \sum_{i=1}^{N_q} w_i L_i^j. \tag{4.5}$$

Applying the moment transformation to equation (4.1) with the quadrature approximation of equation (4.5) the resulting moment equations have the form

$$\begin{aligned} \frac{d\mu_0}{dt} &= B(S;\theta_b), \\ \frac{d\mu_j}{dt} &= j\sum_{i=1}^{N_q} w_i L_i^{j-1} G(S,L_i;\theta_g) + B(S;\theta_b) r_0^j, \quad j = 1,2,3,... \end{aligned} \tag{4.6}$$

Note that the abscissas, L_i, in the QMOM are used to compute the moments only, and are different from the characteristic length L used to characterise the particle size in the PBE. The generic PBE equation (4.1) can be reduced to a system of ODEs by applying the method of characteristics (MOCH). The aim of the MOCH is to solve the PBE by finding characteristic curves in the $L-t$ plane that reduce the partial differential equation to a system of ODEs. The $L-t$ plane is expressed in a parametric form by $L = L(\mathcal{Z})$ and $t = t(\mathcal{Z})$, where the parameter $\mathcal{Z}$ gives a measure of the distance along the characteristic curve (as mentioned in Chapter 2, equation (2.24). Therefore, $f_n(L,t) = f_n(L(\mathcal{Z}),t(\mathcal{Z}))$, and applying the chain rule gives:

$$\frac{dL}{d\mathcal{Z}}\frac{\partial f_n}{\partial L} + \frac{dt}{d\mathcal{Z}}\frac{\partial f_n}{\partial t} = \frac{df_n}{d\mathcal{Z}}. \tag{4.7}$$

The generic growth expression used for size-dependent growth is:

$$G = k_g S^g (1+\gamma L)^p, \tag{4.8}$$

where $\theta_g = [k_g, g, \gamma, p]$ is the growth parameter vector. In the case of generic growth kinetics, equation (4.1) can be rewritten in the form of

$$\frac{\partial f_n(L,t)}{\partial t} + G(S,L;\theta_g)\frac{\partial f_n(L,t)}{\partial L} = -f_n(L,t)\frac{dG(S,L;\theta_g)}{dL} + B(S;\theta_b)\delta(r_0,L). \tag{4.9}$$

Comparing equations (4.7) and (4.9) it can be shown that $\mathcal{Z} = t$ and the characteristic equations are given by the following system of ODEs:

$$\frac{dL}{dt} = G(S, L; \theta_g), \tag{4.10}$$

$$\frac{df_n(L,t)}{dt} = -f_n(L,t)\frac{dG(S,L;\theta_g)}{dL} + B(S;\theta_b)\delta(r_0, L), \tag{4.11}$$

with initial conditions $L = L_0$ and $f_n(L,0) = f_{n,0}(L_0)$, *i.e.* the seed CSD. To obtain the dynamic evolution of the crystal size distribution $f_n(L,t)$, equations (4.10)-(4.11) with prescribed nucleation and growth expressions can be integrated repeatedly for different initial values $[L_0, f_{n,0}(L_0)]$. The initialization of the integrations in the $L-t$ plane are illustrated in Figure 4.1, showing typical evolutions of the characteristic lines during the integration. To simulate the growth of the seed, the initial conditions start from along the L axis of the $L-t$ plane, with values calculated by choosing a discretisation interval ΔL_0 and using $t_0 = 0$ and $L_0 = \max(0, L_{0,\max} - k\Delta L_0)$, $k = 0,1,\ldots,N$, where N is the number of discretisation points for the seed distribution and $L_{0.\max}$ is chosen to be greater or equal to the maximum size range of the seed crystals. The discretisation interval ΔL_0 will determine the number of integrations (the number of characteristic lines) and hence the resolution of the dynamic evolution of the seed CSD, as shown in Figure 4.1. For this part of the integration the initial values for the probability distribution function are calculated from the seed distribution $f_{n,0}(L_0) = f_{seed}(L_0)$ and all integrations start from an initial time $t_0 = 0$.

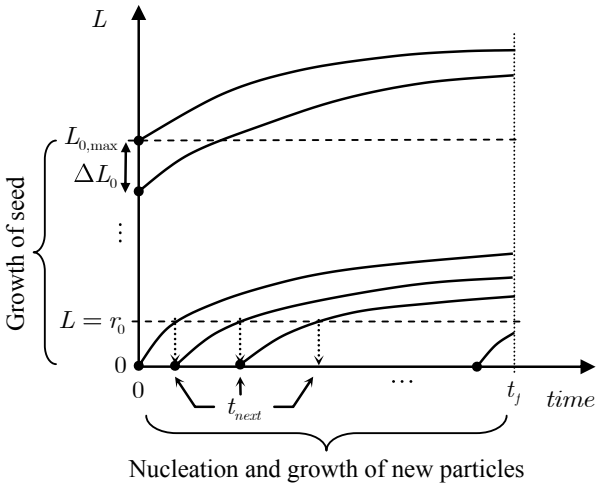

Figure 4.1: Evolution of characteristic lines with the generic approach of calculating the initial conditions for the method of characteristics in the case of growth and nucleation mechanisms.

Figure 4.1 also shows the methods employed to represent the contribution to the overall distribution function from nucleation events, which may occur during the batch. In this case, the characteristic lines for nucleation and growth of new particles, start from initial conditions along the t axis of the $L-t$ plane, using $L_0 = 0$, $f_{n,0}(L_0) = 0$, and $t_0 = t_{next}$. The initial time for the next integration, t_{next}, is calculated by interpolating the characteristic line for $L = r_0$, as shown in Figure 4.1. The number of integrations within this part of the algorithm is not predetermined and will depend on the evolution of the characteristic lines governed by the growth kinetics. This is an adaptive feature of the algorithm, which allows the high resolution prediction of the part of the CSD that result from nucleation events. The iterations are stopped when $t_{next} \geq t_f$ where t_f is the end time of the batch. For the solution of equations (4.10)-(4.11) it is considered that at the moment of nucleation, nuclei can have any size between 0 and r_0. This is described by the modified delta function defined as:

$$\delta(r_0, L) = \begin{cases} 1 & \text{if} \quad L \in [0, r_0] \\ 0 & \text{if} \quad L \notin [0, r_0] \end{cases}. \tag{4.12}$$

Thus nucleation events are assumed to occur for $L \leq r_0$. For seeded crystallisation, secondary nucleation is considered as the dominating nucleation phenomenon, which is generally expressed as a function of the supersaturation and the volume of the existing crystals, given by the third-order moment of the size distribution. Hence in the model the empirical relationship for secondary nucleation is given by,

$$B = k_b S^b \mu_3, \tag{4.13}$$

where $\theta_b = [k_b, b]$ is the nucleation parameter vector. This formulation allows the direct consideration of *apparent* nucleation kinetics in the model, where r_0 is the size of the particles when they are first detected with a particular measurement approach. In this study $r_0 = 1\,\mu m$ is used since it represents approximately the size of particles which can be detected by typical *in situ* process analytical tools based on image analysis or focused beam reflectance measurements.

Both the growth and nucleation rates are functions of the supersaturation S, which can be calculated from the material balance. The solute concentration is given by:

$$C(t) = C(0) - k_v \rho_c (\mu_3(t) - \mu_3(0)), \tag{4.14}$$

where ρ_c is the density of crystals and k_v is the volumetric shape factor, while the supersaturation can be expressed as:

$$S(t) = C(t) - C_{sat}(t). \tag{4.15}$$

The solution of equations (4.10) and (4.11) requires *a priori* knowledge of the dynamic evolution of the supersaturation, $S(t)$ and/or the third moment $\mu_3(t)$, which can be obtained by using the moment transformation of equation (4.1) via the SMOM or QMOM. The main steps of the proposed algorithm are shown in Figure 4.2. In the case of secondary nucleation and size-dependent growth, the ODEs from the QMOM have to be integrated together with equation (4.14), once for the duration of the batch, to predict the evolution of μ_3 and the variation of supersaturation with time. Then $S(t)$ and $\mu_3(t)$ are used in the nucleation and growth kinetic expressions during repeated integrations of equations (4.10)-(4.11) with different initial conditions, to map out the complete evolution of the full CSD via the MOCH, as shown in Figure 4.2.

When nucleation is included in the model, an iterative integration of equations (4.10)-(4.11) is needed, since the number of initial conditions along the t axis, for nucleating and growing particles, is not known *a priori*. In the case of growth only processes the PBM can be solved using the MOCH only, by simultaneously integrating all the ODEs resulting by applying equations (4.10)-(4.11), to the discretised initial conditions. In this case the $\mu_3(t)$ required for the mass balance would be calculated from the discretised f_n and L values, simultaneously with the integration of the characteristic equations.

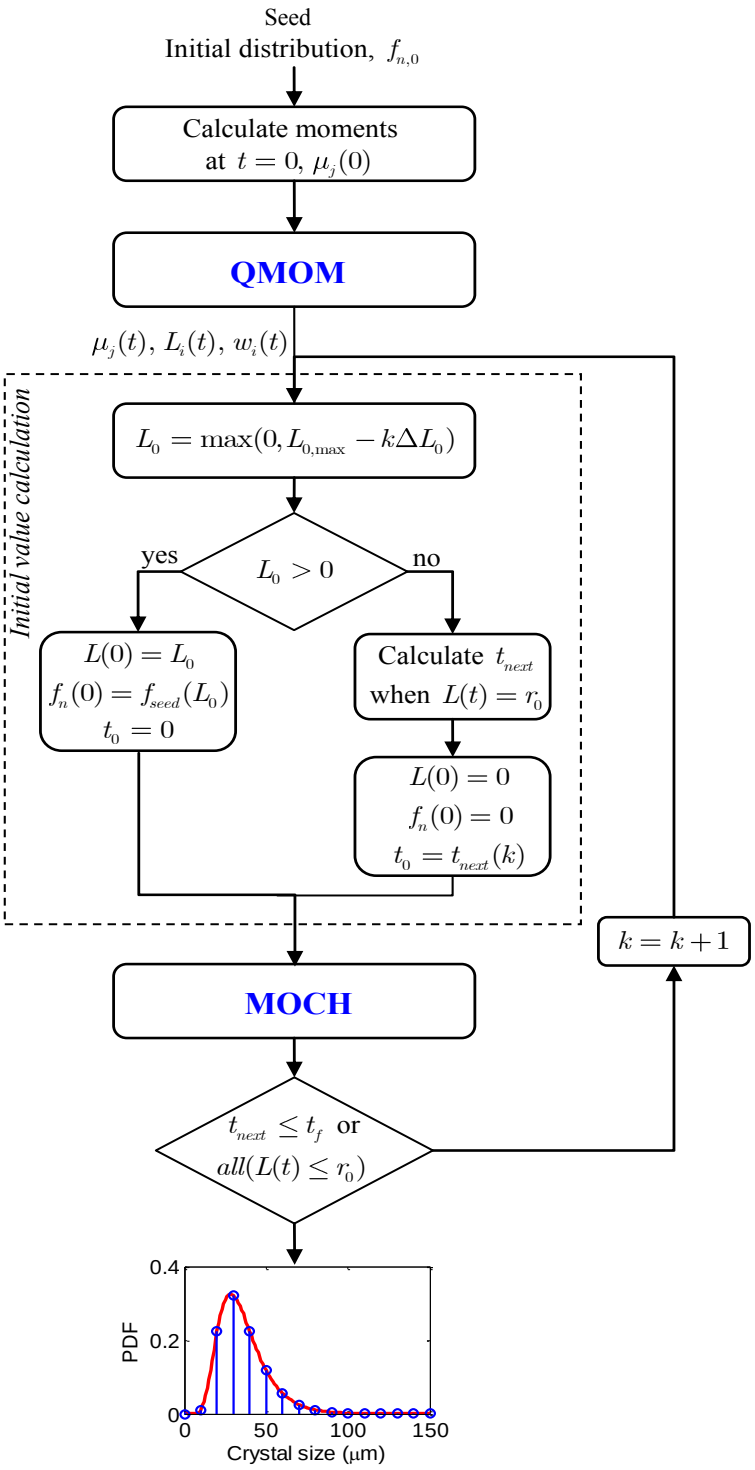

Figure 4.2: Flowchart of the combined QMOM-MOCH approach for the solution of PBEs using size dependent growth and secondary nucleation mechanisms. (Note that "k" is a loop counter in the algorithm).

In this approach high accuracy of $\mu_3(t)$ would require large number of discretisation for the initial conditions, resulting also in large number of ODEs to integrate throughout the entire batch. The application of the QMOM, however, allows a more accurate calculation of the moments (Gimbun *et al.*, 2009) with only a few number of quadrature points, ($N_q = 2,3$ is typically sufficient). Hence the number of discretisation points for the MOCH part can be chosen independently to estimate the shape of the CSD. The combined QMOM-MOCH approach allows for a trade-off between high resolution of the CSD and computational efficiency (coarse approximation of the CSD) without compromising the accuracy of the moments, and hence providing proper closure of the mass balance. Note that the method also applies to dissolution problems and has a potential to be extended for certain breakage and agglomeration mechanisms. Since often controlled dissolution can be an efficient way to control the CSD (Abu Bakar *et al.*, 2009b) and to correct for the effects of unwanted nucleation events, the next section illustrates how the proposed method can be extended to the dissolution mechanism.

4.2.2 Combined QMOM-MOCH approach for size-dependent dissolution

For a one-dimensional dissolution mechanism characterized by a characteristic length L, and a well-mixed system with dissolution as the only dominating phenomena, the population balance equation (PBE) has the form:

$$\frac{\partial f_n(L,t)}{\partial t} + \frac{\partial (D(-S,L;\theta_d) f_n(L,t))}{\partial L} = 0, \tag{4.16}$$

where $f_n(L,t)$ is the crystal size distribution expressed in the number density function ($\#\ crystals / kg\ slurry$), t is time in (s), $D(-S,L;\theta_d)$ is the rate of crystal dissolution ($\mu m\ s^{-1}$), $-S = (C_{sat} - C)$ is the under-saturation ($kg / kg\ slurry$), C is the solute concentration $(kg / kg\ slurry)$, $C_{sat} = C_{sat}(T)$ is the saturation concentration with T being the temperature (in $^{\circ}C$), and θ_d is a vector of dissolution kinetic parameters.

The solution of eq. (4.16) is an initial value problem, with initial condition given by the size distribution of seed, (here seed refers to the initial large sized crystals charged to the system for dissolution) $f_n(L,0) = f_{n,0}(L_0)$. Due to the under-saturated conditions crystals reaching a limit size (r_0) disappear. Hence the left boundary condition was left undefined. The right boundary condition is given by $f_n(\infty,t) = 0$ where the "infinite size" represents any limit size that is larger than the size of any crystal (Fevotte *et al.*, 2007). The generic PBE equation (4.16) can be reduced to a system of ODEs by applying the method of characteristics (MOCH) as described in section 4.2.1. The characteristic equations are given by the following system of ODEs:

$$\frac{dL}{dt} = D(-S, L; \theta_d), \tag{4.17}$$

$$\frac{df_n(L,t)}{dt} = -f_n(L,t)\frac{dD(-S, L; \theta_d)}{dL}, \tag{4.18}$$

with initial conditions $L = L_0$ and $f_n(L,0) = f_{n,0}(L_0)$, *i.e.* the seed CSD (where seed refers to the initial large sized crystals charged to the system for dissolution). To obtain the dynamic evolution of the crystal size distribution $f_n(L,t)$, equations (4.17)-(4.18) with a prescribed dissolution rate expression can be integrated repeatedly for different initial values $[L_0, f_{n,0}(L_0)]$. The initial conditions start with values calculated by choosing a discretisation interval ΔL_0 and using $t_0 = 0$ and $L_0 = \max(0, L_{0,\max} - k\Delta L_0)$, $k = 0,1,\ldots,N$, where N is the number of discretisation points for the seed distribution and $L_{0,\max}$ is chosen to be larger or equal to the maximum size range of the seed crystals. The discretisation interval ΔL_0 will determine the number of integrations and hence the resolution of the dynamic evolution of the CSD. The initial values for the probability distribution function are calculated from the seed distribution $f_{n,0}(L_0) = f_{seed}(L_0)$ and all integrations start from an initial time $t_0 = 0$. The disappearance of fines is assumed to occur for $L \le r_0$, as shown in Figure 4.3. This formulation allows the incorporation of the disappearance of fines in the model, where r_0 is the detectable size of the particles in the bulk solution. In this study $r_0 = 1\,\mu m$ is used since

it represents approximately the size of particles which can be detected by typical *in situ* process analytical tools based on image analysis or focused beam reflectance measurements.

To solve the material balance, equation (4.16) can be transformed into a system of ODEs by applying the standard method of moments (in the case of size-independent dissolution) or the quadrature method of moments (in the more generic case of size-dependent dissolution), similarly as described in detail in section 4.2.1. Applying the moment transformation to equation (4.16), with the quadrature approximation of equation (4.5), the resulting moment equations for size-dependent dissolution have the form,

$$\begin{aligned} &\frac{d\mu_0}{dt} = 0, \\ &\frac{d\mu_j}{dt} = j\sum_{i=1}^{N_q} w_i L_i^{j-1} D(-S, L_i; \theta_d), \quad j = 1,2,3,... \end{aligned} \tag{4.19}$$

The first equation in (4.19) indicates that in this approach the number of particles is considered constant $(\mu_0 = \text{constant})$. However all particles eventually will reach a size of zero or r_0 (i.e. below the detection limits), and hence will disappear, as shown in Figure 4.3. This formulation neglects the kinetics of "disappearance" of particles (the opposite mechanism to nucleation), which would describe how quickly each characteristic line, f_n decays to zero when the corresponding L_i reaches r_0. In this approach it is considered that the particles disappear instantaneously, by having size below the detection limit r_0. The QMOM formulated by the ODE system (4.19) provides asymptotically decreasing moments $(\mu_j, j = 1,2,...)$, and abscissas $(L_i, i = 1,2,...,N_q)$ to zero. Hence the proposed approach with the limiting size $r_0 > 0$ eliminates numerical problems that may arise at the near zero sizes if the disappearance of the particles would be considered at $r_0 = 0$. Figure 4.3 presents the concepts used to model the dissolution phenomenon.

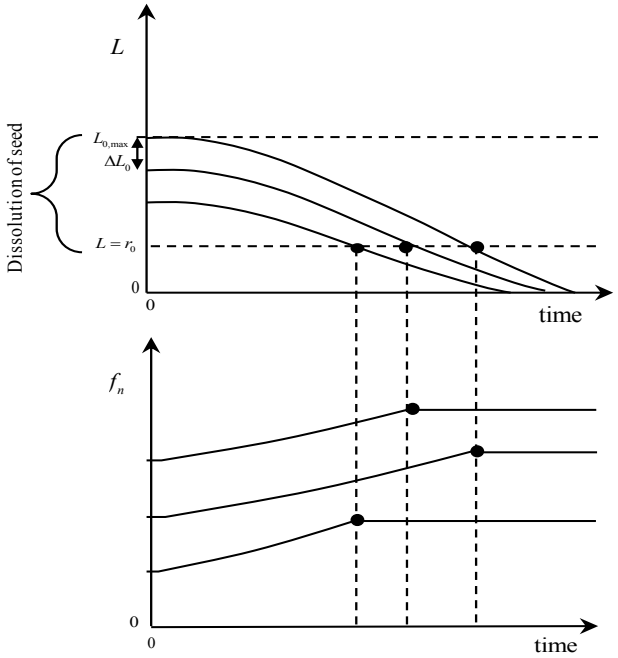

Figure 4.3: Evolution of characteristic lines obtained from the method of characteristics in the case of dissolution mechanism.

The dissolution is a function of the under-saturation,

$$-S(t) = C(t) - C_{sat}(t)\,. \tag{4.20}$$

The generic empirical relationship used for size-dependent dissolution is expressed as,

$$D = -k_d S^d (1 + \zeta L)^q\,, \tag{4.21}$$

where $\theta_d = [k_d, d, \zeta, q]$ is the dissolution parameter vector. The dissolution kinetics for the particles would be considered until the size of particles is $L \geq r_0$. When $L < r_0$ the crystals would be regarded as dissolved and would not be considered for the growth or dissolution unless they are reborn as new nuclei in the supersaturated region.

During crystallisation processes it is important to make use of both supersaturation and under-saturation regions, while designing temperature trajectories to achieve the desired CSD. Therefore in the next section the combined QMOM-MOCH approach is elaborated, taking into account growth, nucleation and dissolution mechanisms together.

4.2.3 Combined QMOM-MOCH approach for nucleation and size-dependent growth and dissolution

The combined QMOM-MOCH can be used for the solution of models in which dissolution, growth and nucleation mechanisms are used together depending on whether the system is supersaturated or under-saturated. Figure 4.4 presents a schematic representation of the approach when dissolution, growth and nucleation mechanisms are used together. In this case both PBEs (one for growth and nucleation, (4.1), and one for the dissolution, (4.16)) are included in the model, and are applied to the CSD, f_n, depending on whether the operating curve is in the supersaturated $(S > 0)$ or under-saturated region $(S < 0)$.

After the initialisation of the method with initial conditions $L = L_0$ and $f_n(L,0) = f_{n,0}(L_0)$, the moments are calculated. Using the quadrature method of moments (QMOM) the dynamic evolution of the supersaturation, $S(t)$ and the third moment $\mu_3(t)$, are computed.

The QMOM is applied with the dissolution or the growth and nucleation mechanisms based on whether the $S < 0$ or $S > 0$, respectively. The dynamic evolution of the supersaturation would suggest whether the system is in supersaturated or under-saturated region. If $S > 0$ the system is in the supersaturated region and the MOCH is applied to the PBE with growth and nucleation kinetics, as shown in Figure 4.4. If $S < 0$ the system is in the under-saturated region and the MOCH is applied to the PBE with dissolution mechanism until the size of particles reaches $L < r_0$, as shown in Figure 4.4. To obtain the dynamic evolution of the CSD, $f_n(L,t)$, equations (4.10)-(4.11) and (4.17)-(4.18) with the corresponding nucleation, growth and dissolution expressions are integrated repeatedly for different initial values $[L_0, f_{n,0}(L_0)]$, as shown in Figure 4.4. In this way the approach is able to consider all three mechanisms i.e. growth, nucleation and dissolution, based on the supersaturated or under-saturated state of the system at a particular time of the batch.

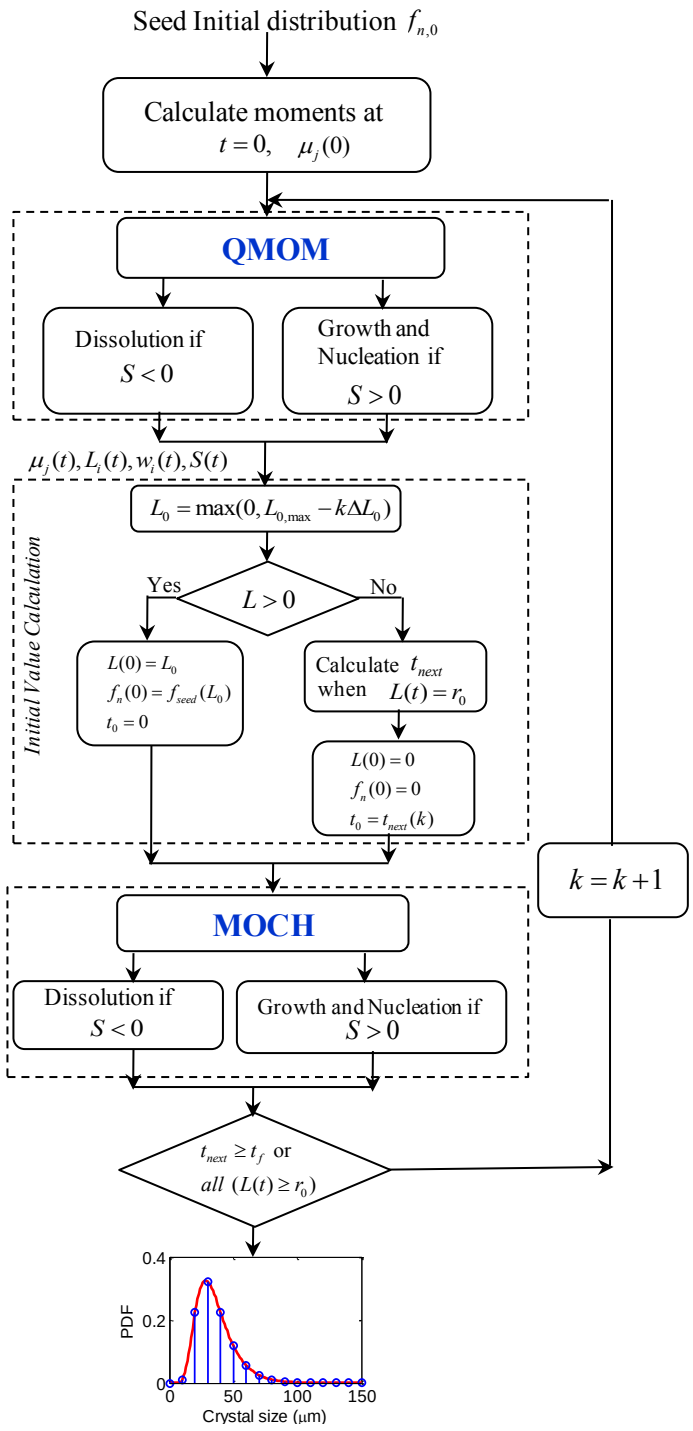

Figure 4.4: Flowchart of the combined QMOM-MOCH approach for the solution of PBE using size-dependent growth and dissolution and nucleation mechanisms for supersaturated and under-saturated regions. (Note that "k" is a loop counter in the algorithm).

4.3 Conclusions

The chapter describes a novel methodology for solving population balance equations. The approach combines the quadrature method of moments (QMOM) with the method of characteristics (MOCH), and provides a computationally efficient method of reconstructing the full shape of the crystal size distribution (CSD). The technique is developed for generic empirical expressions for growth, dissolution and nucleation, allowing for consideration of size-dependent growth, and dissolution and variable supersaturation. The computational efficiency and robustness of the combined QMOM-MOCH technique makes it a suitable approach for off-line or on-line optimisation of batch crystallisation processes.

Chapter 5
Model identification and validation for potash alum-water system

5.1 Introduction

This chapter describes the methods, equipment, procedures and operating conditions of the experiments used for the modelling of the batch crystallisation process of the potash alum-water system. The experiments were used to determine the various kinetic parameters for the seeded batch cooling crystallisation process. These kinetic parameters describe the growth, nucleation and dissolution mechanisms and were identified using a least square optimisation approach solved by applying a sequential quadratic programming (SQP) based non-linear optimisation method implemented in MATLAB. The identified parameters were validated for various sets of experiments operated under different conditions. The operating conditions include variations in the total batch time, initial concentration, supersaturation set-points and seed mass. The state variables, such as concentration, process temperature, jacket temperature and CSD were measured during the experiments using various off-line, on-line and *in situ* measurement techniques. The growth parameters were identified using pilot scale experimental data provided by, the chemical company, BASF, Ludwigshafen, Germany.

To identify the kinetic parameters for dissolution, experiments were carried out at Loughborough University, UK. The experimental data is used for parameter identification and validation in the case of the potash alum-water system.

5.2 Material

Potassium aluminium sulphate dodecahydarte $(KAl_2(SO_4)_2.12H_2O)$ (>99.95% purity, Fisher Bio Reagents) compound was used in all the experiments discussed in this chapter. De-ionised water was used as solvent. The solution was prepared using 11.7 g of potash alum in

100 g of water, corresponding to a saturation temperature of 40 °C (Barrett and Glennon, 2002; Mullin, 2001).

5.3 Experimental set-up for the identification of the growth and nucleation parameters

The experimental data was obtained from an industrial pilot crystallisation system located at BASF (Ludwigshafen, Germany).

5.3.1 Apparatus

A schematic diagram of the experimental setup is shown in Figure 5.1. A 3 L jacketed batch crystalliser was used for the experiments. The cooling and heating of the crystalliser was carried out with a thermostat equipped with an internal compressor to enhance the cooling. A thermocouple (PT100) was immersed in the solution to measure the temperature of the system. To enhance mixing, the crystalliser is equipped with a pitched blade turbine that rotates at a speed of 500 rpm. This agitation speed was chosen to be high enough to guarantee that particles were well suspended throughout the process, but low enough to avoid attrition of crystals or entrainment of bubbles due to vortex formation.

The vessel contained 3 baffles to promote mixing and minimise vortex formation. Two probes were used in the crystalliser to withdraw samples. A Malvern Instruments Insitec, laser diffraction system, was used to obtain the on-line measurements for the dynamic evolution of the crystal size distribution. A peristaltic pump (P1) was used to pump the slurry (solids with solvent) from the crystalliser to the Insitec and then back to the crystalliser. The flow rate of pump was 1.19 L/min to maintain continuous flow of the solution between the Insitec equipment and the crystalliser. The pipeline that transports the suspension from the crystalliser to the Insitec and back to the crystalliser was jacketed and was heated to keep the temperature of the solution constant through the path to avoid any nucleation or dissolution of the crystals. Two thermocouples were inserted in the pipeline before and after the Insitec to measure the suspension temperature.

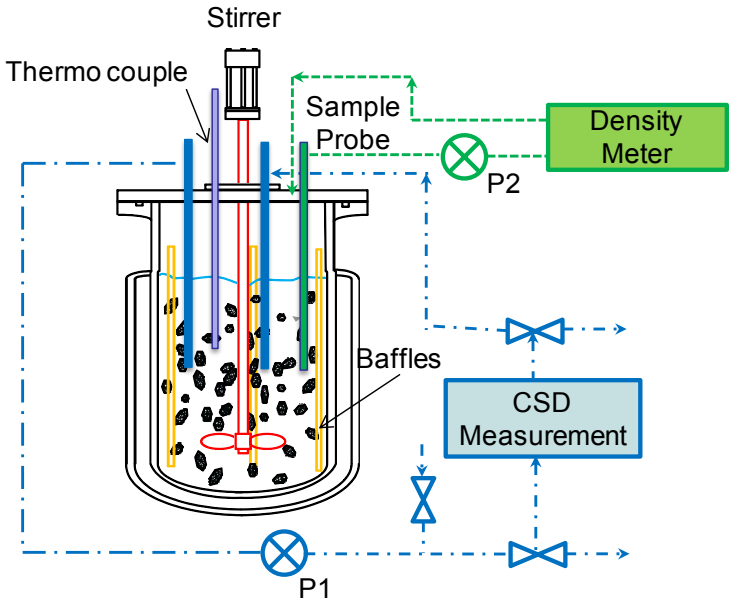

Figure 5.1: A schematic representation of experimental setup for batch cooling crystallisation to determine growth and nucleation parameters. Drawing is for illustration only and may not be a true representation of the actual setup.

A second peristaltic pump (P2) was used to pump the second sample stream from the crystalliser to the DMA 5000 Density Meter to measure the density and hence the concentration of the solution; this stream contained the solution without crystals. A filter element of 60 µm pore size was used to make sure that there were no crystals in the solution stream.

5.3.2 Seed preparation

Seeds were prepared using sieve analysis. A JEL 200 shaker was used for sieving; a stack of sieves was placed in the equipment, with the coarsest sieve opening on the top and the finest sieve at the bottom. The sieve sizes were 1 mm, 350 µm, 250 µm, 125 µm, 90 µm and 63 µm. The run time was 90 minutes and the medium shaking amplitude was selected to distribute the crystals throughout the sieve stack and reduce breakage of the crystals. The product obtained between the sieve sizes of 90-125 µm was collected for seeding.

Potash alum is a hygroscopic substance and adsorbs moisture from air. Seed can aggregate and adhere to each other as moisture from the environment is adsorbed. Thus, to minimize moisture adsorption, seed was stored in a desiccator.

5.3.3 Concentration measurement using density meter

An Anton Paar DMA 5000 density meter was used to measure the concentration throughout the experiment. The Anton Paar density meter combines the well-known Anton Paar U-tube with a reference oscillator and a high-precision platinum thermometer to measure the density. An oscillating U-shaped hollow glass tube of known volume and constant mass oscillates at a frequency (f). The vibration frequency changes when the tube is filled with a sample. The frequency is inversely proportional to the density (ρ) of the filled sample: the higher the mass of the sample, the lower the vibration frequency. This frequency is measured and converted into density using the relationship:

$$\rho = b_0 P + b_1, \tag{5.1}$$

where P is the oscillating period, which can be calculated as $P = 1/f$, and b_0 and b_1 are constants.

Once the instrument has been calibrated with air and water to obtain b_0 and b_1, the density of a sample can be determined. A temperature controller is often necessary to keep the temperature constant as the density of the sample is affected by temperature variations. The measured density was used to calculate the concentration of the solution at the saturation temperature. A correlation between the density and the concentrations of the potash alum can be found by measuring the density of known concentrations.

5.3.4 On-line CSD measurement using Malvern Insitec

The on-line CSD was measured using Malvern Insitec particle size analyzer. The working principle of the equipment is similar to Malvern Mastersizer (i.e. based on laser diffraction) and it can measure particle sizes in the range of 0.108 to 1000 μm. The equipment is designed for real-time measurement of size distribution in solid and liquid suspensions in dilute and concentrated liquid streams. The crystal size distribution was measured after every 5 minutes. The BASF company has made modifications to the equipments to measure on-line Sauter mean diameter (d_{32}) and De-Brocukere mean diameter (d_{43}) measurements after every 2 second. Limited information about the experimental setup was provided by the company due to their data protection policy.

5.3.5 Method

Potash alum was dissolved in water by heating up to 50°C at a rate of 0.8°C/min. The solution was equilibrated at 50°C for 30 minutes, to ensure complete dissolution of solids, which was also indicated by the decrease of the FBRM counts. Then the temperature of the solution was reduced to 38°C at a ramp rate of 0.5°C/min.

Table 5.1: Operating conditions for the seeded-batch cooling crystallisation experiments A and B performed at BASF, Germany.

Operating Conditions	Units	Experiment A	Experiment B
Initial saturation temperature	$°C$	40.0	40.0
Seed mass , (m_{seed})	kg	2.98×10^{-3}	4.00×10^{-3}
Batch time , t_{batch}	min	90.0	160.0
Initial solute concentration (C_i)	kg solute/ kg slurry	0.104	0.108
Sieve sizes for seed, $\mathcal{L}$	μm	90-125	90-125
Initial temperature at seeding and start of profile, (T_0),	$°C$	50	50
Final temperature, (T_f),	$°C$	17.0	30.0
Supersaturation set-point, S_{sp}	$wt\%$	0.60	0.30
Agitation speed	rpm	500	500
Density of crystals, (ρ_c)	kg/m^3	1750	1750
Volumetric shape factor, (k_v)	--	0.62	0.62
Mass of slurry, (m_{slurry})	kg	4	4
Mass flow of CSD measurements, $(\dot{m})$	kg/s	0.02	0.02
Mass of water in the jacket, (m_j)	kg	10.738	10.738
Mass flow of heat transfer medium in the jacket, $(\dot{m}_j)$	kg	0.35	0.35
Heat capacity of slurry, $(c_{p,s})$	$J/(kgK)$	1.4×10^3	1.4×10^3
Heat capacity of water, $(c_{p,w})$	$J/(kgK)$	4.2×10^3	4.2×10^3
Heat of crystallisation, Δh_c	J/kg	2×10^5	2×10^5

The temperature of the solution was maintained for 15 minutes at 38°C prior to the start of experiment, after which sieved seed (in the size range between 90-125 μm) was added and the temperature of the system was decreased. Supersaturation control was implemented during these experiments to maintain constant supersaturation $(S = C - C_{sat})$ throughout the

experiments. During this period, FBRM readings were monitored to check if seed had either dissolved or secondary nucleation had occurred. Throughout the experiments, the concentration was measured using the Anton Paar DMA 5000 density meter and the crystal size distribution was measured on-line using the Malvern Insitec. The same procedure was repeated for all the experiments. Two different experiments were carried out with variations in the initial conditions. These experiments are referred as experiment A and B in Chapter 5 and 6 and Table 5.1 gives the detailed experimental conditions. The raw experimental results for the measured CSD throughout the batch for experiments A and B, are shown in Appendix A. Experiment A is used for parameter identification whereas experiment B is used for model validation.

5.4 Experimental results

Gravimetric analysis was used to obtain the solubility data for the anhydrous potash alum and was validated against literature results. Figure 5.2 illustrates that the experimental solubility measurements are in very good agreement with the literature data (Barrett and Glennon, 2002; Xie *et al.*, 2001; Zhang and Rohani, 2003). The concentration measurements were expressed in mass percentage of anhydrous potash alum, whereas the compound crystallises as dodecahydrate. Thus the solubility curve for the anhydrous compound was calculated as

$$C_{sol,anh} = C_{sol,hyd}\left(\frac{M_{w,anh}}{M_{w,hyd}}\right), \tag{5.2}$$

where $M_{w,anh} = 258.21$ and $M_{w,hyd} = 474.39$ are the molecular weights for the anhydrous and hydrous forms respectively. A second-order polynomial was fitted to the experimental solubility data, obtained at BASF,

$$C_{sat}(T) = a_0 + a_1 T + a_2 T^2, \tag{5.3}$$

where $a_0 = 3.63$, $a_1 = 2.43 \times 10^{-2}$, $a_2 = 3.58 \times 10^{-3}$, T is the temperature in $°C$ and C_{sat} is in weight percentage expressed in the anhydrous potash alum.

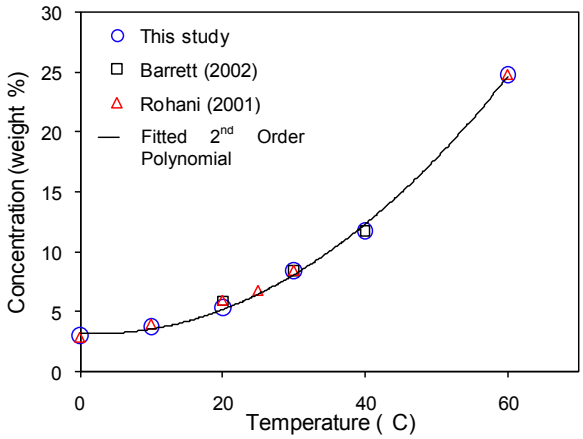

Figure 5.2: Solubility data for anhydrous potash alum-water system.

The operating profiles for the two experimental runs A and B are shown in Figure 5.3. Experiment A was conducted at a supersaturation set-point $S_{sp} = 0.60\%$ (weight percent in kg solute / kg slurry), and experiment B used a constant supersaturation set-point of $S_{sp} = 0.3\%$ (weight percent). The nucleation curve, shown in Figure 5.3, was also determined at BASF.

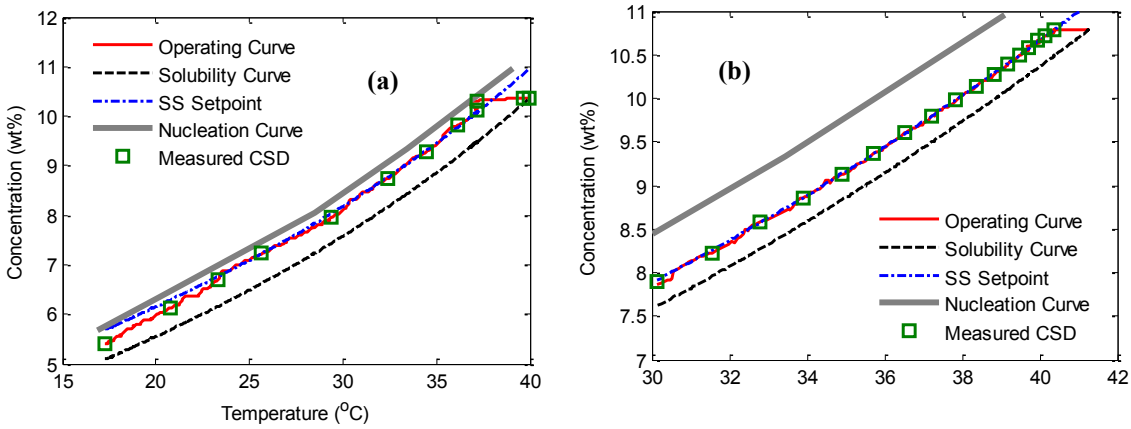

Figure 5.3: Experimental results in the case of supersaturation controlled experiments: (a) Experiment A: $S_{sp} = 0.60$ wt%, used for parameter identification; (b) Experiment B: $S_{sp} = 0.3$ wt%, used for validation.

In the case of experiment A, it can be seen that the supersaturation controller exhibits an overshoot during the initial part of the operating curve, as also shown in Figure 5.4 (a), which leads to secondary nucleation. Both growth and nucleation phenomena occurred in experiment A and hence both mechanisms were included for model parameter identification using the QMOM-MOCH approach described in Section 4.2.1. Experiment B was used for

model validation. Figure 5.4(b) shows (in contrast to experiment A) that supersaturation was very well controlled throughout experiment B.

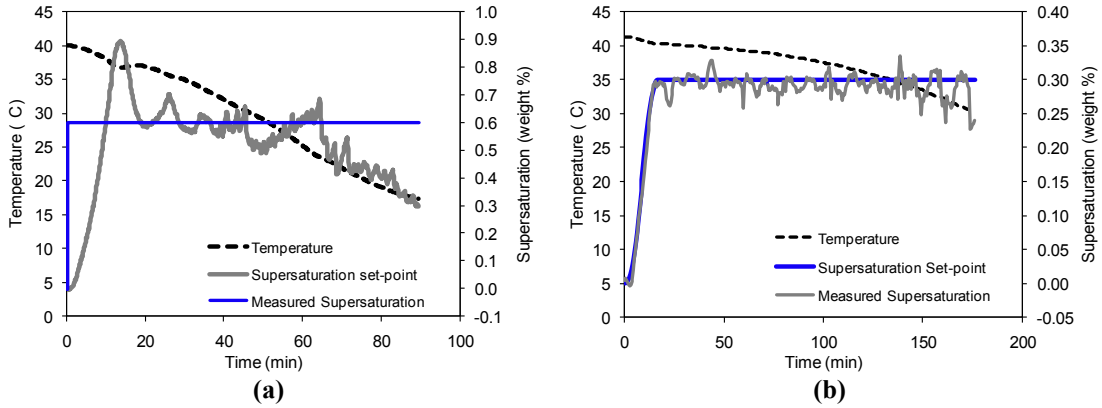

Figure 5.4: Experimental results for temperature, supersaturation set-point and measured supersaturation profile throughout the batch for (a) experiment A and (b) experiment B.

The Sauter mean diameter and the weight mean diameter for the experiments measured throughout the batches are shown in Figure 5.5. For these measurements modifications were made to Malvern Insitec software by BASF, to obtain the data after every 2 seconds.

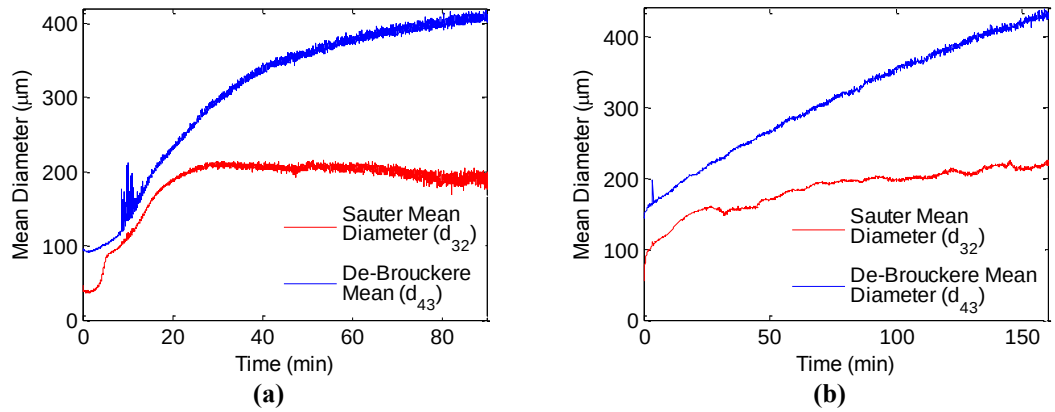

Figure 5.5: Experimental results for Sauter mean diameter and De-Brocukere mean diameter throughout the batch after seed addition for (a) experiment A and (b) experiment B.

Some disturbance can be observed in d_{43} measurement for Experiment A, as shown in Figure 5.5 (a), which happened during the same time when an overshoot was observed in the supersaturation and it is due to the disturbance in the recycle loop.

5.5 Model identification and validation considering size-dependent growth and secondary nucleation

5.5.1 Model identification

For the potash alum system, size dependent growth has been reported in literature (Brecevic and Garside, 1980; Garside and Jancic, 1978; Molnar *et al.*, 1990) and was also observed experimentally in this research. Hence, a generic size-dependent growth rate law described by equation (4.8) and a secondary nucleation rate law described by equation (4.13) were used for model identification. The nucleation and growth parameters were determined to capture the dynamic evolution of the shape of the crystal size distribution, as well as the experimental concentration profile. The optimisation problem for the parameter estimation using concentration and volume population density function is given by,

$$\min_{\theta}\left\{J_{\text{est}} = w_f \sum_{k=1}^{K}\sum_{l=1}^{N_d}(f_{v,k}(L_l) - f_{v,k}^{\exp}(L_l))^2 + w_C \sum_{k=1}^{K}(C_k - C_k^{\exp})^2\right\}, \tag{5.4}$$

$$\text{subject to: } \theta_{\min} \le \theta \le \theta_{\max} \tag{5.5}$$

where $\theta = [k_g, g, \gamma, p, k_b, b]$, is the model parameter vector for the growth and nucleation kinetic parameters, $\theta_{\min}$ and $\theta_{\max}$ are vectors with specified minimum and maximum bounds for each parameter, respectively, C_k and $C_k^{\exp}$ are the simulated and experimental concentration values at the discrete time steps $k = 1,\ldots,K$, $f_{v,k}$ and $f_{v,k}^{\exp}$ are the values of the simulated and experimental volume probability distribution functions, corresponding to the discretised size L_l, $l = 1,\ldots,N_d$, with N_d being the number of experimental size bins, w_f, w_C are objective function weighting factors and J_{est} is the estimation objective function (sum square error). The simulated volume pdf was computed from the number pdf obtained from the MOCH and interpolated for the experimental size range. The conversion from number pdf to volume pdf is given as:

$$f_{v,i} = f_{n,i}L_i^3 \,/\, \sum_{i=1}^{N_d}(f_{n,i}L_i^3\Delta L_i) \tag{5.6}$$

The weighting factors are selected in such a way that the distribution and the concentration are similar in magnitude after multiplication by the scaling factors, and the used values were 10 and 1 for w_j and w_C, respectively. Scaling via these weighing factors will help the optimiser to take into account both the concentration and the crystal size distribution for parameter estimation. The optimisation problem is solved using a sequential quadratic programming (SQP) approach implemented using the MATLAB function *fmincon*. Note that finding the best kinetic parameters is generally a difficult optimisation problem due to the strong correlation between the parameters, and this non-convex optimisation problem is given by equations (5.4)-(5.5). Supersaturation controlled experiments can be used to design experiments, which allow to decouple the identification of the kinetic parameters or quick metastable zone determination experiments can be used for providing experimental data based initial guesses for the parameter identification process (Nagy *et al.*, 2008a). In experiment B the supersaturation control was very good and no nucleation was observed. Therefore experiment A is better for parameter identification, since the overshoot triggered secondary nucleation. Hence using experiment A provides an opportunity to identify the kinetic parameters for growth as well as secondary nucleation.

To evaluate the robustness of the identified model, the confidence intervals of the estimated parameters were also calculated by the method described in detail by (Nagy *et al.*, 2008c). In this approach the objective function is calculated in the discrete time points $t_{0,l} < t_{1,l} < ... < t_{K_l}$ with $l = 1,...,N_{\text{ex}}$ (N_{ex} being the number of experiments) and K_l the number of discrete time points in experiment l. The estimation problem is formulated as:

$$\min_{\theta}\left\{J_{\text{est}} = \sum_{l=1}^{N_{\text{ex}}}\sum_{k=0}^{K_l}\sum_{i=1}^{N_y}\{y(t_{k,l};\theta) - y_i^{\text{exp}}(t_{k,l})\}^2\right\}, \tag{5.7}$$

where N_y is the number of measured model outputs (y) and y_i^{exp} are the experimental values. In the estimation problem presented in this chapter, and comparing equations (5.4)-(5.5) to equation (5.7) it can be seen that, $l = N_{\text{ex}} = 1$ (experiment A), $N_y = N_d + 1$ (corresponding to the CSD values in $N_d = 86$ size bins plus the concentration) and measurements at $K_l = K = 13$ time steps were used. For estimating the confidence interval the measurement matrix (M_θ) is given by the block matrix,

$$M_\theta = \begin{bmatrix} M_\theta^0 \\ M_\theta^1 \\ \vdots \\ M_\theta^{k_{N_{ex}}} \end{bmatrix} \tag{5.8}$$

with $k_{N_{ex}} = \sum_{l=1}^{N_{ex}} K_l = K$, number of $(N_y \times N_\theta)$ sensitivity matrixes,

$$M_\theta^{k_l} = \frac{dy^{k_l}}{d\theta}, \tag{5.9}$$

with $k_l = 0,...,K$. The sensitivity matrices in this study were computed numerically by the central difference scheme. The precision matrix (P), and covariance matrix (V) are given by:

$$P = (M_\theta^T M_\theta)^{-1}, \tag{5.10}$$

$$V = s_R^2 P, \tag{5.11}$$

where the residual variance is given by $s_R^2 = J_{\text{est}} / N_{df}$ with $N_{df} = N_y(k_{N_{ex}} + 1) - N_\theta - 1$ being the number of degrees of freedom. Here $N_{df} = 87(13+1) - 6 - 1 = 1211$. The confidence intervals are calculated using the t-test (Beck and Arnold, 1977) as:

$$\theta = \hat{\theta} \pm t_{\alpha/2, N_{df}} \sqrt{diag(V)} \tag{5.12}$$

where $\hat{\theta}$ is the nominal parameter vector, $t_{\alpha/2, N_{df}}$ is the t distribution with N_{df} degrees of freedom. The 95% confidence intervals are obtained for $\alpha = 0.05$. The resulting model parameters for the potash alum system are presented in Table 5.2 (Aamir *et al.*, 2008; Aamir *et al.*, 2009b).

Table 5.2: Size-dependent growth and nucleation parameters for the crystallisation of potash alum in water (units for S = $kg / kg\ slurry$).

Parameter	Value	Error bounds at 95% confidence interval
Growth Parameters		
Growth rate constant (k_g), $\mu m\ s^{-1}$	8.5708	± 0.036
Growth constant (γ), μm^{-1}	0.0050	± 0.0035
Growth constant (p), --	1.5777	± 0.079
Growth order constant (g), --	1.0000	± 0.095
Nucleation Parameters		
Nucleation rate constant (k_b), $\mu m^{-3} s^{-1}$	0.0380	± 0.044
Nucleation order constant (b), --	3.4174	± 0.037

The dynamic evolution of the modelled and the experimental CSDs are in very good agreement during the entire batch, as shown in Figure 5.6. The CSD broadens with decreasing heights with time, confirming the requirement of size-dependent growth kinetics. The formation of a secondary CSD peak at low particle sizes can also be observed, which is the result of secondary nucleation, which occurred due to overshoot at 10 minutes into the batch, as shown in Figure 5.4 (a). The QMOM-MOCH approach with the model using the identified growth and nucleation parameters is able to describe the main features of the CSD throughout the entire batch. The complete dynamic evolution of the CSD obtained using the combined QMOM-MOCH method for experiment A is given in Appendix B.

Figure 5.7 illustrates the evolution of the characteristic lines and the discretised number distribution function predicted by the simulation of experiment A, using the combined QMOM-MOCH. The evolution of the characteristic lines show the broadening of the distribution function because of the size-dependent growth kinetics, as can be observed from Figure 5.6. The distribution function is initialized at $t = 0$ with values obtained from the seed distribution, after which the values of f_n decrease as the distribution broadens. At different time steps, new nuclei and new characteristic lines appear using the methods described in Section 4.2.1. The discretisation intervals along the time axis depend on the growth kinetics, according to the approach described in Section 4.2.1 and illustrated in Figure 4.1 and Figure 4.2.

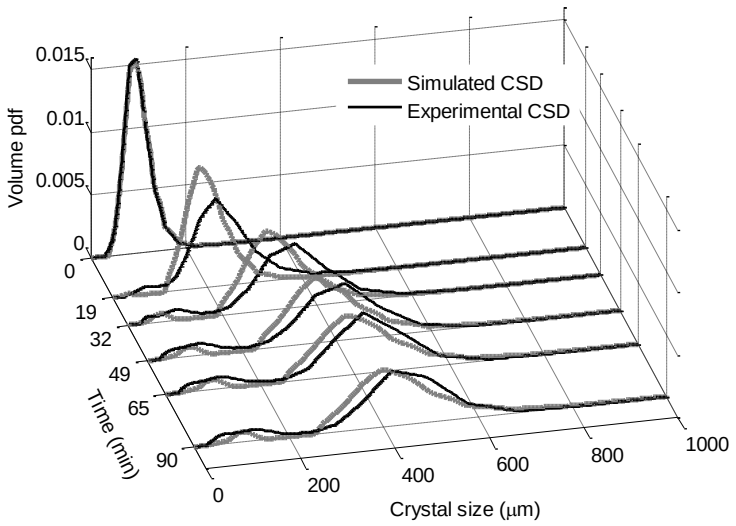

Figure 5.6: Dynamic evolution of the modelled and experimental CSD for experiment A.

It can be observed that during the period 10-30 minutes, the growth is faster and the nucleation rate is also more significant, hence the discretisation is finer compared to the later stages of the batch, which are characterised by slower growth.

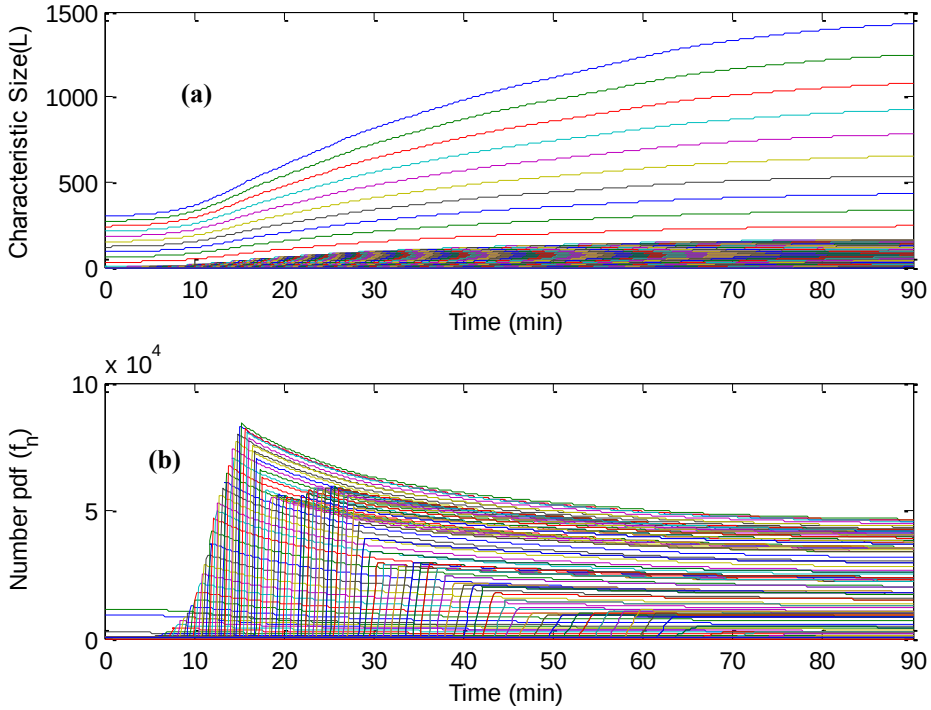

Figure 5.7: Evolution of characteristic lines (a) and number distribution function (b) for the simulated experiment A.

Figure 5.8 shows the comparison between the experimental and the modelled concentrations and weight mean sizes throughout the batch, which are also in relatively good agreement. As it can be seen in Figure 5.8 (b), the model under-predicted d_{43}, which also correlates with the entire CSD prediction shown in Figure 5.6. This indicates that in the simulation the number of larger particles was less than it was measured experimentally. The simulated concentration is lower than the experimental concentration, as shown in Figure 5.8. This may be due to the fact that the number of particles (μ_0) initially calculated from the seed CSD has some error; therefore more concentration was consumed initially during the simulation than in the experiment.

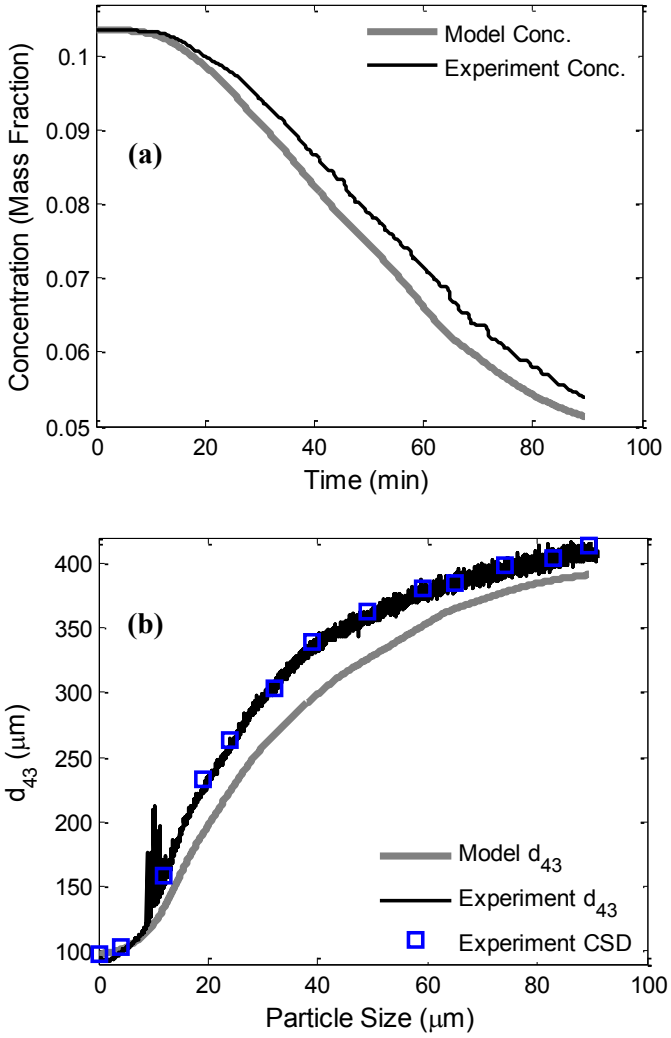

Figure 5.8: Experimental and simulated results: a) concentration b) De-Broucker mean diameter during the entire batch of experiment A.

The combined QMOM-MOCH can be used not only for model parameter identification, but also for CSD prediction. The simulation time for the reconstruction of the entire evolution of the CSD during the batch, takes only a few seconds on a standard PC running MATLAB.

Table 5.3: Computational time for different number of discretisation points using the combined QMOM-MOCH technique, for the entire batch time. (Simulation of experiment A was in MATLAB 7.0 running on a PC with 2.0 GHz Intel Core 2 Duo processor with 4 GB RAM).

No of discretisation	Computational Time (s)	Absolute Tolerance
60	38	1e-10
30	28	1e-10
15	12	1e-10
6	5	1e-10

It can be observed in Table 5.3 that the proposed technique is computationally very effective even using higher discretisation points, to obtain the complete evolution of the CSD. The technique has a potential to be used on-line because of its computational effectiveness and robustness.

Using the combined QMOM-MOCH it is possible to eliminate the problems related to simple inversion or approximation approaches discussed in detail in Chapter 2 and Chapter 3, such as negative values in the pdf, ill-conditioning, or requirement of *a priori* information of the shape of the distribution. The combined technique uses the advantages of both methods i.e. quadrature method of moments and method of characteristics, shown in Table 2.4. As was mentioned in Chapter 2 the quadrature method of moments only gives a coarse approximation of changes in the CSD, but provides complete information about the moments. Similarly using the method of characteristics alone is only feasible for growth and primary nucleation. The combined technique can predict the complete dynamic evolution of the CSD for any empirical growth and nucleation expressions. The QMOM part of the method provides the moment information with high accuracy with only a few quadrature points, which can be used to calculate the overall mass balance throughout the batch allowing the case of varying supersaturation to be studied. The method provides a great improvement for the real-time prediction of the complete CSD in crystallisation processes, while considering size-dependent growth, size-dependent dissolution, and nucleation mechanisms and variable supersaturation.

Another advantage of the technique is in the method employed to represent the contribution from nucleation events to the overall distribution function. The method is adaptive, as the

number of integrations is not predetermined and depends on the evolution of the characteristic lines governed by the growth kinetics. This feature allows high resolution prediction of the part of the CSD that result from nucleation events. An important aspect of this algorithm is the selection of the nuclei size r_0; nucleation is assumed to occur in the range from 0 to r_0. In this work r_0 is the size of the particles that are first detected by a particular measurement approach (e.g. FBRM). The resolution of a CSD will be determined by the discretisation interval ΔL_0 and the size at which the nucleation event occurs r_0. Therefore the selected r_0 value should be small enough, to make sure that the value is close to the original nucleation event detectable by several measurement equipments during crystallisation process. This gives an additional benefit to the technique for direct consideration of *apparent* nucleation kinetics in the model.

The technique is robust and is able to capture the shape of the CSD with less computational burden even with sharp discontinuities in the algorithm (such as related to the calculation of the nucleation events). The technique also has the advantage that it does not exhibit oscillatory behaviour (which could result in negative number densities), or numerical diffusion, which can be major drawbacks in the case of some other numerical techniques used to solve population balance equations.

5.5.2 Model validation

The kinetic parameters identified using experiment A are given in Table 5.2. These identified parameters were used for the validation of the model using experiment B. Good agreement was observed between the experimental and the modelled concentration as well as the weighted mean diameter, as shown in Figure 5.9. The supersaturation was well controlled during experiment B, therefore the simulated concentration is quite close to experimental concentration. Weighted mean diameter is slightly over predicted towards the end of the batch, which can also be observed in Figure 5.10. The model concentration is consumed slightly more than the experimental concentration, due to which d_{43} and CSD were slightly over estimated towards the end of the batch. The dynamic evolution of the modelled and the experimental CSDs are in good agreement during the the first 80 minutes of the batch, as shown in Figure 5.10.

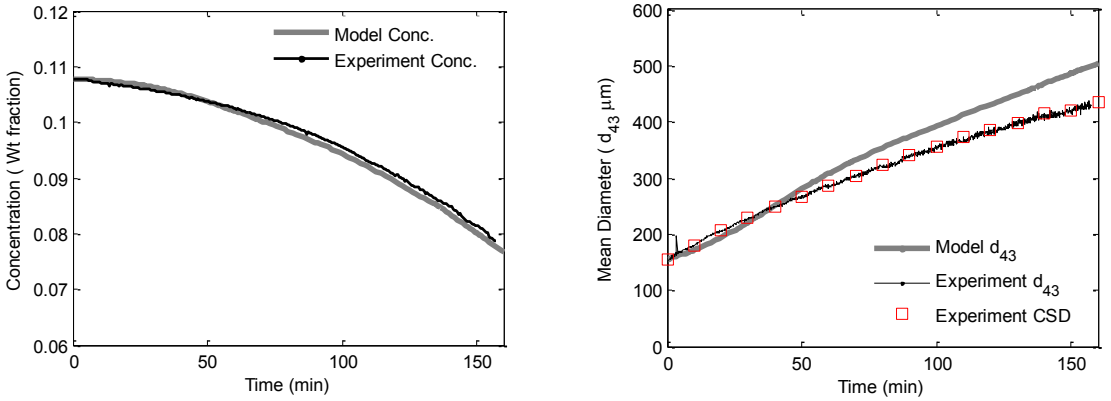

Figure 5.9: Experimental and simulated results: a) concentration b) De-Broucker mean diameter during the entire batch of experiment B.

It can be seen that the CSDs broaden with decreasing height during the batch and the formation of a secondary CSD peak can also be observed. These features are captured by the model prediction. The distribution function is initialized at $t = 0$ with values obtained from the seed distribution used for experiment B, after which the values of f_n decrease as the distribution broadens. New nuclei and new characteristic lines appear at different time steps. The discretisation intervals along the time axis depend on the growth kinetics.

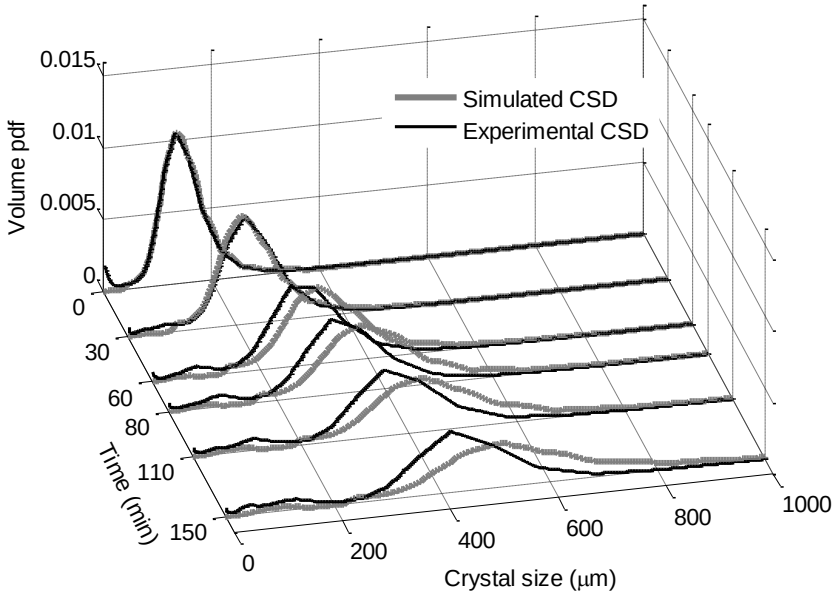

Figure 5.10: Dynamic evolution of the modelled and experimental CSD for experiment B using the kinetic parameters identified using experiment A.

The complete dynamic evolution of the CSD obtained from the combined QMOM-MOCH for experiment B is given in Appendix B. Figure 5.11 (a and b) illustrates the evolution of the characteristic lines and the discretised number distribution function predicted by the simulation of experiment A, using the combined QMOM-MOCH.

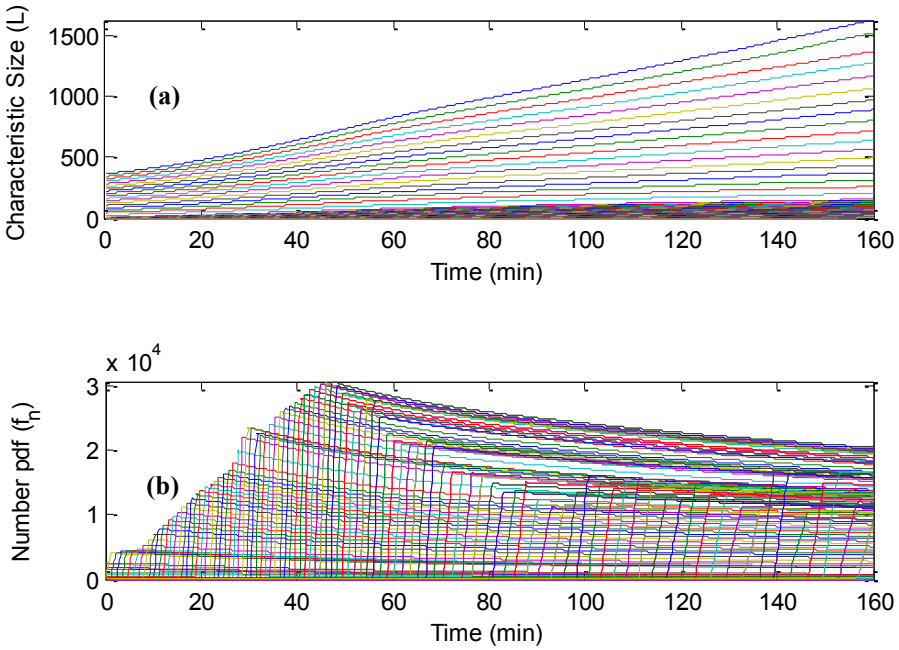

Figure 5.11: Evolution of characteristic lines (a) and number distribution function (b) for the simulated experiment B.

It can be observed in Figure 5.4 (b) that the supersaturation was controlled well throughout the entire experiment B. By controlling the crystallisation process at a small and constant supersaturation, generally growth becomes the dominating phenomenon.

If supersaturation is constant and there is no nucleation then faster computational performance can be achieved, via an analytical solution of equations (4.10) and (4.11), of the form:

$$L = \frac{(((1+\gamma L_0)^{1-p} + k_g S^g t\gamma(1-p))^{\frac{1}{1-p}} - 1)}{\gamma} \tag{5.13}$$

$$f_n(L) = f_{n,0}(L_0)\left(1 + \frac{k_g S^g t\gamma(1-p)}{(1+\gamma L_0)^{1-p}}\right)^{\frac{p}{p-1}} \tag{5.14}$$

The derivation of equations (5.13)-(5.14) is given in Appendix C. Comparison of the experimental and the simulated CSD obtained from the analytical CSD estimator is given in Figure 5.12 at different time intervals. In the simulations the experimental initial concentration, temperature profile and seed distribution were used. The kinetic parameters were based on experiment A (given in Table 5.2). In the case of experiment B, the supersaturation was well maintained at its constant set-point. Figure 5.12 shows that the simulated and the experimental CSDs are in good agreement. However, the experimental CSD shows evidence of secondary nucleation, which is indicated in Figure 5.12 by the secondary CSD peak developed during the crystallisation process.

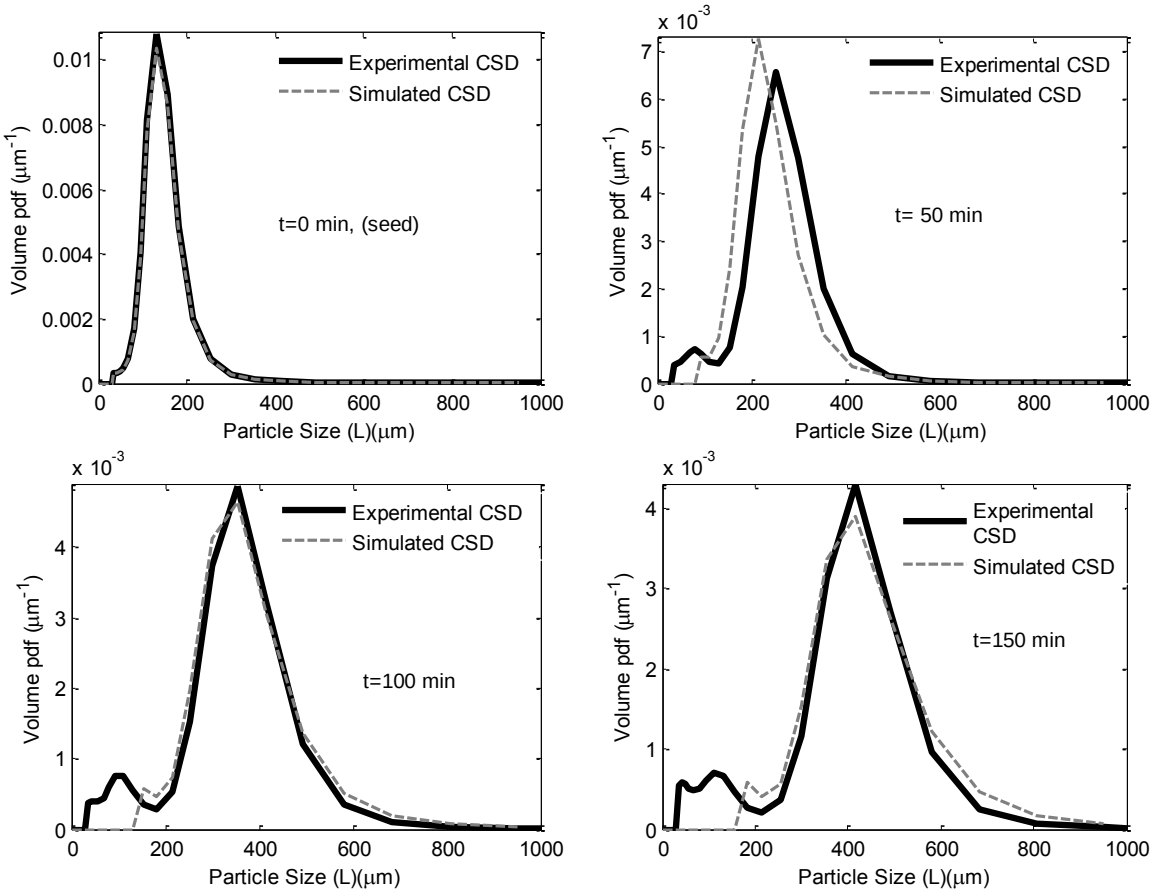

Figure 5.12: Comparison between the measured and the simulated CSD using the analytical CSD estimator (experiment B with supersaturation set point S_{sp} = 0.3%).

The analytical solution is derived based on the assumption of constant supersaturation and no nucleation. Therefore, by initializing the model with the seed CSD and applying it in an open-loop, the analytical solution is not able to predict the development of a secondary

nucleation peak at small crystal sizes. However, in the case of many practical applications, an on-line measurement of the CSD is available, typically with a sampling time in the range of 1-15 min (*e.g.* by using focused beam reflectance measurement coupled with inverse geometric modelling to transform chord length distributions into size distributions) (Hukkanen and Braatz, 2003; Ruf *et al.*, 2000). In these cases the analytical solutions can be used in closed-loop, initialising it with the new CSD measurement every time it becomes available.

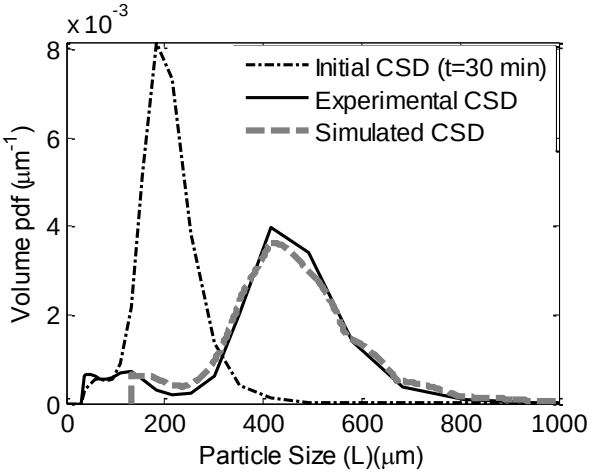

Figure 5.13: Performance of the analytical estimator initialised with CSD at t = 30 min (experiment B).

Figure 5.13 illustrates the results when the analytical estimator was initialised using the measured CSD after 30 min. The effect of the secondary nucleation, which occurred in the first 30 minutes of the batch, on the final CSD is partially predicted. The proposed method can be used as an efficient estimator for monitoring and predicting the CSD at the end of the batch, or in off-line or on-line optimisation approaches for designing crystallisation systems to produce consistently the desired final CSD. The results also show that in practical applications, the analytical technique can be used for estimation of the CSD even if the supersaturation is not constant during the initial phase of the batch. As new CSD measurements become available and the supersaturation reaches its constant set-point value, the predicted CSD will converge to the correct value.

Experiments A and B do not involve any dissolution of small particles. However if Direct Nucleation Control (DNC) (Abu Bakar *et al.*, 2009b) needs to be implemented then the dissolution of fines becomes part of the CSD control strategy. Therefore knowledge of

dissolution kinetics is required for a model-based design of operating policies, which make use of controlled dissolution. The next sections describe the parameter identification of the dissolution kinetics for the potash alum-water system.

5.6 Experimental setup for determination of dissolution parameters

5.6.1 Apparatus

The temperature in a 0.5 L jacketed glass vessel was controlled with a Pt100 thermocouple using a Huber VPC CC3 450 thermostat. An overhead stirrer with a four-blade pitch type impeller was used to agitate the system at 350 rpm. This agitation speed was chosen to be high enough to guarantee that particles were well suspended throughout the process, but low enough to avoid attrition or entrainment of bubbles due to vortex formation. A FBRM probe (model D600, Lasentec) was inserted into the solution to measure chord length distributions. The reproducibility of the FBRM measurement was verified by changing the place and the orientation of the probe in different locations within the crystalliser. The chord length distribution and number of count measurements were reproducible indicating that the crystallisation vessel was well mixed. When the same amount of seed was added to the crystalliser, the total number of counts measured by FBRM was very consistent with in the range of 1000 to 1200 counts/s for all experiments. The concentration was measured *in situ* using conductivity probe. Conductivity (voltage) was measured using a CM 35 meter with WPA-35 conductivity probe. The CSD at the end of runs with different time duration (off-line) was measured using a laser-diffraction equipment, (Mastersizer 2000 with a hydro 2000 SM dispersion unit). Hexane was used to disperse potash-alum crystals to measure the CSD. The samples were analysed off-line. Hence experiments were performed by repeating the same experimental conditions but stopping the experiments at different stages of the batch and analysing the samples obtained at the end. Images of crystals were also taken using a Leica DM LM microscope equipped with a Leica PFC 350 FX camera. A schematic representation of the experimental setup is shown in Figure 5.14. The operating conditions for the experiment are summarised in Table 5.4.

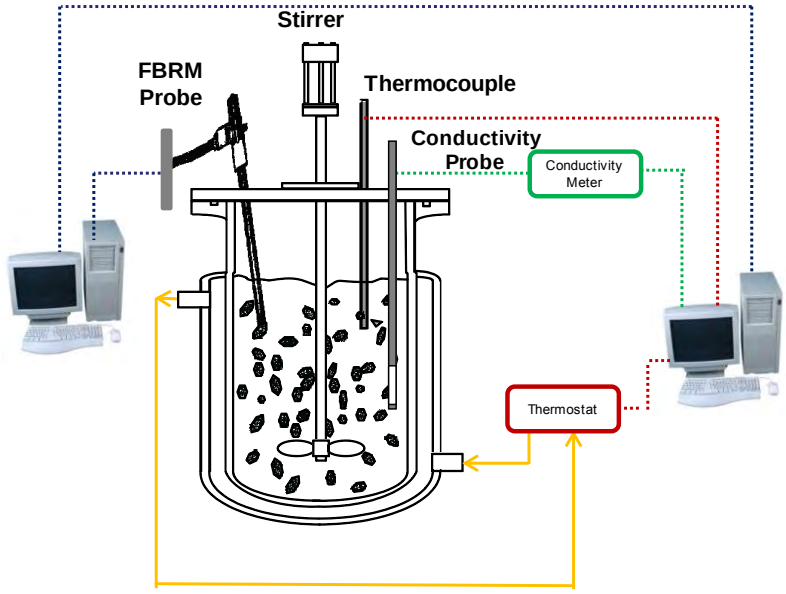

Figure 5.14: A schematic representation of the experimental setup used for the determination of dissolution parameters.

Table 5.4: Operating conditions for dissolution experiment for seeded-batch cooling crystallisation.

Operating Conditions	Units	Experiment
Saturation temperature	$°C$	30
Seed mass , (m_{seed})	kg	1.9×10^{-2}
Batch time, t_{batch}	min	80
Initial solute concentration (C_i)	g solid/ g water	0.084
Initial temperature at seeding and start of profile, (T_0),	$°C$	29
Final temperature, (T_f),	$°C$	35
Temperature profile followed	--	Linear $T_{linear} = T_0 - (T_0 - T_f)(t / t_{batch})$
Points for smooth profile, (N)	--	60
Sampling time for FBRM measurement and conductivity measurement	s	10
Sieve sizes for seed, $\mathcal{L}$	μm	300-355
Agitation speed	rpm	350
Density of crystals (Mullin, 2001), (ρ_c)	kg / m^3	1750
Volumetric shape factor, (k_v)	--	0.62
Mass of slurry, (m_{slurry})	kg	0.52
Number of samples for CSD	--	12

measurements

5.6.2 Seed preparation

Seeds were prepared using sieve analysis. The sieve sizes used were: 500 μm, 355 μm, 300 μm, 300 μm, 280 μm,200 μm, 150 μm and 125 μm. The run time for the sieving operation was set to 120 min, and the rotation and shaking caused the crystals to distribute throughout the sieve stack. The product obtained on the sieve size of 300 μm was collected for seeding and was stored in a desiccator.

5.6.3 Method

A solution of potash alum and water was prepared to obtain the kinetic parameters for dissolution. A 0.5 L jacketed crystallisation vessel equipped with thermocouple, conductivity and focused beam reflectance measurement (FBRM) probes was used. The saturation temperature used for these experiments was 30°C (8.4 g of potash alum dissolved in 100 g of water). Potash alum was dissolved in water by heating to 40°C at a rate of 0.8°C/min. The solution was equilibrated at 40°C for 30 minutes and then the temperature of the solution was reduced to 29°C at a rate of 0.5°C/min. The temperature of the solution was maintained at 29°C prior to the start of experiment. After 10 minutes, 19 g of sieved seed in the size range between 300-355 μm (CSD determined using Malvern Masterizer) was added to the solution and the temperature was maintained at 30°C for 10 minutes. During this period, the conductivity and FBRM readings were monitored to check if any amount of the seed had dissolved. Both FBRM and conductivity meter showed constant readings before and after the addition of the seed, which verified that the seed had not dissolved and the solution was saturated at 30°C. In the next step, the process temperature was increased linearly to 35°C over a duration of 80 minutes. The same initial procedure was used for a sequence of nine runs using batch times of $t = 0,\ 10,\ 20,\ldots,80$ minutes. At the end of each run the temperature profile was stopped and the product was removed for CSD measurement.

5.6.4 Concentration measurement using conductivity meter

Conductivity (voltage) was measured using a CM 35 voltmeter with WPA-35 conductivity probe. For calibration, the conductivity was measured for several concentrations over a range of temperatures, as shown in Figure 5.15, to cover the MSZW and a range of under-saturation conditions, where dissolution occurs. The temperature was decreased by 1°C at each concentration until the system got nucleated. Hence the nucleation points, as shown in Figure 5.15, were determined experimentally. The solubility curve was obtained from literature. The sensitivity of the conductivity measurement to the solid content in the slurry was evaluated by measuring the conductivity at constant temperature in the equilibrated slurry, and changing the agitation speed to vary the solid fraction passing through the electrodes of the conductivity probe. Due to the relatively large surface area of the electrodes the sensitivity was practically negligible; hence the conductivity probe was considered to be suitable for concentration measurement in the slurry.

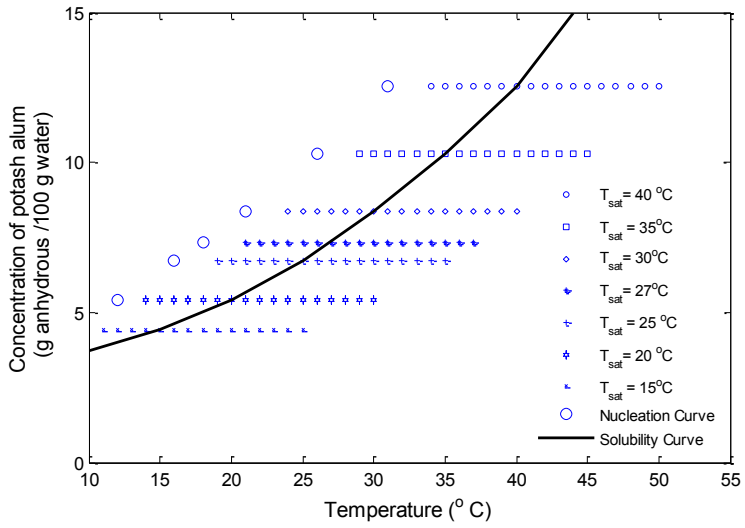

Figure 5.15: Measurement points for conductivity for the used concentrations and temperature ranges including solubility curve (Mullin, 2001) and the detected nucleation points.

Figure 5.16 (a and b) show the dependence of the conductivity on temperature at various concentrations, and the variation of the conductivity with concentrations at different constant temperatures. Both dependences appear to be linear with relatively constant slopes over the

tested temperature and concentration ranges, hence a simple bivariate linear regression based calibration model was used:

$$C_k = a_0 V_k + a_1 T_k + a_2 \tag{5.15}$$

where T is the temperature in ^{o}C, V is the measured voltage (output from the conductivity meter), and C_k is experimental concentration values at the discrete measurement points $k = 1,\ldots,K$.

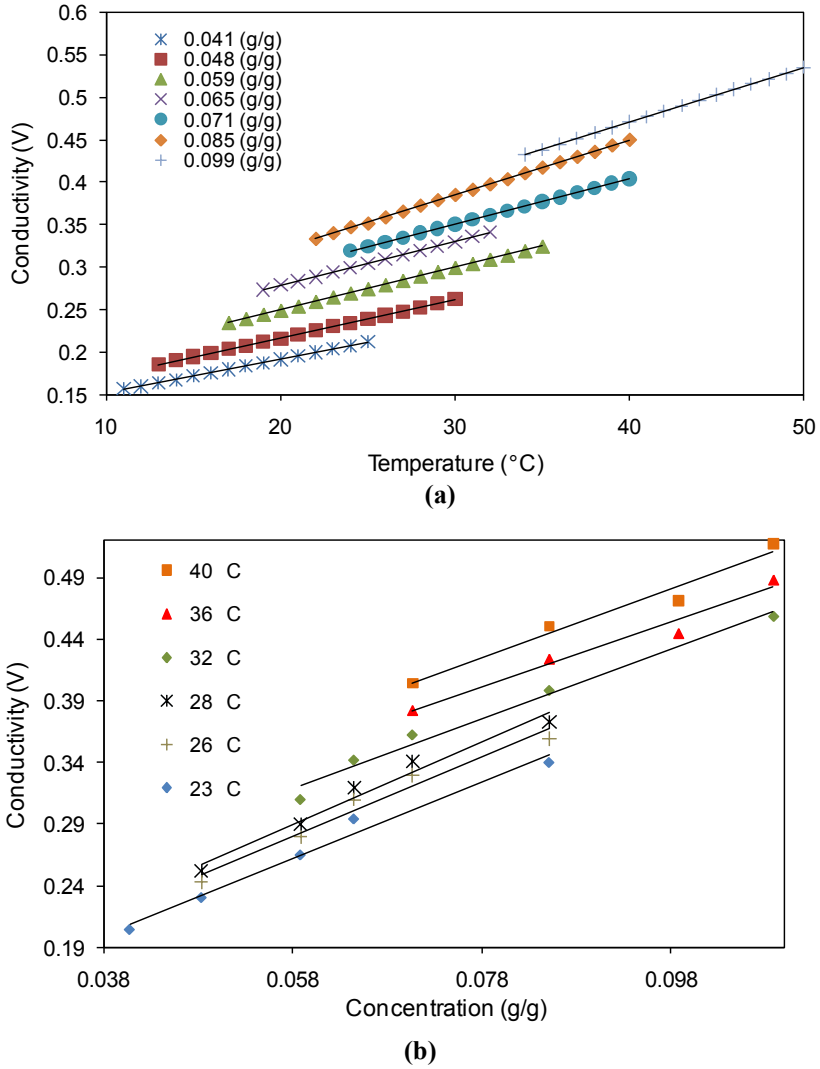

Figure 5.16: Experimentally observed relationship between conductivity and a) temperature and b) concentration.

The parameters for the calibration model were estimated by a least square optimisation approach solved using the *fmincon* function in MATLAB. The optimisation problem for the parameter estimation is given by:

$$\min_{a_i}\left\{\sum_{k=1}^{K}(C_k - C_k^{\exp})^2\right\}. \tag{5.16}$$

where C_k and $C_k^{\exp}$ are the estimated and experimental concentration values at the discrete measurement points $k = 1,\ldots,K$. The fitted parameters for the calibration model are given in Table 5.5.

Table 5.5: Calibration model parameters for concentration measurement using a conductivity probe for potash alum-water system.

Parameters	Values	Error Bound at 95% confidence interval
a_0	0.2994	± 0.0106
a_1	-0.0013	± 0.0008
a_2	0.0091	± 0.0017

The measured and the estimated concentrations using the calibration model show that they are in good agreement (Figure 5.17). The calibration equation (5.15) was validated against literature solubility data for anhydrous potash alum.

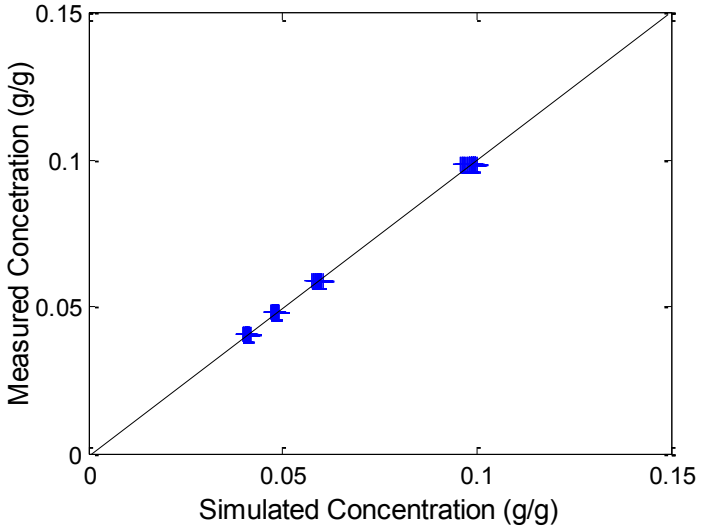

Figure 5.17: Comparison of measured and estimated concentrations using the calibration parameters shown in Table 5.5.

An experiment was conducted in which, the temperature of a slurry containing excess solid was increased in several steps as shown in Figure 5.18 (a). Figure 5.18 (b) shows a comparison between the estimated concentrations for the solubility curve using the calibration model and the literature data (Barrett and Glennon, 2002; Mullin, 2001; Xie *et al.*, 2001; Zhang and Rohani, 2003). Good agreement between the measured results and the literature data was observed, with a sum square error of only 0.002. Since the concentration measurements are expressed in weight fraction of anhydrous potassium alum, the solubility curve is calculated for the anhydrous potash alum as given by equation (5.2).

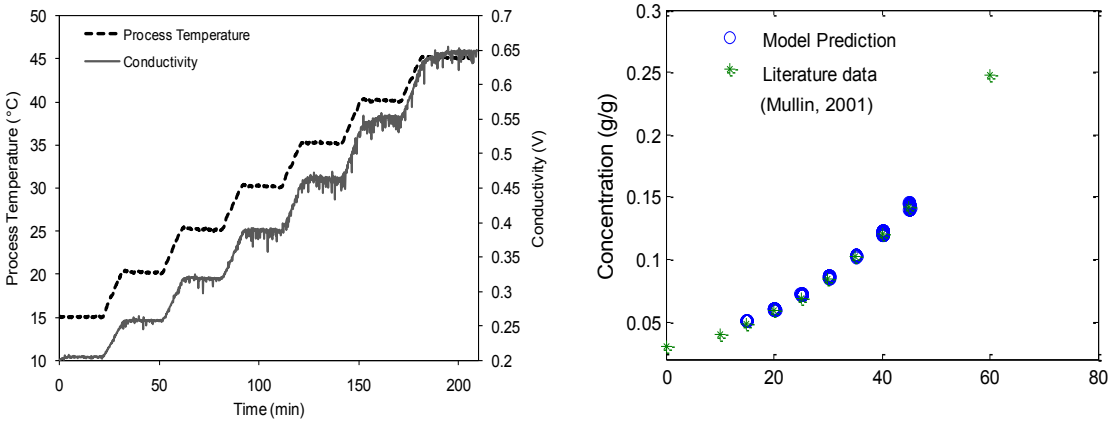

Figure 5.18: a) Determination of the solubility curve to validate the calibration parameters by increasing the temperature from 15 to 45 °C in 5 °C steps while containing 10% excess solids in the slurry throughout the process b) Comparison between the experimental solubility curve using conductivity and literature data.

5.7 Size-dependent dissolution model identification for the potash alum in water system

Repeated dissolution experiments were conducted under identical experimental conditions, but stopping the batches at different times (10, 20, ... , 80 min) for off-line CSD measurement using the Malvern Mastersizer unit. This approach was chosen to avoid disturbances in the mass balance due to samples taken during a single batch run. Details of the operating conditions of the experiments are shown in Table 5.4. The same seed was introduced in each experiment shortly after the process temperature was stabilised at 29°C within ten minutes. Figure 5.19 shows the concentration and FBRM results for the longest batch (80 min). The measurements from the shorter runs were consistent following the trend of the longest batch. The FBRM probe used in the experiments also detected a decrease in

the square weighted mean chord length (*SWMCL*), as shown in Figure 5.19 (a), caused by the disappearance of the smaller particles and the reduction in the size of the larger particles. The change in the concentration throughout the batch is shown in Figure 5.19 (b) indicating a continuous increase with the dissolution of particles. As the temperature was increased from 30 to 35°C, the smaller particles dissolved, whilst the size of the larger particles decreased, hence narrowing the associated distribution. Figure 5.20 shows microscopic images of samples collected during the dissolution experiment. These images provide visual evidence of the disappearance of small particles and the reduction of size of the larger crystals as compared to the size of the seed.

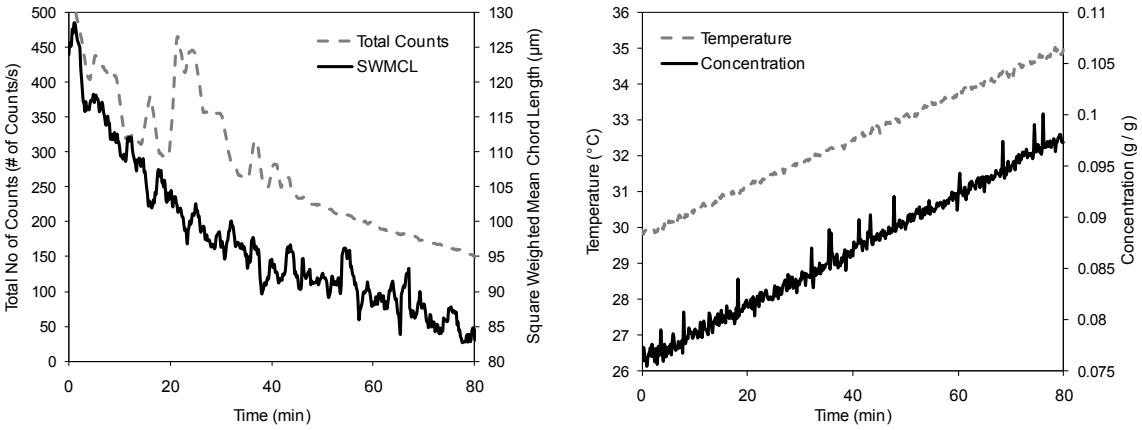

Figure 5.19: a) Measured total number of counts (# /s) and square weighted mean chord length detected by FBRM throughout the experiment; b) Temperature profile and measured concentration throughout the batch; c) Chord length distribution throughout the batch for the dissolution experiment conducted to determine the kinetic parameters.

A total of 8 batches were conducted, leading to 9 CSD measurements (with the seed CSD at $t = 0$, and at $t = 10,\ 20,\ \ldots\ ,\ 80\ \mathrm{min}$). The dynamic evolution of the measured CSD is shown in Figure 5.21. The seed used in the experiments (and simulation) was bimodal as indicated by the two peaks in the distribution at the initial time $(t = 0)$, shown in Figure 5.21. The same bimodal feature of the seed can be observed in the microscopic image in Figure 5.20 (a). As the temperature increased according to the temperature profile in Figure 5.19 (b), the fine particles were dissolved, whilst the size of the larger particles decreased with the concomitant narrowing of the distribution, confirming the size-dependent mechanism of dissolution.

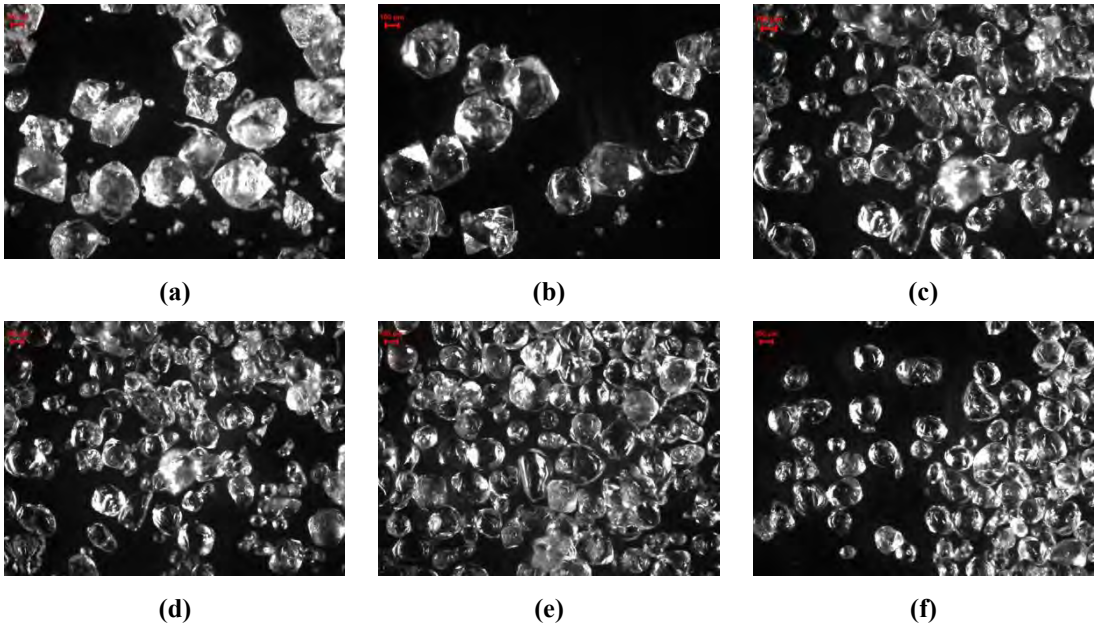

Figure 5.20: Microscopic images of crystals a) seed at t= 0 min, b) t = 16 min, c) t = 32 min, d) t = 48 min, e) t = 64 min and f) t = 80 min at the end of the experiment.

The dissolution parameters were determined to capture the dynamic evolution of the shape of the size distribution, as well as the experimental concentration profile. The optimisation problem for the parameter estimation is given by equation (5.4) and (5.5), having the same form as the problem used for the model identification of the size-dependent growth and nucleation. The size-dependent dissolution parameters were estimated for the empirical relationship shown in equation (4.21).

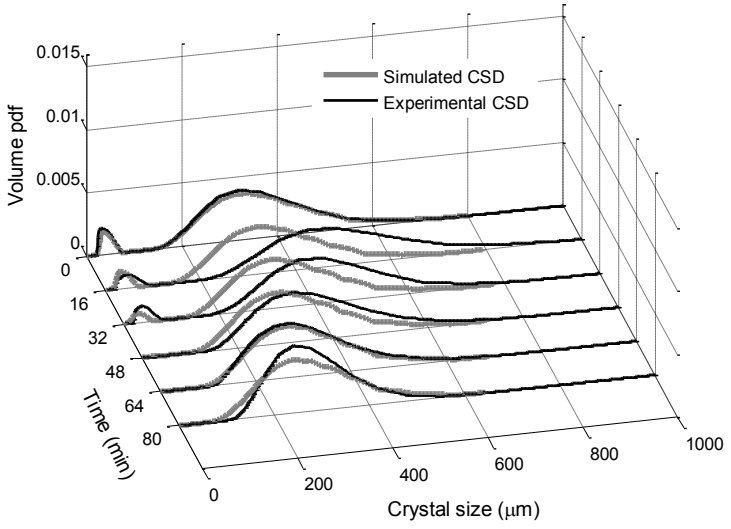

Figure 5.21: Dynamic evolution of the CSD throughout the batch for simulated and experimental CSD during dissolution mechanism.

In this case $\theta = [k_d, d, \zeta, q]$ is the model parameter vector containing the dissolution kinetic parameters. The optimisation problem is solved using a sequential quadratic programming (SQP) based optimisation approach implemented in the MATLAB function *fmincon*. The PBE was solved using the QMOM-MOCH approach, for which the simulation time for the reconstruction of the entire evolution of the CSD during the batch only takes a few seconds on a standard PC running MATLAB. To evaluate the robustness of the identified model, the confidence intervals of the estimated parameters were also calculated using equation (5.8)-(5.12). The resulting dissolution model parameters for the potash alum system are given in Table 5.6:

Table 5.6: Kinetic parameters for size-dependent dissolution for potash alum-water system.

Parameters	Value	Error bound at 95% confidence interval
Dissolution rate constant (k_d), $\mu m\ s^{-1}$	1.28	± 0.072
Dissolution constant (ζ), μm^{-1}	0.02	± 0.063
Dissolution constant (q), --	0.86	± 0.081
Dissolution order constant (d), --	0.98	± 0.062

Figure 5.21 illustrates the dynamic evolution of the simulated and the experimental CSDs, which are in reasonable agreement during the entire batch. The proposed dissolution model with the identified parameters and solution algorithm based on the combined QMOM-MOCH method is able to describe the main features of the CSD throughout the entire batch. The dissolution of the fine particles and the decrease of the size of the particles together with the narrowing of distribution are well captured by the model. Figure 5.22 illustrates the evolution of the characteristic lines and the number distribution function predicted by the simulation for dissolution, using the combined QMOM-MOCH. The evolution of the characteristic lines shows the narrowing of the distribution function due to the size-dependent dissolution kinetics.

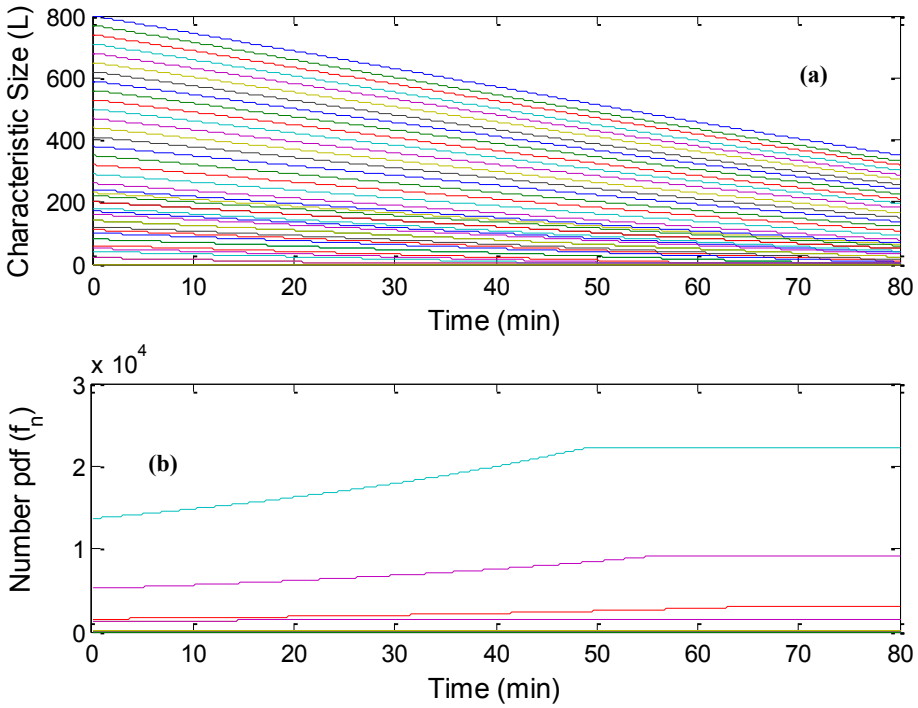

Figure 5.22: Evolution of characteristic lines (a) and number distribution function (b) for the simulated results for dissolution with the identified kinetic parameters.

5.8 Conclusions

The chapter describes the materials and methods used for the experiments carried out to estimate the kinetic parameters for the potash alum-water system. The combined quadrature method of moments and the method of characteristics (QMOM-MOCH) approach was used for the solution of the population balance equations. The combined technique provides a computationally efficient framework for reconstructing the dynamic variation of the whole crystal size distribution (CSD) during the dissolution, growth and nucleation processes. The kinetic parameters for nucleation and growth were determined to capture the dynamic evolution of the shape of the crystal size distribution, as well as the experimental concentration profile.

Size-dependent growth and secondary nucleation parameters were evaluated for the seeded system of potash alum in water, using industrial pilot plant data provided by BASF. The data consists of on-line measurement of CSD using Malvern Insitec and concentration, which was measured using an on-line density meter. The kinetic parameters estimated for size-

dependent growth and nucleation were able to predict the concentration and mean diameters very well and capture the dynamic evolution of crystal size distribution very well for both experiments (identification and validation experiments).

In the second part of the chapter the approach used for the determination of the dissolution parameters for potash alum-water system is described. The kinetic parameters for size dependent dissolution were identified using laboratory scale experiments. During these experiments the CSD was measured off-line using a Malvern Mastersizer. The concentration was measured using a conductivity probe and was converted to concentration using a bivarite linear regression calibration model. The process was also monitored using a focused beam reflectance measurement (FBRM) probe, which showed that smaller particles dissolved, whilst the size of the larger particles decreased and the distribution narrowed. Microscopic images provided the same evidence qualitatively, confirming the size-dependent dissolution mechanism. Parameters with their confidence intervals were identified through a similar least square type non-linear optimisation approach as for the size-dependent growth and nucleation mechanisms. The simulation results were in very good agreement with the experimental data, capturing well the main features of the dynamic evolution of the CSD.

Chapter 6
Dynamic optimisation of temperature trajectories for shaping the product CSD

6.1 Introduction

Objective functions for optimisation of a crystallisation operation can be defined in terms of product purity, filtration time, crystallisation batch time, drying time, particle size, shape of particle size distribution and quality of crystals. Depending upon the definition of the objective functions, different optimal operating conditions may be obtained. For a batch crystalliser the dynamic optimisation of temperature trajectories are often important and hence have been extensively studied (Sarkar *et al.*, 2006; Ward *et al.*, 2006). Mostly single attribute objective functions are considered for the optimisation of batch crystallisation processes. However, in reality during the design of crystallisation processes, the desire is to achieve a CSD, which fulfils multiple objectives such as large mean size, small coefficient of variation, high yield and smaller batch times (Sarkar *et al.*, 2006). This chapter presents studies aimed at obtaining optimal temperature trajectories to produce the desired shape of a crystal size distribution at the completion of a batch. The optimal temperatures trajectories have been achieved by including different kinetic mechanisms for crystallisation processes including growth, nucleation and dissolution. For the optimisation, kinetic parameters have already been identified and were presented in Chapter 5. The dynamic optimisation to obtain the temperature profiles that maintain the supersaturation at optimum levels are discussed for a batch cooling crystalliser for which the PBE is solved using the combined quadrature method of moments and method of characteristics (QMOM-MOCH) approach presented in Chapter 4.

6.2 Model based dynamic optimisation of temperature trajectories using the combined QMOM-MOCH approach

The combined QMOM-MOCH approach described in Chapter 4 was used to solve the population balance model (PBM) in a model-based dynamic optimisation scheme. The aim was to determine the optimal temperature trajectories, which yield desired target CSDs at the end of the batch. The final CSD is dependent on the supersaturation profile created over the batch time and hence the cooling trajectory is of critical importance. During optimisation, both the temperature trajectory and the batch time were optimised. The batch time horizon $[0, t_f]$ was divided into N_b equally spaced time intervals of duration Δt (stages), with discrete time steps $t_k = j\Delta t$, $j = 0,1,\ldots,N_b$ for the solution of the dynamic optimisation problem. The temperature trajectory is approximated by a piece-wise linear function determined by the fixed initial temperature at $t = 0$, $T(0)$ and the slopes $\alpha_T(j)$ in each discretised period Δt. Since the batch time is also optimised, the duration of the time interval Δt is changing during the optimisation, but the number of discretisations N_b is fixed. This formulation allows easy incorporation of the temperature rate constraints as bounds on the decision variables $\alpha_T(j)$, which are important to obtain a practically implementable temperature trajectory. The optimisation problem is formulated as follows:

$$\min_{\alpha_T(j),\, t_f} \sum_{k=1}^{K} \sum_{l=1}^{N_d} (f_{v,k}(L_l) - f_{v,k}^{\text{target}}(L_l))^2 \tag{6.1}$$

subject to:

$$\alpha_{T,\min} \le \alpha_T(j) \le \alpha_{T,\max}, \quad j = 0,1,\ldots,N_b \tag{6.2}$$

$$0 \le t_f \le t_{f,\max} \tag{6.3}$$

$$C(t_f) \le C_{f,\max} \tag{6.4}$$

where $\alpha_T(j)$ are the elements of the vector containing the slopes (dT/dt) for the temperature trajectories depending on the implementable heating and cooling capacity of the

system, t_j is the total batch time, $C(t_f)$ is the solute concentration at the end of the batch, $C_{f,\max}$ is the maximum acceptable concentration at the end of the batch to achieve the required yield, $f_{v,k}$ and $f_{v,k}^{\text{target}}$ are the values of the simulated and the target volume probability distribution functions at the discrete time steps $k = 1,\ldots,K$, where measurement data was available corresponding to the discretised sizes L_l, $l = 1,\ldots,N_d$ with N_d being the number of experimental size bins. The optimisation problem is solved using a sequential quadratic programming (SQP) approach implemented using the MATLAB function *fmincon.* The kinetic parameters were presented in Tables 5.2 and 5.6.

6.3 Simulation results

6.3.1 Optimal temperature trajectory using size-dependent growth and secondary nucleation

Temperature profiles have been optimised for three fictitious target distributions and are described in the following sections.

Case I: Bimodal distribution with pronounced secondary nucleation.

The target bimodal distribution used for the simulations is expressed as:

$$f_{n,\text{bimodal}}^{\text{target}} = 0.98\frac{1}{\sqrt{2\pi}2.35}e^{-(L-55)^2/(2.35^2)} + 0.02\frac{1}{\sqrt{2\pi}2.50}e^{-(L-360)^2/(2.50^2)} \tag{6.5}$$

For these simulations the number of discretisations was $N_b = 50$ and $C(t_f) = 0.4C_{f,\max}\ (kg/kg\ slurry)$. The bounds on the cooling rate were $-0.5\ ^\circ C/\min \le \alpha \le 0$. The value of Δt was calculated as $\Delta t = (t_f - t_0)/N_b$. The seed and target distributions are shown in Figure 6.1 (at $t = 0$). Figure 6.1 shows the dynamic evolution of the CSD, and Figure 6.2 shows the optimal temperature profile, concentration and supersaturation profiles, throughout the batch, for the distribution shaping optimal control.

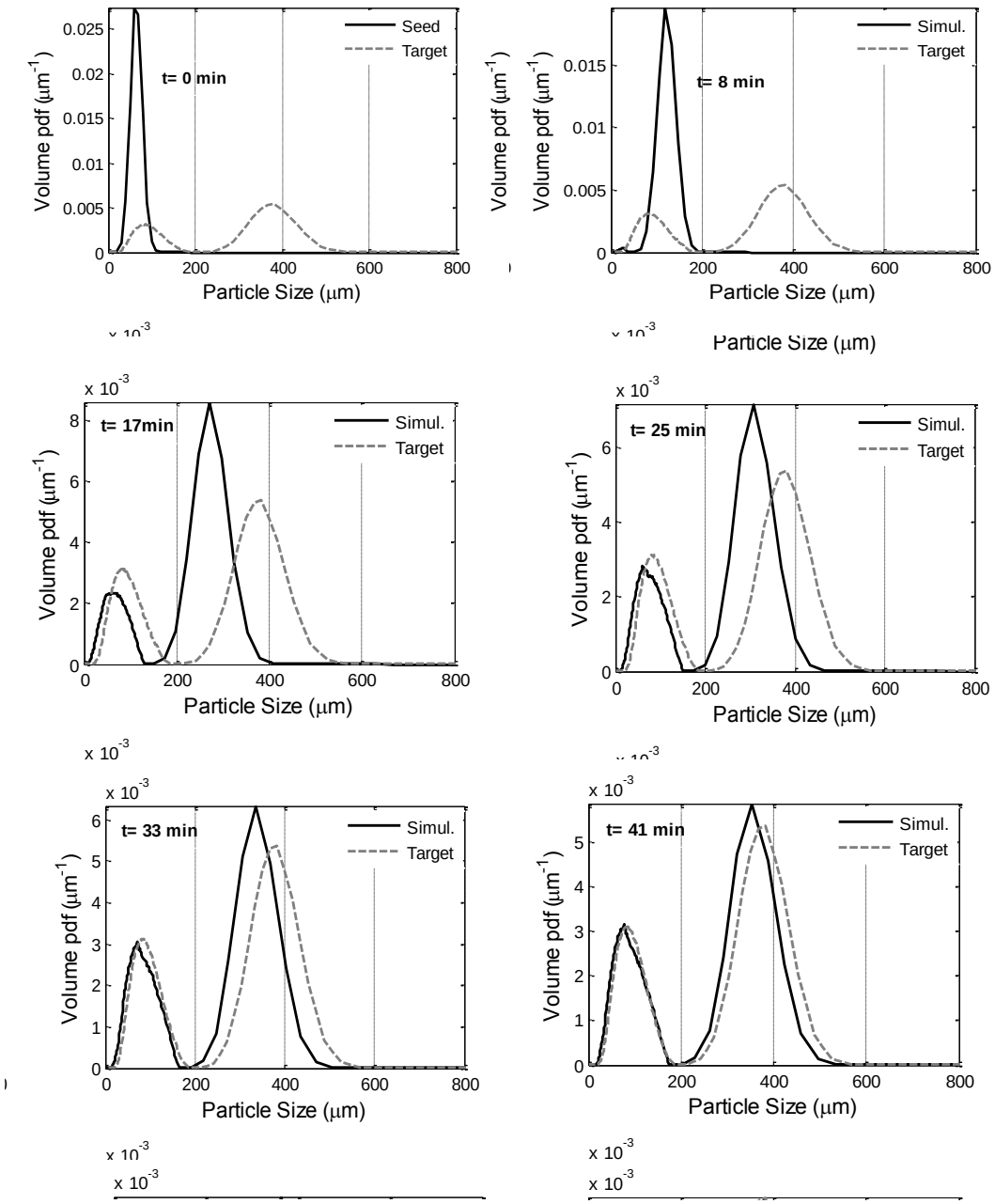

Figure 6.1: Simulated dynamic evolution of CSD with optimal temperature profile throughout the batch.

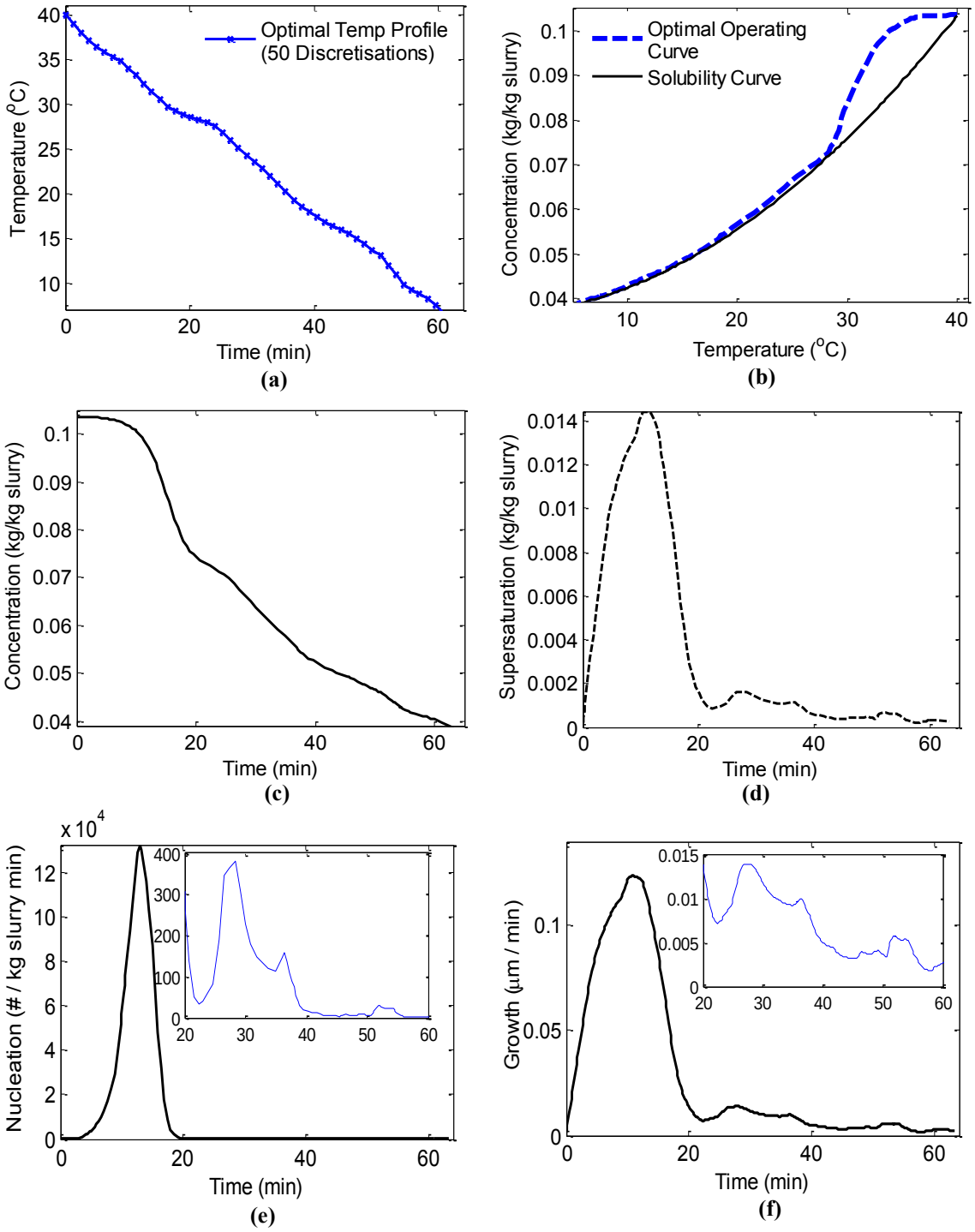

Figure 6.2: Optimal control results of the simulations for bimodal target distribution with pronounced secondary peak: (a) Optimised temperature profile with 50 discretisation points, (b) phase diagram showing solubility and optimal operating curve, (c) concentration profile during the batch, (d) supersaturation $(C - C_{sat})$ profile (*kg/kg slurry*) during the batch, (e) nucleation rate profile during the batch and (f) growth rate profile during the batch.

A mono-modal seed was selected for simulation. Based on a measurement of the seed sizes used in the experiments (Chapter 5) the CSD was represented by a Gaussian distribution with a mean of 54 μm and a standard deviation of 15 μm. Figure 6.1 shows the dynamic evolution of the CSD towards the target bimodal distribution, when the optimal temperature trajectory shown in Figure 6.2 (a) was implemented in the simulation. The final CSD is in good agreement with the target distribution (sum square error between target and simulated distribution was 0.00024). The initial 10-15 min of the batch is mainly devoted to the growth of the seed crystals, which approach rapidly the larger size mode of the target distribution. This was due to the high driving force in this period (i.e. large supersaturation), as can be seen in Figure 6.2 (b) and (d). The supersaturation achieves its peak value at about 10 min as shown in Figure 6.2 (d) yielding the appearance of a second mode because of secondary nucleation, which develops clearly by $t = 17$ min.

The optimal temperature profile, as shown in Figure 6.2 (a), was obtained using 50 discretisation points in the optimisation. The selection of the number of discretisations is a trade-off between computational time and accuracy. The improvement in SSE from 30 to 50 discretisation points was just 0.03%. No significant improvement in the objective function was achieved when the discretisation was increased from 30 to 50 intervals, as shown in Figure 6.3 and hence the finer discretisation was not considered necessary. The target CSD can be achieved within the temperature range of 40°C to 5°C during a batch period of approximately 1 h with the desired yield being larger than 60%, as shown in Figure 6.2 (c).

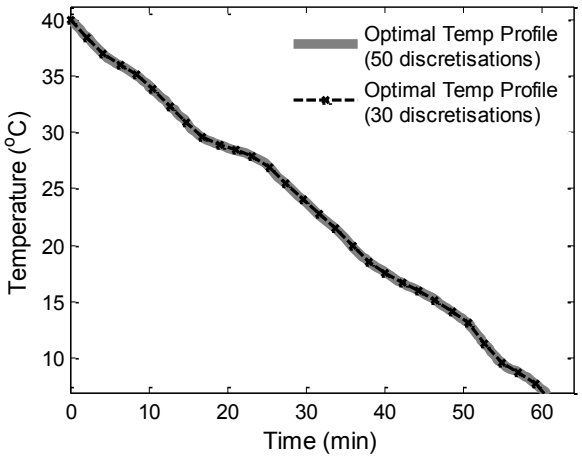

Figure 6.3: Optimal temperature profiles for bimodal target distribution with pronounced secondary with 30 and 50 discretisation points.

The temperature profile shows several distinguishing slope changes, which correspond to the secondary nucleation events generated to achieve the desired shape of the target distribution. After the initial peak at around 10 minutes, the supersaturation rises again between 27-36 minutes and subsequently towards the end of the batch between 50-55 minutes, as can be seen in Figure 6.2 (d). These increases in the supersaturation lead to additional nucleation events and growth required to achieve the target distribution, as shown in Figure 6.2 (e) and (f).

Figure 6.1 shows that the first mode of the bimodal target distribution is skewed, requiring the subsequent nucleation events to improve the shape of the obtained CSD. The third region of the increased supersaturation has significantly smaller values and is mainly to facilitate growth of the larger particles to obtain a better fit to the second mode of the target CSD. Figure 6.1 shows no significant change in the first mode of the CSD after $t = 41$ min, indicating mainly the growth of the second mode. The previous target CSD showed a pronounced secondary peak to illustrate the ability of the approach to achieve a bimodal distribution.

Case II: Bimodal distribution with suppressed secondary nucleation

In industrial scenarios, a major emphasis is to suppress the nucleation and minimise the formation of small particles during the crystallisation process. Therefore, the temperature profile was optimised for another fictitious target CSD distribution (selected based on experimental data to guarantee achievability of the target), with a significantly smaller fraction of fine particles:

$$f_{n,\text{bimodal}}^{\text{target}} = 0.91\frac{1}{\sqrt{2\pi}2.35}e^{-(L-55)^2/(2.35^2)} + 0.09\frac{1}{\sqrt{2\pi}2.60}e^{-(L-380)^2/(2.60^2)} \quad (6.6)$$

For these simulations the number of discretisations (N_b) was 30 and $C(t_f) = 0.4C_{f,\max}$ $(kg/kg\ slurry)$, and same bounds were used on α as in case I. The seed and target distributions are shown in Figure 6.4 (at $t = 0$). Figure 6.4 represents the dynamic evolution of the CSD, and Figure 6.5 shows the optimal temperature profile, concentration and supersaturation profiles, throughout the batch, for the distribution shaping optimal control, for the bimodal target distribution with suppressed secondary nucleation.

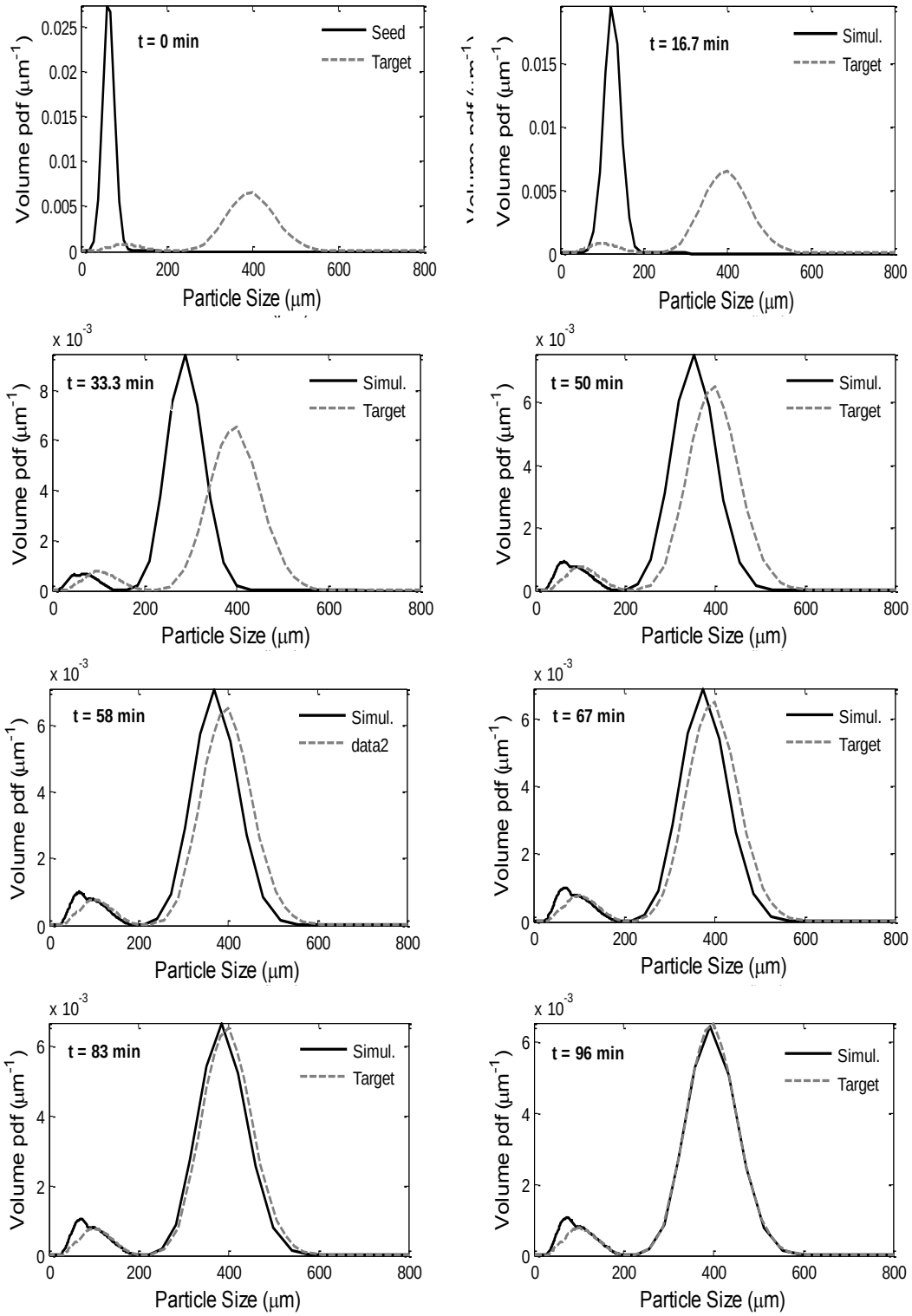

Figure 6.4: Simulated dynamic evolution of CSD with optimal temperature profile throughout the batch.

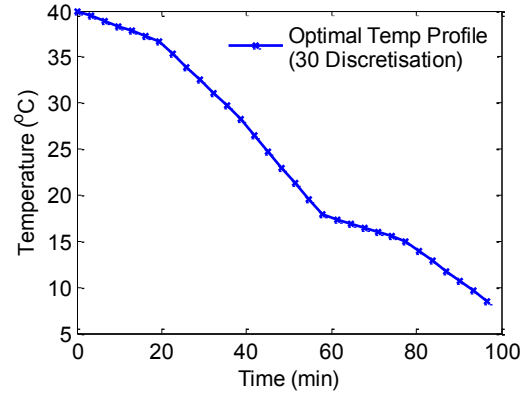

(a)

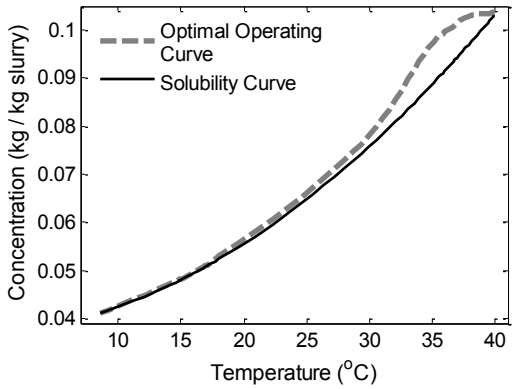

(b)

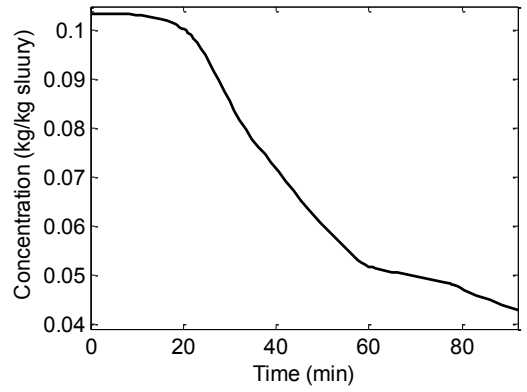

(c)

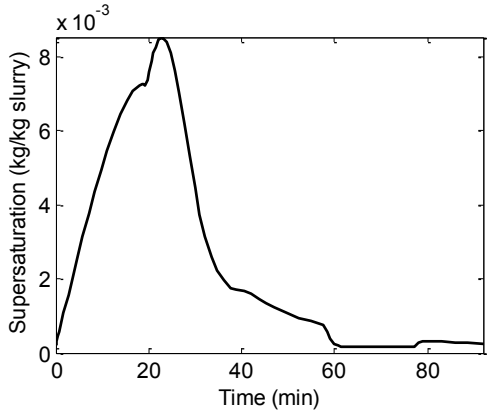

(d)

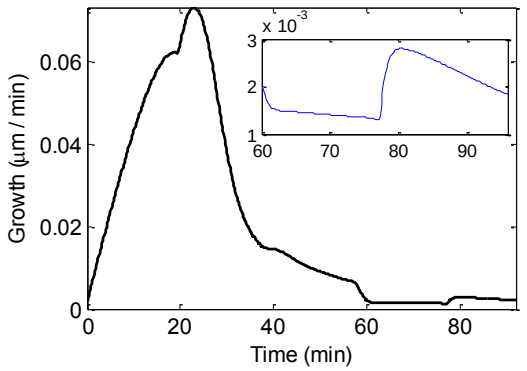

(e)

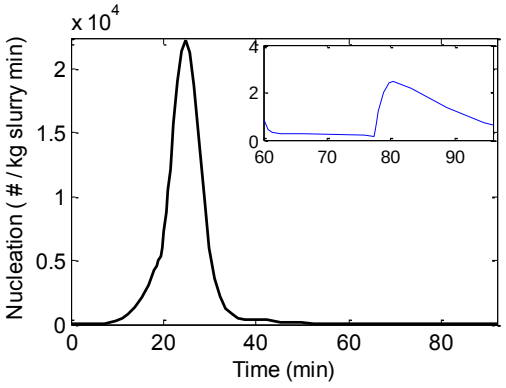

(f)

Figure 6.5: Optimal control results of the simulations for bimodal target distribution with less pronounced secondary peak: (a) optimised temperature profile with 30 discretisation points, (b) phase diagram showing solubility and optimal operating curve, (c) concentration profile during the batch, (d) supersaturation $(C - C_{sat})$ profile (*kg/kg slurry*) during the batch, (e) nucleation rate profile during the batch and (f) growth rate profile during the batch.

Figure 6.4 shows that the CSD predicted by the model is very close to the target distribution. The slight deviation of the first peak from the target distribution indicates that it is not possible to achieve any arbitrary target distribution by simply designing the cooling profile. There are limitations on the attainable CSD shapes given by particular nucleation and growth kinetics as well as the shape of the seed distribution. The optimised temperature profile ranges from 40°C to 7°C, as shown in Figure 6.5 (a). It can be observed in Figure 6.5 (a) that during the first 20 minutes, the cooling rate is slower than the rest of the profile, and mainly devoted to the growth of the crystals. During 20-57 minutes the rate of cooling is higher than the initial 20 minutes, during this time there is a higher supersaturation (driving force), as can be seen in Figure 6.5 (d). The supersaturation achieves its peak value at about 22 minutes as shown in Figure 6.5 (d) yielding the appearance of a second mode because of secondary nucleation, which develops clearly by $t = 33.3$ minutes. During 57-77 minutes of the batch the cooling rate reduces again for another 20 minutes, however the supersaturation level during this period is still relatively high leading to additional nucleation events and growth required to achieve the target distribution. During this period the growth of the crystals was the dominating phenomenon, as shown in Figure 6.5 (e). During the last 19 minutes of the batch the cooling rate increases again. Figure 6.5 (d) shows that at 77 minutes, a slight increase in the supersaturation is observed. This slight increase in supersaturation level is used to complete the growth of the particles to the required size and to achieve the required yield of at least 60%, as shown in Figure 6.5 (c).

The initial 20-30 minutes of the batch are devoted mainly to the growth of the seed crystals because of the high driving force in this period i.e. large supersaturation, as can be seen in Figure 6.5 (b) and (d).

The distinguishing slope change in the temperature profile at 78 minutes corresponds to secondary nucleation, which was generated to achieve the desired shape of the target distribution. After the initial peak in supersaturation at around 22 minutes, the supersaturation raises again at 78 minutes, as shown in Figure 6.5 (d). These increases in the supersaturation lead to additional nucleation and growth, required to achieve the target distribution, as shown in Figure 6.5 (e) and (f).

The batch time for this case has increased with 34% compared to the bimodal distribution (case I) with a more pronounced nucleation peak. In the previous case the total batch time

was 63 minutes whereas for case II the total batch time was approximately 96 min. The number of discretisations used in this case was also 30, as it was described in case I that 30 discretisation was enough to achieve a smooth, practically implementable, temperature trajectory.

Case lll: Mono-modal distribution without any nucleation

After using bimodal distributions as target CSDs, the temperature trajectory was optimised to achieve a fictitious mono-modal distribution, with the aim to try to eliminate completely the effect of secondary nucleation. The target mono-modal distribution can be expressed as:

$$f_{n,\text{mono-modal}}^{\text{target}} = \frac{1}{\sqrt{2\pi}\,2.50} e^{-(L-378)^2/(2.50^2)} \tag{6.7}$$

The same mono-modal seed was used, as in the previous two cases, i.e. a Gaussian distribution with a mean of 54 μm and a standard deviation of 15 μm. Figure 6.6 shows a comparison of the target and the simulated CSD at the end of the batch when the optimal temperature profile was implemented. The simulated CSD is still bimodal despite the target being a mono-modal distribution. The optimal CSD captures the large peak very well, however the optimal operating trajectory, which is constrained in this case to be within the metastable zone $(\alpha \leq 0)$ is unable to avoid the development of the secondary peak due to secondary nucleation.

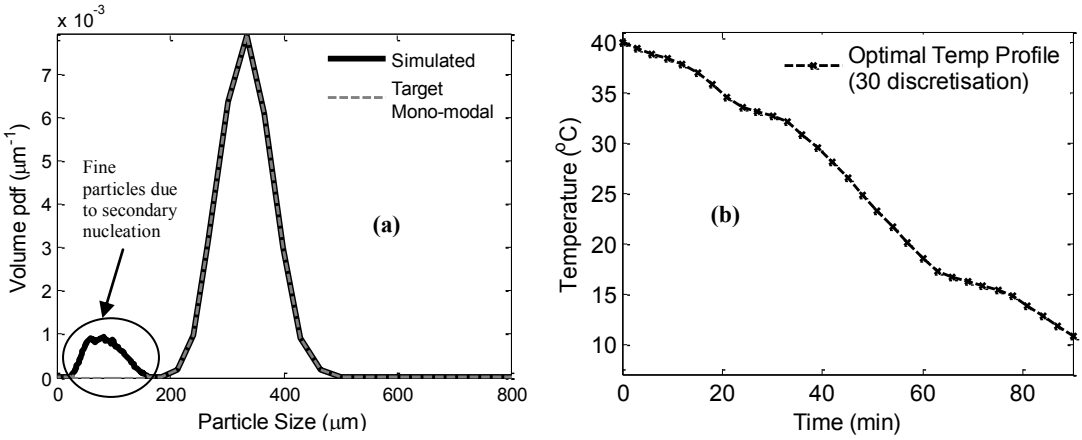

Figure 6.6: a) Comparison of simulated and target mono-modal CSD (b) optimal temperature profile with 30 discretisation points.

The temperature trajectory was designed using growth and secondary nucleation. Both mechanisms occur in the supersaturated solution within the metastable zone. The secondary

nucleation produces fines even when the supersaturation is not very large. This is in correlation with findings by other researchers (Doki *et al.*, 2004) who showed that in the case of particular seed loading in many cases it is practically impossible to avoid the formation of bimodal CSD, due to secondary nucleation. The only way to remove the fine crystals is to cross the solubility curve (C_{sat}) into the under-saturated region, where eventually the fine crystals should preferentially dissolve leading to a mono-modal CSD of large sized crystals. Thus to obtain the desired mono-modal target distribution, an optimal temperature profile can be designed, while using both supersaturated and under-saturated regions.

6.3.2 Designing mono-modal target distribution using size-dependent growth, nucleation and size-dependent dissolution mechanisms

The temperature profile was optimised for the same mono-modal target distribution described in Section 6.3.1 (case III). The under-saturated region and supersaturated region both were used to design the optimal temperature profile, by allowing increase in the temperature $(-0.5\ ^{\circ}C/\min \ \leq \ \alpha \ \leq \ 0.5\ ^{\circ}C/\min)$ and using the model that incorporates growth, nucleation and dissolution mechanisms. The model was solved using the combined QMOM-MOCH technique. The kinetic parameters used are identified in Chapter 5 and are presented in Tables 5.2 and 5.6. Figure 6.7 shows the main results of the optimisation considering growth, nucleation and dissolution mechanisms. The target distribution is very well achieved with no secondary peak (see Figure 6.7 (a)) which was impossible to eliminate while operating within the metastable zone (MSZ) only.

The resulting batch time in this case, was 100 minutes which is more than in both previous cases (bimodal distributions), i.e 37% more than in case I and 4% greater than in case II. It can be observed in Figure 6.7 (b) that the temperature trajectory can be divided in three phases. During the first phase of 40 minutes of the batch, the temperature decreased from 40 to 28°C. In the second phase, the temperature increased from 28 to 32°C from 40 to 74 minutes. In the last phase, the temperature decreased again from 32 to 17°C for the remaining 26 minutes of the batch.

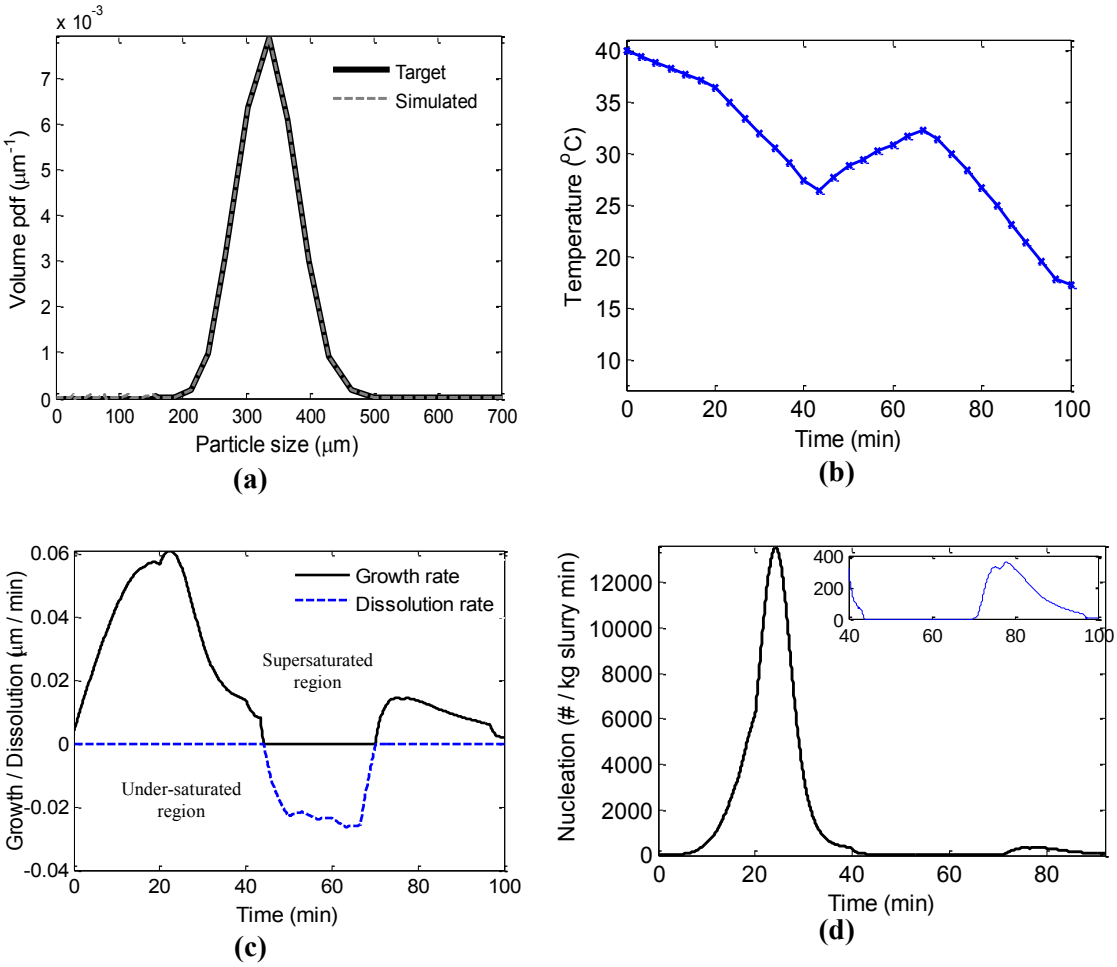

Figure 6.7: a) Comparison of simulated and target mono-modal distribution, b) optimal temperature profile c) growth and dissolution rates and d) nucleation rate profile within the supersaturated and under-saturated region for the mono-modal target distribution, considering dissolution along with growth and nucleation.

The supersaturation profile corresponding to the optimal temperature trajectory is shown in Figure 6.8. The complete dynamic evolution of the CSD is shown in Figure 6.10 and the phase diagram showing the solubility curve along with the optimal temperature trajectory is presented in Figure 6.9. In the latter a dissolution loop can be clearly seen which indicates the initial cooling, followed by a heating stage and then cooling of the system again. When the temperature is decreased from 40 to 28°C the solution was supersaturated.

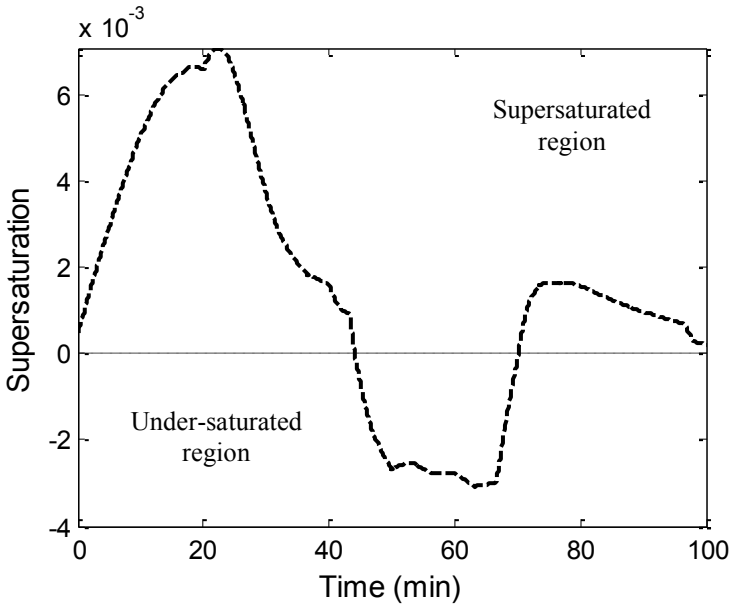

Figure 6.8: Supersaturation and under-saturation profile for mono-modal target distribution.

During this time the supersaturation reached its maximum value at around 22 minutes and then decreased to zero within the next 18 minutes. During this process, the seed has grown, and the apparition of a smaller peak is also observed due to secondary nucleation, as shown in Figure 6.10 at $t = 32$ and $t = 39$ minutes. In the next phase, the temperature was increased from 28°C to 32°C and the system entered the under-saturated region as shown in Figure 6.8.

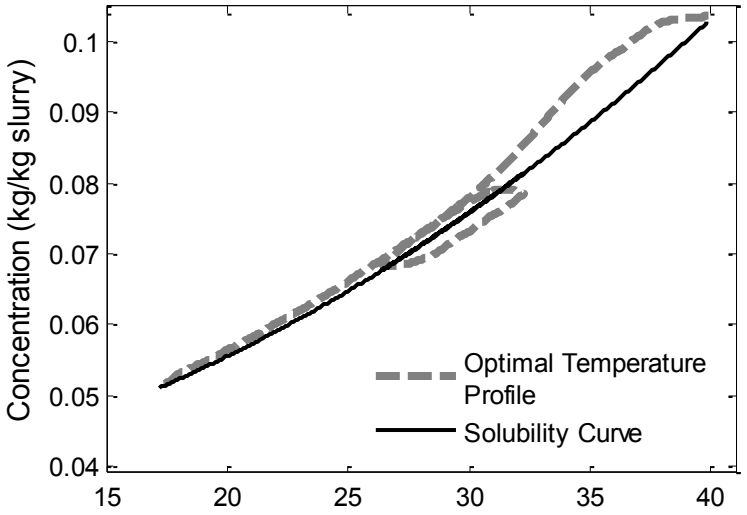

Figure 6.9: Phase diagram showing solubility curve and optimal operating profile with the dissolution loop for mono-modal target distribution.

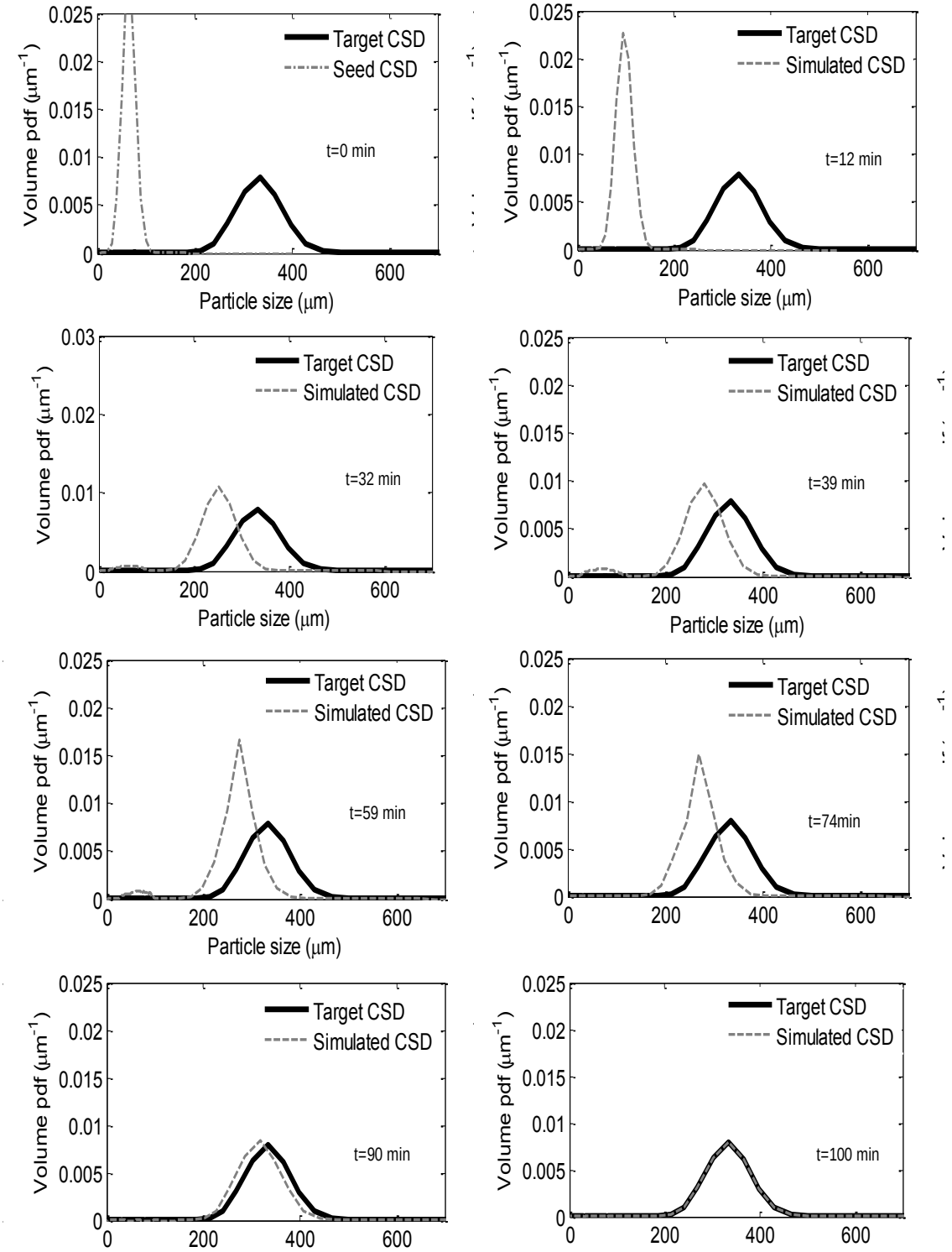

Figure 6.10: Dynamic evolution of CSD using size-dependent growth, secondary nucleation and size-dependent dissolution kinetics for potash alum-water system.

When the temperature is increased, the smaller particles dissolve and the size of the larger particles decrease. The dissolution of particles during this heating phase leads to the

formation of the dissolution loop, shown in Figure 6.9. It can be seen in Figure 6.10 that between $t = 59$ and $t = 74$ minutes, the small peak in the distribution has disappeared and the distribution has become narrower. During this period the supersaturation started increasing and the system re-entered the super-saturated region from the under-saturated region, as shown in Figure 6.8. During the last 26 minutes the temperature decreased from 32 to 17°C within the supersaturated region. The crystals grow in size due to the available super-saturation and due to the size dependent growth the CSD broadened, as shown in Figure 6.10 at $t = 90$ and $t = 100$ minutes. Some secondary nucleation was also observed during the last 26 minutes, but it was not very significant. This secondary nucleation can also be observed in Figure 6.11 (b).

Figure 6.11 (a) shows the characteristic lines (L), which correspond to the combined phenomena of growth, nucleation and dissolution. The characteristic lines correspond to the size-dependent growth in the first 40 minutes, which is indicated by the broadening of these lines. Then these lines started narrowing down as dissolution took place and in the last phase the lines started broadening again to fit the final shape of the distribution. In Figure 6.11 (b) some nucleation can be observed between 74 to 90 minutes which shows that some fine particles were produced due to secondary nucleation, also shown in Figure 6.7 (d). However, secondary nucleation was not significant and hence no fines peak is shown in the final CSD of Figure 6.7 (a).

The described case study shows that by operating both within the metastable zone and in the under-saturated region, it is possible to obtain mono-modal CSD. Using both phases to design an optimal profile provides the possibility to dissolve the fine particles produced by secondary nucleation. The simulation results show that a mono-modal target CSD is difficult to achieve, while just operating within the metastable zone and considering only growth and nucleation mechanisms. Operating within and outside the metastable zone gives more flexibility to design an operating profile to achieve a target CSD using the kinetic rate laws for growth/dissolution and nucleation mechanisms, identified for the system.

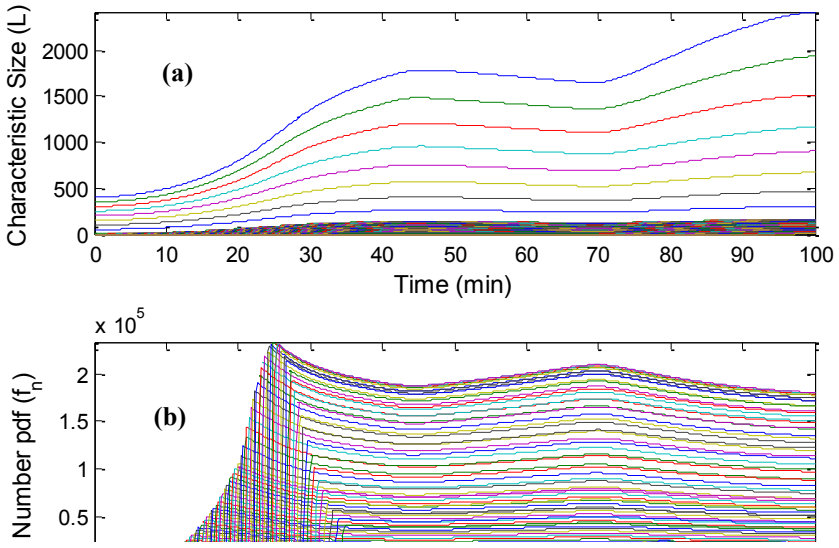

Figure 6.11: Evolution of characteristic lines (a) and number distribution function (b) for the simulated mono-modal target distribution.

6.4 Conclusions

The combined QMOM-MOCH technique was used to solve the PBE in dynamic optimisations formulated to obtain cooling temperature trajectories, which maintain the supersaturation at an optimum level for a batch cooling crystalliser and were used to obtain a variety of desired target CSDs. The final CSD is dependent on the supersaturation profile created over the batch time and therefore, cooling trajectories play a vital role in shaping of final CSD. In the optimisations, both the temperature trajectory and the batch time were optimised. The case studies used both the supersaturated and the under-saturated regions to design the optimal temperature profiles.

Three case-studies were used to obtain optimal temperature trajectories for designing different target CSDs. First, the technique was used to achieve the optimal temperature profile for a fictitious bi-modal target distribution with a pronounced secondary peak. With the resulting optimal temperature trajectory the bimodal target distribution was achievable. However, in industrial scenarios, generally the major emphasis is to suppress nucleation and minimise the formation of small particles during the crystallisation process. Therefore the temperature profile was optimised for another fictitious target distribution, with a

significantly smaller fraction of fine particles. With the implemented optimal temperature trajectory, the target distribution was achievable however with a slight discrepancy in the fine peak compared to the target. These results indicate that it is not always possible to achieve an arbitrary target distribution simply by designing the cooling profile. There are limitations on the potentially attainable CSD shapes given by the particular nucleation and growth kinetics, as well as the shape of the seed distribution.

Lastly, the temperature profile was optimised for a mono-modal target distribution. When the temperature profile was optimised within the metastable limit (allowing growth and secondary nucleation), it was not possible to achieve the desired target CSD. Therefore, to obtain the mono-modal target distribution both the supersaturated and the under-saturated regions were used in the design of the temperature trajectory, making use of the dissolution mechanism to remove the fine crystals.

The simulation results presented in the chapter provide an illustrative case study for using model-based design of controlled dissolution to achieve a target distribution, which cannot be obtained operating within the metastable zone only.

Chapter 7
A systematic framework for CSD control of supersaturation controlled crystallisation processes, using direct design, seed recipe optimisation and dynamic seeding

7.1 Introduction

The first part of this chapter presents a novel methodology for the systematic design of the setpoint operating curves for supersaturation controlled seeded crystallisation processes, which produce a desired target crystal size distribution (CSD). The population balance model is solved using the method of characteristics under the assumptions of constant supersaturation and a growth dominated process, yielding a simplified analytical expression for the evolving size distribution. A design parameter for supersaturation controlled processes is introduced as a function of the supersaturation, time and growth kinetics. Based on the design parameter and the simplified analytical model, the supersaturation setpoint and batch time are determined using an optimisation approach to obtain a target distribution with a desired shape. The methodology can be used to obtain the temperature profiles in the time domain, corresponding to a desired target CSD, providing a systematic direct design approach for practical applications and scale-up.

In the second part of the chapter, two methods are proposed that use seed design in conjunction with supersaturation setpoint control, for shaping the product CSD. The first approach designs a seed recipe as a mixture of crystals resulting, for example, from a standard sieve analysis. In this approach all of the seed is introduced at the beginning of the batch. The second approach proposes a dynamic seed addition profile, which allows an easily implementable methodology to achieve complex target CSDs using seed with mono-modal CSD, as a process actuator to control the desired final CSD. The proposed methods are exemplified for the model system of potash alum in water, for which the apparent size dependent growth kinetic parameters have been identified in Chapter 5.

7.2 Comparison of different approaches for designing the operating curves

Several approaches have been proposed for designing the operating curves for crystallisation systems. Generally speaking, two main categories can be distinguished (Nagy *et al.*, 2008a), which are schematically depicted in Figure 7.1. The model-based design approach involves development of a detailed model, which is used with optimisation techniques to determine temperature versus time or anti-solvent addition rate versus time trajectories (Nowee *et al.*, 2008a, b; Woo *et al.*, 2006), as shown in Figure 7.1. Advantages of the model-based approach include its ability to obtain a theoretically optimal recipe, requiring a much smaller number of experiments, than for statistical experimental design of batches, increased process understanding, and the possibility of incorporating the effects of non-ideal mixing via computational fluid dynamics (Ward *et al.*, 2006).

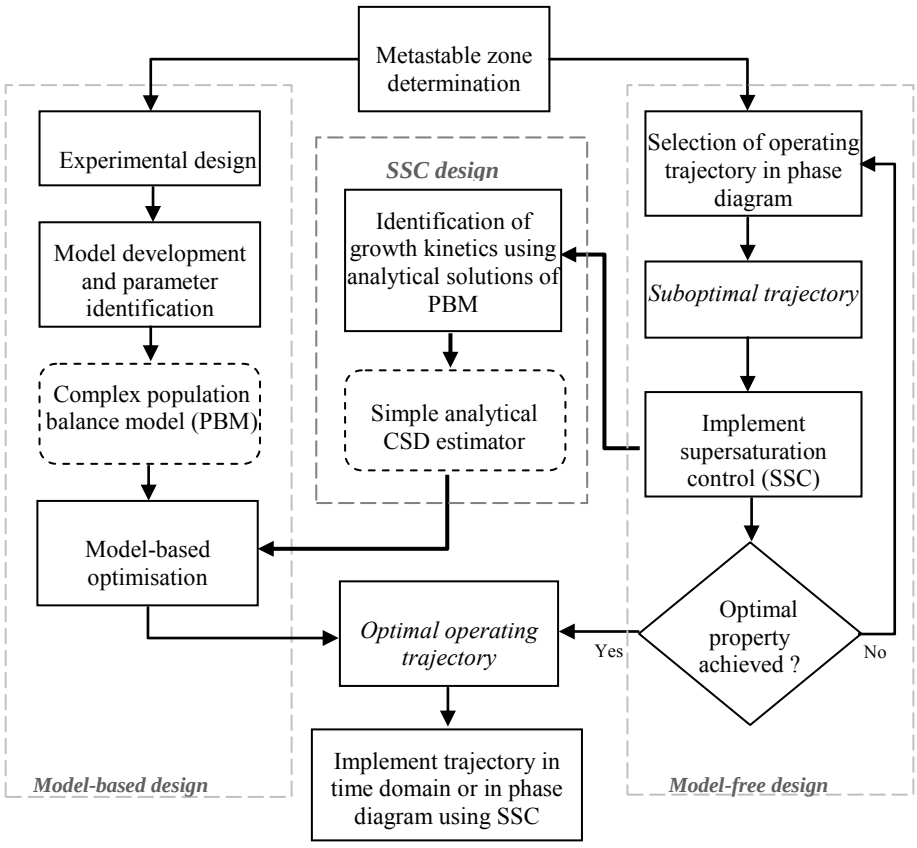

Figure 7.1: Schematic representation of the model-based, model-free and supersaturation control (SSC) design approaches for crystallisation systems.

Disadvantages associated with the model-based approach are mainly related to the difficulty in modelling practical objectives (e.g., filterability, purity, tablet stability, etc.), and the significant time and engineering effort required for the model development. Additionally, the performance of the model-based approach depends on the model accuracy; however the robustness of the approach can be improved by formulating the robust counterpart of the optimisation problem (Hermanto *et al.*, 2007; Nagy and Braatz, 2004).

An alternative way to enhance the control of the CSD is to use supersaturation control (SSC) (Gron *et al.*, 2003; Zhou *et al.*, 2006a) or direct nucleation control (Hojjati and Rohani, 2005; Woo *et al.*, 2009a), which are methodologies that drive the crystallisation process within the metastable zone to avoid nucleation or produce controlled nucleation/dissolution events. Although these approaches have proven to produce high quality crystals, the setpoint operating profiles for the supersaturation controller are usually chosen arbitrarily or by trial-and-error experimentation. Although a complex model-based design of supersaturation controlled processes has been applied recently (Nagy, 2009), until now there have been no systematic procedures reported for the design of supersaturation controlled processes. These designs could exploit the fact that the underlying process is controlled at a constant supersaturation and/or could combine setpoint design with seed recipe optimisation. The proposed framework provides for the first time a link between the model-based and model-free design approaches, as shown in Figure 7.1, using simplified analytical expressions for the estimation of the CSD. In the case of seeded batch cooling crystallisation processes controlled at constant supersaturation, the main governing phenomenon is growth. For these systems an analytical solution of the population balance equation can be obtained, which gives the entire CSD at any moment of the batch. A design parameter, as a function of the batch time and supersaturation, is introduced for supersaturation controlled crystallisation processes. The optimal design parameter is obtained by solving a constrained nonlinear optimization problem with the objective to achieve a desired shape of the CSD at the end of the batch, while maintaining a required minimum yield. The supersaturation setpoint and batch time required to achieve the desired CSD can be obtained from the optimal design parameter, taking into account the boundaries of the metastable zone, with additional uncertainty margins for robust operating profiles. A methodology to derive the temperature versus time profiles from the optimal design parameter is also illustrated, which can be

readily implemented in the case of industrial crystallizers based on classical temperature control systems, using the direct design concept.

7.3 Direct Design Approach

The traditional way of controlling a seeded cooling-crystallisation processes is to follow a predetermined temperature profile in time. Recent developments in the direct design of crystallisation processes have lead to more widespread application of supersaturation control. The direct design approach is based on the idea of operating the system within the metastable zone (as shown in Figure 7.2) bounded by the nucleation and the solubility curves. The nucleation and solubility curves can be predetermined in automated experiments (Barrett and Glennon, 2002; Fujiwara *et al.*, 2002). Operation close to metastable limit (high supersaturation) results in excessive nucleation, increased agglomeration, lower purity and longer filtration times. Operation close to solubility curve (low supersaturation) leads to slow growth and long batch times (Fujiwara *et al.*, 2005).

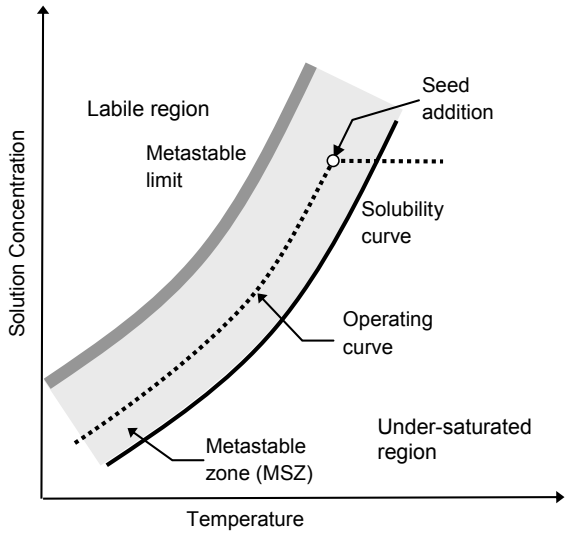

Figure 7.2: Operation of seeded batch cooling crystallisation.

The setpoint supersaturation curve is the result of a compromise between fast crystal growth and a low nucleation rate. Therefore, in this technique a supersaturation setpoint curve is chosen experimentally and it is followed in the phase diagram using a supersaturation feedback controller based on concentration measurement. It is important to control the extent of the supersaturation during crystallisation since the size, shape and solid-state properties of

the product crystals are dependent on the supersaturation. In seeded crystallisation, the supersaturation is usually maintained at the desired constant value throughout the entire batch by application of properly designed control algorithms (Fujiwara *et al.*, 2005; Zhou *et al.*, 2006a). Since direct supersaturation measurement sensors often have limited availability for industrial scale use, the supersaturation profiles can be redefined in terms of the temperature profiles in time, which are developed to maintain the supersaturation at a certain setpoint. In this case supersaturation control using expensive and generally complex concentration measurement hardware and software can be implemented only once, based on the knowledge of the metastable zone. The supersaturation controller will automatically generate a temperature versus time profile (or solvent/anti-solvent addition rate versus time profile for anti-solvent crystallisation, or heat input versus time profile for evaporative crystallisation) by trying to keep the supersaturation at the desired constant value. In subsequent operations the resulting temperature versus time profile can be used without the need of concentration control. This will provide an open loop control strategy that leads to an inferential constant supersaturation control, according to the direct design concept. Since these technologies are becoming increasingly accepted in the pharmaceutical industries, it is important to have a systematic methodology for designing the supersaturation and corresponding temperature trajectories to obtain products with the desired CSD.

7.4 Population Balance Modelling of Supersaturation Controlled, Growth Dominated Batch Crystallisation Processes

Considering a single growth direction with one characteristic length L, and a well-mixed crystalliser with supersaturation control and growth as the only dominating phenomena, the population balance equation (PBE) given in equation (4.1) can be re-written as:

$$\frac{\partial f_n(L,t)}{\partial t} + \frac{\partial (G(S,L;\theta_g) f_n(L,t))}{\partial L} = 0, \tag{7.1}$$

where $f_n(L,t)$ is the crystal size distribution expressed as the number density function (number of crystal per unit mass of slurry), t is time, $G(S,L;\theta_g)$ is the rate of crystal growth,

$S = (C - C_{sat})$ is the absolute supersaturation, C is the solute concentration, $C_{sat} = C_{sat}(T)$ is the saturation concentration, T the temperature, θ_g is a vector of growth kinetic parameters. The generic PBE (7.1) can be reduced to a system of ODEs by applying the method of characteristics (MOCH). When seed is added in the case of supersaturation controlled crystallisation, the process will generally be dominated by growth. For the generic case of apparent size-dependent growth, for which the kinetics is given by equation (4.8), using the initial conditions already described in Chapter 4 and applying the MOCH, reduces equation (7.1) to the following system of two ODEs:

$$\frac{dL}{dt} = k_g S^g (1 + \gamma L)^p, \tag{7.2}$$

$$\frac{df_n(L,t)}{dt} = -k_g S^g \gamma p (1 + \gamma L)^{p-1} f_n(L,t). \tag{7.3}$$

In the case of well-controlled constant supersaturation, which follows the desired set-point value, S_{sp}, the system of equations (7.2)-(7.3) can be solved analytically with the solution given by:

$$L = \frac{(((1 + \gamma L_0)^{1-p} + k_g S^g t \gamma (1-p))^{\frac{1}{1-p}} - 1)}{\gamma} \tag{7.4}$$

$$f_n(L) = f_{n,0}(L_0)\left(1 + \frac{k_g S^g t \gamma (1-p)}{(1 + \gamma L_0)^{1-p}}\right)^{\frac{p}{p-1}} \tag{7.5}$$

Discretizing the initial (seed) distribution $f_{n,0}(L_0) = f_{seed}(L_0)$ for different values of L_0, equations (7.4)-(7.5) can be used to compute the dynamic evolution of the CSD for a generic growth dominated process (the analytical solution is valid for $p \neq 1$ and $\gamma \neq 0$). Table C.1 in Appendix C summarizes the results of the analytical solutions for different growth expressions. The complete derivation of equation (7.4) and (7.5) is given in Appendix C.

7.5 Systematic Design of Supersaturation controlled Crystallisation

The CSD given by the system (7.4)-(7.5) (or alternatively using the equations shown in Table C.1 depending on growth kinetics), is determined by the product between S^g and t. Hence a design parameter (ϕ) can be defined as,

$$\phi = S^g t \,. \tag{7.6}$$

The optimal supersaturation control (SSC) design parameter (ϕ) can be determined by minimizing the difference between the discretised target distribution and the predicted CSD obtained from the analytical estimator (7.4)-(7.5);

$$\min_{\phi} \left\{ \sum_{i=1}^{N_d} (f_{v,i} - \tilde{f}_{v,i})^2 \right\}, \tag{7.7}$$

subject to:

$$0 \le \phi \le \phi_{\max} \,, \tag{7.8}$$

$$C(t_{batch}) \le C_{f,\max} \,, \tag{7.9}$$

where N_d is the number of discretisations, $\tilde{f}_{v,i}$ is the discretised target CSD (volume particle density function); $C(t_{batch})$ is the solute concentration at the end of the batch, t_{batch} is the duration of the batch, and $C_{f,\max}$ is the maximum acceptable concentration at the end of the batch to achieve a required yield. The number density function can be converted to volume particle density function using the relationship given in equation (5.6).

The MATLAB (Math Works Inc.) function *fmincon* was used to solve the constrained non-linear optimisation problem (7.7)-(7.9). Once the design parameter, ϕ ,was optimised for a desired target distribution, by using equation (7.6) it is possible to determine the supersaturation setpoint S_{sp} for a given batch time (t_{batch}), or to calculate the required batch time to achieve the desired distribution by controlling the process at a given supersaturation value. A batch processing unit may be a multi-purpose unit, which is used for several processing phases and may support multi-product manufacturing. In this case, the batch scheduling becomes of key importance due to raw material and time constraints. The control

design parameter, ϕ, gives the flexibility to adjust the supersaturation for a fixed batch time, which can be calculated as,

$$S_{sp} = \left[\phi / t_{batch}\right]^{1/g} \tag{7.10}$$

with $S_{sp} \leq S_{max}$, where S_{max} is the boundary in which the supersaturation can be operated with confidence without producing nuclei, delimiting the robust operating zone (ROZ), and is given by,

$$S_{max} = S_{MSZW} - \Delta S_{MSZW} \tag{7.11}$$

where S_{MSZW} is the metastable zone width and ΔS_{MSZW} is a safety back-off from the MSZ limit to provide robust performance, as shown in Figure 7.3. The ROZ can be determined for example by repeated MSZW experiments under various experimental conditions and scales. These experiments can be easily automated and the results can statistically estimate the potential changes in the MSZW due to scale-up.

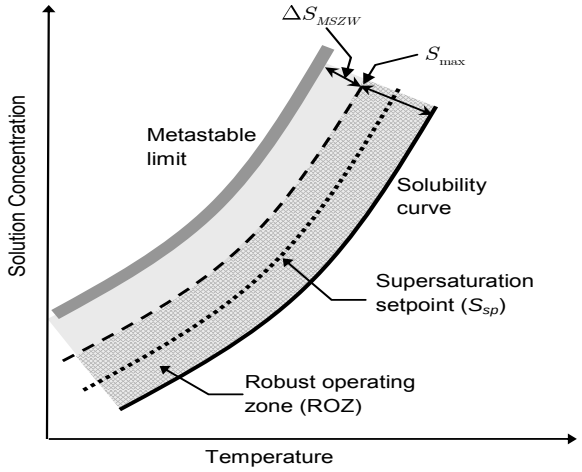

Figure 7.3: The supersaturation boundary limits and the robust operating zone (ROZ) in which the S_{sp} can be chosen with confidence that nucleation or dissolution will be avoided, even under changing process conditions (mixing, impurities, etc.).

The corresponding minimum batch time ($t_{batch,min}$) for the maximum supersaturation considering the ROZ is given by:

$$t_{batch,min} = \phi / S_{max}^{g} \tag{7.12}$$

In the cases of no scheduling limitations the batch time is the preferred design parameter to be adjusted, especially during the batch (e.g. in an on-line optimisation based control scheme) since changes in the setpoint of the supersaturation controller may lead to control problems, such as undesired oscillations or overshoot. Hence, the approach based on the supersaturation control design parameter allows tailoring the batch time in correlation with the supersaturation setpoint, according to the process requirements/limitation, while maintaining a desired target CSD, corresponding to a particular value of ϕ.

In industrial practice, it is often difficult to control supersaturation due to the unavailability of installed sensors for the measurement of concentration. However temperature control systems are readily available for all cooling crystallisation systems. The temperature trajectory in the time domain can be designed for a desired supersaturation setpoint S_{sp}, from the solubility curve and from the dynamic variation of the concentration and moments for the crystal size distribution along the batch. The solubility curve is given as a function of temperature, $C_{sat}(T)$. In the current work, a second-order polynomial was fitted to experimental data for the potash alum-water system and has already been given in equation (5.3) with coefficient values: a_0=3.63$\times 10^{-2}$, $a_1 = 2.43 \times 10^{-4}$, $a_2 = 3.58 \times 10^{-5}$. The change in concentration with time was given by equation (4.14), $C(t) = C(0) - \rho_c k_v [\mu_3(t) - \mu_3(0)]$. The moments of crystal size distribution can be obtained from:

$$\mu_k(t) = \int_0^{\infty} f_n L^k dL \approx \sum_{i=1}^{N_d} (f_{n,i} L_i^k \Delta L_i), \quad \text{where} \quad k = 0,1,2,...\infty \tag{7.13}$$

where f_n is the crystal size distribution expressed as the number density function (number of crystal per unit mass of slurry), L is the particle size in μm, ΔL is the difference between two consecutive size range and N_d is the total number of size ranges. The third moment is required to calculate the mass balance.

The temperature profile in the time domain, used as the setpoint for the temperature controller, $T_{sp} = T(t)$, can be obtained by solving the following nonlinear equation for a given concentration measurement $C(t)$,

$$S_{sp} - C(t) + a_2 T^2 + a_1 T + a_0 = 0. \tag{7.14}$$

Although equation (7.14) was derived considering a simple polynomial representation of the solubility equation the approach works for other solubility expressions, such as the generic van't Hoff type equation.

7.6 Simulation results and discussions

The apparent size-dependent growth parameters for potash alum system in water were obtained using a model-based parameter estimation, assuming a well-mixed system and growth and secondary nucleation mechanisms, with the values given in Table 5.2.

A target CSD was generated by performing a simple experiment using a cubic cooling profile. The total batch time was 90 min. Then the SSC design parameter (ϕ) was optimised in order to achieve the target experimental CSD using the same experimental seed CSD in the simulations, (seed CSD used for experiments described in Chapter 5, Section 5.5.1). The optimal ϕ was next used to obtain either the setpoint for the supersaturation controller or the batch time, using equations (7.10) and (7.12). Results are shown in Figure 7.4 (a) and (b). Since the target CSD was obtained experimentally, it represents a feasible setpoint for the system. Hence the simulated and experimental CSDs are in good agreement. Figure 7.4 (a) and (b) show the results using different pairs of supersaturation values and batch times, corresponding to a constant value of the design parameter ϕ, indicating that the same target CSD can be achieved using different batch times if the process is controlled under a supersaturation chosen according to the SSC design parameter.

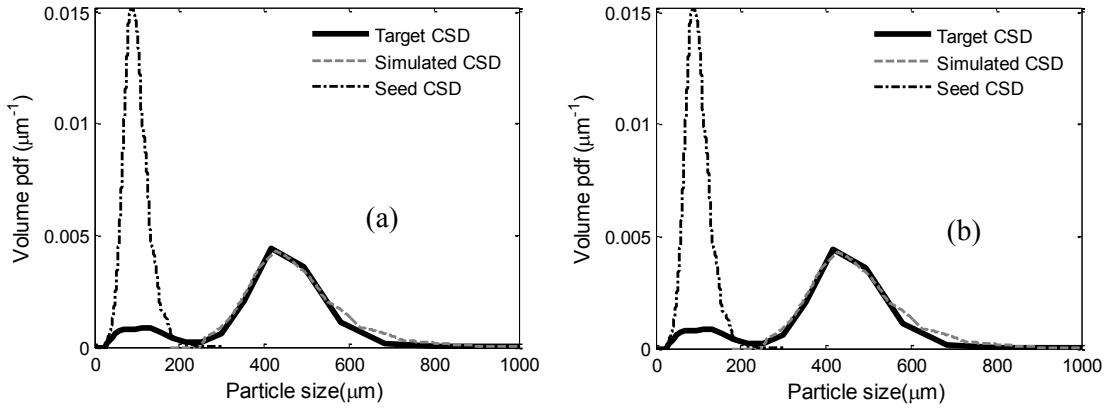

Figure 7.4: Results with the optimized design parameter $\phi = 0.206\ min$, designed to achieve the target experimental CSD; (a) fixed batch time of $t_{batch} = 80\ min$ and calculated $S_{sp} = 0.00257\ (\mathrm{kg/kg})$; (b) fixed supersaturation setpoint $S_{sp} = 0.00215\ (\mathrm{kg/kg})$ and calculated batch time $t_{batch} = 96\ min$. Both cases give the same target CSD corresponding the optimized ϕ.

The experimental target CSD is bimodal showing one of the modes at smaller sizes due to the secondary nucleation during the experiment. Since the methodology considers the growth mechanism only, the mode corresponding to the smaller crystals (newly formed nuclei) is not captured in the simulations.

The approach was also used to design crystallisation systems with arbitrary target CSDs using the same experimental seed CSD as in the previous case. A lognormal target distribution was selected with mean $L_m = 420\ \mu m$ and standard deviation $\sigma = 0.22$, however which is close to the experimental target distribution used on the previous case. Figure 7.5 (a) shows that the system with the optimised supersaturation design parameter of $\phi = 0.203\ \mathrm{min}$ is able to achieve a product CSD in good agreement with the target CSD. As expected, the optimal SSC design parameter is very similar to the previous value since the target distributions also have similar shapes. The actual shape of the CSD, which can be achieved by designing the supersaturation level and/or batch time, is limited and is determined by the seed distribution and growth kinetics of a particular system. Figure 7.5 (b) illustrates the results of the optimal design when the same experimental seed, but a narrower

target distribution (lognormal distribution) is used with the same mean $L_m = 420\ \mu m$, but a smaller standard deviation $\sigma = 0.17$.

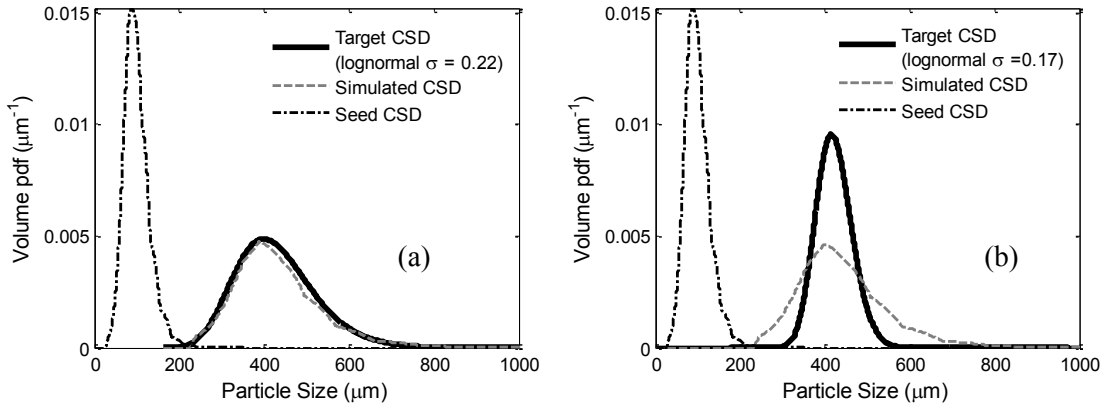

Figure 7.5: a) Results with the optimized design parameter $\phi = 0.203\ min$ obtained to achieve a target lognormal CSD with $L_m = 420\ \mu m$ and $\sigma = 0.22$. b) Results with the optimized design parameter $\phi = 0.198\ min$ obtained to achieve a target lognormal CSD with $L_m = 420\ \mu m$ and $\sigma = 0.17$.

The resulting optimal design parameter $(\phi = 0.198\ \text{min})$ provides a product with similar mean size, however the achievable width of the distribution is limited by the growth kinetics of the system. Since growth rate (G) is a monotonically increasing function of size (L), therefore the CSD has to get wider as the crystals grow. The results demonstrate that since in the case of constant supersaturation controlled processes the only degree of freedom is the SSC design parameter, ϕ; hence it is not possible to independently tailor mean size and width (standard deviation) of the product distribution. Therefore more complex control approaches are needed for higher degree of control of the shape of the product CSD (e.g. by using a variable supersaturation profile, using controlled nucleation and/or dissolution, or including seed CSD and addition time as control variables). Nevertheless the methodology presented here provides a practical framework for systematically designing the setpoint for a supersaturation controller and to produce a relatively quick and robust direct design approach for achieving a consistent product CSD.

The designed supersaturation setpoints can be transformed into temperature profiles using the model inversion approach described in Section 7.5. Figure 7.6 (a) shows the temperature profiles corresponding to a design parameter $\phi = 0.206\ \mathrm{min}$, obtained for different supersaturation setpoints and batch times in the case of the experimental target CSD. All the temperature profiles provide the same target CSD but with different batch times and supersaturations. The corresponding concentration profiles are shown in Figure 7.6 (b). The yields produced are around 61% in all cases, being close to the minimum 60% required in the optimisation.

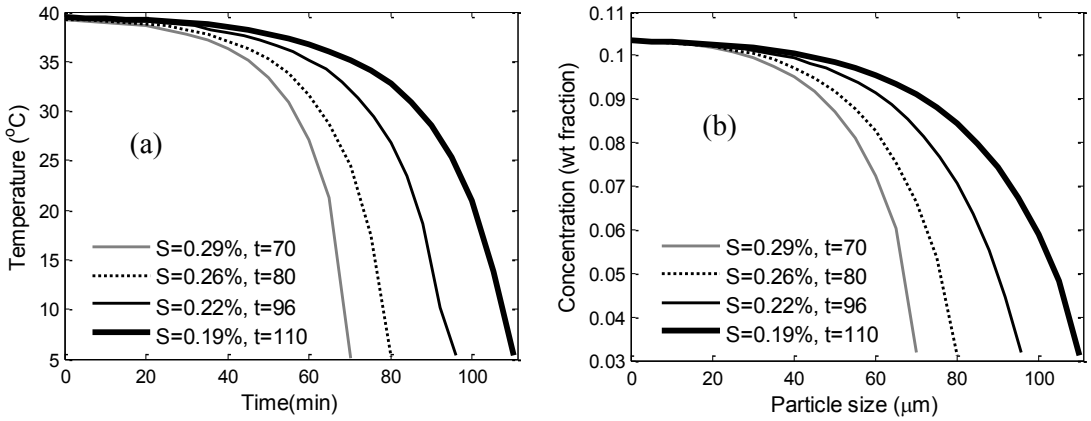

Figure 7.6: a) Temperature profiles and b) concentration profiles obtained at different setpoint supersaturation values (S in weight %), and batch times (t in min) corresponding to the same design parameter $\phi = 0.206\ \mathrm{min}$, optimised to achieve the experimental target CSD.

The proposed simplified model-based direct design approach provides a systematic inferential control approach that allows operating the crystallisation process at a constant supersaturation by controlling a temperature trajectory throughout the batch. Later in Chapter 8 experiments will be discussed which were carried out to implement SSC in terms of temperature trajectories.

7.7 Shaping the CSD through Seed Recipe Design

In addition to the supersaturation and batch time (determined by the SSC design parameter ϕ), the seed recipe (Hojjati and Rohani, 2005; Kubota *et al.*, 2001) may also be optimised to obtain the desired target CSD, which may not be achieved by optimising the SSC design parameter ϕ only. A particular seed CSD can be obtained experimentally by mixing different amounts of seeds with different size distributions. In a generic case the

distributions of various available seed fractions could be represented by their actual experimental distributions, which may be of different type for different fractions. However without loss of generality, for the illustration of the approach here the seed recipe is represented by a sum of Gaussian distribution functions. The optimisation problem, with the objective of shaping the distribution at the end of batch by simultaneously designing the supersaturation controller and the seed recipe, is formulated as follows,

$$\min_{\phi,\, m_{seed},\beta} \sum_{i=1}^{N_d} (f_{v,i}(t_{batch}) - \tilde{f}_{v,i})^2 \,, \tag{7.15}$$

subject to:

$$\sum_{i=1}^{N_G} w_i = 1 \,, \tag{7.16}$$

$$0 < \phi \,, \tag{7.17}$$

$$\beta_{\min} \le \beta \le \beta_{\max} \,, \tag{7.18}$$

$$0 < m_{seed} < 0.05 C(0) m_{slurry} \,, \tag{7.19}$$

$$C(t_{batch}) \le C_{f,\max} \,, \tag{7.20}$$

$$f_{n,seed}(L) = \frac{m_{seed}}{m_{slurry}} \frac{1}{\rho_c k_v} \sum_{i=1}^{N_G} \frac{w_i}{L_{m,i}^3} \mathcal{N}_i(L; L_{m,i}, \sigma_i), \text{ with } \mathcal{N}_i(L; L_{m,i}, \sigma_i) = \frac{1}{\sqrt{2\pi}\sigma_i} e^{-(L-L_{m,i})^2/(2\sigma_i^2)} \tag{7.21}$$

where m_{seed} is the total seed mass (g), and $\beta = [w_1, L_{m,1}, \sigma_1, ..., w_{N_G}, L_{m,N_G}, \sigma_{N_G}]$ is the seed design vector with $w_i \in [0, 1]$ the weight fractions of seeds from particular sieve fractions in the final seed mixture, $L_{m,i}$ the mean sizes (μm) and σ_i (μm) the standard deviations of the respective Gaussians distributions with $i = 1,2,...,N_G$ with N_G being the number of Gaussian distributions (sieve fractions), $\beta_{\min}$ and $\beta_{\max}$ are the vectors of lower and upper bounds on the seed recipe parameters, m_{slurry} is the mass of potash alum solution (g) without seed, $C(0)$ and $C(t_{batch})$ are the solute concentrations at the beginning and end of the batch, respectively. The constraints given by inequalities (7.19) restrict the amount of seed added to a maximum of 5% of the mass of solid dissolved in the system, whereas the constraint given by (7.20) is a productivity constraint with $C_{f,\max}$ being the maximum acceptable concentration at the end of the batch to achieve the required yield. The objective function is expressed as the sum

square error between the simulated ($f_{v,i}$), and target ($\tilde{f}_{v,i}$) volume distributions, respectively.

Since the optimisation problem (7.15)-(7.21) is formulated for a supersaturation-controlled growth-dominated crystallisation process, the predicted CSD can be computed easily using the corresponding analytical solution from Table C.1 (given in Appendix C), and the optimisation problem can be solved with standard non-linear constrained optimisation approaches and tools (e.g. sequential quadratic programming implemented in the MATLAB *fmincon* function).

The seed recipe can be designed for any target CSD, e.g. lognormal or bimodal. Figure 7.7 shows the result of the simultaneous supersaturation control and seed recipe design, for the narrow lognormal target distribution, also shown in Figure 7.5 (b). The mass of slurry is $m_{slurry} = 568\ g$ and the initial concentration of the solution is $C(0) = 0.12$ (g/g). It can be seen that by simultaneously designing the supersaturation controller and the seed recipe, a very good agreement between the target and simulated CSDs can be achieved, even for the case when design based on an optimal ϕ on its own does not give a satisfactory outcome. The results indicate that the optimal SSC design parameter in this case is also $\phi = 0.198\ \min$, however the seed required to produce the target CSD is narrower than the experimental seed used in the previous cases.

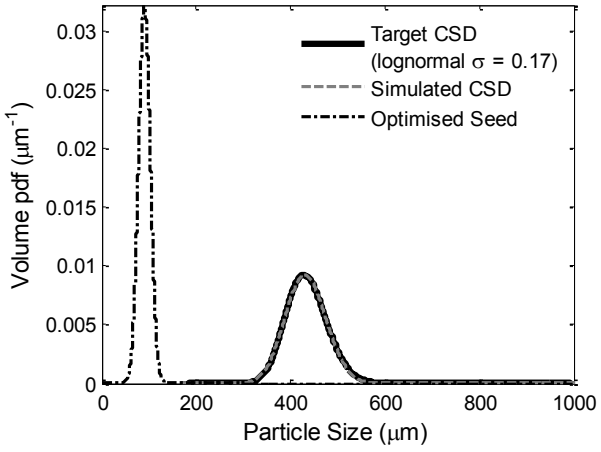

Figure 7.7: Results of the free seed recipe design for the lognormal target CSD shown in Figure 7.5 (b).

The characteristics of the resulting seed recipe are included in Table 7.1. The optimised seed is a mix of two seed fractions, represented by two Gaussians. However the contribution of

the second seed fraction is practically negligible and increasing the number of seed fractions further, $N_G > 2$, does not provide any additional benefit.

Table 7.1: Optimised seed recipe and supersaturation control design parameter for different target crystal size distributions using free seed size distribution.

Target distribution				Optimised seed recipe				SSC
	w	L_m (μm)	σ	w	L_m (μm)	σ (μm)	m_{seed} (g)	ϕ (min)
lognormal	1.00	420	0.17	0.999 0.001	84.9 69.4	12.7 28.3	0.450	0.198
bimodal (sum of two Gaussians)	0.85 0.15	350 600	32 (μm) 45 (μm)	0.85 0.15	57.68 124.11	9.56 10.36	0.334	0.206
trapezoidal				0.157 0.157 0.151 0.154 0.079 0.151 0.151	137.83 121.37 67.49 46.80 148.98 104.17 86.38	7.45 8.0 8.0 8.0 4.72 7.50 8.50	0.985	0.206

The seed recipe design approach was further evaluated for another two, more complex target distributions. Figure 7.8 (a) illustrates the results of the seed design when an arbitrary bimodal distribution was used in the case of fixed $\phi = 0.206$ min. It can be seen that the simulated CSD is in good agreement with the desired bimodal CSD (characteristics of the optimised seed are shown in Table 7.1) using a seed recipe consisting of a mixture of two seed size ranges. The results for a trapezoidal distribution using the optimal supersaturation control design parameter $\phi = 0.206$ min are shown in Figure 7.8 (b). It can be seen that by designing the seed recipe it is possible to capture relatively well even this unusual target distribution; however the seed recipe in this case is a mixture of crystals from 7 size ranges (as shown in Table 7.1). The amount of seed required to obtain the desired minimum yield of 60% varies with the shape of the target distribution.

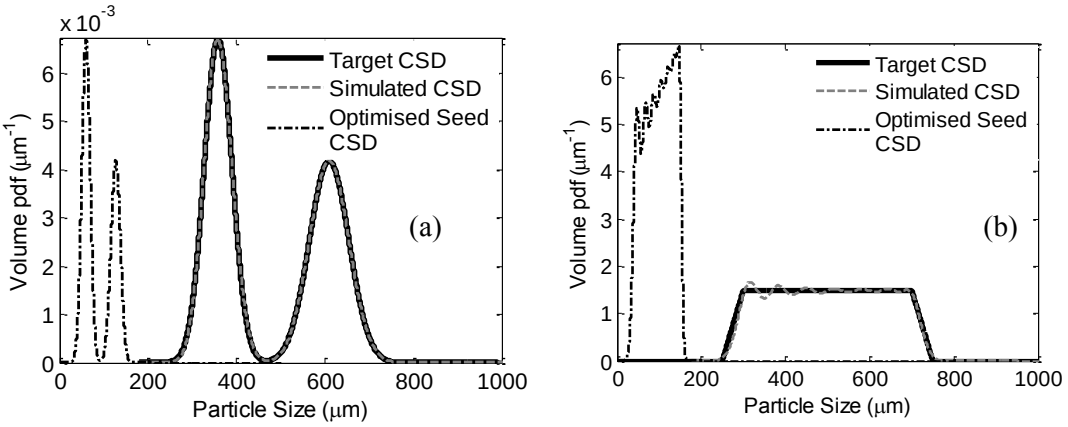

Figure 7.8: Results of the free seed recipe design for (a) bimodal distribution and (b) trapezoidal distribution.

The seed design problem defined by equations (7.15)-(7.21) allows the optimisation of weights of various seed fractions. Additionally, the mean size and standard deviations of the CSD of individual seed distributions are treated as free decision variables, and hence this method is referred to here as free seed design. However in practice it may be difficult to produce seed fractions with size distributions with arbitrary mean sizes and standard deviations. Generally seeds are prepared by sieving using standard sieve sizes. Hence a more practical approach to design seed recipes is to use the size distribution of existing sieve fractions and optimize the weights of the selected fractions only. The most commonly used sieve sizes are shown in Table 7.2 (Perry and Green, 1997).

Table 7.2: Standard sieve series and their equivalents.

Sieve numbers corresponding to selected sieves for simulation	Sieve designation standard (μm)
14	354*
13	297
12	250*
11	210
10	177*
9	149
8	125*
7	105
6	88*
5	74
4	63*
3	53
2	44*
1	37

Note: *Sieve corresponds to those proposed by the International Standard Organisation (ISO).

The seed recipe was optimised for fixed mean and standard deviations based on the selection of relevant sieves. Generally these values are material dependent and would result from the sieve analysis of a particular system. In this work the mean values of the seed distributions were calculated as the arithmetic means of the consecutive sieve sizes, $L_{m,i} = (\mathcal{L}_i + \mathcal{L}_{i+1})/2$, and the standard deviations were considered to be equal to half of the size ranges determined by the corresponding sieves $\sigma_i = (\mathcal{L}_{i+1} - \mathcal{L}_i)/2$, where $\mathcal{L}_i$, $i = 0,1,...,N_G$, are the standard sieve sizes (in μm), with N_G being equal to the total number of selected sieves. These values provide approximately a 2σ overlap between the distributions of seeds from adjacent sieve ranges, and correspond to the experimental observations of the sieve analyses of several compounds. The optimisation was solved considering the SSC design parameter, the total seed mass and the weight fractions of seeds used in the various size ranges, $\beta = [w_1, w_2, \ldots, w_{N_G}]$, as the decision variables. The seed was designed for the same lognormal and bimodal target distributions as used for the free seed design and the results are shown in Table 7.3.

Table 7.3: Total mass for optimised seed to achieve the target CSD distributions using selected sieves.

Target distribution				**Optimised seed recipe**					**SSC**
	w	L_m (μm)	σ	w	L_m (μm)	σ (μm)	m_{seed} (g)	Selected Sieves (μm)	ϕ (min)
lognormal	1.00	420	0.17	1	84	21	0.895	63-105	0.202
Bimodal (sum of two Gaussians)	0.85	350	32 (μm)	0.05	40.5	3.5	1.185	37-44	0.206
	0.15	600	45 (μm)	0.30	48.5	4.5		44-53	
				0.07	58.0	5.0		53-63	
				0.32	68.5	5.5		63-74	
				0.16	115	10		105-125	
				0.10	137	12		125-149	

Figure 7.9 shows the results for the lognormal target distribution, indicating a very good agreement between the simulated and desired product CSDs. Sieve fractions from Table 7.2 were used and the optimisation automatically selected the seed, which would be retained between sieves 63 μm and 105 μm, by setting the weights of other sieve ranges to zero.

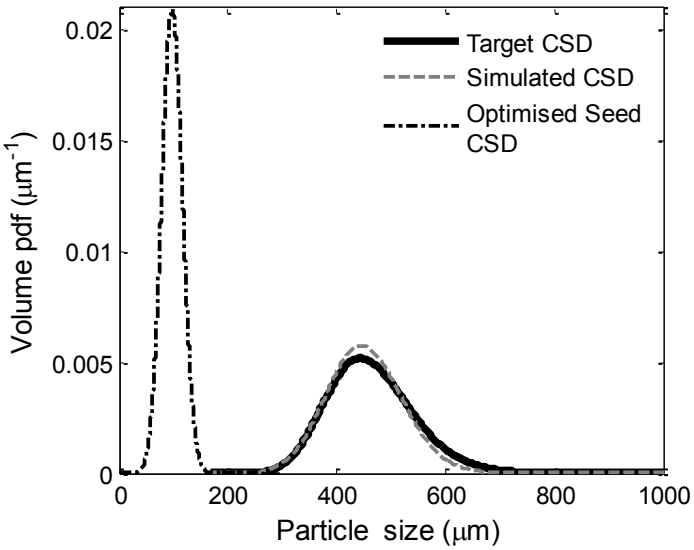

Figure 7.9: Results of the simultaneous supersaturation control design and seed recipe optimisation for a lognormal target distribution using sieved seed fractions.

It can be observed that the mean size of the seed CSD based on the selected sieves is close to the mean size resulting from the free seed design shown for lognormal distribution in Table 7.1. However the standard deviation of the seed CSD corresponding to the selected sieves is broader compared to the free seed design, which was compensated by the optimiser by selecting a larger value for the SSC design parameter, ϕ .

For the bimodal target distribution the optimal supersaturation control parameter is $\phi = 0.206$ and the optimal seed recipe consists of six sieve size ranges (as shown in Table 7.3) automatically selected by the optimisation algorithm. The first four are consecutive size ranges, followed by a gap before the last two consecutive seed size ranges selected. Figure 7.10 (a) illustrates how the seed distribution is constructed as a weighted mixture of the individual seed fractions. The limitation on the existing seed size fractions due to fixed sieve sizes leads to a difference between the simulated optimal CSD and the target CSD, especially for the larger size mode, as seen in Figure 7.10 (b). The trapezoidal target distribution, which was relatively well constructed using the free seed design method, was not possible to obtain using the fixed sieve size ranges. The results indicate that the achievable target distributions for a particular process are determined not only by the growth kinetics of the system, but also by the physical limitations on the size distributions for the

seeds which can be produced. The total amount of seed required to achieve the desired target yield is larger in the case of the sieved seed recipe than for the free seed design.

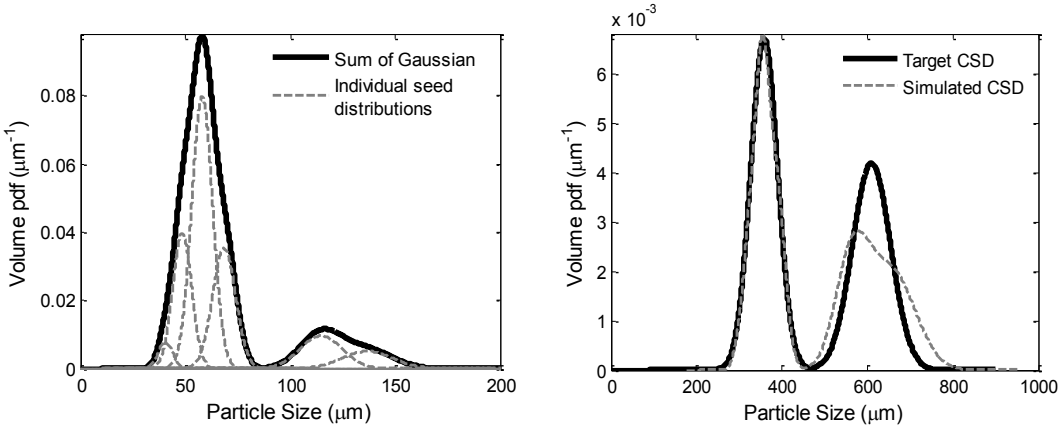

Figure 7.10: Seed design for bimodal target distribution, a) illustration of how the distributions of the individual seed fractions yield the overall seed distribution, b) comparison of target and simulated CSDs at the end of the batch.

Figure 7.11 illustrates the concentration profiles for the bimodal target distribution corresponding to the free seed design, the sieved seed design and in the case when the amount of seed resulting from the free design is used but the seed is prepared from the sieved fractions. In the former two cases the same target yield is achieved since the optimisation tailors the seed masses required to meet the hard constraint on the yield. However if a smaller amount of seed (resulting from the free seed design) is used but with the seed distribution being prepared from the sieved fractions, the final yield would be significantly smaller (20% compared to the target 60%). The results demonstrate that although conceptually seed recipe design has a great potential to be used for CSD design, practical limitations on size ranges of seed fractions may lead to errors in the final distribution or product yield, and may greatly limit the achievable shape of the final distribution. Hence it is important to incorporate into the optimisation problem the limitations on the achievable seed size distributions, as illustrated here. To eliminate some of the disadvantages related to the seed design as a mixture of sieved seed fractions an alternative approach is proposed next, according to which a single mono-modal seed fraction is added at different times during the process to produce a given target distributions.

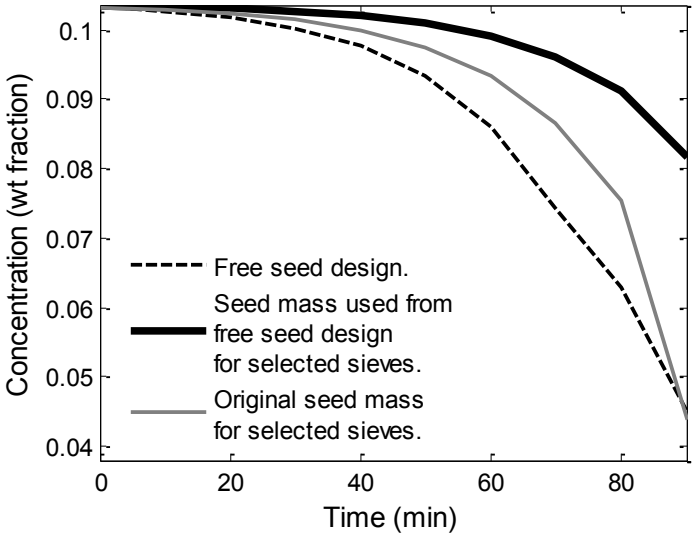

Figure 7.11: Comparison of concentration profiles for three different seed recipes for the same bimodal target distribution.

7.8 Shaping the CSD via optimal dynamic seed addition

Achieving the shape of the final CSD by designing the initial size distribution as a mixture of seed with different size distributions can be difficult to apply in practice due to the limited amount of seed which can be produced and the constraints on the size and width of the CSD in various size ranges. Similar results can be achieved if a mono-modal seed is introduced in the crystalliser during the crystallisation process, using the seed as an actuator rather than an initial condition. For processes with size-dependent growth of the form of equation (4.8) with $p > 0$ the seed CSD must be narrower than the target distribution. The narrower the seed distribution is, the closer the final CSD will be to the target CSD and the more freedom exists in the design of the shape of the target distribution. For the dynamic seed addition approach, the batch period $[0, t_{batch}]$ is divided into N intervals via a series of grid points $0 = \tau_0 < \tau_1 < \tau_2 < \ldots < \tau_N \leq t_{batch}$, where the time steps τ_i, $i = 1,\ldots,N$ are the discrete times when seed is added into the system, and can be equally distributed or at different intervals, fixed or determined by the optimisation. The amounts of seeds and the moments when they are added into the system are determined by solving the following dynamic optimisation problem:

$$\min_{\substack{m_{s,1},\ldots,m_{s,N} \\ \tau_1,\ldots,\tau_N \\ t_{batch}}} \sum_{i=1}^{N_d} (f_{v,i} - \tilde{f}_{v,i})^2 , \tag{7.22}$$

where $m_{s,i}$, $i = 1,2,\ldots,N$, are the amounts of seed introduced into the vessel at discrete times τ_i. In the case of constant supersaturation the final distribution f_v can be computed very efficiently using the analytical expressions from Table C.1, applying for each seed fraction added at time τ_i the growth time $t_{growth,i} = t_{batch} - \tau_i$. Hence the optimisation can be solved using a fine and constant time discretisation, excluding the time steps from the decision variables. In this case the optimisation will eliminate automatically some of the dropping times by setting the corresponding amounts of seeds to zero. The optimisation can be solved using fixed or free batch time, based on practical requirements, and productivity constraints can be added to the problem. Additionally the seeding period may be restricted to a certain initial period of the batch to avoid seeding for the entire duration of the crystallisation, which may not be a practically acceptable procedure.

Figure 7.12 (a)-(d) show the result of the dynamic seed addition optimisation in the case of the same bimodal and trapezoidal target distributions as those used in the previous cases, defined in Table 7.1. For both targets the seed distribution was a mono-modal Gaussian distribution with mean size of 40.5 μm and standard deviation of 3.5 μm, the discretisation interval was 2 min, the batch time was fixed to 120 min and the supersaturation was $S = 0.00257$ kg/kg slurry. It can be seen from Figure 7.12 (a) that the simulated and target distributions are in very good agreement, indicating that the dynamic seed addition approach can provide multimodal target distributions using mono-modal seed only. Figure 7.12 (b) shows that in the case of the bimodal target distribution, seed addition was required during the first 40 min of the batch to achieve the shape of the distribution. All crystals in the product are larger than 200 μm and hence an aging period of at least 80 min is required to grow the crystals to the desired size range. There are clearly two main seeding periods, each corresponding to one of the two modes of the target CSD. One consists of the first three additions during the initial 10 minutes of the batch and contributes to the mode of larger size of the product CSD, whereas the second, between 20-40 minutes, consists of a more fine

control for the smaller size range of the target distribution, consisting of a number of additions of smaller amounts of seed.

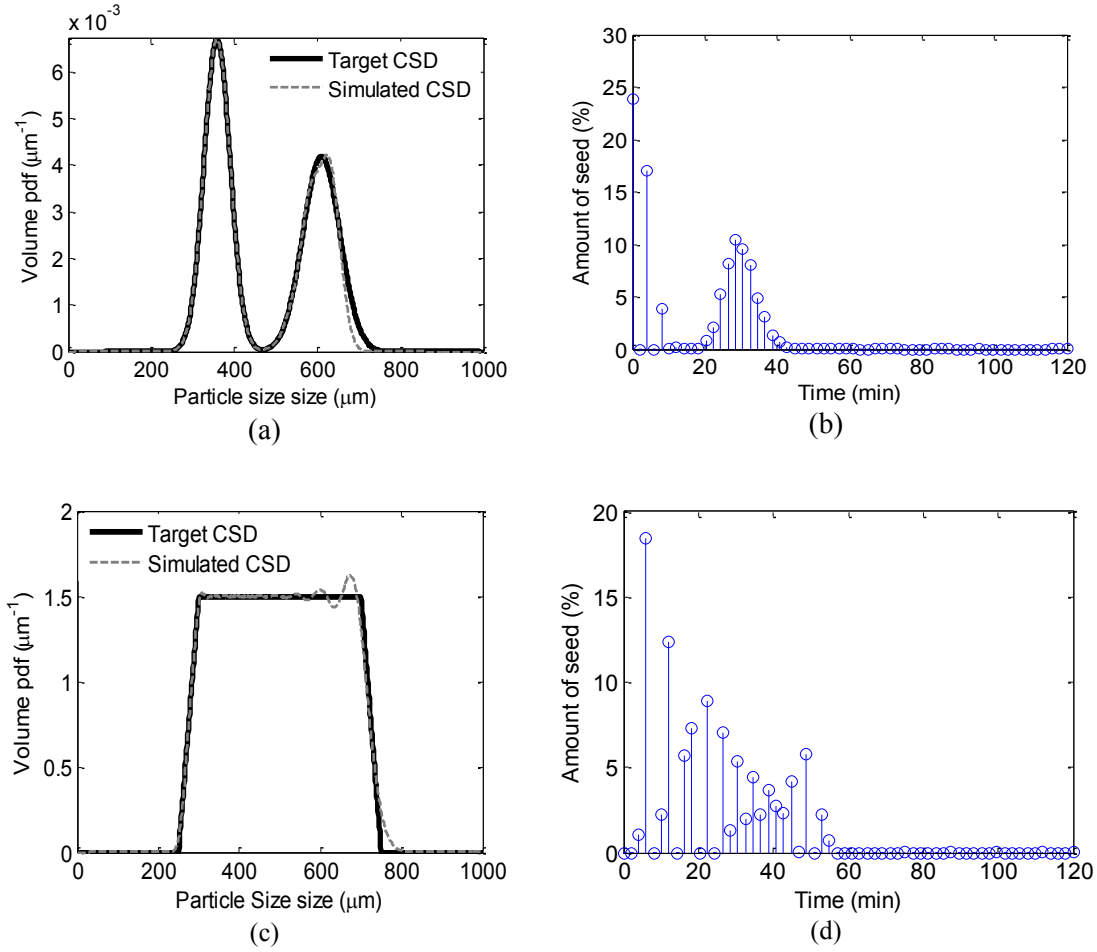

Figure 7.12: Results for the dynamic seed addition for bimodal and trapezoidal distributions; a) and c) show the comparisons of target and simulated CSDs at the end of the batch, and b) and d) illustrate the dynamic seed addition profiles, with amount of seed in weight %.

The results of the dynamic seed optimisation in the case of the trapezoidal target distribution are shown in Figure 7.12 (c) and (d). A good fit of the target distribution is achieved despite the fact that a mono-modal seed was used. The resulting optimal dynamic seed addition profile, shown in Figure 7.12(d), indicates that seed is added into the system during the first half of the batch (60 min). The error in the larger size range of the target distribution is due to the fact that the size dependent growth generates a widening of the seed distribution. Although the seed distribution is narrow, it also has a small mean size requiring a long growth time to develop crystals of the larger size ranges needed for the target CSD. During this longer growth period the distribution of the added seed crystals becomes wider, leading

to the differences between the simulated and target distributions. Overall the distribution matches very well the target CSD, however this is only achievable with a relatively narrow seed distribution only.

To illustrate the importance of a narrow seed distribution for dynamic seed design, simulations were performed using a broader seed, with a mean size of 60 μm and a standard deviation of 35 μm. The results for the bimodal target distribution are shown in Figure 7.13 (a) and (b), indicating that if the seed is too large and/or the distribution too broad the target CSD may not be achievable. Dynamic seed addition can be automated easily using a solid dosing system, or could be achieved by coupling an impinging jet crystallisation process with an aging vessel (Kee *et al.*, 2009; Woo *et al.*, 2009b) providing a practical approach for CSD control. Impinging jet crystallisation has also been recognized recently as a reliable method to produce small crystals with narrow distributions, which are suitable for the dynamic seeding procedure (Woo *et al.*, 2009b).

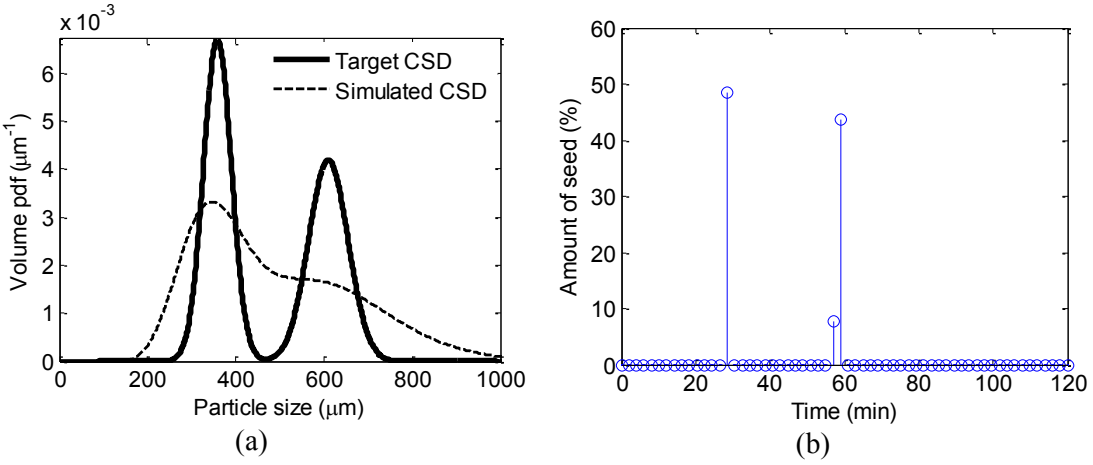

Figure 7.13: Results for the dynamic seed addition for bimodal distribution when larger and broader seed is used with mean size of 60 μm and standard deviation of 35 μm ; a) comparison of target and simulated CSDs; b) resulting seed addition profile.

The results demonstrate that using the design parameter (ϕ) and analytical solutions, supersaturation controlled processes can be designed to obtain certain target distribution, which can be implemented in the phase diagram, or in the time domain, allowing the implementation of novel quality-by-design approaches. However a greater variety of shapes of the product CSD may be obtained if the seed recipe is designed simultaneously with the

supersaturation controller, or if seed is used as an actuator during the process. Figure 7.14 shows the main steps of the proposed comprehensive and systematic methodology for shaping the product CSD for supersaturation controlled crystallisation processes, which combines seed recipe and operating policy designs. Using the growth kinetics of the process, and assuming constant supersaturation control, the analytical solutions shown in Table C.1 in Appendix C can be exploited, and the approach very efficiently provides a supersaturation setpoint and batch time, or temperature versus time setpoint (corresponding to a desired constant supersaturation according to the direct design concept) together with the optimal seed recipe to produce a final product with desired CSD. If the final CSD are linked to other product properties, then the methodology proposed here can be extended for other product property designs or downstream process optimisation.

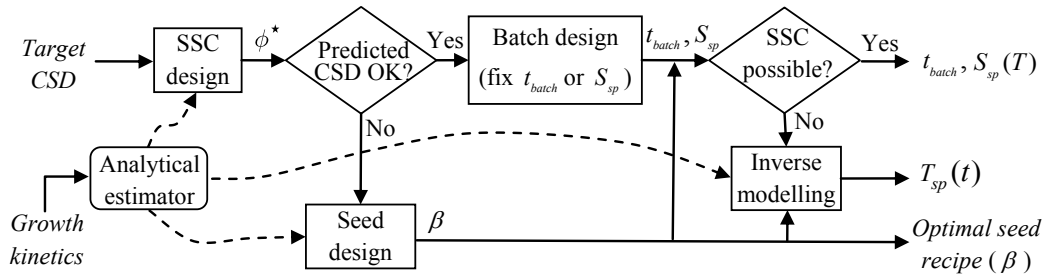

Figure 7.14: Flow chart of the systematic design of supersaturation controlled crystallisation processes, to achieve a desired target CSD.

7.9 Conclusions

The chapter describes a novel methodology for the systematic design of supersaturation controlled crystallisation processes. The approach is based on the idea that in the case of supersaturation-controlled, seeded crystallisation systems the supersaturation is constant throughout the batch and the assumption is that the process is dominated by growth only. A design parameter $(\phi = S^g t)$ for supersaturation controlled seeded batch crystallisation processes is introduced, and a simplified model-based optimisation is used to derive the setpoint operating curve and batch time required to achieve the desired shape of the product CSD. The designed operating curve can be implemented in the phase diagram using

supersaturation control, or in the time domain using classical temperature control. The analytical expressions presented in the chapter based on the assumption of supersaturation controlled process, can be easily implemented in industrial process monitoring software and can serve as an inferential product property estimator or can be used for simple real-time adaptive control strategies. The introduced SSC design parameter also allows the systematic analysis and comparison of supersaturation controlled processes, by quantitatively evaluating the trade-off between batch time and supersaturation level, in terms of the product CSD.

An approach to design an optimal seed recipe is also presented, which can be used to achieve a desired shape of the product CSD, in conjunction with the supersaturation control design. The technique is used to design different target distributions i.e. lognormal, bimodal and trapezoidal distributions. The seed design problem allows the optimisation of weights, means and standard deviations of various seed fractions of the CSD. However in practice it may be difficult to produce seed fractions with size distributions of arbitrary mean size and standard deviations. Therefore the technique was modified for known sieve fractions. The seed recipe was optimised for fixed mean and standard deviations based on the selection of relevant sieves. However, note that not all target distributions are achievable because there are some practical limitations related to the yield and shape of seed distribution.

An alternative seeding approach is also presented, based on the idea of using seed as a process actuator to control the final shape of the product CSD. This approach uses dynamic seed addition during the batch and is able to produce complex CSDs using a mono-modal seed. All methods are exemplified in the case of the batch cooling crystallisation of potash alum system in water.

Chapter 8
Experimental evaluation of the direct design approach for SSC crystallisation processes for shaping the CSD

8.1 Introduction

This chapter describes the experimental evaluation of the direct design approach described in detail in Chapter 7, for supersaturation controlled crystallisation processes. All experiments were carried out for the potassium dichromate-water system. The kinetic parameters for the system were identified and validated based on the methodology and technique described in detail in Chapters 4 and 5. The first part of the chapter describes the operating conditions and experimental procedures for the experiments carried out for parameter estimation and validation. The batch crystallisation model was solved using the combined QMOM-MOCH technique. The parameters were identified using a sequential-quadratic-programming (SQP) type non-linear optimisation approach implemented in MATLAB (as described in Chapter 5). For *in situ* measurement of concentration ATR-UV/Vis probe was used. A multi-linear calibration model was adopted to calculate the concentration from the absorbance measured by the ATR-UV/Vis probe.

The second part of the chapter describes the experiments, which were carried out for the implementation of the direct design approach. The direct design approach is based on the idea of operating the system within the MSZ bounded by the nucleation and the solubility curves. The setpoint supersaturation (S_{sp}) curve is the result of the compromise between fast crystal growth and low nucleation rate. Therefore a supersaturation setpoint curve is chosen experimentally and is followed in the phase diagram using a supersaturation controller based on concentration measurement. Since direct supersaturation measurement sensors are at prototype stage (Loffelmann and Mersmann, 2002) and are often not available for industrial scale use, the supersaturation profiles can be redefined in terms of the temperature profiles in time, which are designed to maintain the supersaturation at a certain setpoint. Experimental

evaluations of two temperature trajectories with low and higher supersaturation levels were carried out to acquire the desired target shape of the CSD. The experiments illustrates that it is possible to design different temperature profiles and hence batch times, which lead to similar product CSD.

For all the experiments discussed in this chapter, off-line concentration was measured using gravimetric analysis and *in situ* measurement of concentration was carried out using ATR-UV/Vis spectroscopy. CSD was measured off-line using Sympatec Qicpic, whilst Malvern Mastersizer was used for on-line CSD measurements. FBRM (focused beam reflectance measurement) was used for *in situ* measurement of the CLD and particle counts. Microscopic images were taken at the end of the batches using optical and scanning electron microscopy (SEM).

8.2 Experimental set-up

The experimental investigation of the batch cooling crystallisation for an inorganic compound was carried out to determine the kinetic parameters for the system. The experimental data was obtained from a laboratory scale crystallisation system at Loughborough University. This section describes the experimental setup in detail.

8.2.1 Material

Potassium dichromate $(K_2Cr_2O_7)$ (>99.95% purity, Fisher Bio Reagents) compound with de-ionised water as a solvent was used in the experiments. The solution was prepared, corresponding to a solubility of 20.0 g of potassium dichromate in 100 g of water at 30 °C (Mullin, 2001).

Potassium dichromate is a common inorganic chemical reagent. It is a crystalline ionic solid with a very bright, red-orange colour with monoclinic crystals, as shown in Figure 8.1. It is mostly used as an oxidising agent in various laboratory and industrial application. In biological field, potassium dichromate is used as an adhesive for preservation of tissue sections. It is potentially harmful for health and must be handled and disposed off appropriately.

Figure 8.1: Potassium dichromate crystals with very bright, red-orange colour and monoclinic shape.

8.2.2 Apparatus

Schematic representation of the experimental setup is shown in Figure 8.2. Temperature in the 0.5 L jacketed glass vessel was controlled with a Pt100 thermocouple using a Huber VPC CC3 450 thermostat, controlled via a specially designed crystallisation control interface in Labview (National Instruments). An overhead stirrer with a four-blade marine type impeller was used to agitate the system at 380 rpm. This agitation speed was chosen to be high enough to guarantee that particles were well suspended throughout the process as the potassium dichromate crystals have relatively high density and require high agitation speed for proper suspension. However, the agitation speed was low enough to avoid attrition or generation of bubbles due to vortex formation. An FBRM probe (model A100, Lasentec) was inserted into the solution to measure chord length distributions in the range of 0.8 to 1000 μm at every 20 s. An ATR-UV/Vis spectrometer (model MCS 621, Carl Zeiss) with a deuterium source (UV-Vis/CLD 600) was used to measure the concentration. The absorbance was recorded every 20 s over a wavelength range of 240 – 720 nm, and the absorbance values at selected wavelengths were used in calibration to determine the concentration.

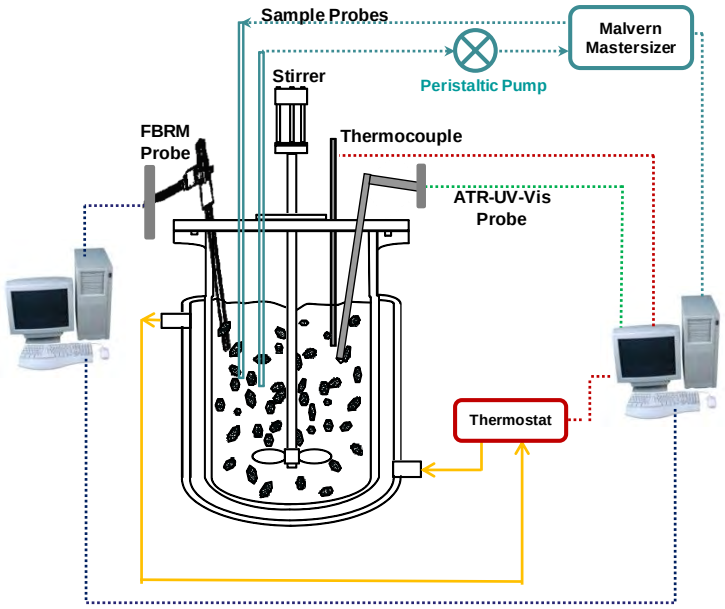

Figure 8.2: A schematic representation of the experimental setup for the batch cooling crystallisation of potassium dichromate-water system.

The CSD was measured after every 3 minutes using a Malvern Mastersizer 2000 laser-diffraction equipment. A peristaltic pump was used to circulate the slurry (solids with solvent) between the crystalliser and the Mastersizer. The pump flow rate was adjusted in such a way that the Mastersizer cell does not saturate with crystals and the solids remain in the allowable range to 10-20% of the total volume. The refractive index for potassium dichromate-water system (potassium dichromate dissolved in water) was measured using refractometer, and was 1.52, at 25°C. The refractive index of potassium dichromate crystals is 1.72. The difference between the refractive index of crystals and solution (solvent with dissolved solids) was significantly different for suitable CSD measurement. To measure the CSD the background measurement was taken only once, to align the laser, before the seed addition and was kept constant for all readings throughout the batch. The length of the piping was minimised and the crystallisation experiments were carried out in a relatively narrow temperature range of 29-20°C, close to room temperature, to avoid nucleation. The initial solution at the initial temperature was circulated continuously throughout the tubes and Mastersizer until a constant temperature was achieved in the whole system. After equilibration, the temperature was gradually decreased from 40°C to 29°C while maintaining the circulation of the solution throughout the experimental setup to avoid nucleation in the

silicon tubing. The FBRM probe was used to detect nucleation in the system. Samples were taken at the end of each batch for microscopic analyses carried out using a Leica DM LM microscope equipped with a Leica PFC 350 FX camera. An image of the experimental setup is shown in Appendix D.

8.2.3 Seed preparation

Seeds were prepared using laboratory scale sieves. The consecutive sieve sizes used were: 355-300, 300-250, 250-212, 212-180, 180-150, 150-125, 125-106, 106-90, 90-75, 75-63 and 63-45 μm, (coarser sizes were placed on the top and finer at the bottom). The sieving time was 120 minutes, and the rotation and shaking caused the crystals to distribute throughout the sieve stack. The product obtained between the sieve sizes of 106-125 μm was collected for seeding in the parameter identification and validation experiments. The required amount of the seed mass was achieved after running four batches of sieving. The seed quantities obtained on each sieve are shown in Figure 8.3.

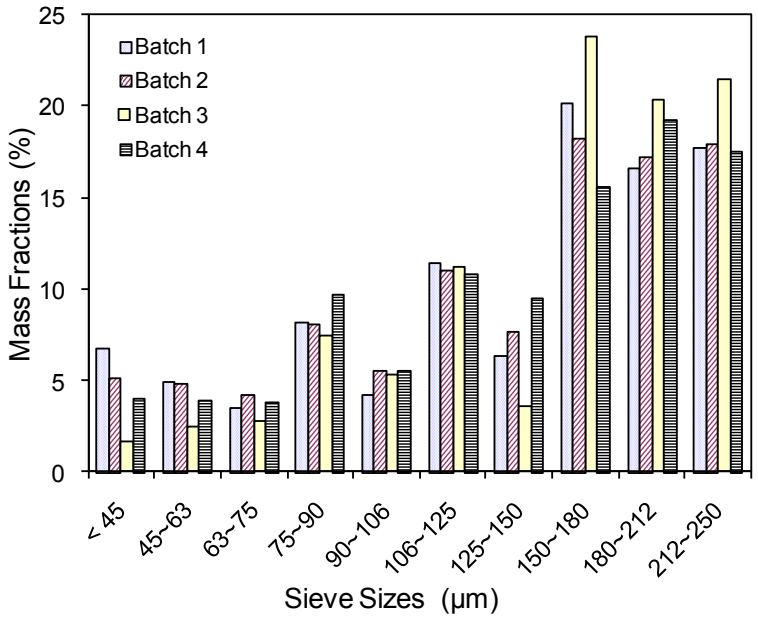

Figure 8.3: Mass fractions obtained between different sieve sizes at the end of four batches.

Microscopic images of the seeds obtained in sieve fraction 106-125 μm at the end of the four batches are shown in Figure 8.4. It can be observed in Figure 8.4 that batches 3 and 4 contained less fine particles then batches 1 and 2. The crystal shape is irregular in all the

batches. The seeds obtained from Batch 3 were used for all experiments. The comparison of other seed fractions for all four batches is shown in Appendix E.

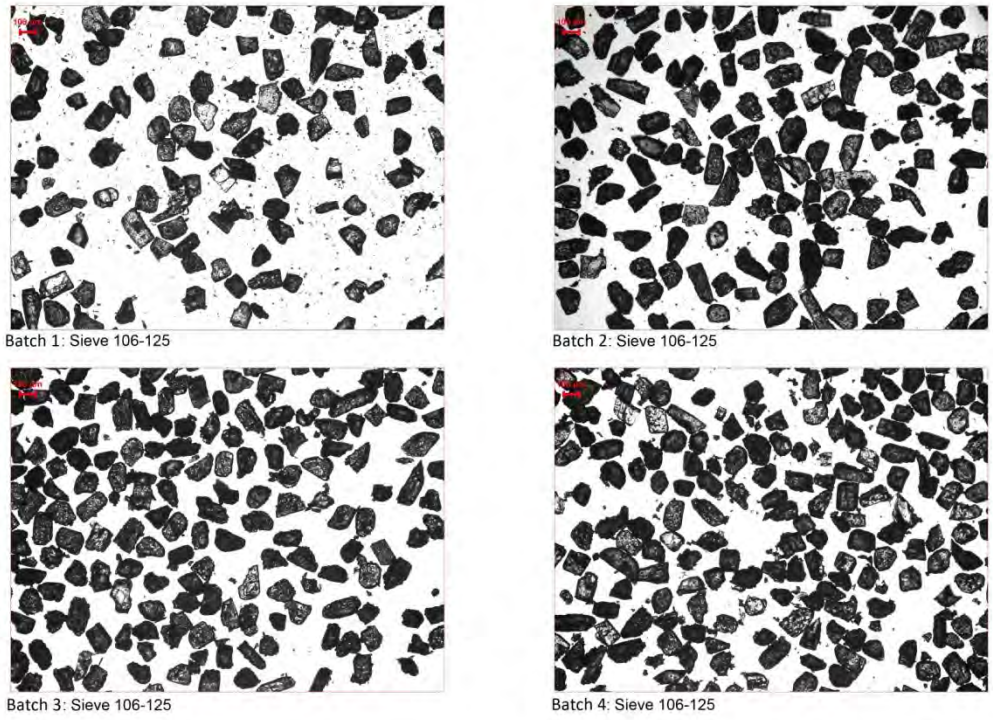

Figure 8.4: Comparison of seed fraction 106-125 μm obtained at the end of four sieving batches.

8.3 Methods

Potassium dichromate was dissolved in water by heating to 40°C at a rate of 0.8°C/min. The solution was equilibrated at 40 °C for 20 minutes, to ensure complete dissolution of the solids, which was indicated by the decrease of the FBRM counts. Temperature of the solution was then reduced to 29°C (one degree below saturation) at a rate of 0.5°C/min and was maintained for 10 minutes prior to the start of the experiment, after which 1.2 g of sieved seed (in the size range between 106-125 μm) was added to the solution and the slurry was cooled to 20°C over a duration of 60 minutes following a cubic profile. During this period, the FBRM readings were monitored to check if the seed dissolved or secondary nucleation occurred. The ATR-UV/Vis spectrometer was used to measure the absorbance throughout the experiment, which was calibrated to provide *in situ* concentration measurement. Malvern Mastersizer 2000 was used to measure online the CSD with a

sampling time of 3 minutes. The whole experimental procedure was repeated for a linear temperature profile. The details of the operating conditions are summarized in Table 8.1.

Table 8.1: Operating conditions for potassium dichromate-water system for seeded-batch cooling crystallisation.

Operating conditions	Units	Experiment A	Experiment B
Saturation temperature , (T_{sat})	$^{\circ}C$	30	30
Seed mass, (m_{seed})	kg	1.2×10^{-3}	1.2×10^{-3}
Seed loading	%	1.5 % of total solid	1.5 % of total solid
Batch time, (t_{batch})	$\min$	60	60
Initial solute concentration (C_i)	kg solid/ kg water	0.20	0.20
Initial temperature at seeding and start of profile, (T_0)	$^{\circ}C$	29	29
Final temperature, (T_f)	$^{\circ}C$	20	20
Temperature profile followed	--	Cubic $T_{cubic} = T_0 - (T_0 - T_f)(t / t_{bacth})^3$	Linear $T_{linear} = T_0 - (T_0 - T_f)(t / t_{batch})$
Points for smooth profile, (N)	--	60	60
Sieve sizes for seed, $\mathcal{L}$	μm	106-125	106-125
Agitation speed	rpm	380	380
Density of crystals, (ρ_c)	kg / m^3	2676	2676
Volumetric shape factor, (k_v)	--	0.80	0.80
Mass of slurry, (m_{slurry})	kg	0.49	0.49
Sampling time for ATR/UV-Vis and FBRM measurement	s	20	20
Sampling time for CSD measurement	min	3	3

8.4 Concentration measurement using ATR/UV-Vis spectroscopy

The absorbance of the solution was measured using an ATR-UV/Vis spectrometer at different concentrations and temperatures. Figure 8.5 shows sample spectra of potassium dichromate solution in water at different concentrations. The spectrum of potassium

dichromate system in water indicates two absorbance peaks at wavelengths 270.15 nm and 377.89 nm.

For the calibration model the absorbance values were measured for several concentrations at different temperature ranges, as shown in Figure 8.6. The temperature was decreased in steps of 1°C for each concentration until the system nucleated. Hence the nucleation points shown in Figure 8.6 were determined experimentally. The solubility curve was obtained from literature. A second order polynomial is fitted to the literature data to obtain the solubility curve,

$$C_{sat}(T) = a_0 + a_1 T + a_2 T^2 , \tag{8.1}$$

where $a_0 = 3.29$, $a_1 = 4.48 \times 10^{-1}$, $a_2 = 3.30 \times 10^{-3}$, T is the temperature in $°C$ and C_{sat} is in g/100 g of water.

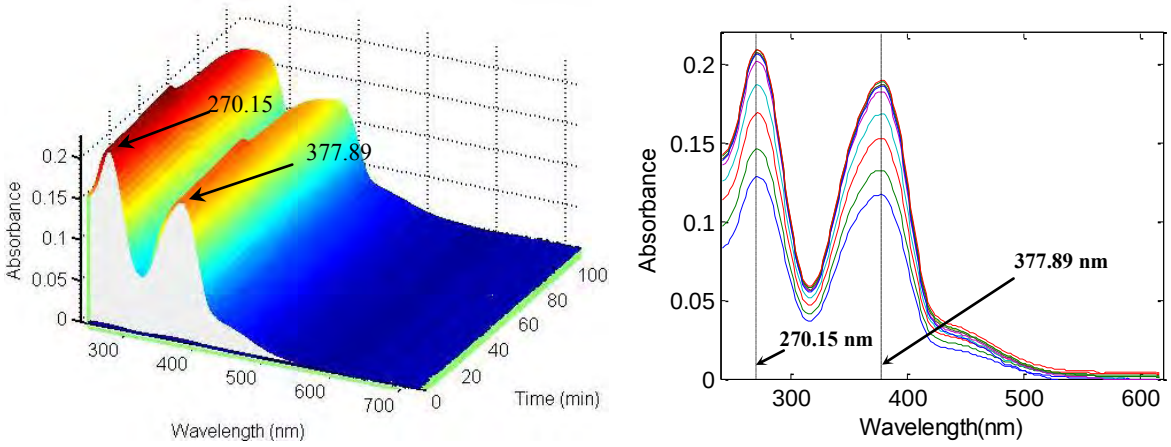

(a) (b)

Figure 8.5: UV/Vis spectra of potassium dichromate in water at different concentrations obtained using *in situ* ATR-UV/Vis spectroscopy.

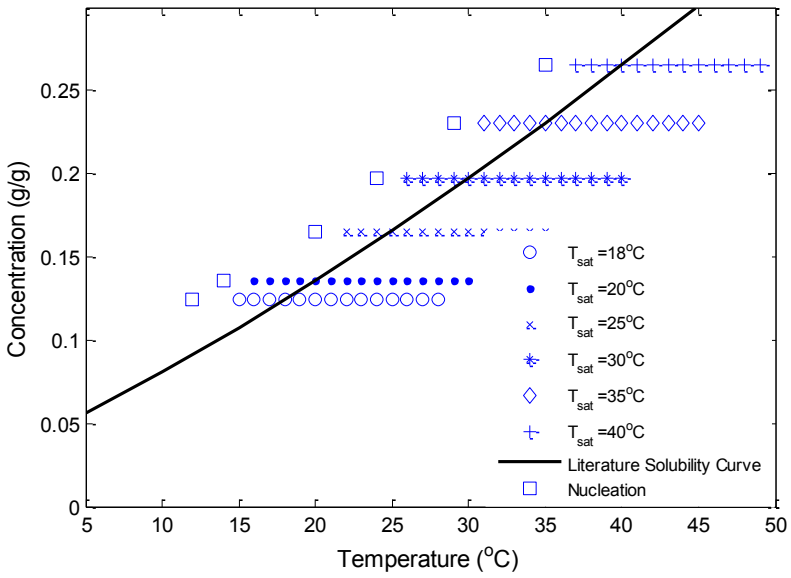

Figure 8.6: Measurement points for absorbance values for the used concentrations and the temperature ranges, including solubility curve (Mullin, 2001) and the nucleation points.

A linear relationship between concentration and absorbance was observed for both wavelengths at 270.15 nm and 377.89 nm, as shown in Figure 8.7 (a and b).

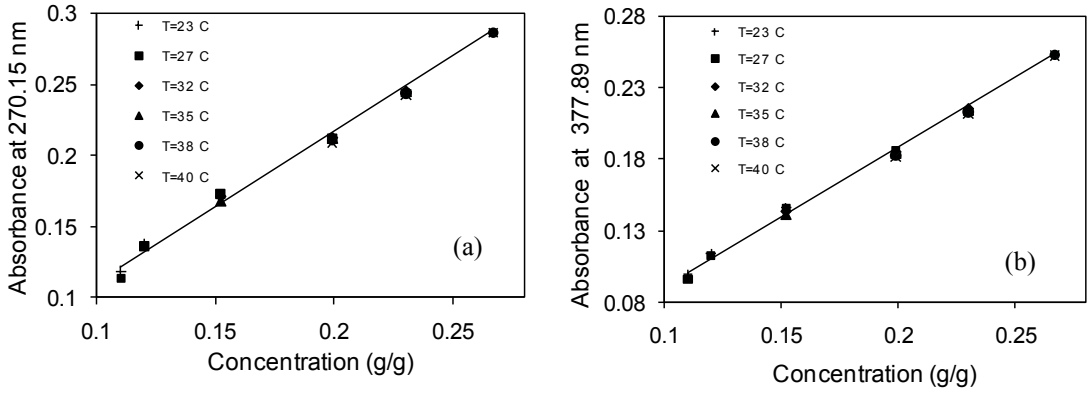

Figure 8.7: Effect of absorbance vs. concentration for six different temperatures a) absorbance at 270.15 nm and b) absorbance at 377.89 nm.

A linear relationship between absorbance and temperature was observed for both wavelengths at 270.15 and 377.89 nm. The slopes for both wave lengths at different temperatures were quite uniform, as shown in Figure 8.8 (a and b). The effect of temperature

on the absorbance is relatively small, as shown by the very small spread of points on Figure 8.7 (a and b) and by the small slopes of trend lines in Figure 8.8 (a and b). However, temperature effect was considered in the calibration model to increase the accuracy and precision of the concentration predictions. Based on the analysis of Figure 8.7 and Figure 8.8, various forms of the calibration model were evaluated (shown in Appendix F) using different absorbance values. It was found that using the two peak absorbance values along with temperature significantly improves the prediction accuracy of the calibration model.

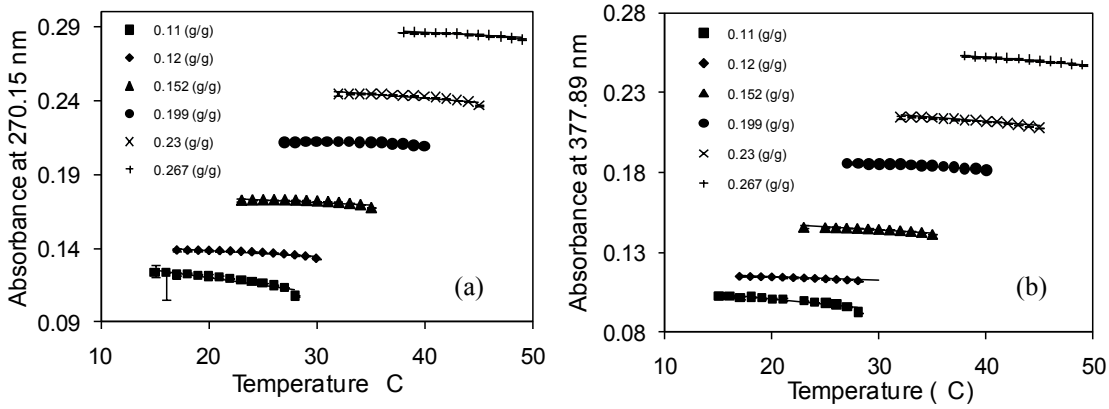

Figure 8.8: Effect of absorbance vs. temperature for six different concentrations a) absorbance at 270.15 nm and b) absorbance at 377.89 nm.

Therefore the following multi-linear calibration model was adopted:

$$C = a_0 + a_1 A_1 + a_2 A_2 + a_3 T \,, \tag{8.2}$$

where A_1 and A_2 are the absorbance values at the two wavelengths 270.15 nm and 377.89 nm, respectively, C is the concentration (g/g solvent) and T is the temperature (°C). The parameters for the calibration model (a_i with $i = 0,1,...,3$) were estimated using the *fmincon* function in MATLAB, by a standard least-squares optimisation approach. The optimisation problem for the parameter estimation is given by:

$$\min_{a_i} \sum_{k=1}^{K} (C_k - C_k^{\exp})^2, \tag{8.3}$$

where C_k and $C_k^{\exp}$ are the simulated and the experimental concentration values at the discrete measurement steps $k = 1,\ldots,K$, respectively, with K being the number of

measurement points. The parameters obtained with their uncertainty bounds (representing the 95% confidence interval) are shown in Table 8.2. Figure 8.9 (a) indicates that the simple form given by Equation (8.2) provides a very good calibration model, hence more complex robust chemometrics based calibration was not considered necessary in this case.

Table 8.2: Estimated parameters for calibration of the ATR-UV/Vis spectrometer.

Parameter	Value	Error bounds at 95 % Confidence Interval
a_0	0.0086	$\pm$0.0002
a_1	-0.6737	$\pm$0.0025
a_2	1.7332	$\pm$0.0013
a_3	0.0004	$\pm$0.0001

Figure 8.9 (a) shows the comparison of the estimated and the simulated concentrations using the calibration model with parameters shown in Table 8.2, which are in good agreement. The validation point of a concentration, which was not included in the calibration model development, also indicates good accuracy of the calibration model. The excellent agreement between the experimental and the predicted concentrations and the very small error bounds (95% confidence interval) on the parameters of the calibration model provide evidence that the ATR-UV/Vis, with calibration models of relatively simple forms, can be used as a reliable *in situ* process analytical technology (PAT) tool for real-time concentration monitoring of crystallisation processes (Abu Bakar *et al.*, 2009a).

The calibration model (8.2) was further validated against literature solubility data for potassium dichromate-water system (already shown in Section 8.4 equation (8.1)). An experiment was performed in which the temperature of a slurry containing excess solid was increased in several steps, as shown in Figure 8.9 (c). The temperature at each step was maintained for 45 minutes to ensure the complete equilibrium at that temperature. The samples for gravimetric analysis were taken around 40 minutes. The measured FBRM counts and absorbance values throughout the experiment are shown in Figure 8.9 (c). The number of FBRM counts/s has decreased as the temperature was increased from 15 to 45°C, because more solids dissolved with the increase of temperature. However, the absorbance has increased as the temperature has increased from 15 to 45°C. As the dissolution of particles increased in the solution due to increase in temperature the absorbance increased

with time. This effect was more significant than the week inverse relationship between absorbance and temperature. Figure 8.9 (b) shows a comparison between estimated concentrations for the solubility curve using the calibration model, literature data (Mullin, 2001) and the gravimetric analysis carried out at various temperatures. Very good agreement is observed, indicating the reliability of the calibration model.

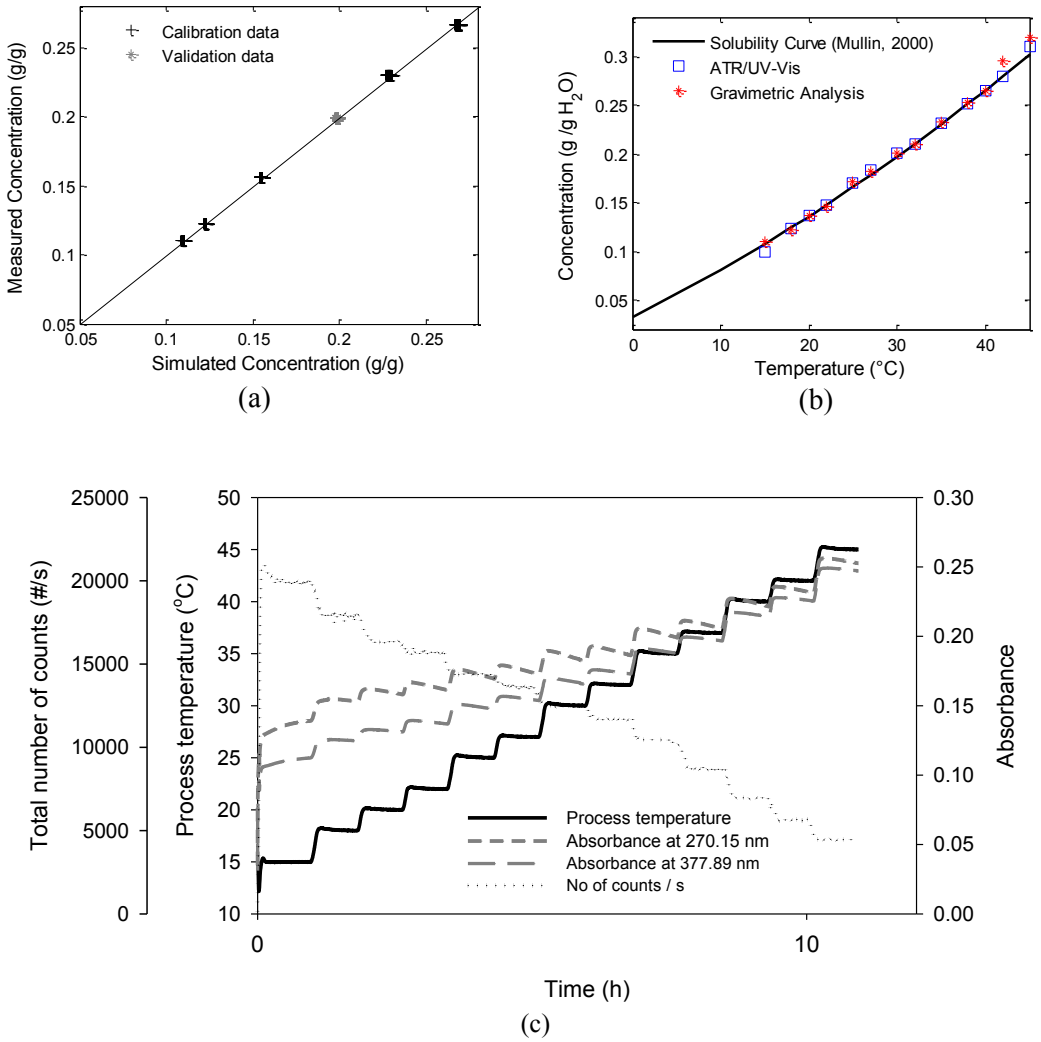

Figure 8.9: a) Estimation and validation of calibration parameters using measured and simulated concentrations; b) Comparison of concentration for solubility curve obtained from gravimetric analysis, experimental concentration and literature data to validate the calibration parameters; c) Process temperature, FBRM counts/s and absorbance values versus time during the equilibrated slurry experiment.

8.5 CSD measurements

On-line CSD measurement was carried out using a laser diffraction based, Malvern Mastersizer. The equipment can measure particle sizes from 0.108 to 1000 µm. The on-line

crystal size distribution was measured after every 3 minutes during the experiments. Symaptec Qicpic was used to measure the CSDs off-line. The equipment is based on image analysis and can measure particle size from 1 μm to 20 mm. Sympatec equipment can be used to measure CSD using both wet and dry dispersion methods and can be used for both on-line and off-line measurements.

8.5.1 Comparison of off-line and on-line measured CSD using different measurement techniques

An off-line comparison of the CSD measurements was carried out. Sampling of materials play a key role in these measurements therefore British sampling standard BS 5309-4 (British standard, 1976) was followed to make sure that samples were best representatives of the original product, especially for the off-line measurements. For comparison of the distributions using two different equipments, these measurements were converted into their pdf's and interpolated for the same number of size bins (discretisation) for the particle size range. The CSD measurements are highly effected by measurement techniques and for this purpose the laser diffraction based Malven Mastersizer was compared to the image analysis based Sympatec Qicpic equipment.

Figure 8.10 shows comparison of the off-line measured CSD using Malvern Mastersizer and Symaptec Qipcic, for five sieve size fractions: 63-75, 75-90,106-125, 150-180 and 212-250 μm. It can be observed from the results (shown in Figure 8.10) that the measured CSD's show the same trends for the same sieve fractions. The Off-line measurements using Sympatec Qicpic were narrower than the off-line measurements using Malvern Mastersizer for the same sieve fractions. The Symaptec Qicpic results are generally shifted towards smaller size particles compared to the distributions measured with the Malvern Mastersizer and showed narrower distributions. This can be due to the reason that both equipments have different measurement principle, and used different sample dispersion techniques. In Malven Masteriszer wet dispersion technique was used to measure the distribution. The solvent used to disperse the solid crystals was hexane (with refractive index of 1.38). However in case of Sympatec Qicpic dry dispersion method was used to measure the CSD. The dispersion technique may also influence whether particles in the samples agglomerated or not.

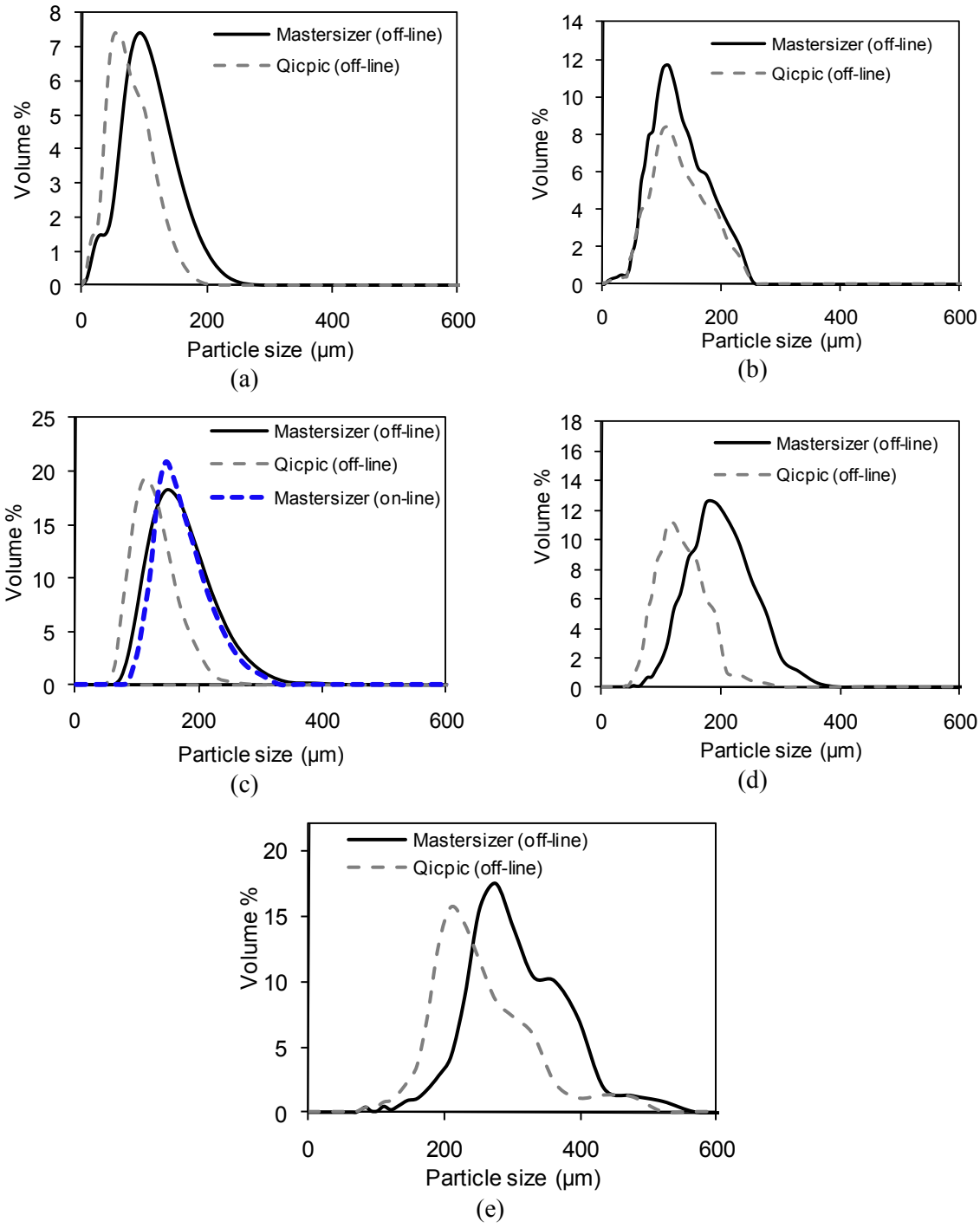

Figure 8.10: Comparison of CSD measured off-line and on-line a) 63-75 µm b) 75-90 µm c) 106-125 µm d) 150-180 µm and e) 212-250 µm, sieve fractions.

The comparisons of the CSD, using different equipment, measured off-line indicate that the reproducibility of the shape of the CSD is acceptable and the measurements can be useful for the model-based control strategies. However these results also demonstrate that the model parameters will also depend on the measurement technique used in the experiments.

Additionally, the off-line and on-line measured CSD's were compared for the size range used in the experiments to evaluate the efficiency of the on-line sampling method. This comparison is important to check the reproducibility of the measured CSD as there is always a chance of sedimentation and/or nucleation in the tubing. Additionally the refractive index of solvents hexane (in case of off-line measurement) and potassium dichromate dissolved in water (in case of online measurement) are significantly different from each other and may influence the CSD measurement. Therefore it was important to compare the off-line and on-line measurement for the same size fraction to make sure that the on-line configuration of Malvern Masteriszer was working correctly and there were no sedimentation or breakage problems. Figure 8.10 (c) shows that the CSD measured off-line and on-line using Malvern Mastersizer were very close, hence the setup with the on-line sampling loop can be considered to provide representative measurements.

8.6 Model identification and validation using combined QMOM-MOCH technique

8.6.1 Experimental results for model identification and validation

The operating conditions for the identification and validation experiments are given in Table 8.1. In experiment A a cubic profile was followed throughout the batch whereas in experiment B simple linear cooling was used. In both cases, seed was introduced, shortly after the supersaturated state had been reached and the process temperature was stabilised at 29 °C for ten minutes. Figure 8.11 (a) indicates that in the case of experiment A (with cubic cooling profile), no nucleation happened during the crystallisation since the FBRM number of counts/s is practically constant throughout the batch after the initial increase corresponding to the seed addition. However in experiment B, some secondary nucleation was observed, as shown in Figure 8.11(b). This secondary nucleation was observed around 35 minutes from the start of the batch and was the result of the fast supersaturation generation by the linear cooling profile. Experiment A was used for model parameter identification (following the same approach as described in Chapter 5) with the PBM solved using the QMOM-MOCH approach (described in Chapter 4), whereas experiment B was used for validation purposes.

Figure 8.11: Total counts measured by FBRM throughout the entire batch a) when the cubic profile b) when the linear profile was run for a duration of 60 minutes.

8.6.2 Model identification

The size-dependent growth parameters were determined for the batch cooling crystallisation of the inorganic compound, potassium dichromate ($K_2Cr_2O_7$) in water. The generic apparent size-dependent growth expression, given by equation (4.8), was used in the model identification. The optimisation problem for the parameter estimation and the calculation of error bounds was described in Section 5.5.1 and 5.5.2. The resulting model parameters for the potassium dichromate system are presented in Table 8.3. The dynamic evolutions of the experimental and modelled CSDs are in very good agreement during the entire batch, as shown in Figure 8.12 (a). It can be seen that due to the particular size-dependent growth kinetics of this system, the CSD broadens with decreasing height during the batch. The PBM with the identified growth parameters is able to describe the main features of the CSD throughout the entire batch. Figure 8.12 (b) and (c) show comparison between the experimental and modelled concentrations and weight mean size (d_{43}) throughout the batch, which are also in very good agreement.

Table 8.3: Estimated parameters for potassium dichromate-water system considering size-dependent growth.

Parameter	Units	Value	Error bonds at 95% confidence interval
Growth rate constant, (k_g)	$\mu m\, s^{-1}$	9.56	± 0.0832
Growth constant, (γ)	μm^{-1}	$7.5 \cdot 10^{-3}$	± 0.0021
Growth constant, (p)	--	1.24	± 0.0633
Growth order constant, (g)	--	0.80	± 0.2411

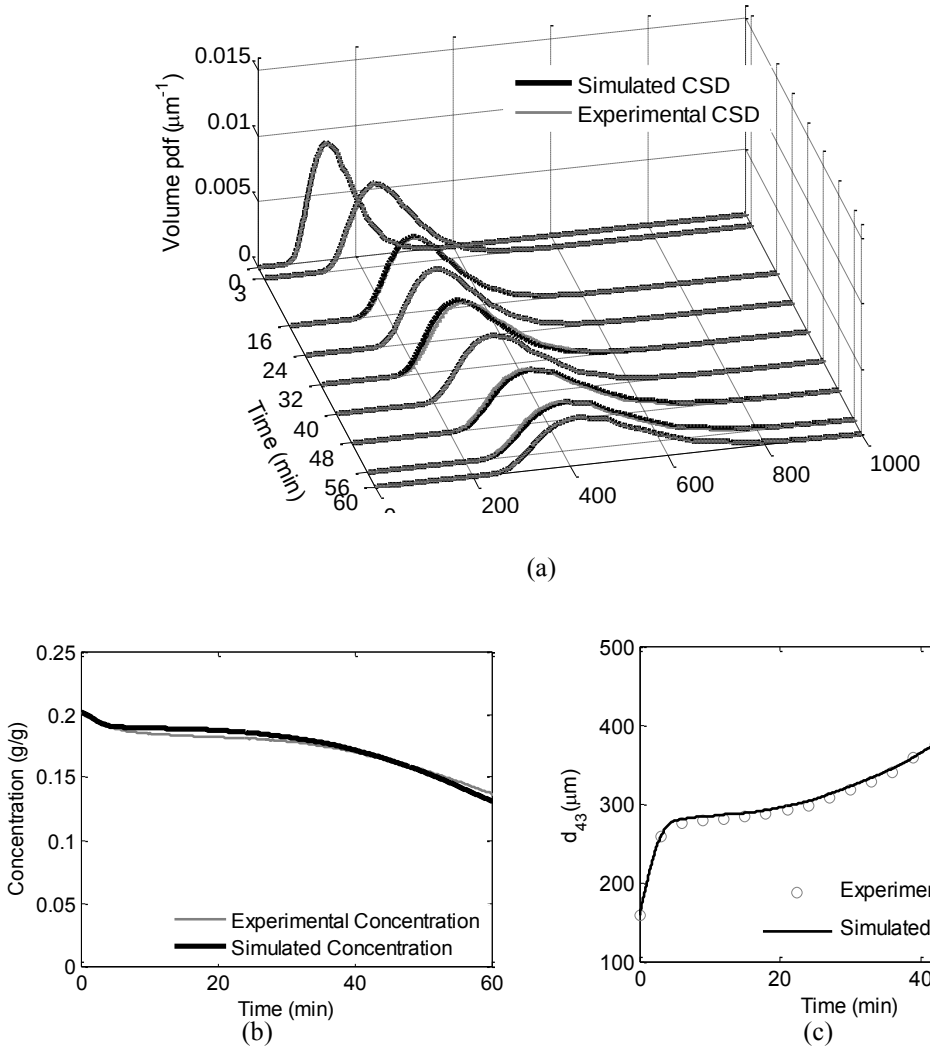

Figure 8.12: a) Dynamic evolution of the modelled and experimental CSD for potassium dichromate in water system for experiment A (seeded crystallisation with cubic cooling profile). Experimental and simulated results: b) concentration c) De Brouckere mean diameter (d_{43}) during the entire batch of experiment A.

8.6.3 Model validation

The linear profile was used for model validation. Figure 8.13 (a and b) show the validation results for the CSD and concentration for experiment B. Figure 8.13 (a) shows that towards the end of the batch, the CSD is slightly over predicted. Additionally, Figure 8.13 (a) indicates the apparition of a small (as volume pdf) secondary peak in the experimental CSD at 35 minutes during the process, which was due to the secondary nucleation event detected by the FBRM approximately at the same time, as shown in Figure 8.11 (b). This nucleation event was not considered in the model, which was based only on the growth kinetics and hence contributes to the over-prediction of the measured CSD by the simulation. Nevertheless, the maximum difference between the simulated and the experimental concentration is only 6.5%, which corresponds to higher consumption of solute concentration in the simulation, as shown in Figure 8.13 (b). This higher consumption of solute concentration also corresponds to the over-prediction of the experimental CSD by the simulation.

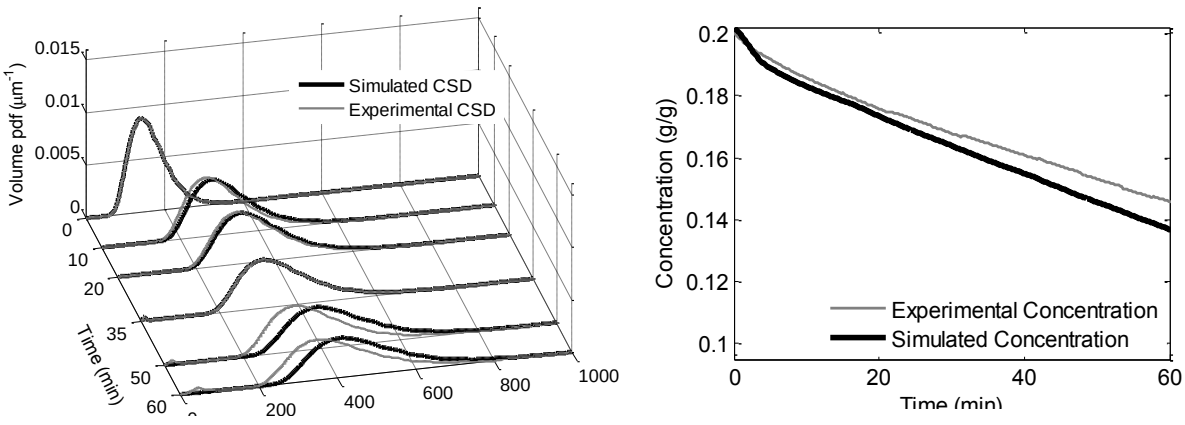

Figure 8.13: Experimental and simulated results for experiment B (linear cooling) to validate the modal parameters. a) Dynamic evolution of CSD and b) concentration throughout the batch.

For both experiments, A and B, the same amount of seed was used, which was retained between sieve sizes 106-125 μm (as described in Table 8.1). A sample microscopic image of the seed used in the experiments is shown in Figure 8.14 (a). Microscopic images of the products obtained at the end of experiments A and B are shown in Figure 8.14 (b and c),

respectively. It can be observed that the crystals obtained at the end of the cubic profile are larger and more uniform in size with few fines and very few agglomerates. However, the crystals obtained at the end of the linear profile are smaller, more agglomerated and with clear evidence of the existence of fine particles due to secondary nucleation, also indicated by the CSD measurement shown in Figure 8.13 (a).

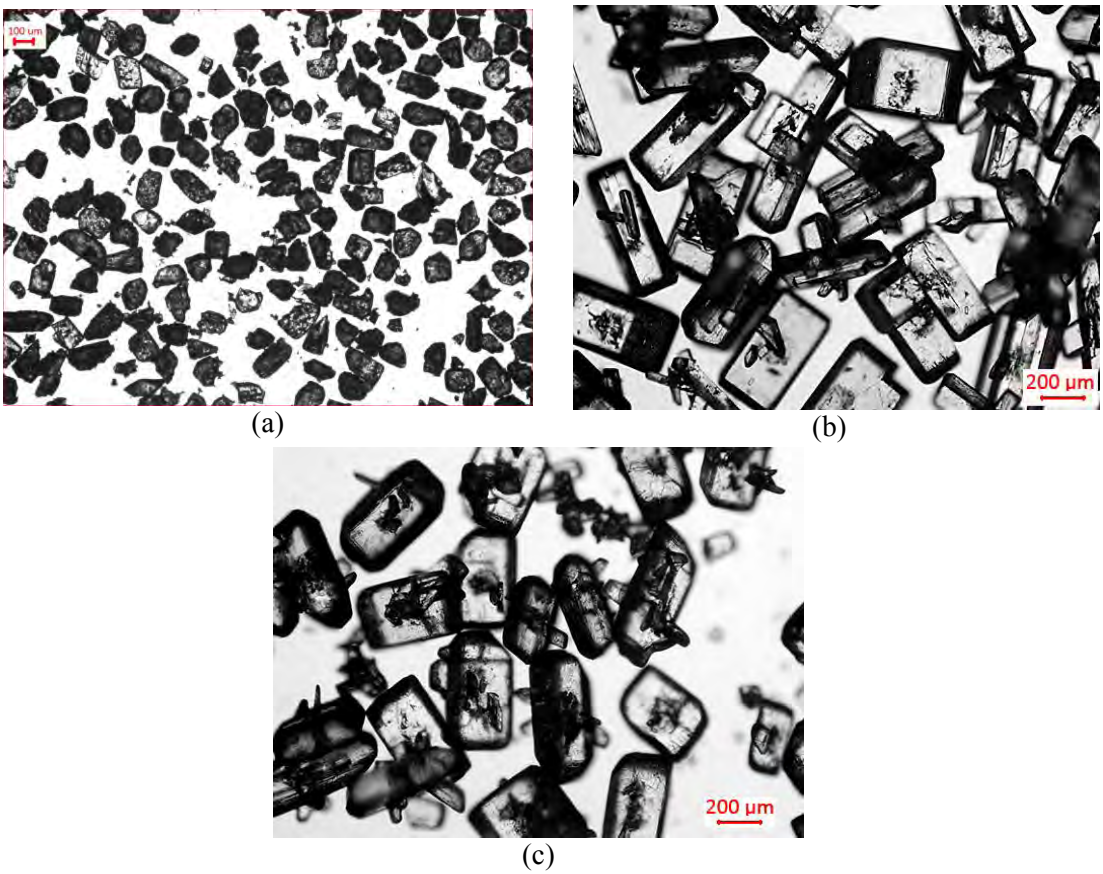

(a) (b)

(c)

Figure 8.14: Microscopic images of the a) seed crystals and b) crystals obtained at the end of experiment A (cubic profile) and c) crystals obtained at the end of experiment B (linear profile).

After parameter identification the experimental evaluation of the direct design approach is presented as previously discussed in Section 7.5 - 7.6. The direct design approach is based on the idea of operating the system within the MSZ. The supersaturation setpoint designed in the phase diagram is redefined in terms of temperature vs. time profile for practical implementation. Experimental evaluation of two temperature trajectories corresponding to lower and higher supersaturation levels was carried out with the aim to obtain the same target CSD. The two experiments are referred to as experiments C and D. The temperature

trajectories were optimised using the analytical CSD estimator, under constant supersaturation assumption.

8.7 Experimental evaluation of the direct design approach of supersaturation controlled crystallisation processes

8.7.1 Experimental setup

The schematic diagram of the experimental setup is shown in Figure 8.2. Same material, apparatus and seed preparation techniques were used as described in Sections 8.2.1- 8.2.3.

8.7.2 Determination of control design parameter (ϕ) for potassium dichromate-water system

For the implementation of the temperature trajectories for constant supersaturation, first the control design parameter is determined, using equations (7.6) - (7.9) by minimising the difference between the discretised target distribution and the predicted CSD obtained from the analytical estimator. The distribution obtained at the end of experiment A (cubic profile) was taken as target distribution. For this simulation, the same experimental conditions were used as shown in Table 8.1 (used for cubic profile). The initial seed distribution corresponds to the experimental seed CSD. Figure 8.15 shows the result of the control design parameter optimisation. The predicted CSD using the analytical CSD estimator was in good agreement with the target distribution. The optimised control design parameter for potassium dichromate-water system, corresponding to the chosen target distribution was $\phi = 0.1357\ (\min)$. Once the design parameters ϕ is obtained, it is possible to determine the temperature trajectories for a chosen supersaturation setpoint, S_{sp} or batch time, t_{batch}. The process conditions used for simulation are summarised in Table 8.4, for two different batch times, 180 min and 90 min, respectively. The corresponding supersaturation values were calculated using the optimal control design parameter ϕ. The growth parameters used for these simulations are given in Table 8.3.

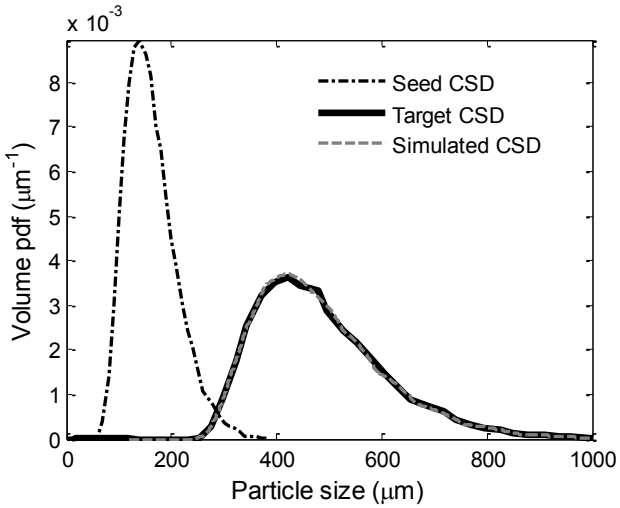

Figure 8.15: Comparison between simulated and target (experimental) product distributions using the optimised control design parameter $\phi = 0.1357$ min. Seed distribution corresponds to the experimental seed distribution.

Table 8.4: Operating conditions for simulations to design the temperature trajectories for selected batch times.

Process conditions	Experiment C	Experiment D
Initial concentration, (g/g of water)	0.1928	0.1928
Seed loading, (%)	1.5 % of solid content	1.5 % of solid content
Seed mass, (g)	1.2	1.2
Saturation temperature, T_{sat}, (°C)	30	30
Initial temperature (at seeding and start of profile), T_0, (°C)	29	29
End temperature, T_j (°C)	20	20
Supersaturation setpoint, S_{sp} (g/g of water)	1.2490×10^{-4}	2.9706×10^{-4}
Total batch time, t_{batch}, (min)	180	90
Control design parameter, (ϕ)	0.1357	0.1357

8.7.3 Results and discussion

Two temperature trajectories were designed (as described in Chapter 7) to achieve the same target distributions for a lower and a higher supersaturation set-point. The first temperature trajectory was designed for a batch time of $t_{batch} = 180$ min (experiment C). For the second

experiment (experiment D) the aim was to achieve the same target distribution within a smaller batch time. Therefore for the second experiment the batch time was reduced to 90 mins which results in a corresponding higher supersaturation setpoint than for experiment C. The resulting temperature trajectories for the corresponding supersaturation setpoints (S_{sp}) are shown in Figure 8.16.

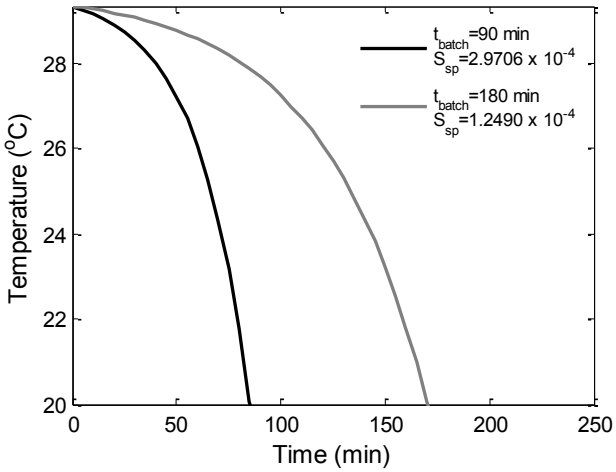

Figure 8.16: Temperature profiles obtained for different batch times (t_{batch}) and corresponding supersaturation setpoints (S_{sp}), corresponding to the same design parameter $\phi = 0.1357$ min .

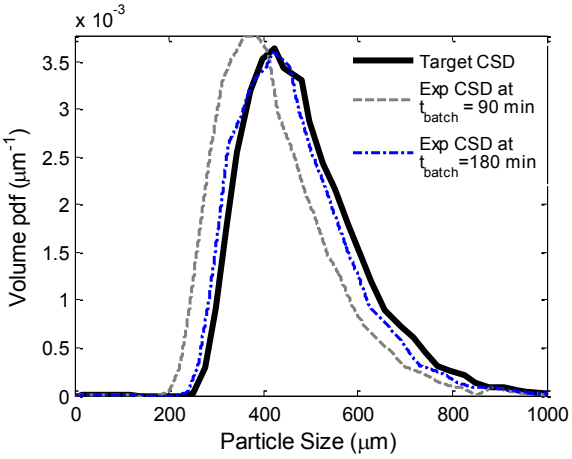

Figure 8.17: Comparison of measured product CSDs for experiments C and D and the target distribution for which the temperature trajectories were designed.

The designed temperature trajectories were implemented as setpoints for the temperature controller in the experiments according to the direct design concept described in Chapter 7.

Figure 8.17 depicts the final product CSDs obtained at the end of experiments C and D (measured with Malvern Mastersizer) in comparison with the target distribution used for the SSC design (corresponding to $\phi = 0.1357$ min). It can be seen that the product CSD obtained from experiment C is very close to the target. The batch time for experiment D was only half of the duration of experiment C. The product CSD resulting from experiment D is shifted to smaller crystal sizes however it is still relatively close to the desired target distribution. These results indicate that using the direct design concept it is possible to achieve similar product distributions with significantly reduced batch time. The microscopic images of the products shown in Figure 8.18 also provide evidence for the similar product qualities from the two experiments, with somewhat smaller crystals from the shorter batch (experiment D).

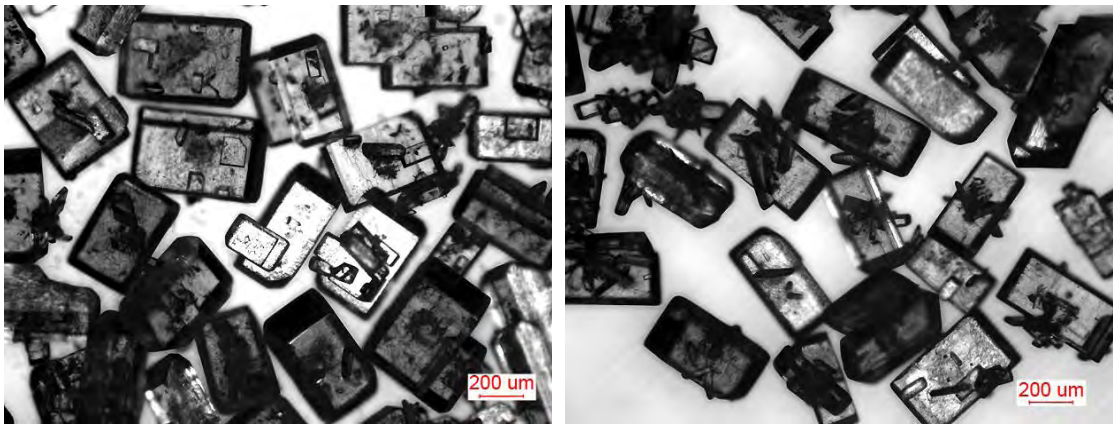

Figure 8.18: Microscopic images for the products at the end of the batches a) experiment C (180 minutes) and b) experiment D (90 minutes).

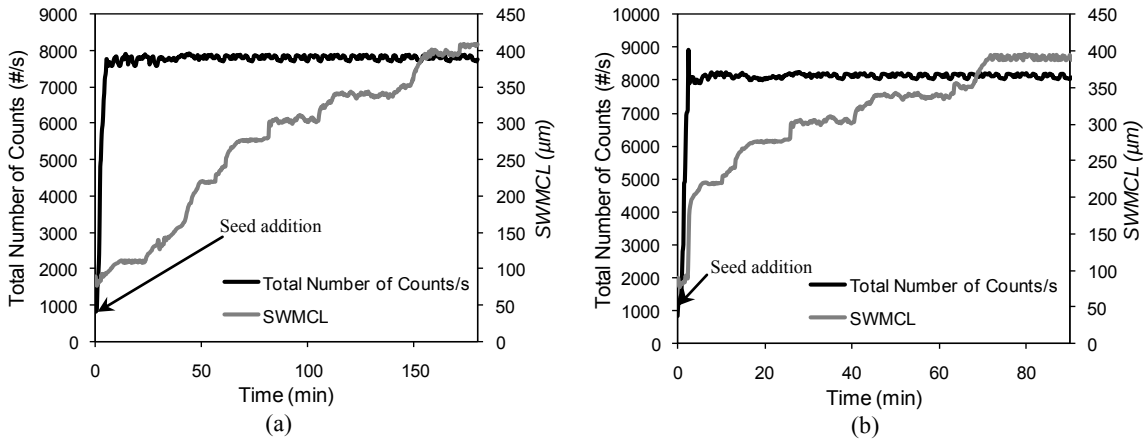

Figure 8.19: Total number of counts/s and square weighted mean chord length (*SWMCL*) measured throughout the experiments for a) experiment C and b) experiment D.

The total number of counts/s and square weighted mean chord length (*SWMCL*) were also measured throughout the experiments C and D, and are shown in Figure 8.19 (a and b). It can be observed that the total number of counts/s remained constant throughout both experiments, indicating that no nucleation has occurred during the batches. The square weighted mean chord length (*SWMCL)* has increased during both experiments indicating significant growth throughout the batches. The *SWMCL* at the end of experiment C is slightly larger than at the end of experiment D, also indicating somewhat more crystal growth during the longer batch.

Theoretically the two experiments should have yielded the same product CSDs. To explain the differences between the resulting product CSDs the supersaturation profiles during the experiments are shown in Figure 8.20 together with the setpoint and actual process temperatures during the two experiments. For both experiments the measured supersaturation values are generally higher than the theoretical setpoints (which were 1.2490×10^{-4} g/g water for experiment C and 2.9706×10^{-4} g/g water for experiment D). However, overall the measured supersaturations exhibit relatively constant profiles during the batches. Figure 8.20 (b) indicates that for experiment D initially the supersaturation was significantly higher than the desired setpoint, however it rapidly decayed to a relatively constant value for the duration of the rest of the batch. For experiment C the supersaturation was maintained more constant during the entire batch. The measured supersaturation appears to be larger than the theoretical setpoints in both cases; however the product distributions are close to the target (very close for experiment C) and shifted towards smaller crystals for experiment D. This is in contradiction with the consistently larger supersaturation values measured (which should have yielded larger product CSD than the target for both cases), indicating that most likely the concentration measurement was affected by errors. The potassium dichromate in water is a very fast growing system, thus the theoretical supersaturation setpoints are very close to the equilibrium. The precision of the concentration measurement is not sufficient to indicate accurately such small levels of supersaturation. However the setpoint temperature profiles were relatively well followed, except during the last 20 min of the batches, when the steep decrease in the temperature setpoints was difficult to track by the temperature controller. Nevertheless, these results indicate the practical advantages of the direct design approach, which allows the

implementation of an inferential constant supersaturation trajectory by tracking a properly designed temperature profile. Since temperature measurement is more accessible with high accuracy even in industrial setups, the direct design approach can lead to good CSD control (as shown in Figure 8.17) even when the lack of accurate concentration measurement makes the supersaturation control impractical.

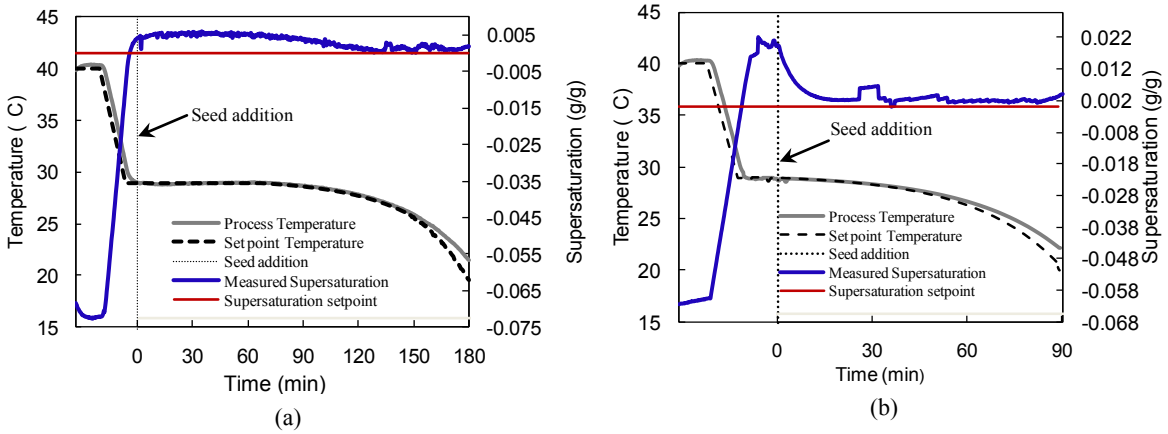

Figure 8.20: Measured and designed process temperature and measured supersaturation with setpoint supersaturation, throughout the two experiments a) experiment C (180 min) and b) experiment D (90 min).

The methodology suggests that even with errors in the supersaturation measurement if the temperature trajectories are designed and implemented properly, it is possible to produce the desired product distribution. The key parameter for designing the temperature trajectories is the supersaturation control design parameter ϕ. The parameter ϕ can also be used for the evaluation and comparison of supersaturation controlled processes in terms of the product CSD. Since increasing the supersaturation setpoint to enhance growth rate, leads to decreased batch time and hence shorter time period in which crystals are allowed to grow, there is an inherent compromise between the chosen supersaturation setpoint and the resulting batch time. By knowing the supersaturation values and the duration of the corresponding batches, calculating ϕ, indicates which batch will produce larger crystals. The larger the value of ϕ, the larger the crystals will be (under the assumption of growth dominated process).

To evaluate the difference in the final distributions obtained at the end of the two experiments the supersaturation control design parameter (ϕ) was calculated for both experiments using the average values of the measured supersaturation. For experiment C, with $t_{batch} = 180 \text{ min}$, the average value of supersaturation for the entire batch was $S_{avg} = 0.00331$. The actual value of the supersaturation control design parameter was $\phi = 1.86504 \text{ min}$. In the case of experiment D, with $t_{batch} = 90 \text{ min}$, the average value of supersaturation was $S_{avg} = 0.00364$ corresponding to a value of $\phi = 1.0077 \text{ min}$. The supersaturation control design parameter value for experiment C was larger than for experiment D, which corresponds to the larger growth of the crystals. The larger error in the product CSD for the faster batch (experiment D) may be explained by the larger error in the temperature control (especially during the last 20 min of the batch, as shown in Figure 8.20), caused by the difficulty in tracking the steep nonlinear temperature trajectory by the standard PID controller. Additionally conducting the crystallisation at a larger supersaturation may have triggered additional mechanisms not considered in the model, such as agglomeration and nucleation. Although the FBRM results do not indicate significant increase in the number of counts/s for experiment D, some evidence of smaller crystals and agglomerates was observed by the microscopic examination of the product from experiment D, as also indicated by Figure 8.18 (b).

To investigate further the differences between the product CSDs obtained in the two experiments, the actual experimental process temperature trajectories for both experiments were simulated, using the population balance model solved by the combined QMOM-MOCH technique. The simulated distributions were compared with the target and experimental CSDs obtained at the end of the two experiments. Figure 8.21 (a) indicates that the simulated distribution for experiment C (long batch, lower supersaturation) was very close to the measured and target distributions. In case of experiment D (short batch, higher supersaturation) the simulated CSD is closer to the measured CSD, as shown in Figure 8.21 (b). This suggests that for experiment D, the difference between the experimental product CSD and target distribution is partially indeed due to the larger error in tracking the theoretical temperature setpoint profile during the experiment. However, since the simulated CSD still shows some difference compared to the measured CSD, it is likely that other

mechanisms not included in the model (e.g. nucleation, and agglomeration promoted by the higher supersaturation) have also contributed to the observed discrepancy between the product and target CSDs. Additionally, since in the case of the short profile (90 min) the actual process temperature was lagging behind the setpoint, at the end of the 90 min the actual final temperature in the simulation was higher than the target temperature value at that moment. This leads to smaller yield for the faster experiment, hence the simulated CSD is shifted to the left.

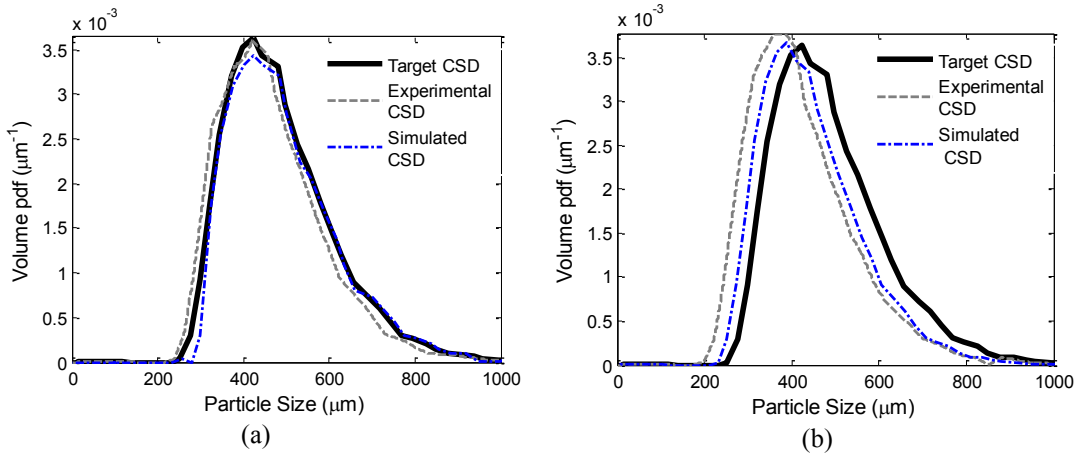

Figure 8.21: Comparison of target distribution, measured distribution and simulated distribution using the measured process temperature trajectories for a) experiment C (180 min) and b) experiment D (90 min).

8.8 Conclusions

The chapter describes the materials and methods used for the experiments carried out to estimate the parameters for the size-dependent growth kinetics for the seeded-batch cooling crystallisation process of potassium dichromate-water system. A specially designed experimental setup was developed for the experiments, which included several PAT tools, such as ATR-UV/Vis spectroscopy for *in situ* concentration measurement, particle counts and chord length measurement with FBRM, as well as on-line CSD measurement using a laser diffraction equipment with a sampling loop (Malvern Mastersizer). To obtain the concentration, a multivariate linear regression-based calibration model was developed that

correlated the two peak absorbance values of the potassium dichromate-water system measured by the ATR-UV/Vis probe with the concentration, correcting for the effect of the temperature on the absorbance.

The experimental CSD and concentration measurements were used to identify the size-dependent growth kinetics for the system. The combined quadrature method of moments and method of characteristics (QMOM-MOCH) approach was used for the solution of the population balance equation. The kinetic parameters for size-dependent growth were determined to capture the dynamic evolution of the shape of the crystal size distribution, as well as the experimental concentration profile. The model was validated against experimental data and the results indicated a very good agreement between simulations and experiments.

In the second part of the chapter, the direct design approach for supersaturation controlled growth dominated processes was implemented for the potassium dichromate-water system. The supersaturation control (SSC) design parameter was determined via nonlinear optimisation to achieve a desired target distribution. The SSC design parameter was used to determine the temperature trajectories which would lead to the same product CSDs for a longer and a shorter batch, using the constant supersaturation and growth dominated process assumptions. The resulting temperature trajectories with lower and higher supersaturation levels (longer and shorter batches) were implemented to achieve the desired target shape of the CSD. The results indicate that with suitable temperature control it is possible to achieve the required shape of the crystal size distribution and maintain constant supersaturation level, while the batch time can be reduced significantly. However the approach has to be applied with caution since by reducing the batch time the corresponding supersaturation level increases, which may trigger other mechanisms (e.g. nucleation, agglomeration) not conserved in the direct design approach.

Chapter 9
Experimental and simulation-based evaluation of seed quality on product CSD and seed recipe design for shaping the product CSD in batch crystallisation

9.1 Introduction

Usually, most batch crystallisation processes involve seeding. Seed loading varies from as low as 0.5% to as high as 10% depending on the size and volume of the batch crystalliser. Seeding has been known for a long time as an effective technique to stabilise batch crystallisation processes (Mullin, 2001). In seeded crystallisation, the supersaturation is maintained at a low value away from the nucleation curve, by slow cooling, optimal cooling (or anti-solvent addition), or in more recent systems, at a desired constant value throughout the entire batch by application of properly designed control algorithms, using either model-based optimisation (Chung *et al.*, 1999; Nagy, 2009; Ward *et al.*, 2006; Xie *et al.*, 2001) or model-free approaches based on supersaturation control (Sarkar *et al.*, 2006; Zhou *et al.*, 2006a) and direct design concepts (Abu Bakar *et al.*, 2009b; Woo *et al.*, 2009a). These approaches can be implemented in open-loop or closed-loop structure with respect to the product property. Although product property-based closed-loop implementation will show a certain level of inherent robustness to uncertainties (Heffels and Kind, 1999; Nagy and Braatz, 2003a), and robust open-loop control strategies have also been developed (Nagy and Braatz, 2004), these advanced control approaches are very seldom applied in practice due to their increased implementation complexity. In the vast majority of cases crystallisation processes are controlled by tracking operating trajectories determined off-line by nominal open-loop optimisation or trial-and-error procedures. In these cases the properties of seed play an important role and strongly affect the quality of the crystal size distribution obtained at the end of the batch. Although several techniques have been proposed for the *in situ* generation of seeds via controlled nucleation/dissolution events (Abu Bakar *et al.*, 2009b; Woo *et al.*, 2009a), seeded crystallisation is still predominantly applied in the chemical and pharmaceutical industries using seeds generated from the crystallisation product.

Generally many steps are involved during the preparation of seed, such as milling, blending, grinding, sieving, washing etc. (Adi *et al.*, 2007; Wibowo *et al.*, 2001; Wibowo and Ng, 2001). All these processes affect the quality and properties of the seed and significant variations in seed quality may be observed based on the method used to produce the seed (Jagadesh *et al.*, 1996; Kubota *et al.*, 2001; Ludwick and Henderson, 1968). In addition, quantitative information on the quality and property of seeds, and the variation in these, are seldom considered in the control of the process. Variations in seed CSD and properties are generally considered as uncertainties rather than actuators for the control of final CSD. Seeding seems to be treated as an art rather than science (Adi *et al.*, 2007). There is a very limited amount of work available in the literature, which considers the effect of seed on the final CSD, and all focus on empirical evaluations of the operating conditions and seed amount on the final product, or on the design of the shape of the seed distribution to achieve a desired target distribution (Bohlin and Rasmuson, 1996; Kalbasenka, 2009; Lung-Somarriba *et al.*, 2004).

The first part of the chapter provides and experimental and simulation based analysis of the effect of seed quality on the shape of the crystal size distribution obtained at the end of the batch. To study these effects seeds were prepared using different processes, such as milling, washing and sieving. Process Analytical Technology (PAT) equipment can play an important role in studying and monitoring the seed quality and its effect on the product (Yu *et al.*, 2004). The application of these tools has lead to novel control approaches for crystallisation processes, which can lead to significant product quality improvements (Braatz, 2002; Fujiwara *et al.*, 2005). The data provided by these instruments during the development stage can provide key information about the seed quality and help to improve and maintain the end results consistent. In this study focused beam reflectance measurement (FBRM) is used to detect the evolution of the number of particles during the crystallisation process. The data is used in combination with on-line CSD measurement techniques, using laser diffraction equipment (Malvern Mastersizer). The final CSD is dependent on the supersaturation profile created during the batch time. In this work the concentration is measured *in situ* using attenuated total reflectance (ATR) UV/Vis spectroscopy, calibrated by correlating the change in absorbance to the concentration variation and correcting for the effect of temperature. The results obtained from these *in situ* and on-line PAT instruments

are analysed to evaluate the effect of the seed quality, resulting from various preparation protocols, on the product CSD. The experiments illustrate that seeds having a large amount of very fine particles resulting from the milling process (which usually appear as dust) give rise to agglomeration of these small particles. Additionally, the irregular morphology of milled crystals can influence the shape of the crystal size distribution at the end of the batch. The fine particles in the seed lead to the formation of bimodal product distribution with significant amount of fines and agglomerates. These can affect the efficiency of the downstream processes such as filtration and drying since fine particles can clog filters and agglomerate, causing solvent inclusion in the product. The selected model system was potassium dichromate in water, for which a population balance model (PBM) was also developed and validated using experimental data. The process is growth dominated and an apparent size dependent growth mechanism can describe the dynamic evolution of the experimental CSD and concentration. The model is solved using an efficient solution approach based on a combined quadrature method of moment and method of characteristics (QMOM-MOCH) (Aamir *et al.*, 2010; Aamir *et al.*, 2009b). The simulation results combined with the experimental evaluation, supported by the use of a set of PAT tools, show that during the process development stages the variation in seed quality can be detected and should be taken into account in model-based control strategies.

9.2 Seed preparation to analyse the quality of seed

Three different types of potassium dichromate seeds were prepared using different combinations of milling, sieving and washing methods. Table 9.1 summarises the process conditions used for each method of seed preparation.

9.2.1 Crystallised and sieved seed (seed A)

Potassium dichromate and water solution was prepared corresponding to a solubility of 20 g of potassium dichromate per 100 g of water at 30°C. Potassium dichromate was dissolved in water by heating to 40°C at a rate of 0.8°C/min. The solution was equilibrated at 40 °C for 20 minutes, to ensure complete dissolution of solids and then the temperature of the solution was reduced from 40°C to 18°C following a linear cooling profile at a rate of 0.5°C/min. The solution was left at 18°C for 15 minutes so that newly nucleated crystals could grow.

The crystals obtained were filtered, dried and then sieved. The sieve sizes used were: 500 μm, 355 μm, 300 μm, 250 μm, 300 μm, 200 μm, 150 μm, 125 μm, 106 μm, and 90 μm (coarser size on the top and finer at the bottom). The run time was set to 90 minutes, and the rotation and shaking caused the crystals to distribute throughout the sieve stack. The product retained between sieve sizes 106-125 μm was collected for seeding. Figure 9.1 (a) and (b) show the SEM images of the obtained seed. It can be clearly observed that seed contains no fine particles. Crystals have distinctive shape and they look uniform in size and shape. However, a small amount of broken crystals can also be observed. This seed would be referred to as "Seed A" hereafter.

Table 9.1: Process conditions used for the preparation of seed.

Process conditions	Crystallised sieved seed	Milled washed sieved seed	Milled sieved seed
Crystallisation	√	√	√
Milling	-	√	√
Milling time	-	45 min	45 min
Washing	-	√	-
Washing time	-	25 mins	-
Solvent for washing	-	Iso-Proponal (IPA)	-
Drying after washing with solvent	-	√	-
Drying time (min)	-	20	-
Sieving	√	√	√
Sieving time	90 min	25 min	25 min
Sieve size $\mathcal{L}$ (μm)	106-125	106-125	106-125
Referred as	Seed A	Seed B	Seed C
Remarks	Crystallised seed retained on 106 μm sieve was collected as crystallised and sieved seed.	Half of milled seed was washed with solvent and sieved. The seed retained on 106 μm sieve was collected as milled washed sieved seed.	Remaining half of milled seed was sieved without washing. The seed retained on 106 μm sieve was collected as milled sieved seed.

9.2.2 Milled, washed and sieved seed (seed B)

The crystallised seed retained between sieve sizes 300 to 500 μm was collected and milled in a traditional ball mill. The milling was carried out for 45 minutes with four metallic balls.

After every 5 minutes, the sample was taken out and sieved to reduce excessive powder formation. In total, 20 g of milled seed was collected at the end of the milling. Half of the collected seed (10 g) was washed thoroughly with iso-proponol (IPA) solvent for 25 minutes to remove fine particles and dust (very fine particles).

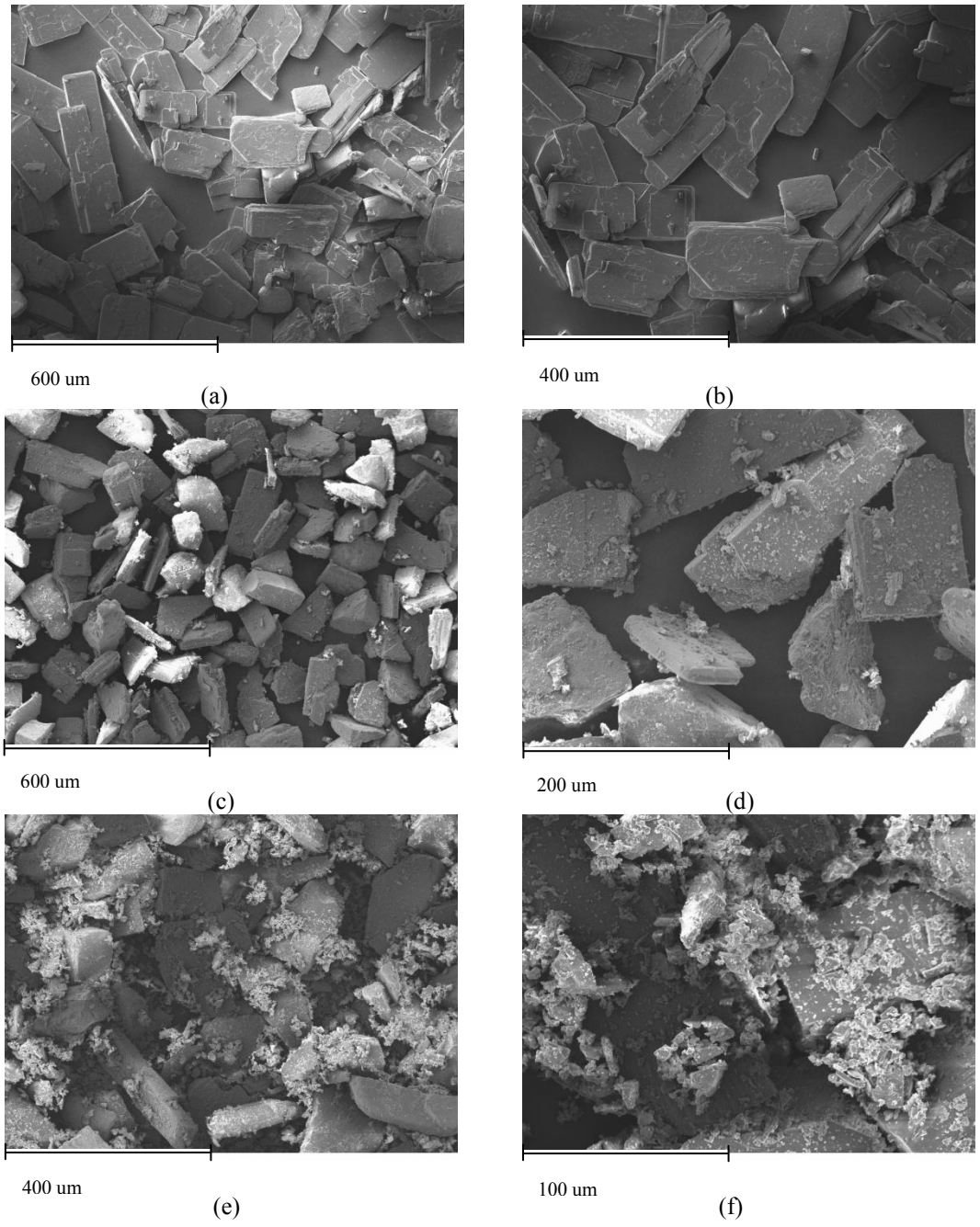

Figure 9.1: SEM images showing the size and the surface of crystals prepared by three different methods. Crystallised-sieved seed (a-b) , milled-washed-sieved seed (c-d) and milled-sieved seed (e-f).

After washing, the seed was dried for 20 minutes, then sieved again and the seed retained between sieve sizes 106 -125 μm was collected as final product. Figure 9.1 (c) and (d) show the SEM images of the milled, washed and sieved seed. Due to milling, there is no distinctive shape of the crystals and the majority of particles are broken. Some dust (very fine particles) and small particles attached to the surface of the crystals can be clearly observed, despite the seed being thoroughly washed with IPA. This seed is referred to as "seed B" hereafter.

9.2.3 Milled and sieved seed (seed C)

The other 10 g of seed obtained after milling was sieved without any washing and the solid retained between sieve sizes 106-125 μm was collected as seed. Figure 9.1 (e) and (f) show the SEM images of the milled and sieved seed. As expected, the SEM images indicate that the seed produced by milling and then sieving has the worst quality compared to seeds A and B, having large amount of very fine particles (dust). This seed is referred to as "seed C" hereafter.

9.3 Results and discussion

Experimental investigations of the batch cooling crystallisation of potassium dichromate in water were carried out. The material used for these experiments is described in Section 8.2.1 and the experimental setup is shown in Figure 8.2. The experimental data was obtained using a laboratory scale cooling crystallisation system. The experimental conditions are summarised in Table 9.2.

During these experiments FBRM was used to monitor the dissolution, Ostwald ripening or secondary nucleation. ATR/UV-Vis spectrometer was used to measure the concentration and the on-line Malvern Mastersizer was employed to measure the crystal size distribution. Sampling time for on-line CSD measurement was 3 minutes. The same amount of seed was added in all three experiments (1.2. g, corresponding to 1.5 % seed loading), and the same initial concentration was prepared for all cases. The relative errors calculated between the concentrations prepared and the values measured by the ATR-UV/Vis, after complete dissolution, for the three different experiments were 0.5 %, 0.25 % and 1.5 %, respectively, indicating that the initial concentration was reproducible, within reasonable limits.

Temperature was maintained at 29°C for 10 minutes and the seed was added before implementing the cubic trajectory. The same procedure was repeated for all three experiments.

Table 9.2: Operating conditions for experiments using different quality seeds.

Operating conditions	Values
Temperature profile followed	Cubic $T_{cubic} = T_0 - (T_0 - T_f)(t / t_{bacth})^3$
Points for smooth profile, (N)	60
Initial concentration, (g/g of water)	0.19
Seed loading, (%)	1.5 % of solid content
Sieve sizes for seed, (μm)	106-125
Seed mass, (g)	1.2
Saturation temperature, T_{sat}, (°C)	30
Initial temperature (at seeding and start of profile), T_0, (°C)	29
End temperature, T_j (°C)	20
Relative error between prepared and measured initial concentration for three experiments	
Experiment when seed A was used	0.50 %
Experiment when seed B was used	0.25 %
Experiment when seed C was used	1.50 %
Sampling time for on-line measurements of CSD, (min)	3
Sampling time for ATR-UV/Vis and FBRM (s)	20
Batch time, t_{batch} (min)	60

9.3.1 Comparison of FBRM data

The FBRM counts were monitored throughout the experiments. Figure 9.2 shows the FBRM data resulting from the three experiments. The total counts for FBRM increased after seed addition. Seed A yields the smallest number of counts/s (around 8200 counts/s), after introduction into the system, whereas in the case of seed B the total counts increased to 9500 counts/s. This is in correlation with the seed quality shown in Figure 9.1 that indicates more fines in the case of seed B. For seeds A and B after addition, the total counts/s measured by

FBRM show no further increase or decrease, which indicates that these systems were supersaturated and there was no secondary nucleation throughout the experiment.

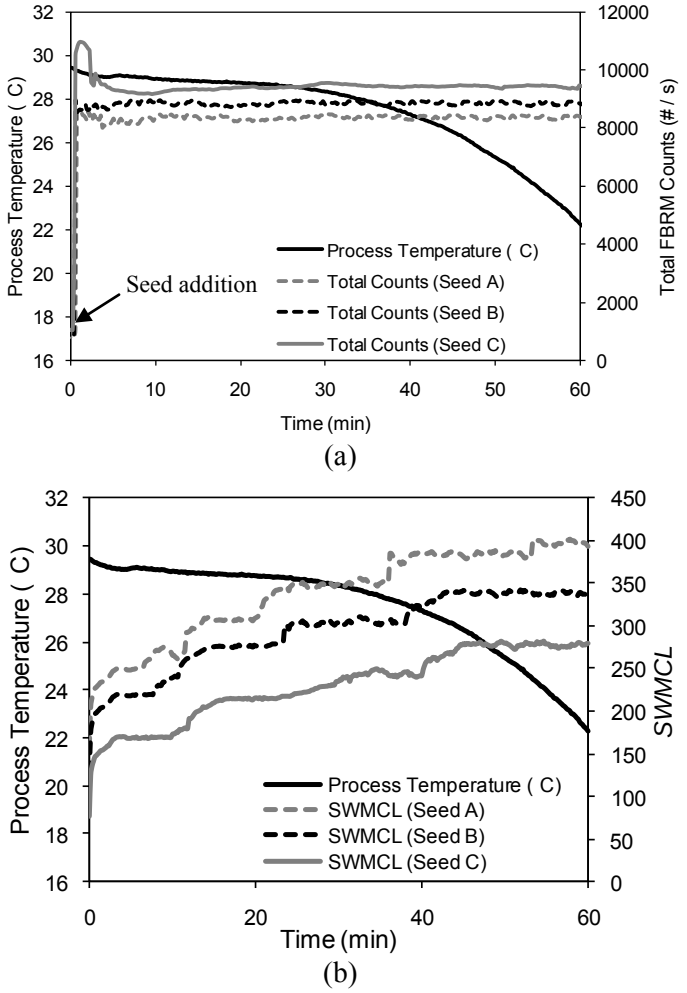

Figure 9.2: a) Comparison of measured total counts/s using FBRM and b) comparison of square weighted mean chord length (SWMCL) for the experiments using the three seeds (A,B and C) of different quality.

In the case of the experiment with seed C, immediately after the introduction of the seed, the total counts increased to the highest value of 11,000 counts/s. As expected, this indicates a significantly larger number of particles compared to the case of seeds A and B, due to the large amount of fines contained in the seed (as shown in Figure 9.1). After the initial increase to 11,000 counts/s the number of counts deceased to 9500 counts/s. The sudden decrease in the number of counts, without increase in concentration, as shown in Figure 9.3, can be explained by Ostwald ripening. During Ostwald ripening the smaller crystals act as nutrients for the bigger crystals. As the larger crystals grow, the area around them is depleted of smaller crystals. The disappearance of smaller particles and solute deposition on larger

particles is a spontaneous process. Molecules on the surface are energetically less stable than the ones already well-organized in the crystal system. Large crystals, with their greater volume to surface area ratio, represent a lower energy state than smaller crystals, that have larger surface area to volume ratio. Thus the small particles disappear and the large ones grow. In case of seed C there is a large amount of very fine particles. Thus, ripening can be observed during the experiment and process analytical equipment such as FBRM is able to detect this process. Figure 9.3 indicates that the concentration decreased during the initial period of the batch. Hence the decrease in the number of counts is not caused by dissolution, further supporting the occurrence of the ripening phenomenon.

The square weighted mean chord lengths were also measured throughout the batch, and are shown in Figure 9.2 (b). It can be observed that in case of experiment with seed A the initial *SWMCL* is larger and the crystal growth was more pronounced than in the case of the experiments with seeds B and C, which contain more fines. The smallest initial size and least crystal growth was observed in case of the experiment with seed C.

9.3.2 Comparison of concentration profiles

The absorbance was measured during all three experiments and was converted to concentration (using the calibration parameters shown in Table 8.2). Figure 9.3 indicates that at the time of seed addition the initial concentrations were close and the solution was supersaturated (no increase in concentration after seed addition). Potassium dichromate is a fast growing system, which is also indicated by the rapid decrease in the concentration for all three experiments during the 1 hour batch, during which the FBRM indicated no nucleation. The concentration profiles obtained from the experiments with the three different seeds suggest that the crystalline seed has consumed the most solute. Based on the final concentration, the yields for the experiments with seeds A, B and C were 33%, 31% and 26%, respectively. The final concentration in the case of seeds A and B are relatively close, whereas the experiment with seed C shows the least solute consumption. Thus, the most growth of crystals is expected in case of seed A, whereas least growth is expected in the case of seed C, which was also indicated by the *SWMCL,* as shown in Figure 9.2 (b). The microscopic images of the crystalline product obtained at the end of the batch also confirm the same conclusion, as shown in Figure 9.4 (b), (d) and (f).

Figure 9.3 also suggests that the experiment with seed A not only results in higher yield at the end of the batch, but also indicates a faster initial growth during the first few minutes of the batch. This can be explained on one hand by the slightly larger initial supersaturation than for the experiments with seed B and C, but also by the form of the growth kinetics, and the lack of very fine particles, which could promote Ostwald ripening. The size dependent growth expression given by eq. (4.8) indicates that larger crystals grow faster. The initial shape of seeds A was in general uniform (as shown in Figure 9.4 (a)) and the average size is significantly larger than for seeds B and C (compare Figure 9.4 (a), (c) and (e)), hence a more pronounced growth can be expected.

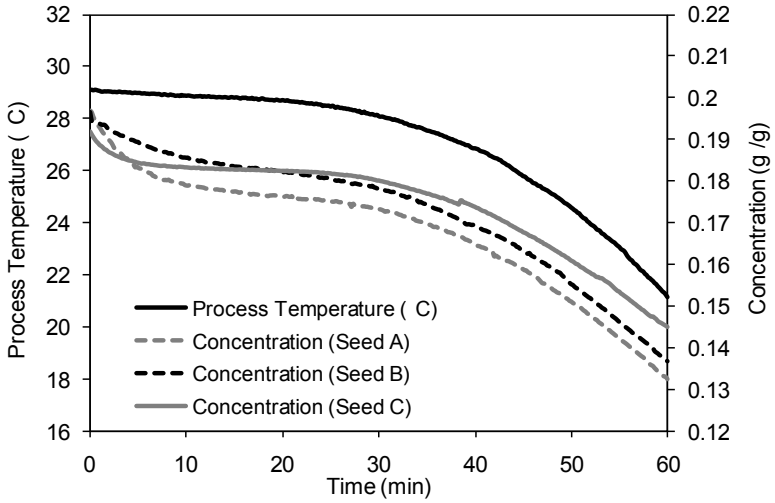

Figure 9.3: Comparison of concentration profiles measured using ATR-UV/Vis spectroscopy for the experiments with the three seeds (A, B and C) of different quality.

In the case of seed C, the presence of a large amount of small particles causes a smaller decrease in the initial concentration. This can be explained by the fact that in this case, the growth initially is mainly governed by the Ostwald ripening phenomenon. Thus the nutrient for the growth of part of the seed crystals initially comes from the very fine particles and not from the solute, yielding slower depletion of the solute concentration.

9.3.3 Comparison of microscopic images

The microscopic images shown in Figure 9.1 and Figure 9.4 (a), (c) and (e) indicate a significant variation in quality, despite the seeds were obtained from the same sieve fraction.

In case of seed A, the crystals have distinctive shapes and contain very few fine particles, as shown in Figure 9.4 (a). In case of seed B the particles appear under irregular shapes caused by the breakage due to milling. The seed was thoroughly washed to remove fines and dust but some fine particles can still be observed, as shown in Figure 9.1 (c)-(d) and Figure 9.4 (c). Seed C particles have no distinctive shapes and contain a significant amount of fines with many small particles attached to the surface of the crystals as shown in Figure 9.1 (e)-(f) and Figure 9.4 (e).

As expected the end products obtained from these three seeds are also significantly different from each other, as shown in Figure 9.4 (b), (d) and (f). The end crystals obtained from seed A are uniform and large in size, (as shown in Figure 9.4 (b)). The crystals obtained at the end of the batch using seed B have distinctive shape but relatively significant agglomeration can also be observed, as seen in Figure 9.4 (d). The growth of crystals is less than in the case of the final product obtained from seed A. Figure 9.4 (f) indicates that for the experiment with seed C, the end product has a large quantity of agglomerates and fines with fewer large crystals. The overall growth of crystals is less than in both previous cases. The agglomeration observed in the product crystals is the result of the increased tendency of small particles to agglomerate. The agglomeration of the fine particles in the seed competes with their consumption through Ostwald ripening. Hence when seed C is introduced in the solution some of the fine particles agglomerate and then grow into agglomerated product crystals, whereas others are consumed through Ostwald ripening. From a practical perspective the level of agglomeration could be decreased by applying temperature cycling, when the heating phases would promote de-agglomeration of the initially loosely bound fine particles and promote their elimination through Ostwald ripening (Abu Bakar *et al.*, 2009a) .

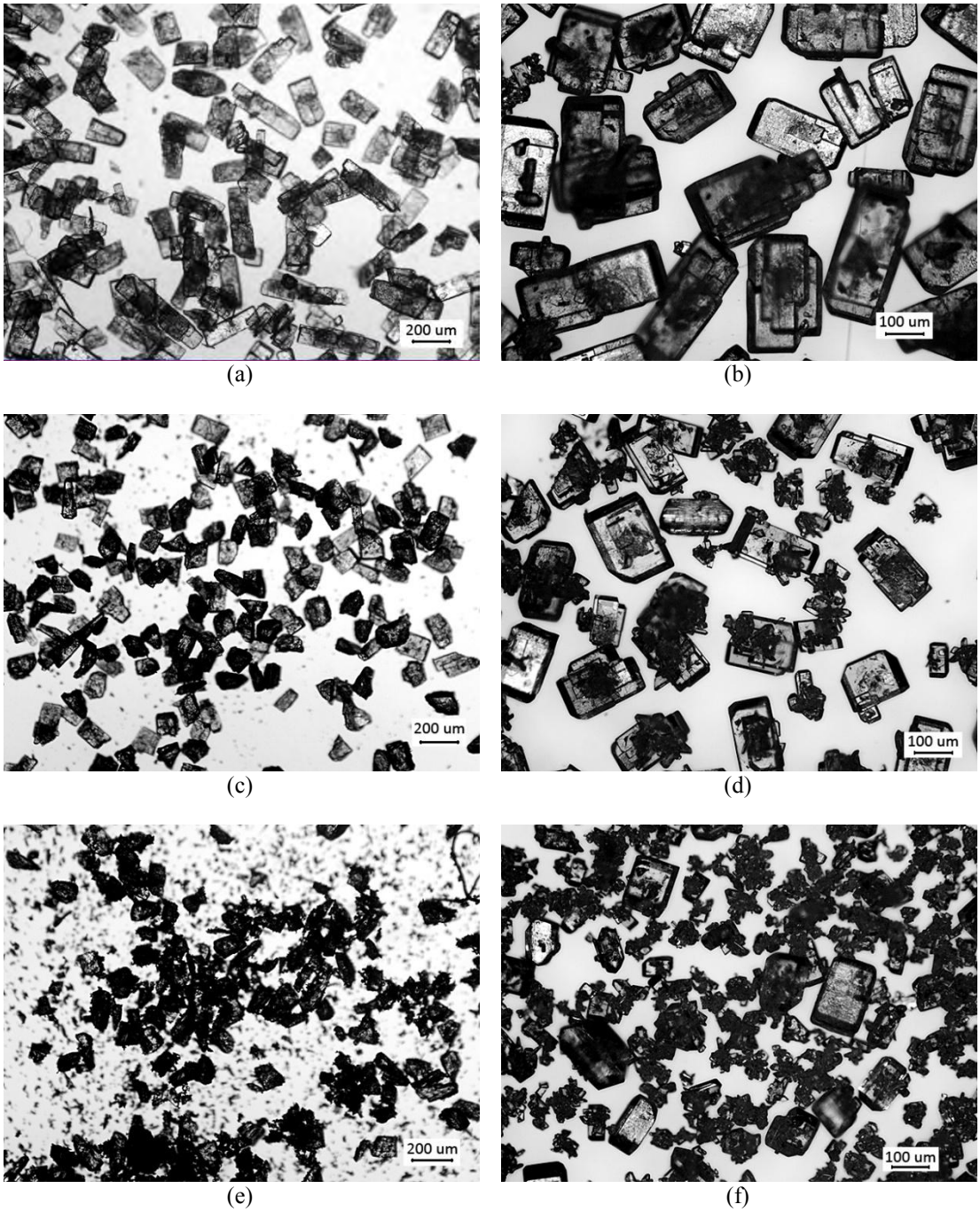

Figure 9.4: Microscopic images of seed A, B and C crystals (a, c, e) and the corresponding final product crystals when seed A, B and C were used for seeding (b, d, f).

9.3.4 Comparison of seed and product size distributions using on-line laser diffraction measurement

The measured CSDs for the seeds and the final distribution using the on-line laser diffraction (Malvern Mastersizer) are shown in Figure 9.5 (a) and (b). The results are shown in volume %, as obtained from the instrument and on logarithmic size scale, to better distinguish the particular features of the three distributions. Figure 9.5 (a) indicates that seed C contains a large amount of very small particles (dust of size below 1 μm) and the distribution appears to be tri-modal with a pronounced shoulder due to small particles (with size of 10-40 μm). In case of seed B, it can be seen that washing eliminated the dust and decreased significantly the amount of fines. The distribution for seed B is bimodal due to the presence of small particles (with size of 10-40 μm), which were not removed during washing. However the peak in this size range (10-40 μm) is significantly smaller than in the case of seed C. Seed A has a narrow, mono-modal distribution, corresponding to the uniform shape and size with negligible traces of fines shown in the micrograph in Figure 9.4 (a). The product CSDs are also in correlation with the micrographs in Figure 9.4 (b), (d) and (f). The product resulting from seed A shows the most significant growth and narrow mono-modal distribution. The product from seed B indicates significant growth for the majority of particles but the distribution exhibits a long tail due to the fines present in the seed.

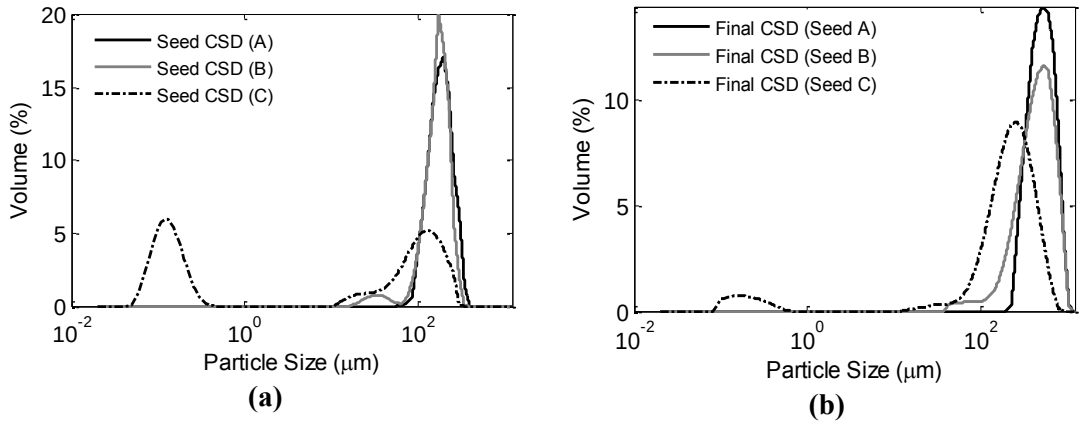

Figure 9.5: Comparison of distributions (volume %) measured online using Malvern Mastersizer a) seed (beginning of batch) and b) product (at the end of the batch) for the experiments with seeds A, B and C.

The product distribution resulting from seed C suggests the least growth and in addition to the long tail, due to smaller particles, the product distribution also shows a third peak at small particle range (below 1 μm). These results are also in correlation with the size-dependent growth mechanism, which suggests that larger particles should exhibit more growth than fines. Larger particles have higher terminal velocities hence in the case of diffusion controlled growth the larger the crystal size the faster the growth.

The results also show that the very fine particles (dust with size < 1 μm) barely grow. This can be explained by the fact that these small particles have very small terminal velocities and sizes smaller than that of the turbulent eddy's. Thus these particles grow in a virtually stagnant medium even in an apparently well agitated vessel. Additionally, since the potassium dichromate in water, is a very fast growing system, growth happens at very low supersaturation. Close to the equilibrium, the Gibbs-Thomson effect (Mullin, 2001) becomes significant, according to which particles near nucleic size (e.g. 1-2 μm) may grow at extremely slow rate due to their higher solubility (and hence lower supersaturation).

The experimental results demonstrate that under the same process conditions, the properties of the product obtained at the end of the batch can be significantly influenced by the properties of the initial seed.

9.3.5 Evaluation of seed quality on the product CSD through model-based simulations

Combined QMOM-MOCH technique (described in Chapter 4, Section 4.2.1) was used to predict the product CSDs using the distributions of seeds A, B and C, together with the corresponding initial concentrations as initial conditions in the model. The experimental cubic temperature profile was used in the simulations and the product CSDs predicted are compared with the experimental CSDs. The growth parameter used for these simulations are shown in Table 8.3, and were obtained from an experiment that used seed A. Therefore, as expected the prediction of the product CSD (shown in Figure 9.6) is in very good agreement with the measured CSD. Figure 9.7 compares the simulated and experimental product CSDs when seed B was used as initial condition in the simulation. The simulated product CSD indicates more growth than the experimental final CSD with a bimodal shape, similarly to

the seed CSD. Despite the bimodal seed distribution the experimental product CSD is mono-modal, which can be explained by the agglomeration of the small particles, which can also be observed in Figure 9.4 (d).

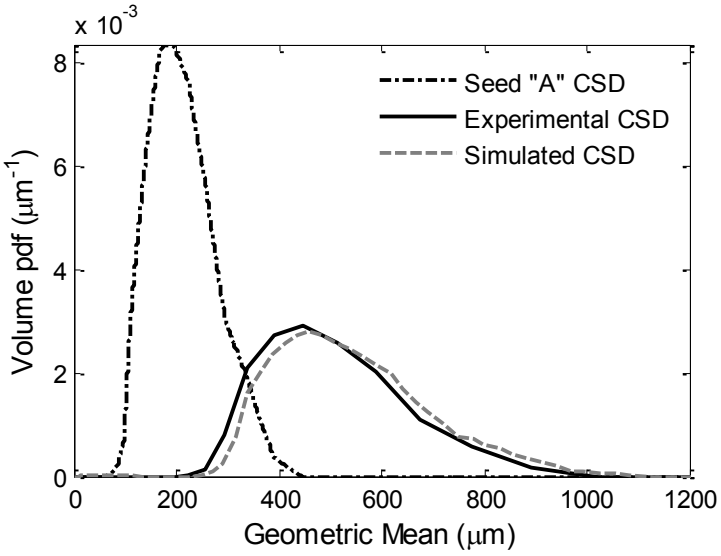

Figure 9.6: Comparison of simulated and experiment CSDs at the end of the batch when the CSD of seed A was used as initial condition for the simulation.

Agglomeration competes with growth, hence part of the supersaturation is used to form the bonds between the particles in the agglomerates, resulting overall in less growth compared to the simulated CSD. Hence experimentally the fines are eliminated through agglomeration but overall less growth can be observed for the larger seed particles. Agglomeration is not taken into account in the model, hence all supersaturation is used for growth in the simulation, leading to over-estimation of the overall growth. Additionally, due to the different preparation mode of seed B (milling and washing) compared to seed A (crystalline seed) the surface properties can differ significantly (e.g. exhibiting very different kink densities and surface dislocations), leading to differences in the growth rates (surface integration kinetics). Since the parameters for the growth kinetics were identified using the crystalline seed, these parameters may not be suitable when another seed is used with significantly different surface properties (e.g. due to milling).

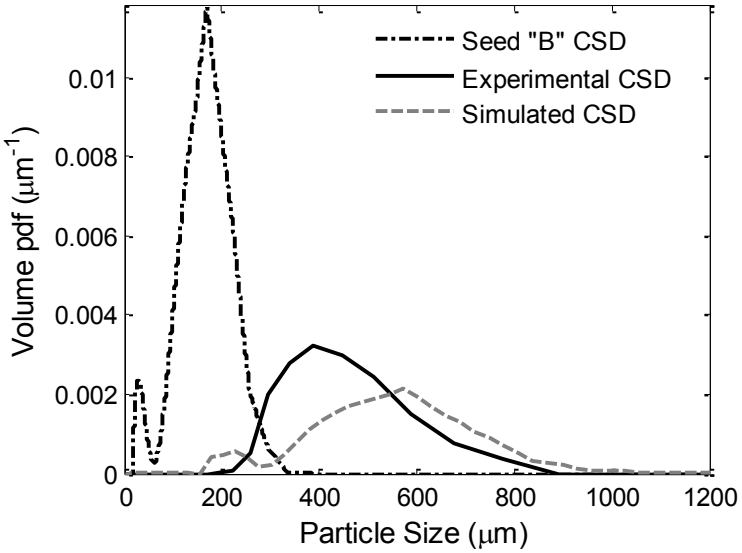

Figure 9.7: Comparison of simulated and experiment CSDs at the end of the batch when the CSD of seed B was usd as initial condition for the simulation.

Figure 9.8 indicates that using seed C to initialise the model, the simulated distribution highly over-predicts the experimental CSD. The simulated product distribution has a tri-modal shape, which is in correlation with the experimental observation (best seen in Figure 9.5 (b)), however the modes at the smaller size ranges are significantly more pronounced in the simulation than in the case of the experimental CSD. Seed C contains a large amount of very fine particles (dust), which initially generate growth through the mechanism of Ostwald ripening (Gibbs-Thomson effect), leading to slower growth. Additionally, the milled seed including the dust particles most likely have very different surface properties compared to the crystalline seed A (similarly as in the case of seed B), and may grow much slower due to their smaller size than the size of the turbulent eddies. The microscopic image of the product CSD (Figure 9.4 (f)) also indicates significant agglomeration. Since the mechanisms of Ostwald ripening, agglomeration and effect of mixing are not included in the simulation model, and due to the variation of growth rates due to the significantly different surface properties of the seed C, there are considerable differences between the shape and size of the predicted and experimental product CSDs.

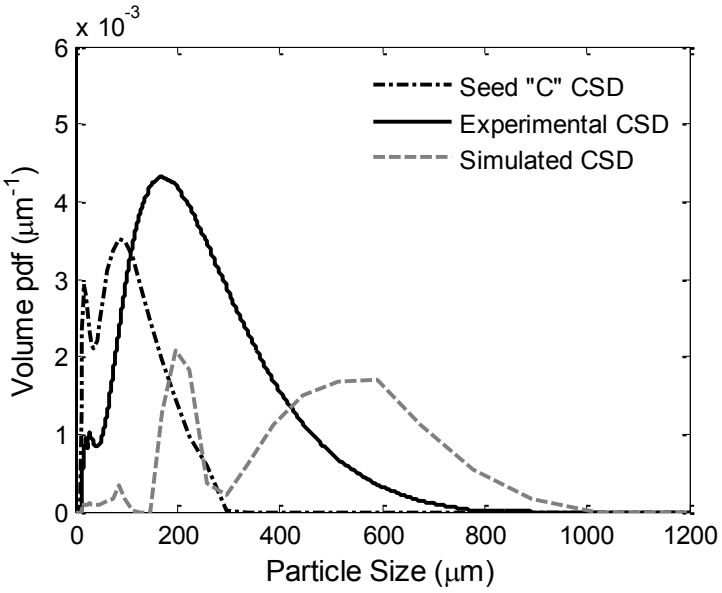

Figure 9.8: Comparison of simulated and experiment CSDs at the end of the batch when the CSD of seed C was used as initial condition for the simulation.

The simulation results indicate that in the case of open-loop control strategies, which do not account for changes in the seed property, the variations in the quality of seed can lead to major differences in the product CSD. These results also underline the importance of analysing the effects of seed preparation on the product property, and emphasize the requirement for careful seed preparation protocols, which can yield seed with consistent properties. Milled seeds which contain large amounts of fine particles can produce large amount of agglomerated crystals, which not only reduces the efficiency of the downstream processes but can have great impact on the bioavailability and purity of active pharmaceutical ingredients. In case of milling, washing should be applied properly to remove the small particles. When variation in the seed properties are difficult to avoid, more advanced crystallisation control strategies can be used, which are able to decrease the variability of the product CSD due to changes in the seed quality, such as temperature cycling (Abu Bakar *et al.*, 2009a), direct nucleation control (Abu Bakar *et al.*, 2009b) or *in situ* seed generation (Woo *et al.*, 2009a).

9.4 Summary for effect of seed preparation method on the product CSD

Seeding is a well-known technique to stabilise the crystallisation processes, however the quality of seed has a large impact on the final crystalline product. This section provides an experimental and simulation based evaluation of the effect of the seed quality, determined by the preparation protocol, on the product crystal size distribution (CSD). A set of experiments were carried out for potassium dichromate in water system using seeds from the same sieve fraction but prepared using different methods. Experiments with crystalline-sieved, milled-washed-sieved, and milled-sieved seeds were carried out. The distributions of three different seeds were also used as initial conditions in a simulation model and the results were compared with the measured distributions. Experimental results were in good agreement with the model-based CSD prediction, when the quality of seed was good with less fine particles. However the product distribution was over-predicted by the model in the case of the seeds, which contained fine particles or dust (very fine particles). These differences could be explained by changes in the growth mechanisms due to the different surface properties (different kink densities) of the milled and crystalline seeds, the existence of Ostwald ripening (Gibbs-Thomson effect) indicated by focused beam reflectance measurement promoted by the very fine particles, the pronounced agglomeration of the fine particles (in case of the milled seeds with fines), and by the effect of the mixing on the growth of the particles with different sizes. These phenomena were not included in the simulation model hence have lead to considerable difference between the predicted and measured product CSDs compared to the excellent prediction when the crystalline seed was used. This section also illustrates the simultaneous application of *in situ* process analytical tools, such as focused beam reflectance measurement (FBRM) for the detection of Ostwald ripening, attenuated total reflection (ATR) UV/Vis spectroscopy for concentration monitoring, as well as the on-line use of a laser diffraction instrument (Malvern Mastersizer) for real-time CSD measurement in the case of the potassium dichromate in water system.

9.5 Experimental evaluation of the CSD design using mixture of seeds

The seed recipe design methodology was described in Chapter 7, Section 7.7. To evaluate the seed design methodology using mixtures of different seeds an arbitrary bimodal distribution was selected as target:

$$f_n^{tar} = 0.72\frac{1}{\sqrt{2\pi}2.40}e^{-(L-280)^2/(2.40^2)} + 0.28\frac{1}{\sqrt{2\pi}2.68}e^{-(L-470)^2/(2.68^2)} \tag{9.1}$$

Equation (9.1) was converted to volume pdf using the equation (5.6) and was taken as the target distribution in an optimisation problem defined similarly to equations (7.15)-(7.21) as follows:

$$\min_{m_{seed},w_i|_{i=1,\ldots,N_G}} \sum_{i=1}^{N_d}(f_{v,i}(t_{batch}) - f_{v,i}^{tar})^2\,, \tag{9.2}$$

subject to:
$$\sum_{i=1}^{N_G} w_i = 1\,, \tag{9.3}$$

$$0 \le w_i \le 1 \text{ for } i = 1,\ldots,N_G\,, \tag{9.4}$$

$$0 < m_{seed} < 0.1C(0)m_{sol}\,, \tag{9.5}$$

$$C(t_{batch}) \le C_{f,\max}\,, \tag{9.6}$$

$$f_{n,seed}(L) = \frac{m_{seed}}{m_{sol}}\frac{1}{\rho_c k_v}\sum_{i=1}^{N_G}\frac{w_i}{L_{m,i}^3}\mathcal{N}_i(L;L_{m,i},\sigma_i)\text{, with } \mathcal{N}_i(L;L_{m,i},\sigma_i) = \frac{1}{\sqrt{2\pi}\sigma_i}e^{-(L-L_{m,i})^2/(2\sigma_i^2)} \tag{9.7}$$

where m_{seed} is the total seed mass (g), w_i are the weight fractions of seeds from a particular sieve fraction in the final seed mixture, $i = 1,2,\ldots,N_G$, N_G is the number of Gaussians corresponding to the CSDs of a particular seed fraction, $L_{m,i}$ the mean sizes (μm), σ_i (μm) the standard deviations of the respective Gaussian distributions, m_{sol} is the mass of water used as solvent (g), $C(0)$ and $C(t_{batch})$ are the solute concentrations at the beginning and end of the batch, respectively. The constraints given by inequalities (9.5) restrict the amount of seed added to a maximum of 10% of the mass of solid dissolved in the system, whereas the

constraint given by (9.6) is a productivity constraint with $C_{f,\max}$ being the maximum acceptable concentration at the end of the batch to achieve the required yield. The seed recipe design is formulated for the practical situation when the mean and standard deviations characterizing the seeds in a particular size ranges are fixed, being determined by the method and equipment used to produce the particles (here sieving), and only the total amount of seed and the weight fractions in which the various size ranges are mixed together are optimised, with the vector of decision variables being defined as $[m_{seed}, w_1, w_2, \ldots, w_{N_a}]$. The mean values of the seed distributions were calculated as the arithmetic means of the consecutive sieve sizes and the standard deviations were considered to be equal to half of the size ranges determined by the corresponding sieves. In this case a fixed cubic temperature profile was used (cooling from 29°C to 20°C within 60 min, as shown in Figure 8.11(a)), hence the SSC parameter ϕ was not included in the optimisation. The model was solved using the QMOM-MOCH method under variable supersaturation, corresponding to the fixed temperature profile. This is a more practical scenario, since the implementation of a particular predetermined temperature profile is easier and more reliable than the application of supersaturation control, especially at the low supersaturation values required by this fast growing system (as discussed in Chapter 8). The initial concentration of the system was 0.2 g/g of water corresponding to an equilibrium temperature of 30°C, and seed was added at 29°C.

The target distribution is shown in Figure 9.9 (b). In the seed recipe optimisation consecutive sieve sizes were used, which defined a set of seven sieve size ranges $\mathcal{L} = \{37-88, 88-105, 105-177, 177-210, 210-250, 250-297, 297-354\}$. The optimal seed is the result of a mixture of four Gaussian distributions with parameters, $w = [0.73,\ 0.02,\ 0.23,\ 0.02]$, $L_m = [62.5\,\mu\text{m},\ 96.5\,\mu\text{m},\ 141.0\,\mu\text{m},\ 193.5\,\mu\text{m}]$ and $\sigma = [25.5\,\mu\text{m},\ 8.5\,\mu\text{m},\ 36\,\mu\text{m},\ 16.5\,\mu\text{m}]$ corresponding to the selected sieve size ranges of $\mathcal{L}^* = \{37-88, 88-105, 105-177, 177-210\}$ and the optimised mass of seed was 1.214 g.

An experiment was designed to achieve the target bimodal distribution described by equation (9.1). The schematic of experimental setup is shown in Figure 8.2. Same material, apparatus and seed preparation technique were used as described in Section 8.2.1- 8.2.3.The sieve analysis of the raw material indicated that the seed fractions available in considerable

quantity were only in the size ranges of 40-63, 63-90 and 90-106 µm. Hence the seed recipe optimisation was performed again for these size ranges only. The optimised seed was a mixture of two Gaussians with parameters $w = [0.50, 0.50]$, $L_m = [51.5\,\mu\text{m}, 98\,\mu\text{m}]$ and $\sigma = [11.5\,\mu\text{m}, 8\,\mu\text{m}]$ corresponding to the selected sieve sizes of 40-63 and 90-106 µm and the optimised mass of seed was 1.118 g. Hence, the seed used for the experiment was a blend of two sieve fractions retained between 40-63 µm and 90-106 µm. Figure 9.9 (a) shows the comparison between the optimised seed as four Gaussians, the optimal seed as two Gaussians, and the actual seed used for the experiment (measured using Malvern Mastersizer).

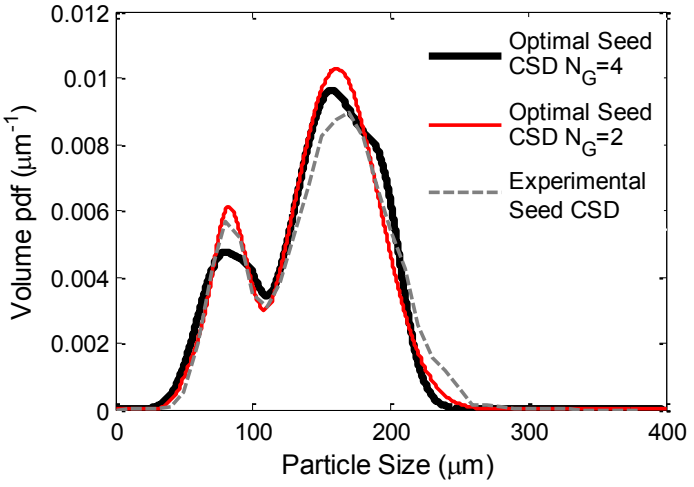

(a)

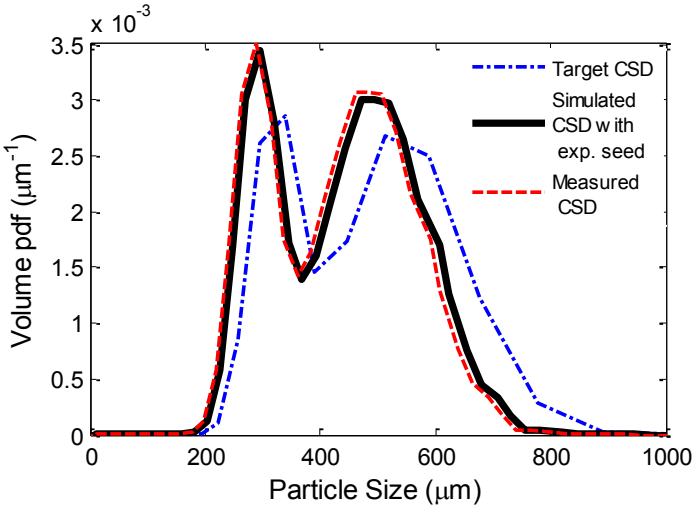

(b)

Figure 9.9: Comparison of a) experimental and optimal seed distribution, and b) experimental and target distribution (for which a mixture of seed was optimised) at the end of the batch and the simulated distribution with the experimental seed used as the initial condition in the model.

It can be observed that the experimental and optimal seed distributions are very close, although the two optimal seeds were blend of different sieve size ranges in different amounts (weight fractions). These results indicate that a particular optimal seed CSD can be the result of blending different sieved seed fractions. The optimal seed recipe resulting from the mixture of the two seed fractions was used in an experiment with the cubic temperature trajectory, (cooling the solution from 29°C to 20°C during a 60 minutes duration) using the experimental setup as described in Chapter 8, Section 8.2.1- 8.2.3. The initial concentration of the system was 0.20 g/g water corresponding to an equilibrium temperature of 30°C and seed was added at 29°C. These experimental conditions are identical to the ones used in the simulations.

Figure 9.9 (b) shows a comparison between the target and the experimental CSDs at the end of the batch. The final product CSD measured is shifted towards slightly smaller particles compared to the target distribution. Nonetheless, the seed recipe design procedure was able to provide a product distribution which is remarkably close to the target distribution. The difference between the target and product CSDs may be caused by the discrepancy between the theoretical optimal seed recipe and the actual seed recipe prepared experimentally as shown in Figure 9.9 (a). Although the differences in the seed CSDs are small, they may be amplified during the crystallisation processes, leading to increasingly larger errors between the experimental and target CSD. Additionally, although the model identification indicated that the process model is in very good agreement with the experimental data a certain level of model prediction error is present, which may lead to errors in the theoretical seed recipe. To further evaluate this, a simulation was carried out using the measured experimental seed CSD as initial condition in the model. Figure 9.9 (b) shows that the experimental and simulated CSDs are very close when the model was initiated with the measured experimental seed. These results indicate that the model prediction is very good, and the difference between the target and experimental product CSDs is caused by the accumulating prediction error due to the discrepancy between the optimal and experimental seed recipes.

The absorbance was measured using the ATR-UV/Vis spectrometer throughout the experiment and was converted to concentrations, using the parameters shown in Table 8.2. A comparison between the simulated and experimental concentrations is shown in Figure 9.10.

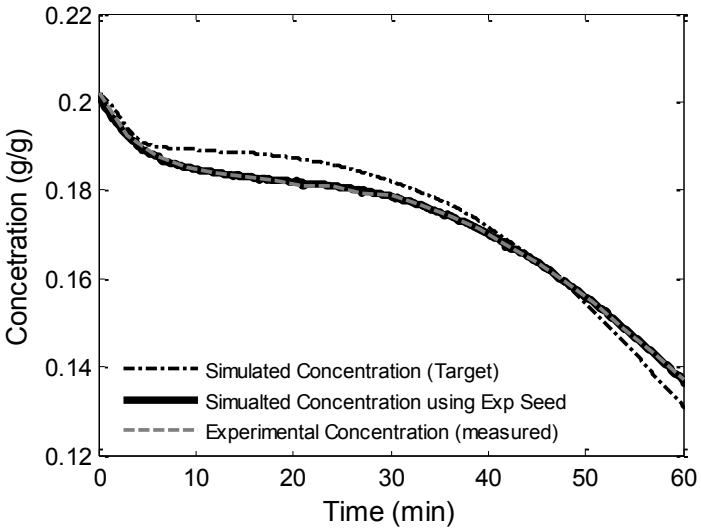

Figure 9.10: Comparison of experimental concentration, simulated concentration with theoretical seed recipe and the simulated concentration when the experimental seed was used.

The simulated concentration falls below the experimental concentration (error of 1.74%), which also agrees with the discrepancy between the experimental and target CSDs. However when the simulations are initiated with the experimental seed CSD, the simulated and experimental concentration profiles are in very good agreement, reinforcing that the model developed with the identified kinetic parameters, describes very well the real process. Figure 9.11 (a and b) show the microscopic images for the mixture of the seed and the final distribution obtained at the end of the experiment and indicate that the final distribution of crystals is indeed a mixture of two different sizes.

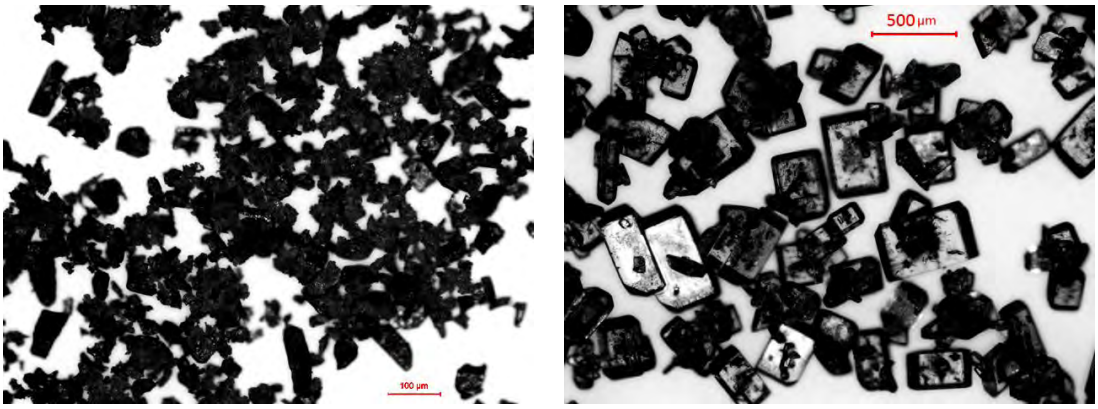

(a) (b)

Figure 9.11: Microscopic image of the a) seed (blend 1), and b) product crystals obtained at the end of the batch (using seed blend 1).

To provide further experimental evidence of the seed recipe design approach an additional target bimodal distribution was designed, given by

$$f_{n,\text{bimodal}}^{tar} = 0.60\frac{1}{\sqrt{2\pi}2.18}e^{-(L-210)^2/(2.18^2)} + 0.40\frac{1}{\sqrt{2\pi}2.76}e^{-(L-370)^2/(2.76^2)} \quad (9.8)$$

To carry out the experiments, the seed was optimised for the available sieve sizes, 40-63 and 90-125 μm. The optimised seed was a mixture of two Gaussians with weight fractions $w = [0.54,\ 0.46]$. The means and standard deviations of the seed fractions are $L_m = [51.5\,\mu\text{m},\ 107.5\,\mu\text{m}]$ and $\sigma = [11.5\,\mu\text{m}, 17.5\,\mu\text{m}]$, respectively, corresponding to the selected sieve sizes of 40-63 and 90-125 μm. The optimised mass of seed was 1.115 g. Figure 9.12 (a) shows the comparison between the optimised seed as two Gaussians and the actual seed used for the experiment (measured using Malvern Mastersizer). It can be observed that the experimental and optimal seed distributions are close but not in as good agreement as in the previous case.

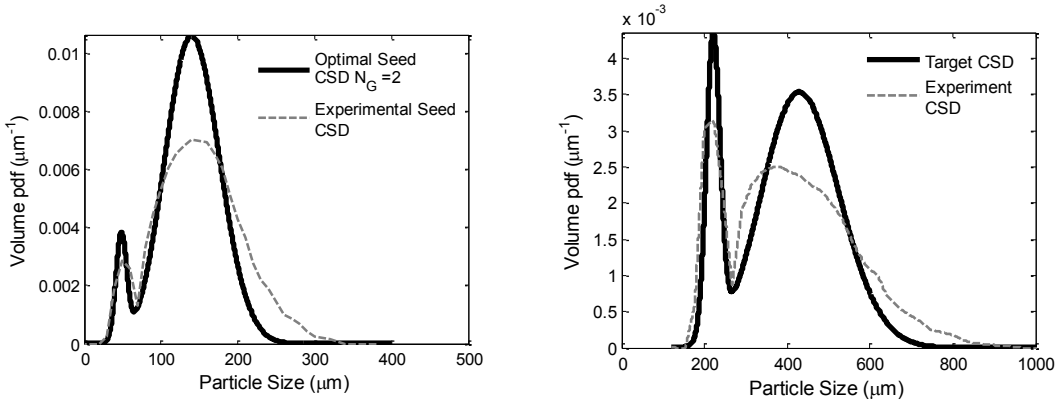

Figure 9.12: Comparison of a) experimental and optimal seed distributions; b) Comparison of experimental and target distribution (for which a mixture of seed was optimised) at the end of the batch.

For the second seed blend the experiment was carried out under the same conditions as for the first seed blend. The same cubic temperature trajectory was used, cooling the solution from 29°C to 20°C during a 60 minutes period. The initial concentration of the system was 0.20 g/g of water corresponding to an equilibrium temperature of 30°C and seed was added at 29°C. The experimental characteristics of the optimised seed recipes for both experiments are summarised in Table 9.3.

Table 9.3: Optimised seed parameters for the arbitrary bimodal target CSDs designed for experimental investigation.

Simulation Conditions	Seed blend 1	Seed blend 2
Target distributions, (f_n^{tar})	$f_n^{tar} = 0.72\frac{1}{\sqrt{2\pi}2.40}e^{-(L-280)^2/(2.40^2)} + 0.28\frac{1}{\sqrt{2\pi}2.68}e^{-(L-470)^2/(2.68^2)}$	$f_n^{tar} = 0.60\frac{1}{\sqrt{2\pi}2.18}e^{-(L-210)^2/(2.18^2)} + 0.40\frac{1}{\sqrt{2\pi}2.76}e^{-(L-370)^2/(2.76^2)}$
Sieve fractions, (μm)	40-63, 90-106	40-63, 90-125
Number of Gaussians, (N_G)	2	2
Seed mass, (m_{seed}), (g)	1.118	1.115
Mean, (L_m), (µm)	51.5, 98	51.5, 107.5
Weight fractions, (w)	0.50, 0.50	0.54 , 0.46
Standard deviations, $(\sigma), (\mu m)$	11.5, 8	11.5, 17.5

Figure 9.12 (b) shows the comparison between the target and the experimental CSDs resulting at the end of the batch for the second arbitrary bimodal distribution. The final product CSD showed smaller but broader peaks than the target distribution. Overall the shape of the product distribution is close to the target distribution, relative to the differences in the experimental and optimal seeds, indicating that the seed recipe design procedure was able to provide a product CSD relatively close to a desired target. The comparison between the simulated and experimental concentrations is shown in Figure 9.13. The simulated concentration indicates a higher solute consumption, which is also in correlation with the discrepancy between the experimental and target distributions.

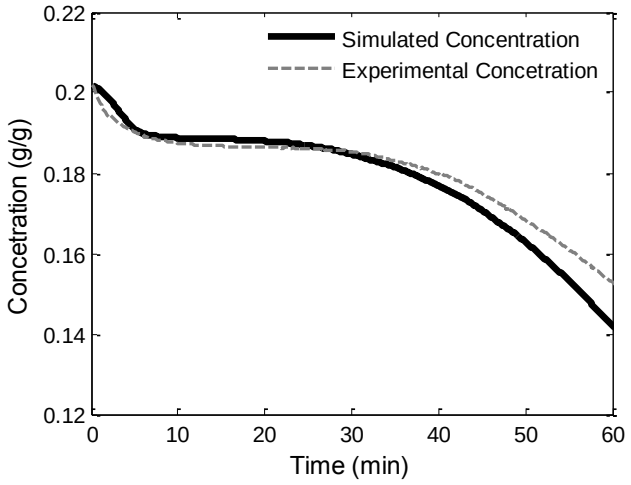

Figure 9.13: Comparison of experimental and simulated concentration throughout the entire batch (for seed blend 2).

The difference between measured and simulated concentrations at the end of the batch is 4.63%. This is greater than in the previous experiment (1.73%), which is also in correlation with the larger difference between the target and experimental CSDs, and is the result of the more significant discrepancy between the optimal and experimental seed CSDs, compared to the experiments with seed blend 1.

Figure 9.14 (a and b) show the microscopic images for the mixture of the seed and the final distribution obtained at the end of the experiment for the second seed blend. The microscopic images also indicate that both the seed and the final distribution of crystals are mixtures of two different size ranges. The experimental results show that it is possible to achieve a desired multimodal distribution by a model-based optimal design of an appropriate seed blend from various fractions of sieved seeds. The methodology provides a systematic approach to obtain seed mixture recipes by using available sieve sizes, which will yield the required shape of the product CSD. This can be used to achieve e.g. a desired therapeutic effect by designing dissolution profiles, or to achieve improved packing properties during the formulation of the final product.

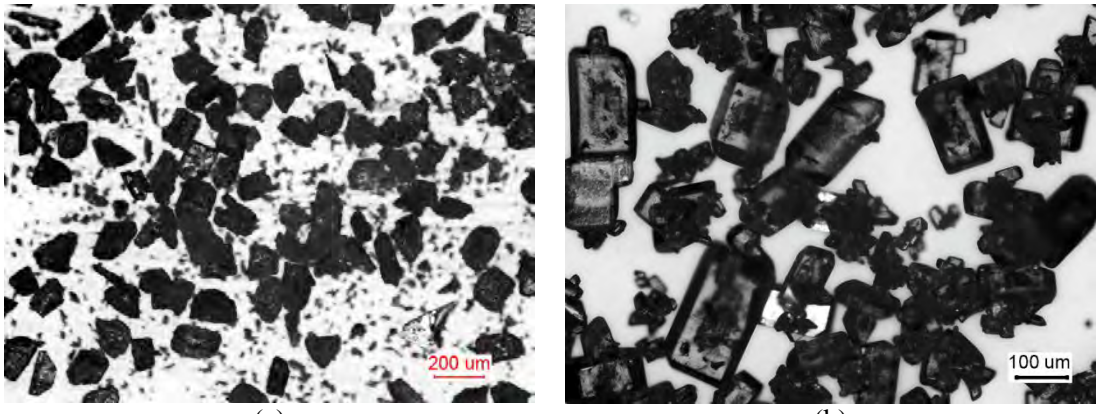

(a) (b)

Figure 9.14: Microscopic image of a) seed (blend 2), and b) product crystals at the end of the batch (using seed blend 2).

Summary of seed recipe design

The second part of the chapter provides an experimental evaluation of the seed recipe design approach as mixtures of sieved fractions to achieve a target distribution. Seed recipes were

optimised for two arbitrary bimodal target distributions. For the first target distribution the prepared seed CSD was very close to the optimised seed distribution. The final product CSD (measured) was remarkably close to the target distribution, indicating that the seed recipe design procedure was able to provide a product CSD very close to a desired target. For the second target distribution the prepared seed distribution was broader than the theoretical optimal seed distribution. Consequently, the final product CSD was also broader than the target distribution, however overall the shape of the target CSD was well achieved. The experimental results indicate that it is possible to achieve desired multimodal distributions by a model-based optimal design of an appropriate seed blend from various fractions of sieved seeds.

9.6 Conclusions

Seed is an important control variable for batch crystallisation processes. For achieving a target distribution it is important to take into account the characteristics of the seed. There is a lack of systematic evaluation of the seed preparation methods. The chapter provides systematic analyses of the effect of the seed characteristics (determined by the preparation method) on the product distribution. It is shown that large variations in seed size (presence of very fine particles) and difference in the surface properties can lead to large errors between the predicted and experimental CSDs, while very good prediction is achieved when seed with similar quality is used in the experiments as for the model identification. If growth is the only dominating phenomenon, then the degree of size enlargement of crystals depends on the amount of dissolved material in the supersaturated solution that is available for crystallisation and the total crystal surface in the suspension. The number of particles is constant and hence the mass balance can be used to estimate the evolution of the CSD. The chapter also provides an experimental evaluation of the seed recipe design approach described in Chapter 7.

Chapter 10
Conclusions and recommendations for future work

10.1 Conclusions

The thesis presents a new methodology for solving population balance equations (PBE). The approach combines the quadrature method of moments (QMOM) with the method of characteristics (MOCH), and provides a computationally efficient technique for the reconstruction of the whole crystal size distribution (CSD), for generic size-dependent growth, size-dependent dissolution, and nucleation mechanisms.

The approach was evaluated in the case of a seeded system of potash alum in water. The size-dependent growth and secondary nucleation kinetic parameters for the process were identified using industrial pilot plant data, provided by BASF, Germany. The concentration was measured on-line using density meter and the *in situ* CSD was measured using Malvern Insitec. The size dependent dissolution kinetics was identified using laboratory experimental data consisting of off-line CSD measurements and *in situ* concentration measurement based on a conductivity probe. The process was also monitored using a focused beam reflectance measurement (FBRM) probe.

Optimal temperature trajectories have also been designed for various bimodal target CSDs. The results demonstrate the computational efficiency of the approach based on the combined QMOM-MOCH method for the off-line or on-line optimisation of batch crystallisation processes. The simulation case studies indicated that it was possible to achieve bimodal distributions while operating within the metastable zone width for the case when size-dependent growth and secondary nucleation are considered. However to eliminate the effect of secondary nucleation and achieve a mono-modal product distribution the optimal temperature trajectories has to be designed using both the under-saturated and supersaturated regions of the phase diagram, considering all three phenomena: size-dependent dissolution, size-dependent growth and secondary nucleation. The proposed approach generates optimal operating temperature profiles, which provides fine removal by controlled dissolution and can achieve target distributions with shapes unachievable operating within the metastable zone only.

The combined QMOM-MOCH method can be used to solve the PBE under considering dynamic supersaturation. Additionally, the population balance model was solved using the MOCH under the assumption of constant supersaturation. At constant supersaturation growth is the dominating phenomenon, yielding a simplified analytical expression for the prediction of the CSD. A design parameter for supersaturation controlled processes was introduced as a function of the supersaturation, time and growth kinetics. Based on the design parameter and the simplified analytical model, the supersaturation set-point and batch time are determined using an optimisation approach to obtain a target distribution with a desired shape.

The methodology was used to obtain the temperature profiles in the time domain, which will lead to constant supersaturation corresponding to a desired target CSD, providing a systematic direct design approach for practical applications and scale-up. Temperature trajectories in the time domain were designed for a desired supersaturation point or batch time from the solubility curve, concentration and moments of the crystal size distribution. The experimental validation of the novel direct design methodology for the systematic design of the setpoint operating curves, which produce desired target CSDs at the end of the batch was presented.

Kinetic parameters of the apparent size-dependent growth rate expression were identified for the potassium dichromate water system, using an experimental setup developed at Loughborough University. The experiments presented in the thesis also illustrates the simultaneous application of *in situ* process analytical tools, such as focused beam reflectance measurement (FBRM) for nucleation detection, attenuated total reflection (ATR) UV/Vis spectroscopy for concentration monitoring, as well as the in-line use of a Malvern Mastersizer for real-time CSD measurement in the case of the potassium dichromate in water system.

Two experiments were carried out for the potassium dichromate water system by redefining the supersaturation trajectories in terms of temperature trajectories corresponding to the same supersaturation control design parameter and hence same target CSD. The experimental results indicated that defining the supersaturation trajectories in terms of temperature trajectories is a powerful technique to control the supersaturation throughout the batch. The temperature trajectories are easy to implement because of the availability of good quality temperature sensors. Another advantage is the flexibility for adjusting the batch time or the supersaturation, which provides an additional benefit for industrial scale usage.

Two additional methods were proposed that use the seed in conjunction with the supersaturation setpoint design, and analytical CSD estimator for shaping the product CSD. The first approach designs a seed recipe as a mixture of crystals resulting for example from standard sieve analysis. In this approach the seed was introduced at the beginning of the batch. The second approach proposes a dynamic seed addition profile, which allows an easily implementable methodology to achieve complex target CSDs using seed with mono-modal CSD as a process actuator to control the desired final CSD.

The optimal seed recipe design for crystallisation processes, by automatically determining the amounts of seeds from various sieved seed fractions required to achieve a desired shape of the product CSD, was also proposed. To evaluate the methodology experiments were carried out for the potassium dichromate-water system. The estimated parameters were used to optimise the seed recipe by mixing different amounts of sieved seed fractions. Seed mixtures were represented as a sum of Gaussian distributions, with each Gaussian corresponding to the seed distribution in a particular sieve size range. Experimental results were in good agreement with the model-based CSD design, providing evidence that it is possible to achieve a desired multimodal product distribution by designing appropriate seed mixtures from various fractions of sieved seeds. The quality of the model-based prediction and hence the benefits of the model-based optimisation of temperature trajectories and seed recipes strongly depends on the seed quality. Experimental and simulation-based investigation provided evidence of the importance of developing suitable seed preparation protocols and to provide a comprehensive seed characterisation framework to achieve consistent product quality. The thesis provides a comprehensive and systematic framework of combined methodologies for the CSD shaping control for seeded batch cooling crystallisation processes.

10.2 Future Work

The proposed QMOM-MOCH can be extended for the solution of PBE incorporating breakage and aggregation mechanism too. Additionally the models could be developed to incorporate micro-scale and molecular level information in the mechanisms, such as the Gibbs-Thomson effect to incorporate Ostwald ripening, to include surface properties and surface integration mechanisms for better growth rate prediction. All these features with the consideration of non-ideal mixing and better integration with computation fluid dynamics (CFD) models, would not only enhance the prediction ability of the approaches but would

also open new opportunities for additional novel CSD control approaches, e.g. via controlled Ostwald ripening or induced and controlled agglomeration/breakage.

The described methodologies have been evaluated for open loop control. However these can be extended to real-time closed loop control strategies. The methods can be used for on-line optimisation using closed loop control strategies to predict, monitor and control the crystal size distribution in a nonlinear model predictive control framework. This could be applied both within the batch, and in a batch-to-batch framework using a model-based iterative learning control approach.

The CSD shaping control could be linked with end-product properties by integrating the crystallisation process with the downstream processes. The model-based optimisation, design and control of the integrated separation-formulation process could provide significant efficiency improvements and increase in the consistency of the final product properties.

The model based optimisation approaches could be further developed to take the model parameter uncertainties into account to design robust operating policies which decrease the variability in the product quality. These robust optimal control approaches could be combined with model-based experimental design techniques, which would maximise the information content for the model identification experiments, and hence decrease the uncertainties in the model parameters, consequently providing better robustness of the optimal control policies.

The thesis focused on the investigation of the proposed approaches in the case of two inorganic compounds. The applicability of the methodologies for organic compounds (e.g. pharmaceuticals, agrochemicals) could be evaluated to investigate their benefits in the case of high value-added products.

References

Aamir, E., Nagy, Z.K., Rielly, C.D., 2009a. Population balance modelling of the dynamic evolution of the crystal size distribution under a size-dependent dissolution mechanism., in: Louhi-Kultanen, M., Hatakka, H. (Eds.), Proc. of the 16th Int. Workshop on Industrial Crystallization, Lappeenranta, Finland, pp. 61-68.

Aamir, E., Nagy, Z.K., Rielly, C.D., 2010. Optimal seed recipe design for crystal size distribution control for batch cooling crystallisation processes. *Chem. Eng. Sci*. **65**, 3602-3614.

Aamir, E., Nagy, Z.K., Rielly, C.D., Kleinert, T., Judat, B., 2008. Efficient crystal size distribution estimation approach for growth dominated crystallisation processes., in: Jansens, J.P., Ulrich, J. (Eds.), Proc. of the 17th International Symposium on Industrial Crystallisation, Maastricht -The Netherlands, pp. 1733-1740.

Aamir, E., Nagy, Z.K., Rielly, C.D., Kleinert, T., Judat, B., 2009b. Combined quadrature method of moments and mthod of characteristics approach for efficient solution of population balance models for dynamic modelling and crystal size distribution control of crystallisation processes. *Ind. Eng. Chem. Res*. **48**, 8575-8584.

Abu Bakar, M.R., Nagy, Z.K., Rielly, C.D., 2009a. Seeded batch cooling crystallisation with temperature cycling for the control of size uniformity and polymorphic purity of sulfathiazole crystals. *Org. Process Res. Dev*. **13**, 1343-1356.

Abu Bakar, M.R., Nagy, Z.K., Saleemi, A.N., Rielly, C.D., 2009b. The impact of direct nucleation control on crystal size distribution in pharmaceutical crystallization processes. *Cryst. Growth Des*. **9**, 1378-1384.

Adi, H., Larson, I., Stewart, P., 2007. Use of milling and wet sieving to produce narrow particle size distributions of lactose monohyrate in the sub-sieve range. *Powder Technol*. **179**, 95-99.

Alopaeus, V., Laakkonen, M., Aittamaa, J., 2006. Numerical solution of moment-transformed population balance equation with fixed quadrature points. *Chem. Eng. Sci*. **61**, 4919-4929.

BS 5309-4: 1976. Methods for sampling chemical products. Sampling of solids.

Bakeev, K.A., 2005. Process Analytical Technology: Spectroscopic tools and implemenetation strategies for the Chemical and Pharmaceutical industries. Wiley-Blackwell.

Barker, M., Rawtani, J., 2005. Practical Batch Process Management. IDC Technologies.

Barrett, P., Glennon, B., 2002. Characterizing the metastable zone width and solubility curve using Lasentec FBRM and PVM. *Trans IChemE, Part A* **80**, 799-805.

Beck, J.V., Arnold, K.J., 1977. Estimation in Engineering and Science. Wiley, New York.

Beckmann, J.R., Randolph, A.D., 1977. Crystal size distribution dynamics in a classified crystallizer: Part II. Simulated control of crystal size distribution. *AlChE J*. **23**, 510-520.

Bennett, M.K., Rohani, S., 2001. Solution of population balance equations with a new combined Lax-Wendroff/Crank-Nicholson method. *Chem. Eng. Sci*. **56**, 6623-6633.

Berglund, K.A., Feng, L., 2002. ATR-FTIR for determining optimal cooling curves for batch crystallisation of succinic acid. *Cryst. Growth Des*. **2**, 492-452.

Blandin, A.F., Mangin, D., Nallet, V., Klein, J.P., Bossoutrot, J.M., 2001. Kinetics identification of salicilic acid precipitation through experiments in batch stirred vessel and a T-Mixer. *Chem. Eng. J*. **81**, 91-100.

Bohlin, M., Rasmuson, A.C., 1996. Application of controlled cooling and seeding in batch crystallisation. *Can. J. Chem. Eng*. **70**, 120-126.

Borcho, K., 2002. The importance of population balance dynamics from the prespective of the chemical industry. *Chem. Eng. Sci*. **57**, 4257-4266.

Bove, S., Solberg, T., Hjertager, B.H., 2005. A novel algorithm for solving population balance equations: The parallel parent and daughter classes. Diversion, analysis and testing. *Chem. Eng. Sci*. **60**, 1449-1464.

Braatz, R.D., 2002. Advanced control of crystallisation processes. *Annual Reviews in Control*. **26**, 87-99.

Braatz, R.D., Fujiwara, M., Ma, D.L., Togkalidou, T., Tafti, D.K., 2002. Simulation and new sensor technologies for industrial crystallisation: A review. *International Journal of Modern Physics* **16**, 346-353.

Braatz, R.D., Hasebe, S., 2002. Particle size and shape control in crystallisation processes. *AIChE Symp. Series* **98,** 307-327.

Braatz, R.D., Togkalidou, T., Fujiwara, M., Patel, S., 2001. Solute concentration prediction uing chemometrices and ATR-FTIR spectroscopy. *J. Cryst. Growth* **231**, 534-543.

Bravi, M., Mazzarotta, B., 1998. Size dependency of citric acid monohydrate growth kinetics. *Chem. Eng. J*. **70**, 203-207.

Brecevic, L., Garside, J., 1980. On the measurement of crystal size distributions in the micrometer size range. *Chem. Eng. Sci*. **36**, 867-869.

Chang, C.T., Epstein, M., 1982. Identification of batch crytsallisation control strategies using characteristic curves. In: nucleation, growth and impurity effects in crystallisation process engineering., AIChE series, New York.

Chew, J.W., Black, S.N., Chow, P.S., Tan, R.B.H., 2007. Comparison between open-loop temperature control and closed loop supersaturation control for cooling crystallisation of Glycine. *Ind. Eng. Chem. Res*. **46**, 830-838.

Chiu, T.Y., Christofides, P.D., 2000. Robust control of particulate processes using uncertain population balances. *AIChE J*. **46**, 266-280.

Choong, K.L., Smith, R., 2004a. Novel strategies for optimization of batch, semibatch and heating/cooling evaporative crystallization. *Chem. Eng. Sci*. **59**, 329-343.

Choong, K.L., Smith, R., 2004b. Optimization of batch cooling crystallization. *Chem. Eng. Sci*. **59**, 313-327.

Christofides, P.D., El-Farra, N.H., Li, M., Mhaskar, P., 2008. Model based control of a particulate systems. *Chem. Eng. Sci*. **63**, 1156-1172.

Chung, S.H., Ma, D.L., Braatz, R.D., 1999. Optimal seeding in batch crystallisation. *Can. J. Chem. Eng.* **77**, 590-595.

Chung, S.H., Ma, D.L., Braatz, R.D., 2000. Optimal model-based experimental design in batch crystallisation. *Chemom. Intell. Lab. Syst*. **50**, 83-90.

Costa, C.B.B., Costa, A.C., Filho, R.M., 2005. Mathematical modelling and optimal control strategy development for an adipic acid crystallisation process. *Chem. Eng. Process*. **44**, 737-753.

Costa, C.B.B., Maciel, M.R.W., Filho, R.M., 2007. Considerations on the crystallisation modelling: Population balance solution. *Comput. Chem. Eng*. **31**, 206-218.

David, R., Paulaime, A.M., Espitalier, F., Rouleau, L., 2003. Modelling of multiple-mechanism agglomeration in a crystallization process. *Powder Technol*. **130**, 338-344.

David, R., Villermaux, J., Marchal, P., Klein, J.P., 1991. Crystallisation and precipitation engineering-lV. Kinetic model of adipic acid crystallisation. *Chem. Eng. Sci*. **46**, 1129-1136.

De Anda, J.C., Wang, X.Z., Lai, X., Roberts, K.J., 2005. Classifying organic crystals via in-process image analysis and the use of monitoring charts to follow polymorphic and morphological changes. *J. Process Control* **15**, 785-797.

Dharmayat, S., De Anda, J.C., Hammond, R.B., Lai, X.J., Roberts, K.J., Wang, X.Z., 2006. Polymorphic transformation of L-glutamic acid monitored using combined on-line video microscopy and x-ray diffraction. *J.Cryst. Growth* **294**, 35-40.

Diemer, R.B., Olson, J.H., 2002a. A moment methodolgy for coagulation and breakage problems: Part 2 - moment models and distribution reconstruction. *Chem. Eng. Sci.* **57**, 2211-2228.

Diemer, R.B., Olson, J.H., 2002b. A moment methodology for coagulation and breakage problems: Part 3 - generalized daughter distribution functions. *Chem. Eng. Sci.* **57**, 4187-4198.

Diemer, R.B., Olson, J.H., 2002c. A moment methodology for coagulation and breakage problems: Part I- analytical solution of the steady - state population balance. *Chem. Eng. Sci*. **57**, 2193-2209.

Dixit, N.M., Zukoski, C.F., 2002. Nucleation rates and induction times during colloidal crystallization: Links between models and experiments. *Phys. Rev. Lett*. **66**, 1-10.

Doki, N., Seki, H., Takano, K., Asatani, H., Yokota, M., Kubota, N., 2004. Process control of seeded batch cooling crystallisation of the metastable alpha-form glycine using an in-situ ATR-FTIR spectrometer and an in-situ FBRM particle counter. *Cryst. Growth Des*. **4**, 949-953.

Doyle, I.F.J., Soroush, M., Cordeiro, C., 2002. Control of product quality in polymerization processes., in: Rawlings, J.B., Ogunnaike, B.A., Eaton, J.W. (Eds.), AIChE Symp. Series, New York, pp. 290-306.

Dunham, S.T., Clejan, I., Gencer, A.H., 1997. Accurate and efficient modelling of nucleation and growth processes. *Mater. Sci. Eng., A* **A238**, 152-159.

Dunuwila, D., D, Berglund, K.A., 1997. ATR-FTIR spectroscopy for *in situ* measurement of supersaturation. *J. Cryst. Growth* **179**, 185-193.

Eek, R.A., Dijkstra, S., 1995. Design and experimental evaluation of a state estimator for a crystallisation process. *Ind. Eng. Chem. Res*. **34**, 567-574.

El-Farra, N.H., Shi, D., Li, M., Mhaskar, P., Christofides, P.D., 2006. Predictive control of particle size distribution in particulate processes. *Chem. Eng. Sci*. **61**, 268-281.

Fan, R., Marchisio, D.L., Fox, R.O., 2004. Application of the direct quadrature method of moments to polydisperse gas-solide fluidized beds. *Powder Technol*. **139**, 7-20.

Fevotte, G., 2002. New perspectives for the on-line monitoring of pharmaceutical crystallisation processes using *in situ* infrared spectroscopy. *Int. J. Pharm*. **241**, 263-278.

Fevotte, G., Alexander C., Nida, S.O., 2007. A population balance model of the solution-mediated phase transition of citric acid.. *AIChE J*. **53**, 2578-2589.

Flood, A.E., 2002. Thoughts on recovering particle size distributions from the moment form of the population balance. *Dev Chemical Engineering Mineral Process* **10**, 501-519.

Fujiwara, M., Chow, P.S., Ma, D.L., Braatz, R.D., 2002. Paracetamol crystallisation using laser backscattering and ATR-FTIR spectroscopy: metastability, agglomeration and control. *Cryst. Growth Des*. **2**, 363-370.

Fujiwara, M., Nagy, Z.K., Chew, J.W., Braatz, R.D., 2005. First-principles and direct design approaches for the control of pharmaceutical crystallisation. *J. Process Control* **15**, 493-504.

Garcia, E., Veesler, S., Boistelle, R., Hoff, C., 1999. Crystallisation and dissolution of pharmaceutical compounds an experimental approach. *J. Cryst. Growth* **198/199**, 1360-1364.

Garside, J., 1984. Advances in the characterisation of crystal growth. *AIChE Symp. Series* **80**, 194-198.

Garside, J., 1985. Industrial crystallization from solution. *Chem. Eng. Sci.* **40**, 3-26.

Garside, J., Davey, R., 1980. Secondary contact nucleation: Kinetics growth and scale up. *Chem. Eng. Commun* **4**, 393-424.

Garside, J., Jancic, S.J., 1978. Prediction and measurement of crystal size distributions for size dependent growth. *Chem. Eng. Sci*. **33**, 1623-1630.

Ge, M., Wang, Q.-G., Chiu, M.-S., Lee, T.-H., Hang, C.-C., Teo, K.-H., 2000. An effective technique for batch process optimisation with application of crystallisation *Trans IChemE, Part A* **78**, 99-106.

Gerstlauer, A., Gahn, C., Zhou, H., Rauls, M., Schreiber, M., 2006. Application of population balances in the chemical industry - current status and future needs. *Chem. Eng. Sci.* **61**, 205-217.

Gerstlauer, A., Mitrovic, A., Motz, S., Gilles, E.D., 2001. A population model for crystallisation processes using two independent particle properties. *Chem. Eng. Sci*. **56**, 2553-2565.

Giaya, A., Thompson, R.W., 2004. Recovering the crystal size distribution from the moments equations. *AIChE J*. **50**, 879-882.

Gimbun, J., Nagy, Z.K., Rielly , C.D., 2009. Simultaneous quadrature method of moments for the solution of population balance equations, using a differential algebraic equation framework. *Ind. Eng. Chem. Res*. **48**, 7798-7812.

Gordon, R.G., 1968. Error bounds in equilibrium statistical mechanics. *J Math Phys***. 9**, 655-663.

Granberg, R.A., Rasmuson, A.C., 2005. Crystal growth rates of paracetamol in mixtures of water+acetone+toluene. *AIChE J*. **51**, 2441-2456.

Gron, H., Borissova, A., Roberts, K.J., 2003. In-process ATR-FTIR spectroscopy for closed-loop supersaturation control of a batch crystallizer producing monosodium glutamate crystals of define size. *Ind. Eng. Chem. Res*. **42**, 198-206.

Gron, H., Roberts, K.J., 1999. Application of ATR-FTIR spectroscopy for on-line determination of solute concentration and solute supersaturation., Proc. of the14th Int Symposium on Industrial Crystallisation Cambridge , UK, pp. 1-9.

Grosso, M., Galan, O., Baratti, R., Romagnoli, J.A., 2009. A novel approach for the prediction of PSD in antisolvent mediated crystallisation. *Chem. Eng. Sci*. **27**, 291-296.

Gunawan, R., Fusman, I., Braatz, R.D., 2004. High resolution algorithms for multidimensional population balance equations. *AIChE J*. **34**, 1821-1832.

Gunawan, R., Fusman, I., Braatz, R.D., 2008. Parallel high resolution simulation of particulate processes with nucleation, growth and aggregation. *AIChE J*. **54**, 1449-1458.

Hardenberg, J.v., Kenning, D.B.R., Xing, H., Smith, L.A., 2004. Identification of nucleation site interactions. *International Journal of Heat and Fluid Flow* **25**, 298-304.

Hartel, R.W., 2002. Crystallization in Foods, in: Myerson, A.S. (Ed.), Handbook of Industrial Crystallisation, 2nd ed. Butterworth-Heinemann, Oxford, UK, pp. 287-304.

Haseltine, E.L., Patience, D.B., Rawlings, J.B., 2005. On the stochastic simulation of particulate systems. *Chem. Eng. Sci*. **60**, 2627-2641.

Heffels, C.M.G., Kind, M., 1999. Seeding technology: an underestimated critical success factor for crystallisation., Proc. of the 14th International Symposium on Industrial Crystallisation., pp. 2234-2246.

Henson, M.A., Muller, D., Reuss, M., 2002. Cell population modelling of yeast glycolytic oscillations. *Biochem. J*. **368**, 433-446.

Hermanto, M.W., Chiu, M.-S., Woo, X.Y., Braatz, R.D., 2007. Robust optimal control of polymorphic transformation in batch crystallisation. *AIChE J*. **53**, 2643-2650.

Hlozny, L., Sato, K., Kubota, N., 1992. On-line measurement of supersaturation during batch cooling crystallisation of Ammonium Alum. *J. Chem. Eng. Jpn*. **25**, 604-606.

Hojjati, H., Rohani, S., 2005. Cooling and seeding effect on supersaturation and final crystal size distribution (CSD) of ammonium sulphate in a batch crystallizer. *Chem. Eng. Process.* **44**, 949-957.

Hounslow, M.J., 1998. The population balance as a tool for understanding particle rate processes. *Kona Powder and Particle* **16**, 1821-1832.

Hounslow, M.J., Reynolds, G.K., 2006. Product engineering for crystal size distribution. *AIChE J*. **52**, 2507-2517.

Hounslow, M.J., Ryall, R.L., Marshall, V.R., 1988. A discretized population balance for nucleation, growth and aggregation. *AIChE J*. **34**, 1821-1832.

Hu, Q., Rohani, S., Wang, D.X., Jutan, A., 2005. Optimal control of a batch cooling seeded crystalliser. *Powder Technol*. **156**, 170-176.

Hukkanen, E.J., Braatz, R.D., 2003. Measurement of particle size distribution in suspension polymerization using in situ laser backscattering. *Sensors and Actuators B: Chemical* **96**, 451-459.

Hulburt, H.M., Katz, S., 1964. Some problems in particle technology - A statistical mechanical formulation. *Chem. Eng. Sci*. **19**, 555-574.

Immanuel, C.D., Doyle, I.F.J., 2002. Open-loop control of particle size distribution in semi-batch emulsion copolymerization using a genetic algorithm. *Chem. Eng. Sci*. **57**, 4415-4427.

Immanuel, C.D., Doyle, I.F.J., 2003. Computationally efficient solution of population balance models incorporating nucleation, growth, coagulation: Application to emulsion polymerization. *Chem. Eng. Sci*. **58**, 3681-3698.

Jagadesh, D., Kubota, N., Yokota, M., Sato, A., Tavare, N.S., 1996. Large and mono-sized product crystals from natural cooling mode batch crystalliser. *J. Chem. Eng. Jpn*. **29**, 865-873.

John, V., Angelov, I., Oncul, A.A., Sundmacher, K., Thevenin, D., 2005. Towards the optimal reconstruction of a distribution from its moments, AIChE Annual meeting, Cincinnati, OH, USA.

Jones, A.G., 1974. Optimal operation of a batch cooling crystallizer. *Chem. Eng. Sci*. **29**, 1075-1087.

Jones, A.G., 2002. Crystallization process systems. Butterworth heinemann, Oxford, UK.

Jones, A.G., Chianese, A., Berardino, F.D., 1993. On the effect of secondary nucleation on the crystal size distribution from a seeded batch crystallizer. *Chem. Eng. Sci*. **48**, 551-560.

Jones, A.G., Mullin, J.W., 1974. Programmed cooling crystallization of potassium sulphate solutions. *Chem. Eng. Sci*. **29**, 105-118.

Kalani, A., Christofides, P.D., 2000. Modelling and control of a titania aerosol reactor. *Aerosol Sci. Tech* **32**, 369-391.

Kalani, A., Christofides, P.D., 2002. Simulation, estimation and control of size distribution in aerosol processes with simultaneous reaction, nucleation, condensation and coagulation. *Comput. Chem. Eng*. **26**, 1153-1169.

Kalbasenka, A.N., 2009. Model-based control of industrial batch crystallisers. Experiments on enhanced controllability by seeding actuation., Department of Chemical Engineering. Delft University of Technology, pp. 1-325, PhD thesis.

Kalbasenka, A.N., Spierings, L.C.P., Huesman, A.E.M., Kramer, H.J.M., 2007. Application of seeding as a process actuator in a model predictive control framework for fed-batch crystallisation of ammonium sulphate. *Part. Part. Syst. Charact*. **24**, 40-48.

Kee, N., Woo, X.Y., Tan, R.B.H., Braatz, R.D., 2009. Precise tailoring of the crystal size distribution by optimal seeding time profile., AIChE Annual Meeting.

Kempkes, M., Eggers, J., Mazzotti, M., 2008. Measurement of particle size and shape by FBRM and *in situ* microscopy. *Chem. Eng. Sci*. **63**, 4656-4675.

Kiparissides, C.A., Meimaroglou, D., Roussos, A.I., 2006. Part IV: Dynamic evolution of the particle size distribution in particulate processes. A comparative study between Monte Carlo and the generalized method of moments. *Chem. Eng. Sci*. **61**, 5620-5635.

Kougoulos, E., Jones, A.G., Jennings, K.H., Wood-Kaczmar, M.W., 2005. Use of focused beam reflectance measurement (FBRM) and process video imaging (PVI) in a modified mixed suspension mixed product removal (MSMPR) cooling crystallizer. *J Cryst. Growth* **273**, 529-534.

Kubota, N., Doki, N., Yokota, M., Sato, A., 2001. Seeding policy in batch cooling crystallisation. *Powder Technol*. **121**, 31-38.

Kumar, S., Ramkrishna, D., 1996a. On the solution of population balance equations by discretization - I. A fixed pivot technique. *Chem. Eng. Sci*. **51**, 1311-1332.

Kumar, S., Ramkrishna, D., 1996b. On the solution of population balance equations by discretizations-II. A moving pivot technique. *Chem. Eng. Sci*. **51**, 1311-1332.

Kumar, S., Ramkrishna, D., 1997. On the solution of population balance equations by discretization- III. Nucleation, growth and aggregation of particles. *Chem. Eng. Sci*. **52**, 4659-4679.

Larsen, P.A., Patience, D.B., Rawlings, J.B., 2006. Industrial crystallisation process control. *IEEE Control Systems Magazine* **26**, 70-80.

Larson, M.A., Helt, J.E., 1977. Effect of temperature on the crystallisation of potassium nitrate by direct measurement of supersaturation. *AIChE J*. **23**, 822-830.

Lawrence, X.Y., Robert, A.L., RAw, A.S., D'Costa, R., Wu, H., Hussain, A.S., 2004. Applications of process analytical technology to crystallisation processes. *Adv. Drug Delivery Rev.* **56**, 349-369.

Lee, G., Yoon, E.S., Lim, Y.-I., Lann, J.M.L., Meyer, X.n.-M., Joulia, X., 2001. Adaptive mesh method for the simulation of crystallization processes including agglomeration and breakage: the potassium sulfate system. *Ind. Eng. Chem. Res*. **40**, 6228-6235.

Lee, K., Lee, J.H., Fujiwara, M., Ma, D.L., Braatz, R.D., 2002. Run-to-run contol of multidimensional cystal size distribution in a batch crystalliser., Proc. of the American Control Conference; IEEE Press Piscataway, NJ, pp. 1013-1018.

LeVeque, R.J., 1992. Numerical methods for conservation laws. Birkhauser Verlag, Basel, Switzerland.

Lewiner, F., Fevotte, G., Klein, J.P., Pfefer, G., 1999. Application of *in situ* ATR-FTIR to the on-line monitoring of batch crystallisation with agglomeration, 14th Int Symposium of Industrial crystallisation, Cambridge, UK, pp. 145-152.

Li, M., Shi, D., Christofides, P.D., 2004. Diamond jet hybrid HVOF thermal spray: gas-phase and particle behaviour modeling and feedback control design. *Ind. Eng. Chem. Res*. **43**, 3632-3652.

Liotta, V., Sabesan, V., 2004. Monitoring and feedback control of supersaturation using ATR-FTIR to produce an active pharmaceutical ingredient of a desired crystal size. *Org. Process Res. Dev*. **8**, 488-494.

Litster, J.D., Smith, D.J., Hounslow, M.J., 1995. Adjustable discretized population balance for growth and aggregation. *AIChE J*. **41**, 591-603.

Loffelmann, M., Mersmann, A., 1999. Innovative supersaturation sensor for industrial crystallisation, Proc. of the 14th Int. Symp. on Industrial crystallisation, Cambridge, UK, pp. 210-216.

Loffelmann, M., Mersmann, A., 2002. How to measure supersaturation? *Chem. Eng. Sci*. **57**, 4301-4310.

Ludwick, J.C., Henderson, P.L., 1968. Particle shape and inference of size from sieving. *Sedimentology* **11**, 197-235.

Lung-Somarriba, B.L.M., Moscosa-Santillan, M., Porte, C., Delacroix, A., 2004. Effect of seeded surface area on crystal size distribution in glycine batch cooling crystallisation: a seeding methodology. *J Cryst. Growth* **270**, 624-632.

Ma, D.L., Tafti, D.K., Braatz, R.D., 2002a. High resolution simulation of multidimensional crystal growth. *Ind. Eng. Chem. Res*. **41**, 6217-6223.

Ma, D.L., Tafti, D.K., Braatz, R.D., 2002b. Optimal control and simulation of multidimensional crystallisation processes. *Comput. Chem. Eng*. **23**, 1103-1116.

MacDonald, M.J., Chu, C.F., Guilloit, P.P., Ng, K.M., 1991. A generalized Blake-Kozeny equation for multisized spherical particles. *AIChE J*. **37**, 1583-1588.

Mahoney, A.W., Ramkrishna, D., 2002a. Efficient solution of population balance equations with discontinuties by finite elements. *Chem. Eng. Sci*. **57**, 1102-1119.

Mahoney, A.W., Ramkrishna, D., 2002b. Population balance modelling: Promise for the future. *Chem. Eng. Sci.* **57**, 595-606.

Mangin, D., Garcia, E., Gerard, S., Hoff, C., Klein, J.P., Veesler, S., 2006. Modeling and dissolution of a pharmceutical compound. *J. Cryst. Growth* **286**, 121-125.

Marchisio, D.L., Pikturna, J.T., Fox, R.O., Vigil, R.D., Barresi, A., 2003a. Quadrature method of moments for population-balance equations. *AlChE J*. **49**, 1266-1276.

Marchisio, D.L., Vigil, R.D., Fox, R.O., 2003b. Quadrature method of moments for aggregation–breakage processes. *J Colloid Interf. Sci*. **258**, 322-334.

MathWorld, W., 2009. Orthagonal Polynomials.

MathWorld, W., Arfken, 1985. Laguerre Polynomials.

Matthews, H.B.M., Rawlings, J.B., 1996. Model identification for crystallization: Theory and experimental verification. *Powder Technol*. **88**, 227-235.

McCoy, B.J., Madras, G., 2004. Reversible crystal growth-dissolution and aggregation-breakage: numerical and moment solutions for population balance equations. *Powder Technol*. **143-144**, 297-307.

McGraw, R., 1997. Description of aerosol dynamics by the quadrature method of moments. *Aerosol Sci. Technol*. **27**, 255-265.

McGraw, R., Wright, D.L., 2003. Chemically resolved aerosol dynamics for internal mixtures by the quadrature method of moments. *J Aerosol Sci*. **34**, 189-209.

Mesbah, A., Kramer, H.J.M., Huesman, E.M., Van den Hof, P.M.J., 2009. A comparative study on the numerical solution of the poplation balance equation for crystallisation processes. *Chem. Eng. Sci*. **64**, 4262-4277.

Middlebrooks, S.A., 2001. Modelling and control of Silicon and Germanium thin film chemical vapor deposition. University of Wisconsin-Madison, PhD thesis.

Miller, S.M., Rawlings, J.B., 1994. Model identification and control strategies for batch cooling crystallisers. *AIChE J.* **40**, 1312-1327.

Molnar, I., Halasz, S., Blickle, T., 1990. Determination of size-dependent growth crystal growth characteristics from batch experiments. *Chem. Eng. Sci*. **45**, 1243-1251.

Monnier, O., Fevotte, G., Hoff, C., Klein, J.P., 1997. Model identification of batch cooling crystallization through calorimetry and image analysis. *Chem. Eng. Sci*. **52**, 1125-1139.

Monnier, O., Klein, J.P., Hoff, C., Ratsimba, B., 1996. Particle size determination by laser reflection: methodology and problems. *Part. Part. Syst. Charact* **13**, 10-17.

Motz, S., Gilles, E.D., 2008. State estimation in batch crystallisation using reduced population balance models. *J. Process Control* **18**, 361-337.

Mullin, J.W., 2001. Crystallization, Fourth ed. Butterworth Heinemann: London, UK.

Mullin, J.W., Nyvlt, J., 1971. Programmed cooling of batch crystallisers. *Chem. Eng. Sci*. **26**, 369-377.

Nagy, Z.K., 2009. Model-based robust control approach for batch crystallisation product design. *Comput. Chem. Eng*. **33**, 1685-1691.

Nagy, Z.K., Braatz, R.D., 2003a. Robust nonlinear model predictive control of batch processes. *AIChE J*. **49**, 1776-1786.

Nagy, Z.K., Braatz, R.D., 2003b. Worst-case and distributional robustness analysis of finite-time control trajectory for non-linear distributed parameter systems. *IEEE Transactions on Control Systems Technology*. **11**, 694-704.

Nagy, Z.K., Braatz, R.D., 2004. Open-loop and closed-loop robust optimal control of batch processes using distributional and worst-case analysis. J. *Process Control* **14**, 411-422.

Nagy, Z.K., Chew, J.W., Braatz, R.D., 2008a. Comparative performance of concentration and temperature controlled crystallisation. *J. Process Control* **18**, 399-407.

Nagy, Z.K., Fujiwara, M., Braatz, R.D., 2006a. Optimal control of combined cooling and anti-solvent pharamceutical crystallisation., Proc. of the 13th International Workshop on Industrial Crystallisation., Delft, The Netherlands, pp. 16-23.

Nagy, Z.K., Fujiwara, M., Braatz, R.D., 2006b. Recent advances in the modelling and control of cooling and anti-solvent crystallisation of pharmaceuticals., Proc. of the 8th International IFAC Symp.on Dynamics and Control of Process Systems., Cancun, Mexico, pp. 29-38.

Nagy, Z.K., Fujiwara, M., Braatz, R.D., 2008b. Modelling and control of combined cooling and anti-solvent crystallisation processes. *J. Process Control* **18**, 856-894.

Nagy, Z.K., Fujiwara, M., Woo, X.Y., Braatz, R.D., 2008c. Determination of the kinetic parameters for the crystallisation of paracetamol from water using metastable zone width experiments. *Ind. Eng. Chem. Res* **47**, 1245-1252.

Nallet, V., Mangin, D., Klein, J.P., 1998. Model identification of batch precipitations: Application to salicylic acid. *Comput. Chem. Eng*. **22**, S649-S652.

Nicmanis, M., Hounslow, M.J., 1998. Finite element methods of steady state population balance equations. *AIChE J*. **44**, 2258-2272.

Nowee, S.M., Abbas, A., Romagnoli, J.A., 2008a. Direct control of particle size in anti-solvent crystallisation Part I: Model indentification, experimental validation and dynamic simulation. *Chem. Eng. Sci*. **63**, 2046-2054.

Nowee, S.M., Abbas, A., Romagnoli, J.A., 2008b. Model-based optimal strategies for controlling particle size in antisolvent crystallisation operations. *Cryst. Growth Des*. **8**, 2698-2806.

Nyvlt, J., Karel, M., Pisarik, S., 1994. Measurement of supersaturation. *Cryst. Res. Technol.* **29**, 409-415.

O'Sullivan, B., Glennon, B., 2005. Application of *in situ* FBRM and ATR-FTIR to the monitoring of the polymorphic transformation of D-mannitol. *Org. Process Res Dev*. **9**, 884-889.

Olesberg, J.T., Arnold, M.A., Hu, S.-Y.B., Wiencek, J.M., 2000. Temperature-insensitive near-infrared method for determination of protein concentration during protein crystal growth. *Analytical Chemistry* **72**, 4985-4990.

Ono, T., Kramer, H.J.M., Ter Horst, J.H., Jansens, P.J., 2004. Process modelling of the polymorphic transformation of L-glutamic acid. *Cryst. Growth Des*. **4**, 1161-1167.

Ouchiyama, N., Tanaka, T., 1984. Porosity estimation for random packings of spherical particles. *Ind. Eng. Chem. Fundam* **23**, 490-493.

Patankar, S., 1980. Numerical heat transfer and fluid flow. Hemisphere Publishing, New York.

Patience, D.B., 2002. Crystal engineering through particle size and shape monitoring, modeling and control, Department of Chemical Engineering. University of Wisconsin - Madison, pp. 1-233, PhD thesis.

Patience, D.B., Hartel, R.W., Illingworth, D., 1999. Crystallization and pressure filtration of anhydrous milk fat: mixing effects. *Journal of the American Oils Chemists' Society* **76**, 585-594.

Peglow, M., Kumar, J., Warnecke, G., Heinrich, S., Tsotsas, E., Morl, L., Hounslow, M.J., 2006. An improved discretized tracer mass distribution of Hounslow *et al. AIChE J*. **52**, 1326-1332.

Perry, R.H., Green, D.W., 1997. Perry's Chemical Engineer's Handbook. McGraw-Hill, London, UK.

Pollanen, A.K., Hakkinen, A., Reinikainen, S.P., Rantanen, J., Minkkinen, P., 2006. Dynamic PCA-based MSPC charts for nucleation prediction in batch cooling crystallization processes. *Chemom. Intell. Lab. Syst*. **84**, 126-133.

Pollanen, K., Hakkinena, A., Reinikainen, S.-P., Louhi-Kultanen, M., Nystrom, L., 2005. ATR-FTIR in monitoring of crystallization processes: comparison of indirect and direct OSC methods. *Chemom. Intell. Lab. Syst*. **76**, 25-35.

Puel, F., Fevotte, G., Klein, J.P., 2003a. Simulation and analysis of industrial crystallization processes through multidimensional population balance equations. Part 2: a study of semi-batch crystallization. *Chem. Eng. Sci.* **58**, 3729-3740.

Puel, F., Fevotte, G., Klein, J.P., 2003b. Simulation and analysis of industrial crystallization processes through multidimensional population balance equations. Part I: a resolution algorithm based on method of classes. Chem. Eng. Sci. 58, 3715-3727.

Ramkrishna, D., 1981. Analysis of population balance-IV. The precise connection between Monte Carlo and population balances. *Chem. Eng. Sci.* **36**, 1203-1209.

Ramkrishna, D., 2000. Population Balances. Theory and Applications to Particulate Systems in Engineering. Academic Press San Diego, USA.

Ramkrishna, D., Borwanker, J.D., 1973. A puristic analysis of population balance - I. *Chem. Eng. Sci.* **28**, 1423-1435.

Ramkrishna, D., Borwanker, J.D., 1974. A puristic analysis of population balance - II. *Chem. Eng. Sci*. **29**, 1711-1721.

Randolph, A.D., Larson, M.A., 1971. Theory of particulate processes: Analysis and Techniques of Continuous Crystallisation. Academic Press, San Diego, USA.

Randolph, A.D., Larson, M.A., 1988. Theory of Particulate Processes. Academic Press, NewYork, USA.

Rawlings, J.B., 2000. Tutorial overview of model predictive control. *IEEE Control Systems Magazine* **20**, 38-52.

Rawlings, J.B., Miller, A.G., Witkowaski, W.R., 1993. Model identification and control of solution crystallisation processes: A review. *Ind. Eng. Chem. Res*. **32**, 1275-1296.

Rawlings, J.B., Witkowaski, W.R., Eaton, J.W., 1992. Modelling and control of crystallisers. *Powder Technol*. **69**, 3-9.

Rigopoulos, S., Jones, A.G., 2003. Finite element scheme for solution of the dynamic population balance equation. *AIChE J*. **49**, 1127-1139.

Rod, V., Misek, t., 1982. Stochastic modelling of dispersion formation in agitated liquid-liquid systems. *Trans IChemE* **60**, 48-53.

Roffel, B., Betlem, B., 2006. Process dynamics and control: Modeling for control and prediction. John Wiley & Sons Ltd, Wets Sussex, England.

Rosner, D.E., McGraw, R., Tandon, P., 2003. Multivariate population balances via moment and monte carlo simulation methods: An important sol reaction engineering bivariate example and "mixed" moments for the estimation of deposition, scavenging, and optical properties for populations of nonspherical suspended particles. *Ind. Eng. Chem. Res*. **42**, 2699-2711.

Rosner, D.E., Pyykonen, J.J., 2002. Bivariate moment simulation of coagulation and sintering nanopartilces in flames. *AIChE J*. **48**, 476-491.

Ruf, A., Worlitschek, J., Mazzotti, M., 2000. Modelling and experimental analysis of PSD measurements through FBRM. *Part. Part. Syst. Charact*. **17**, 167-179.

Rusli, E., Lee, J.H., Braatz, R.D., 2006. Optimal distributional control of crystal size and shape., Proc. of the 5th World Congress on Particle Technology., Orlando, FL, p. 240f.

Sahin, O., Ozdemir, M., Kendirci, H., Bulutcu, A.N., 2000. Determination of growth and dissolution mass rate of boric acid crystals by a simple computer program. *J. Cryst. Growth* **219**, 75-82.

Salvatori, F., Muhr, H., Plasari, E., 2005. A new solution for closure problem in crystallisation modeling using moments method. *Powder Technol.* **157**, 27-32.

Sarkar, D., Rohani, S., Jutan, A., 2006. Multi-objective optimisation of seeded batch crystallisation processes. *Chem. Eng. Sci*. **61**, 5282-5295.

Scott, T.D., Clejan, I., Gencer, A.H., 1997. Accurate and efficient modeling of nucleation and growth processes. *Materials Science and Engineering A* **A238**, 152-159.

Shah, M.B., Borwanker, J.D., Ramkrishna, D., 1977. Simulation of particulate systems using the concept of the interval of quiescence. *AIChE J*. **23**, 897-904.

Sheikhzadeh, M., Trifkovic, M., Rohani, S., 2008a. Adaptive MIMO neuro-fuzzy logic control of a seeded and an unseeded anti-solvent semi-batch crystalliser. *Chem. Eng. Sci*. **63**, 1261-1272.

Sheikhzadeh, M., Trifkovic, M., Rohani, S., 2008b. Fuzzy logic and rigid control of a seeded semi-batch, anti solvent, isothermel crystalliser. *Chem. Eng. Sci*. **63**, 991-1002.

Shi, D., El-Farra, N.H., Li, M., Mhaskar, P., Christofides, P.D., 2006. Predictive control of particle size distribution in particulate processes. *Chem. Eng. Sci*. **61**, 268-281.

Shi, D., Mhaskar, P., El-Farra, N.H., Christofides, P.D., 2005. Predictive control of crystal size distribution in protein crystallisation. *Nanotechnology* **16**, S562-S574.

Simon, L.L., Nagy, Z.K., Hungerbuhler, K., 2009a. Comparison of external bulk video imaging with focused beam reflectance measurement and ultra-violet visible spectroscopy for metastable zone identification in food and pharmaceutical crystallisation processes. *Chem. Eng. Sci*. **64**, 3344-3351.

Simon, L.L., Nagy, Z.K., Hungerbuhler, K., 2009b. Endoscopy-based *in situ* bulk video imaging of batch crystallisation processes. *Org. Process Res Dev*. **13**, 1254-1261.

Smith, R., 2005. Chemical Process Design and Integration. John Wiley and Sons limited, West Sussex, UK.

Sohnel, O., Garside, J., 1992. Precipitation. Butterworth-Heinemann, Oxford, UK.

Soos, M., Sefcik, J., Morbidelli, M., 2006. Investigation of aggregation, breakage and restructuring kinetics of colloidal dispersions in turbulent flows by population balance modelling and static light scattering. *Chem. Eng. Sci*. **61**, 2349-2363.

Spielman, L.A., Levenspiel, O., 1965. A monte carlo simulation of population balances. *Chem. Eng. Sci*. **53**, 1777-1786.

Stelling, J., Sauer, U., Szallasi, Z., Doyle, I.F.J., Doyle, J., 2004. Robustness of cellular functions. *Cell* **118**, 675-685.

Tavare, N.S., Chivate, M.R., 1977. Analysis of batch evaporative crystallisers. *Chem Eng J.* **14**, 175-180.

Tavare, N.S., Chivate, M.R., 1995. Industrial Crystallisation. Process Simulation Analysis and Design. Plenum Press, NewYork, USA.

Volmer, M., 1939. Kinetic der Phasenbildung. Steinkopff, Leipzig.

Vu, T.T.L., Durham, R.J., Hourigan, J.A., Sleigh, R.W., 2006. Dynamic modelling optimisation and control of lactose crystallisations: Comparison of process alternatives. *Sep. Purif. Technol.* **48**, 159-166.

Wachi, S., Jones, A.G., 1992. Dynamic modelling of particle size distribution and degree of agglomeration during precipitation. *Chem. Eng. Sci*. **47**, 3145-3148.

Wakeman, R.J., Tarleton, E.S., 1999. Filtration: Equipment Selection, Modelling and Process Simulation., Oxford, UK.

Wang, F.Y., Ge, X.Y., Balliu, N., Cameron, I.T., 2006. Optimal control and operation of drug granulation processes. *Chem. Eng. Sci*. **61**, 257-267.

Ward, J.D., Mellichamp, D.A., Doherty, M.F., 2006. Choosing an operating policy for seeded batch crystallisation. *AIChE J.* **52**, 2046-2054.

White, W.H., 1990. Particle size distributions that cannot be distinguished by their integral moments. *J Colloid Interf. Sci*. **135**, 297-299.

Wibowo, C., Chang, W.-C., Ng, K.M., 2001. Design of integrated crystallisation systems. *AlChE J*. **47**, 2474-2492.

Wibowo, C., Ng, K.M., 2001. Operational issues in solids processing plants: systems view. *AIChE J*. **47**, 107-125.

Wiencek, J.M., 2002. Crystallisation of proteins, in: Myerson, A.S. (Ed.), Handbook of Industrial Crystallisation, 2nd ed. Butterworth-Heinemann, Oxford, UK, pp. 267-285.

Woo, X.Y., Nagy, Z.K., Tan, R.B.H., Braatz, R.D., 2009a. Adaptive concentration control of cooling and antisolvent crystallisation with laser backscattering measurement. *Cryst. Growth Des*. **9**, 182-190

Woo, X.Y., Tan, R.B.H., Braatz, R.D., 2009b. Modelling and computational fluid dynamic-population balance equation-micromixing simulation of impinging jet crystallisers. *Cryst. Growth Des*. **9**, 156-164.

Woo, X.Y., Tan, R.B.H., Chow, P.S., Braatz, R.D., 2006. Simulation of mixing effects and antisolvent cystallisation using a coupled CFD-PDF-PBE approach. *Cryst. Growth Des*. **6**, 1291-1303.

Worlitschek, J., Mazzotti, M., 2004. Model based optimization of particle size distribution in batch cooling crystallization of Paracetamol. *Cryst. Growth Des*. **4**, 891-903.

Wright, D.L., McGraw, R., Rosner, D.E., 2001. Bivariate extension of the quadrature method of moments for modelling simultaneous coagulation and sintering of particle populations. *J Colloid Interf. Sci*. **236**, 242-251.

Xie, W., Rohani, S., Phoenix, A., 2001. Dynamic modelling and operation of a seeded batch cooling crystalliser. *Chem. Eng. Commun*. **187**, 229-249.

Yu, L.X., Lionbergera, R.A., Rawa, A.S., D'Costa, R., Wub, H., Hussain, A.S., 2004. Applications of process analytical technology to crystallisation processes. *Adv. Drug Delivery Rev.* **56**, 349-369.

Yu, Z.Q., Chew, J.W., Chow, P.S., Tan, R.B.H., 2007. Recent advances in crystallisation control. An industrial perspective. *Chem. Eng. Res. Des.* **85**, 893-905.

Yu, Z.Q., Chow, P.S., Reginald, B.H.T., 2006. Seeding and constant-supersaturation control by ATR-FTIR in anti-solvent crystallisation. *Org. Process Res. Dev*. **10**, 717-722.

Yu, Z.Q., Tan, R.B.H., Chow, P.S., 2005. Effects of operating conditions on agglomeration and habit of paracetamol crystals in anti-solvent crystallisation. *J Cryst. Growth* **279**, 477-488.

Zhang, G.P., Rohani, S., 2003. On-line optimal control of a seeded batch cooling crystalliser. *Chem. Eng. Sci*. **58**, 1887-1896.

Zhao, H., Zheng, C., Xu, M., 2005a. Multi monte carlo method for particle coagulation and condensation/evaporation in dispersed systems. *J Colloid Interf. Sci*. **286**, 195-208.

Zhao, H., Zheng, C., Xu, M., 2005b. Multi monte carlo method for particle coagulation: description and validation. *Applied Mathematics and Computation* **167**, 1383-1399.

Zhou, H., Fujiwara, M., Woo, X.Y., Rusli, E., Tung, H.H., Starbuck, C., Davidson, O., Ge, Z.H., Braatz, R.D., 2006a. Direct design of pharmaceutical antisolvent crystallisation through concentration control. *Cryst. Growth Des*. **6**, 892-898.

Zhou, J., Moehary, F., Gross, B., Ahmed, S., 2006b. Particle size and refractive index retrieval from the backscattering spectrum of white light using the two way iterative method: simulation and experiment. *Applied Optics* **45**, 6676-6685.

Zhu, G.Y., Zamamiri, A., Henson, M.A., Hjortso, M.A., 2000. Model predictive control of continuous yeast bioreactors using cell population balance models. *Chem. Eng. Sci*. **55**, 6155-6167.

Zumstein, R.C., Rousseau, R.W., 1989. Agglomeration of copper sulfate pentahydrate crystals within well-mixed crystallisers. *Chem. Eng. Sci*. **44**, 2149-2155.

Appendix A

The CSD was measured throughout the batch for experiment A and B using Malvern Insitec. The results are shown below.

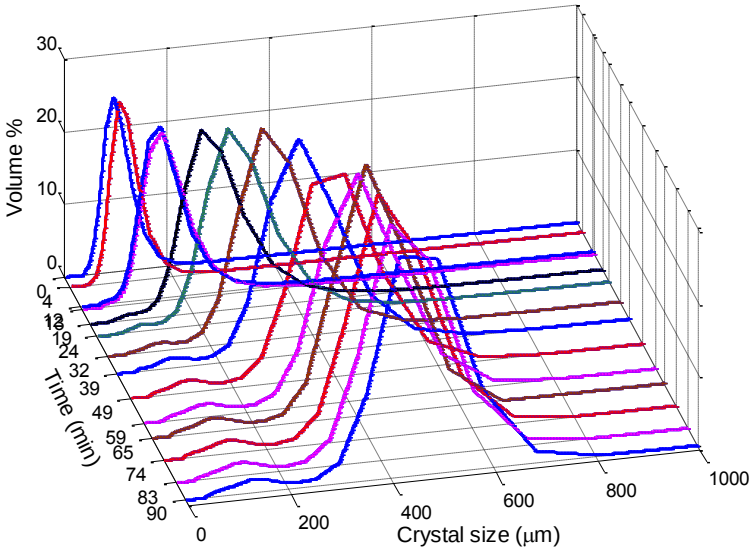

(a)

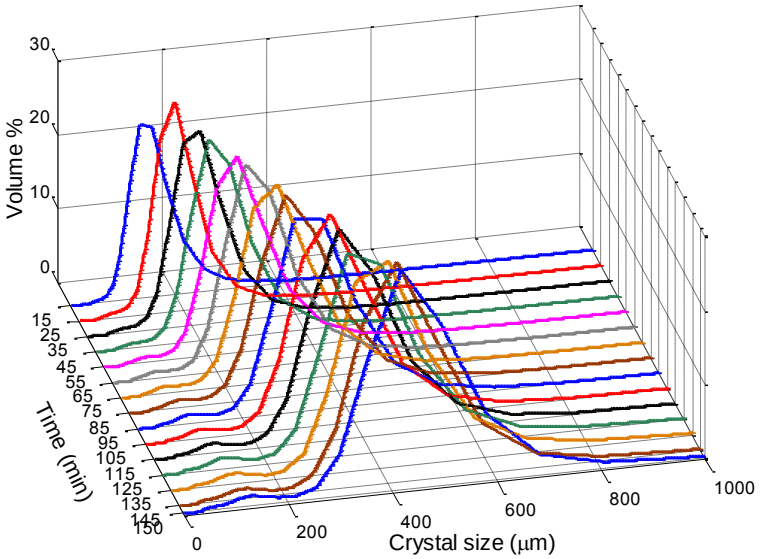

(b)

Figure A.1: Volume % measured by Malvern Insitec at BASF company throughout the batch, used for parameter identification and validation in chapter 5 a) experiment A and b) experiment B.

Appendix B

The simulated CSD for experiments A and B throughout the batch using the combined QMOM-MOCH technique.

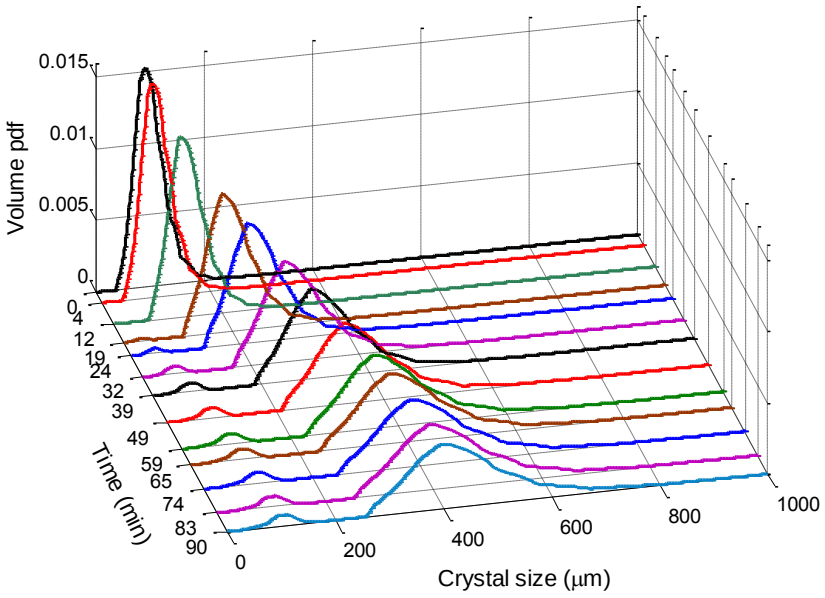

(a)

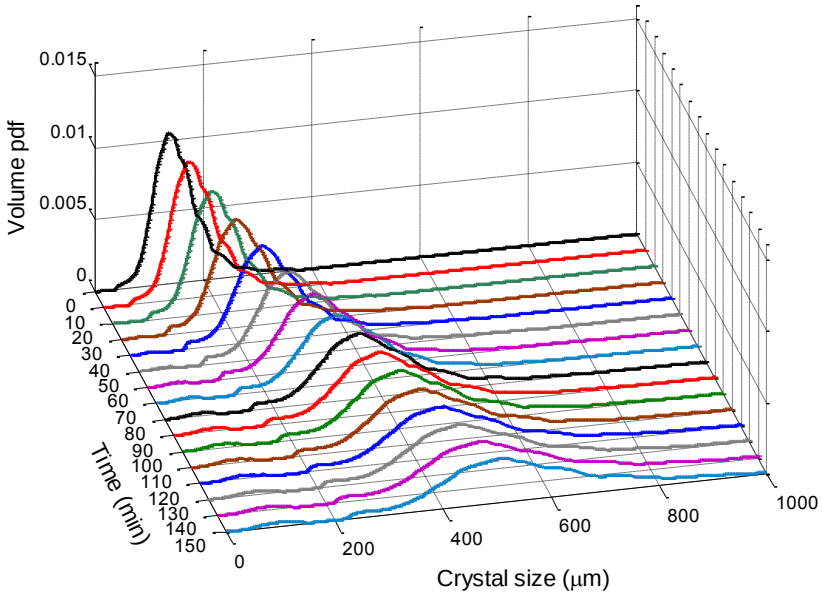

(b)

Figure B.1: The dynamic evolution of the CSD predicted using the combined QMOM and MOCH solution technique for the experiments performed at BASF a) experiment A and b) experiment B.

Appendix C

Derivation of the analytical expression for the pdf in the case of size dependent growth at constant supersaturation.

The population balance equation for batch crystallisation is given as

$$\frac{\partial f_n}{\partial t} + \frac{\partial \left[f_n G(L) \right]}{\partial L} = 0,$$
$$\frac{\partial f_n}{\partial t} + f_n \frac{\partial G}{\partial L} + G \frac{\partial f_n}{\partial L} = 0,$$

$$\frac{\partial f_n}{\partial t} + G \frac{\partial f_n}{\partial L} = -f_n \frac{\partial G}{\partial L}. \tag{C.1}$$

The expression for growth is given by:

$$G = k_g S^q (1 + \gamma L)^p. \tag{C.2}$$

Supersaturation is constant which is possible in controlled crystallisation. In equation (C.2), $S = C(t) - C_{sat}(t)$. Now differentiating equation (C.2) w.r.t. characteristic size,

$$\frac{dG}{dL} = k_g S^q p\gamma (1 + \gamma L)^{p-1}. \tag{C.3}$$

As $f_n(L,t) = f_n[L(\mathcal{Z}), t(\mathcal{Z})]$,

so, $$\frac{dL}{d\mathcal{Z}} \frac{\partial f_n}{\partial L} + \frac{dt}{d\mathcal{Z}} \frac{\partial f_n}{\partial t} = \frac{df_n}{d\mathcal{Z}}. \tag{C.4}$$

Comparing equation (C.1) and (C.4) we have

$$\frac{dt}{d\mathcal{Z}} = 1,$$

$$\frac{dL}{d\mathcal{Z}} = G,$$

$$\frac{df_n}{d\mathcal{Z}} = -f_n \frac{\partial G}{\partial L}.$$

Substituting the values in above, we can have the required odes.

$$\frac{dt}{d\mathcal{Z}} = 1\,, \tag{C.5}$$

$$\frac{dL}{d\mathcal{Z}} = k_g S^g (1+\gamma L)^p\,, \tag{C.6}$$

$$\frac{df_n}{d\mathcal{Z}} = -f_n k_g S^g \gamma p (1+\gamma L)^{p-1}\,. \tag{C.7}$$

Integrating equation (C.5) with limits

$$\frac{dt}{d\mathcal{Z}} = 1,$$

$$\int_{t_0}^{t} dt = \int_{\mathcal{Z}_0}^{\mathcal{Z}} d\mathcal{Z}\,, \quad \text{where } t_0 = \mathcal{Z}_0 = 0$$

$$t = \mathcal{Z} \tag{C.8}$$

Now integrating equation (C.6) with limits,

$$\frac{dL}{d\mathcal{Z}} = k_g S^g (1+\gamma L)^p\,,$$

As $dt = d\mathcal{Z}$, therefore, $\frac{dL}{dt} = k_g S^g (1+\gamma L)^p\,,$

$$\frac{dL}{k_g S^g (1+\gamma L)^p} = dt\,,$$

$$\int_{L_0}^{L} \frac{dL}{k_g S^g (1+\gamma L)^p} = \int_{0}^{t} dt\,,$$

$$\frac{1}{1-p}\left[(1+\gamma L)^{1-p} - (1+\gamma L_0)^{1-p}\right] = k_g S^g \gamma t,$$

$$(1+\gamma L)^{1-p} = (1+\gamma L_0)^{1-p} + (k_g S^g \gamma t)(1-p)\,, \tag{C.9}$$

$$(1+\gamma L) = \left[(1+\gamma L_0)^{1-p} + (1-p) k_g S^g \gamma t\right]^{\frac{1}{1-p}}\,,$$

$$L = \frac{\left[(1+\gamma L_0)^{1-p} + k_g S^g \gamma t (1-p)\right]^{\frac{1}{1-p}}}{\gamma} - \frac{1}{\gamma},$$

$$L = \frac{\left[\left[(1+\gamma L_0)^{1-p} + k_g S^g \gamma t (1-p)\right]^{\frac{1}{1-p}} - 1\right]}{\gamma}. \tag{C.10}$$

Now integrating equation (C.7) with limits

$$\frac{df_n}{d\mathcal{Z}} = -nk_g S^g \gamma p (1+\gamma L)^{p-1}.$$

As $dt = d\mathcal{Z}$, therefore,

$$\frac{df_n}{dt} = -nk_g S^g \gamma p (1+\gamma L)^{p-1},$$

$$\int_{f_{n,0}}^{f_n} \frac{df_n}{f_n} = -k_g S^g \gamma p \int_0^t (1+\gamma L)^{p-1} dt,$$

$$\int_{f_{n,0}}^{f_n} \frac{df_n}{f_n} = -k_g S^g \gamma p \int_0^t \frac{dt}{(1+\gamma L)^{1-p}}, \tag{C.11}$$

Substituting the value of $(1+\gamma L)^{1-p}$ in the above equation

$$\int_{f_{n,0}}^{f_n} \frac{df_n}{f_n} = -k_g S^g \gamma p \int_o^t \frac{dt}{(1+\gamma L_0)^{1-p} + k_g S^g t \gamma (1-p)},$$

$$\ln\left(\frac{f_n}{f_{n,0}}\right) = k_g S^g \gamma p \frac{1}{k_g S^g \gamma (p-1)} \ln\left[\frac{(1+\gamma L_0)^{1-p} + k_g S^g t \gamma (1-p)}{(1+\gamma L_0)^{1-p}}\right],$$

$$\ln\left(\frac{f_n}{f_{n,0}}\right) = \frac{p}{p-1} \ln\left[1 + \frac{k_g S^g t \gamma (1-p)}{(1+\gamma L_0)^{1-p}}\right],$$

$$\frac{f_n}{f_{n,0}} = \left[1 + \frac{k_g S^g t \gamma (1-p)}{(1+\gamma L_0)^{1-p}}\right]^{\frac{p}{p-1}},$$

$$f_n = f_{n,0}\left[1 + \frac{k_g S^g t \gamma (1-p)}{(1+\gamma L_0)^{1-p}}\right]^{\frac{p}{p-1}}. \tag{C.12}$$

Now calculating the value of L_0 from equation (C.9),

$$(1+\gamma L_0)^{1-p} = (1+\gamma L)^{1-p} - (1-p)k_g S^g t\gamma,$$
$$(1+\gamma L_0) = \left[(1+\gamma L)^{1-p} - (1-p)k_g S^g t\gamma\right]^{\frac{1}{1-p}},$$

$$L_0 = \frac{\left[(1+\gamma L)^{1-p} - (1-p)k_g S^g t\gamma\right]^{\frac{1}{1-p}}}{\gamma} - \frac{1}{\gamma}, \tag{C.13}$$

$$f_n = f_{n,0}(L_0)\left[1 + \frac{k_g S^g t\gamma(1-p)}{(1+\gamma L_0)^{1-p}}\right]^{\frac{p}{p-1}}.$$

Now substituting the value of $(1+\gamma L_0)^{1-p}$ in the equation above,

$$f_n = f_{n,0}(L_0)\left[1 - \frac{k_g S^g t\gamma(1-p)}{(1+\gamma L)^{1-p}}\right]^{\frac{p}{1-p}}.$$

The CSD can be obtained at any moment t by giving values to L_0 and calculating the seed distribution $f_{n,0}(L_0)$ and the L and corresponding pdf values f_n.

Table C.1: Analytical solutions for different growth kinetics of the PBE for supersaturation controlled (growth dominated) crystallisation processes.

Growth expressions	Analytical solution	Validity conditions
$G = k_g S^g (1+\gamma L)^p$	$L = \frac{(((1+\gamma L_0)^{1-p} + k_g S^g t\gamma(1-p))^{\frac{1}{1-p}} - 1)}{\gamma}$ $f_n(L) = f_{n,0}(L_0)\left[1 + \frac{k_g S^g \gamma t(1-p)}{(1+\gamma L_0)^{1-p}}\right]^{\frac{p}{p-1}}.$	$(\gamma \neq 0, p \neq 1).$
$G = k_g S^g$	$L = L_0 + k_g S^g t,$ $f_n(L) = f_{n_0}(L_0).$	$(\gamma = 0, p = 1).$
$G = k_g S^g (1+\gamma L)$	$L = \left[\frac{e^{\gamma k_g S^g t}(1+\gamma L_0) - 1}{\gamma}\right],$ $f_n(L) = f_{n,0}(L_0)e^{-k_g S^g t\gamma}.$	$(\gamma \neq 0, p = 1).$
$G = k_g S^g L^p$	$L = \left[L_0^{1-p} + (1-p)k_g S^g t\right],$ $f_n(L) = f_{n,0}(L_0)\left[1 + \frac{(1-p)k_g S^g t}{L_0^{1-p}}\right]^{\frac{p}{p-1}}.$	$(p \neq 1).$

Appendix D Experimental setup

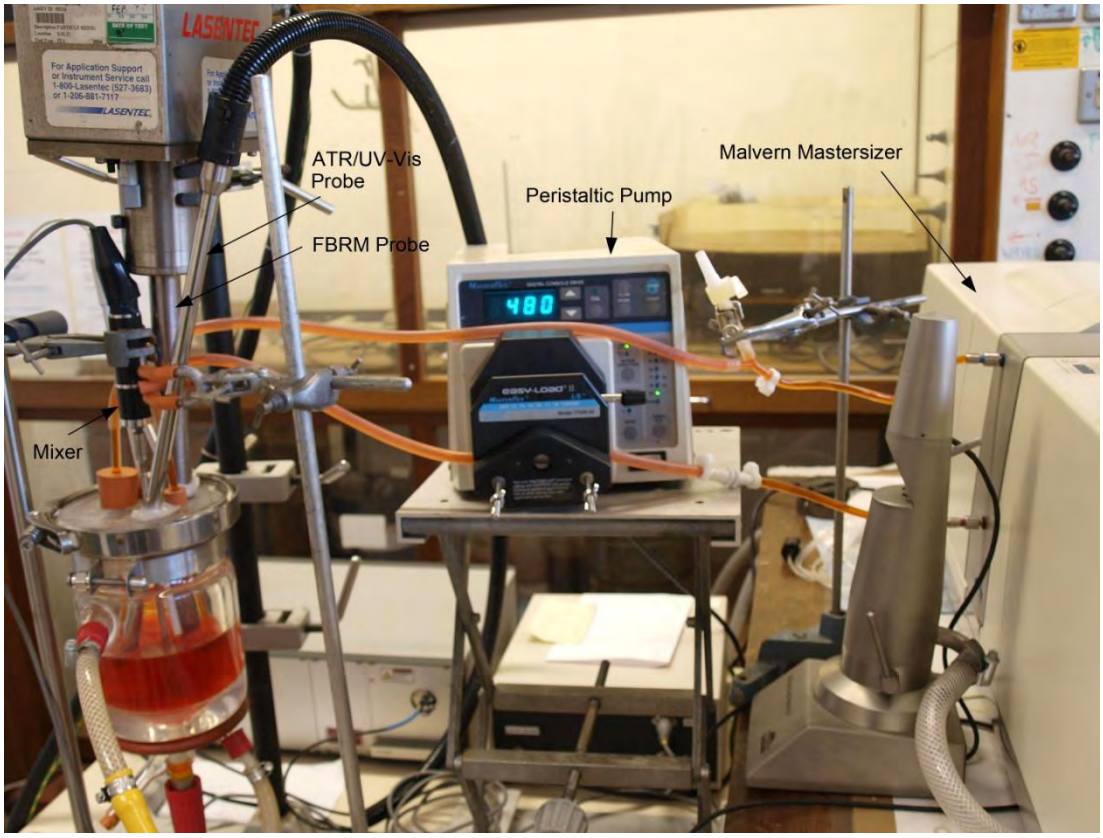

Figure D.1: Image of the experimental setup used to carry out the experiments for the potassium dichromate water system. *In situ* measurement for concentration and chord length distribution was obtained using ATR-UV/Vis and FBRM probes and CSD was measured on-line using a Malvern Mastersizer.

Appendix E Comparison of seed fractions

Microscopic images for different sieve fractions from four different batches of potassium dichromate.

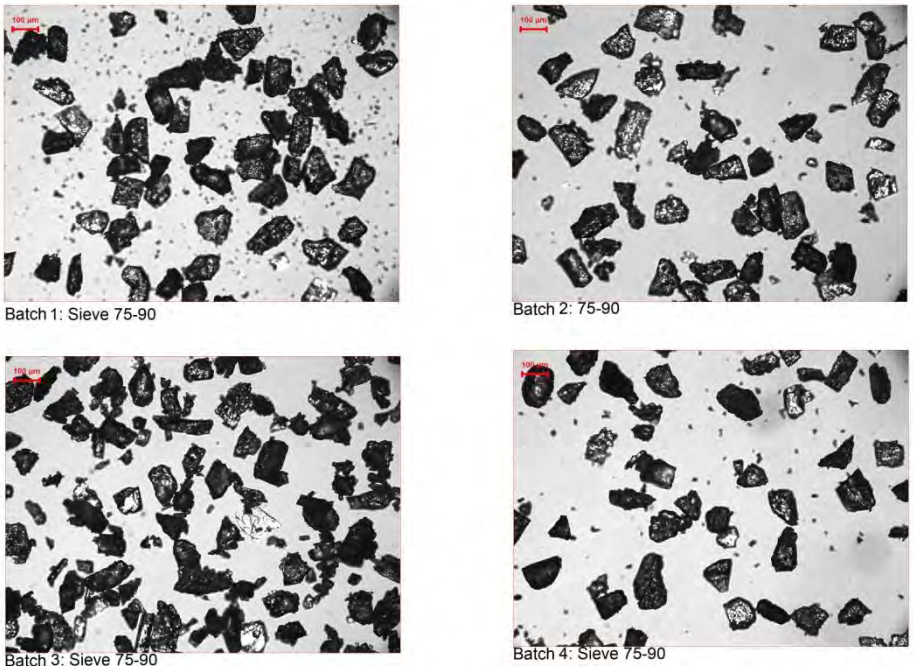

Figure E.1: Comparison of seed fraction 75-90 µm obtained at the end of the four sieve batches.

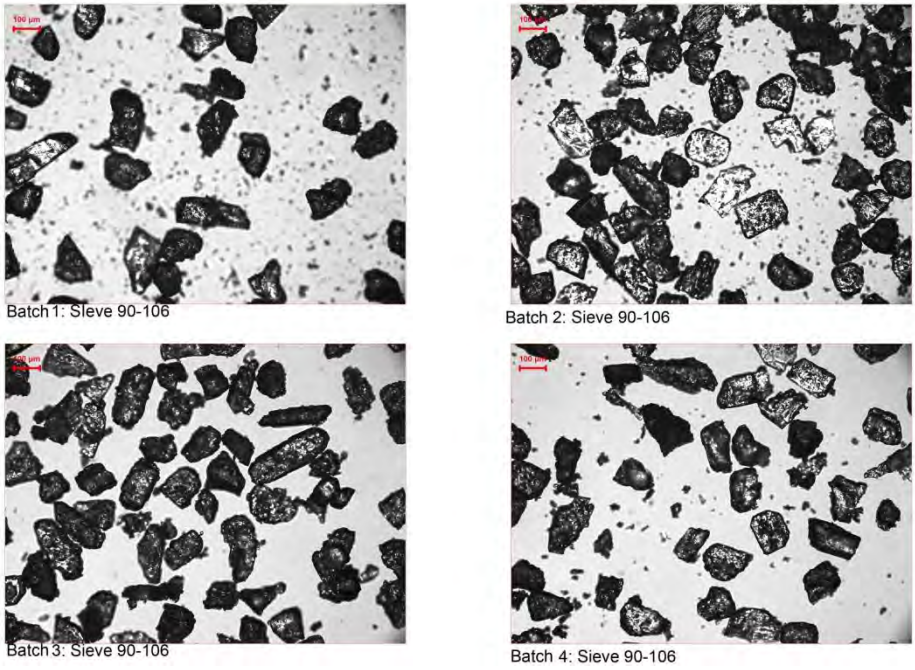

Figure E.2: Comparison of seed fraction 90-106 µm obtained at the end of the four sieve batches.

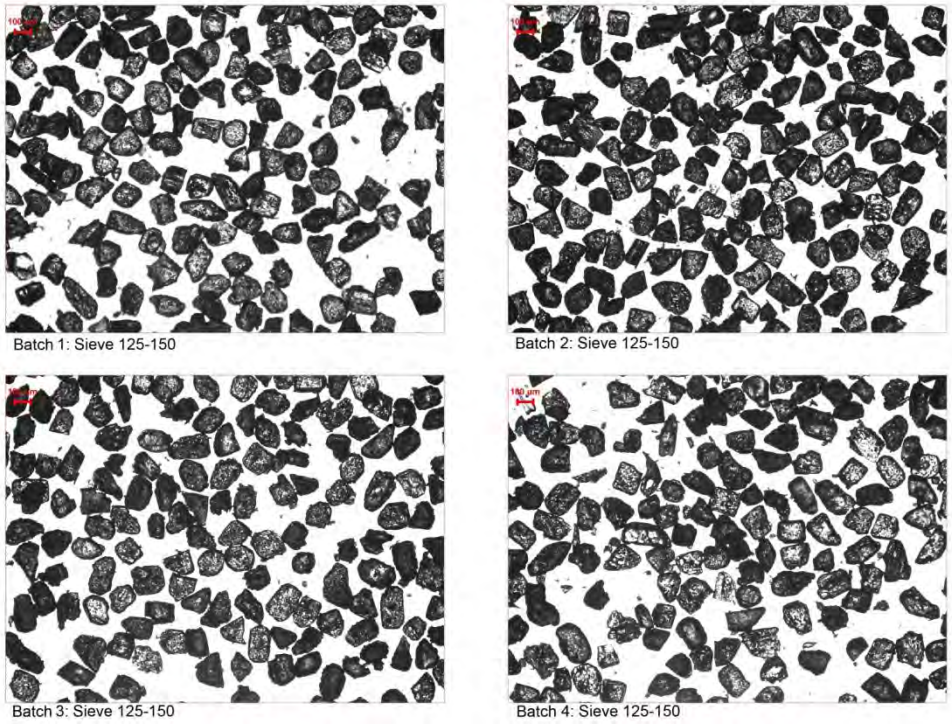

Figure E.3: Comparison of seed fraction 125-150 µm obtained at the end of the four sieve batches.

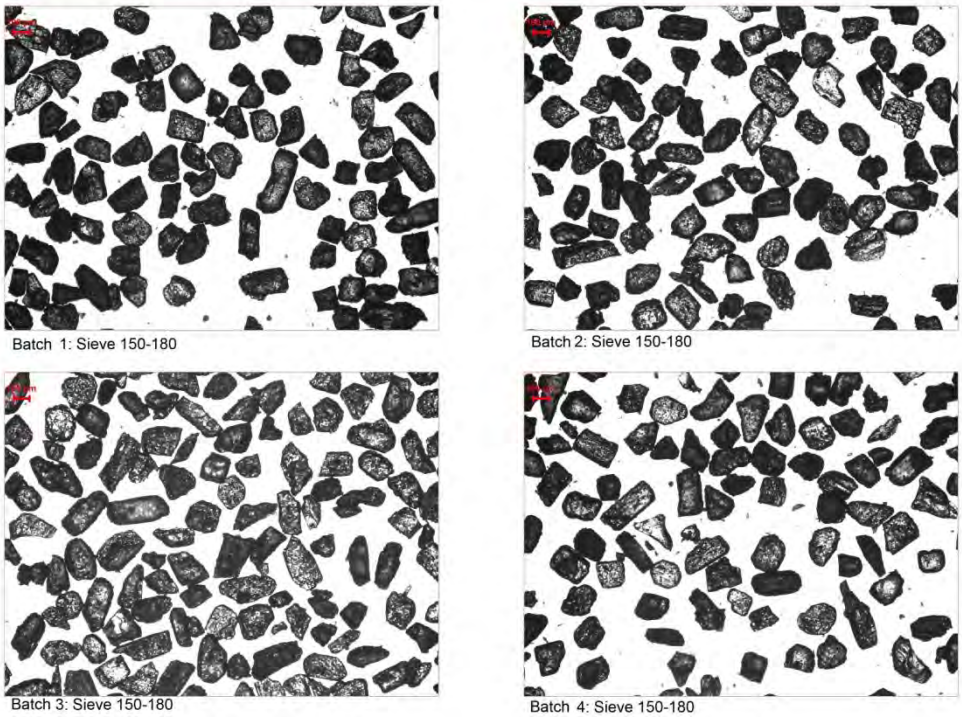

Figure E.4: Comparison of seed fraction 150-180 µm obtained at the end of the four sieve batches.

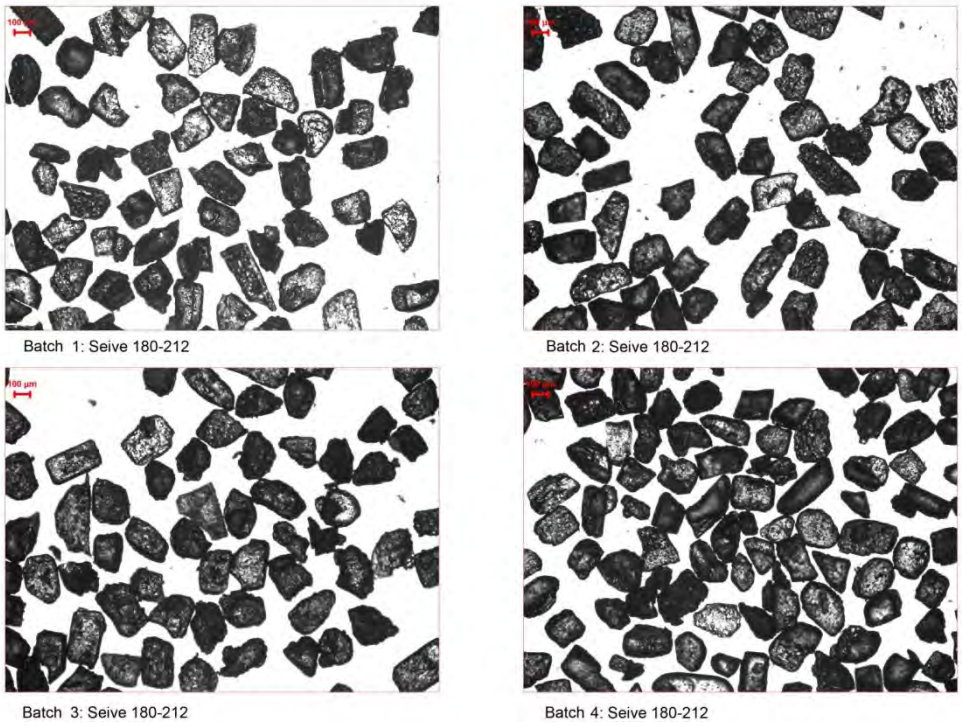

Figure E.5: Comparison of seed fraction 180-212 µm obtained at the end of the four sieve batches.

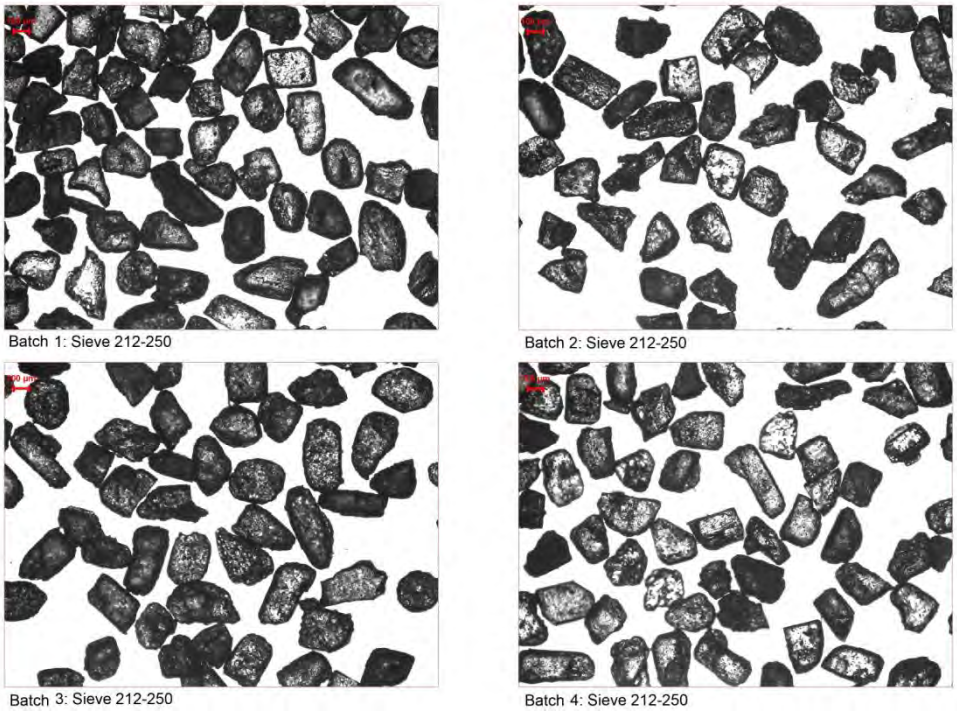

Figure E.6: Comparison of seed fraction 212-250 µm obtained at the end of the four sieve batches.

Appendix F Comparison of different calibration models

Case 1: Both absorbance, and temperature were used to estimate the parameters

For the different models the variables are defined as follows: C is the simulated concentration, A_1 is the absorbance measured at 270.15 nm, A_2 is the absorbance measured at 377.89 nm, a_0, a_1, a_2 & a_3 are the coefficients and T is the temperature in °C.

Expression used	$C = a_0 + a_1A_1 + a_2A_2 + a_3T$	$C = a_0 + a_1A_1 + a_2A_2$
Parameters	**Values**	**Values**
a_0	0.0086	0.0137
a_1	-0.6737	-0.8194
a_2	1.7332	1.9491
a_3	0.0004	--
SSE	0.0021	0.83

$C = a_0 + a_1A_1 + a_2A_2 + a_3T$

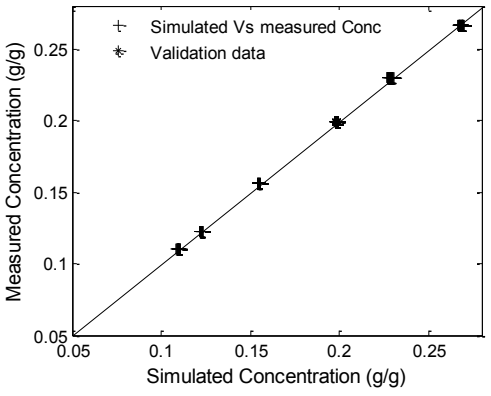

Figure F.1: Comparison between simulated and measured concentration using absorbance and temperature

$C = a_0 + a_1A_1 + a_2A_2$

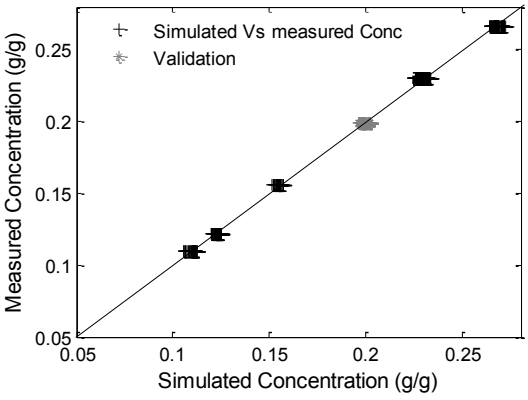

Figure F.2: Comparison between simulated and measured concentration using absorbance only

Case 2: Absorbance 270.15 and temperature was used in the calibration model

Expression used	$C = a_0 + a_1 A_1 + a_2 T$	$C = a_0 + a_1 A_1$
Parameters	**Values**	**Values**
a_0	-0.0132	-0.0098
a_1	0.9133	0.9867
a_2	0.0005	--
SSE	1.9647	3.1544

$C = a_0 + a_1 A_1 + a_2 T$

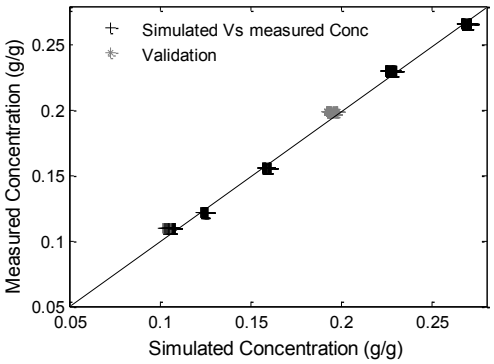

Figure F.3: Comparison between simulated and measured concentration using absorbance 270.15 (nm) only

$C = a_0 + a_1 A_1$

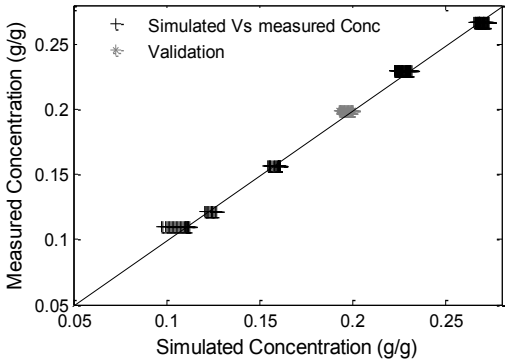

Figure F.5: Comparison between simulated and measured concentration using absorbance 270.15 (nm) and temperature

Case 3: Absorbance 377.89 and temperature were used in the calibration model

Expression	$C = a_0 + a_1 A_2 + a_2 T$	$C = a_0 + a_1 A_2$
Parameters	**Values**	**Values**
a_0	-0.0007	0.0029
a_1	1.0005	1.0658
a_2	0.0005	--
SSE	0.05249	1.3103

$$C = a_0 + a_1 A_2 + a_2 T$$

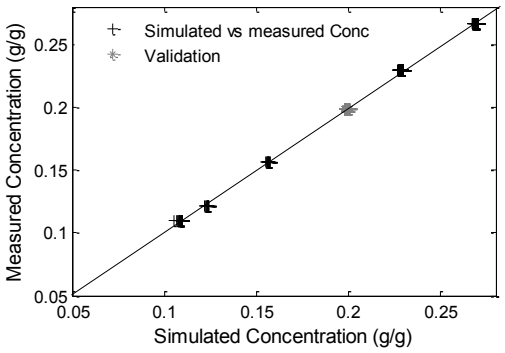

Figure F.6: Comparison between simulated and measured concentration using absorbance 377.83 (nm) only

$$C = a_0 + a_1 A_2$$

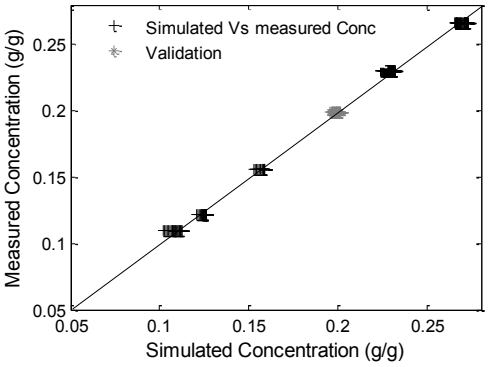

Figure F.7: Comparison between simulated and measured concentration using absorbance 377.83 (nm) and temperature

Hence the smallest SSE between the simulated and the measured concentrations was obtained when the model took into account both absorbance values as well as the temperature.

Publications

Journal Publications

1. E. Aamir, Z. K. Nagy, C.D. Rielly, T. Kleinert, and B. Judat. Combined quadrature method of moments and method of characteristics approach for efficient solution of population balance models for dynamic modelling and crystal size distribution control of crystallisation processes. Ind. Eng. Chem. Res. **2009**, 48, 8575-8584.

2. E. Aamir, Z. K. Nagy and C.D. Rielly. Optimal seed recipe design for crystal size distribution control for batch cooling crystallisation processes. Chem. Eng. Sci. **2010**, 65, 3602-3614.

3. E. Aamir, Z. K. Nagy and C.D. Rielly. Systematic design of supersaturation controlled crystallisation processes for shaping the crystal size distribution. Submitted to AIChE Journal.

4. E. Aamir, Z. K. Nagy and C.D. Rielly. Evaluation of the effect of seed preparation method on the product crystal size distribution for batch cooling crystallisation processes. Accepted. Journal of Crystal Growth and Design.

5. E. Aamir, Z. K. Nagy and C.D. Rielly. Model based control of crystal size distribution under dissolution, growth and nucleation mechanisms. Submitted to Journal of Crystal Growth and Design.

Conference Publications

1. E. Aamir, Z. K. Nagy, C.D. Rielly, Systematic design of supersaturation controlled crystallisation processes for shaping the crystal size distribution, in *Proc. of the 15th International Workshop on Industrial Crystallization (BIWIC 2008)*, Magdeburg, Germany, ISBN 978-952-214-806-3, September 9-11, 280-287, 2008.

2. E. Aamir, Z. K. Nagy, C.D. Rielly, Systematic design of supersaturation controlled crystallization processes, in *Proc. of AIChE 2008: Annual Meeting of American Institute of Chemical Engineering*, Philadelphia, PA, USA, ISBN 978 978-0-8169-1050-2 , November 20-22, 1-9, 2008.

3. E. Aamir, Z. K. Nagy, C.D. Rielly, T. Kleinert, and B. Judat, Efficient crystal size distribution estimation approach for growth dominated crystallisation processes, in *Proc. of the 17th International Symposium of Industrial Crystallization (ISIC 2008)*, Maastricht-The Netherlands, ISBN 978-952-214-806-3, September 15-17, 1733-1740, 2008.

4. E. Aamir, Z. K. Nagy, C.D. Rielly, Seed recipe design for shaping the crystal size distribution for supersaturation controlled crystallisation processes, in M. Louhi-Kultanen, H. Hatakka, (Eds.) *Proc. of the 16th International Workshop on Industrial Crystallization (BIWIC 2009)*, Lappeenranta, Finland, ISBN 978-952-214-806-3, September 9-11, 61-68, 2009.

5. E. Aamir, Z. K. Nagy, C.D. Rielly, Population balance modelling of the dynamic evolution of the crystal size distribution under a size-dependent dissolution mechanism, in M. Louhi-Kultanen, H. Hatakka, (Eds.) *Proc. of the 16th International Workshop on Industrial Crystallization (BIWIC 2009)*, Lappeenranta, Finland, ISBN 978-952-214-806-3, September 9-11, 61-68, 2009.

6. E. Aamir, Z. K. Nagy, C.D. Rielly, Simulation and experimental evaluation of seed and supersaturation control design approaches for crystallisation processes, in S. Pierucci and G. Buzzi Ferraris (Eds.), *Computer-Aided Chemical Engineering 27 – 20th European Symposium on Computer Aided Process Engineering (ESCAPE)*, Elsevier Science, Ischia, Italy, June 6-9, 2010, accepted.

Awards

1. Young researchers award at 8th UKPTF. Won first prize for presenting research work “Model based control of crystal size distribution under dissolution, growth and nucleation mechanisms”.

2. Won first prize at 7th Annual Conference on Polymerisation and Crystallisation. The poster was presented related to research work “Model based control of crystal size distribution under dissolution, growth and nucleation mechanisms”.

Extended Conference abstracts (Peer-reviewed)

1. E. Aamir, Z. K. Nagy, C.D. Rielly, Seed recipe design for shaping the CSD using systematic approach for supersaturation controlled processes, in *Proc. of the 2008 Conference of the British Association for Crystal Growth*, Loughborough, U.K., 6-8 September, 46, 2008.

2. E. Aamir, Z. K. Nagy, C.D. Rielly, Model based control of crystal size distribution under dissolution, growth and nucleation mechanisms, in *Proc. of the 2009 Conference of the British Association for Crystal Growth*, Bristol, U.K., 6-8 September, 61, 2009.

Presentations

1. Systematic design of supersaturation controlled crystallisation processes for shaping the crystal size distribution, poster presentation at *15th International Workshop on Industrial Crystallization (BIWIC 2008)*, held at Magdeburg, Germany, September 9-11, 2008.

2. Efficient crystal size distribution estimation approach for growth dominated crystallisation processes, poster presentation at *17th International Symposium of Industrial Crystallization (ISIC 2008)*, held at Maastricht-The Netherlands, September 15-17, 2008.

3. Model based control of crystal size distribution under dissolution, growth and nucleation mechanisms, oral presentation at *8th UK Particle Technology Forum (UKPTF 2009),* held at Birmingham, U.K., 1-2 June, 2009.

4. Model based control of crystal size distribution under dissolution, growth and nucleation mechanisms, poster presentation, *7th Annual Conference on Polymerisation and Crystallisation*, held at London, U.K., 15-17 March, 2010.